Experimental and computational studies of turbulent separating internal flows

OLLE TÖRNBLOM



Doctoral Thesis in Fluid Mechanics Stockholm, Sweden 2006

Experimental and computational studies of turbulent separating internal flows

by

Olle Törnblom

June 2006 Technical Report from KTH Mechanics SE-100 44 Stockholm, Sweden ISBN 91-7178-416-0

	Typsatt med pdf ETEX och TEXShop.
	•
s d b	Akademisk avhandling som med tillstånd av Kungliga Tekniska Högskolan Stockholm framlägges till offentlig granskning för avläggande av teknolog doktorsexamen fredagen den 8 september 2006 kl 10.15 i Salongen på KTI biblioteket, Osquars backe 31, Kungliga Tekniska Högskolan, Stockholm. Opponent på avhandlingen är Professor Michel Stanislas från École Centra
	de Lille.
	© Olle Törnblom 2006
Ţ	Universitetsservice US AB, Stockholm 2006

Experimental and computational studies of turbulent separating internal flows

Olle Törnblom 2006

KTH Mechanics SE-100 44 Stockholm, Sweden

Abstract

The separating turbulent flow in a plane asymmetric diffuser with 8.5 degrees opening angle is investigated experimentally and computationally. The considered flow case is suitable for fundamental studies of separation, separation control and turbulence modelling. The flow case has been studied in a specially designed wind-tunnel under well controlled conditions. The average velocity and fluctuation fields have been mapped out with stereoscopic particle image velocimetry (PIV). Knowledge of all velocity components allows the study of several quantities of interest in turbulence modelling such as the turbulence kinetic energy, the turbulence anisotropy tensor and the turbulence production rate tensor. Pressures are measured through the diffuser. The measured data will form a reference database which can be used for evaluation of turbulence models and other computational investigations. Time-resolved stereoscopic PIV is used in an investigation of turbulence structures in the flow and their temporal evolution. A comparative study is made where the measured turbulence data are used to evaluate an explicit algebraic Reynolds stress turbulence model (EARSM). A discussion regarding the underlying reasons for the discrepancies found between the experimental and the model results is made. A model for investigations of separation suppression by means of vortex generating devices is presented together with results from the model in the plane asymmetric diffuser geometry. A short article on the importance of negative production-rates of turbulent kinetic energy for the reverse flow region in separated flows is presented. A detailed description of the experimental setup and PIV measurement procedures is given in a technical report.

Descriptors: Fluid mechanics, turbulence, flow separation, turbulence modelling, asymmetric diffuser, boundary layer, PIV, vortex generator, separation control.

Preface

This thesis is an experimental and computational study of turbulent separating flow and its control. The thesis is based on and contains the following articles.

- **Paper 1.** TÖRNBLOM O., LINDGREN, B. & JOHANSSON, A. V. 2006 Measurements of mean flow statistics in a plane asymmetric diffuser with 8.5° opening angle. To be submitted.
- Paper 2. TÖRNBLOM O. & JOHANSSON, A. V. 2006 Structural and temporal characteristics of the flow in a plane asymmetric diffuser with 8.5° opening angle. To be submitted.
- Paper 3. TÖRNBLOM O, & JOHANSSON, A. V. 2006 A Reynolds stress closure description of separation control with vortex generators in a plane asymmetric diffuser. Under consideration for publication in Physics of Fluids.
- Paper 4. Gullman-Strand, J., Törnblom, O., Lindgren, B., Amberg, G. & Johansson, A. V. 2004 Numerical and experimental study of separated flow in a plane asymmetric diffuser. *Int. J. of Heat and Fluid Flow* 25, 451–460.
- Paper 5. TÖRNBLOM O. & JOHANSSON, A. V. 2006 A note on the influence of negative turbulence production on separating flows. To be submitted.
- Paper 6. TÖRNBLOM O., LINDGREN, B. & JOHANSSON, A. V. 2006 Experimental procedures for the investigation of the turbulent flow in a plane asymmetric diffuser by means of stereoscopic high-speed PIV. Technical report.

Division of work between paper authors

The papers included in this thesis have been written in collaboration with other researchers. Below follows a description of the contribution the respondent made to the different papers. Arne V. Johansson acted as supervisor and project leader in all investigations. The respondent made a major part of the writing of the papers, if not otherwise stated below. If parts of the work contained in the article have been presented elsewhere this is also stated.

Paper 1. Early stages of this work were made in collaboration with Björn Lindgren. The stereoscopic PIV measurements were performed by the respondent alone. Minor parts of the early work was presented at the 9th European Turbulence Conference, Southampton, UK, 2002 by the respondent, at the 11th International symposium on application of laser techniques to fluid mechanics, Lisbon, Portugal, 2002 by Björn Lindgren and at the 3rd International Symposium on Turbulence and Shear Flow Phenomena, Sendai, Japan, 2003 by the respondent, with written contributions to the conference proceedings.

Paper 2. The experimental work and data evaluation was done by the respondent.

Paper 3. The theory for the model, the implementation in the computational code and the computations were done by the respondent. Minor parts of the work has been presented at the 5th Symposium on Smart Control of Turbulence, Tokyo, Japan, 2004 by Arne V. Johansson, with written contributions to the conference proceedings.

Paper 4. The article is a blend of two separate written contributions to the 3rd International Symposium on Turbulence and Shear Flow Phenomena in Sendai, Japan, 2003, with the respondent and Johan Gullman-Strand as first authors. The experimental results were a joint work of the respondent and Björn Lindgren and the computations were done by Johan Gullman-Strand. The writing was done both by the respondent and Johan Gullman-Strand. Gustav Amberg and Arne V. Johansson acted as supervisors.

Paper 5. The data evaluation was done by the respondent.

Paper 6. The design, construction and testing of the diffuser wind-tunnel was done on equal terms by Björn Lindgren and the respondent. The PIV setup was done by the respondent alone.

Contents

Prefac	ee	V
Divi	sion of work between paper authors	vi
Chapt	er 1. Introduction	1
Chapt	er 2. Basic concepts	5
2.1.	Governing equations	5
2.2.	Turbulence modelling	6
2.3.	Turbulent separation	8
2.4.	Experimental techniques	13
Chapt	er 3. Results	16
3.1.	Experiments	16
3.2.	Turbulence modelling	19
3.3.	Separation control model	21
3.4.	Negative production in the reattachment zone	24
Chapt	er 4. Concluding remarks and outlook	26
Ackno	wledgments	28
Biblio	graphy	29
Paper	5	
Paper	1. Measurements of mean flow statistics in a plane asymmetric diffuser with 8.5° opening angle	37
Paper	2. Structural and temporal characteristics of the flow in a plane asymmetric diffuser with 8.5° opening angle	73

viii CONTENTS

Paper 3.	control with vortex generators in a plane asymmetric diffuser	93
	umusei	90
Paper 4.	Numerical and experimental study of separated flow	
	in a plane asymmetric diffuser	123
Paper 5.	A note on the influence of negative turbulence producti	on
	on separating flows	143
Paper 6.	Experimental procedures for the investigation of the	

means of stereoscopic high-speed PIV

turbulent flow in a plane asymmetric diffuser by

155



CHAPTER 1

Introduction

Fluid flow is omnipresent in the world we inhabit. This is good for us, because it is hard to imagine life in an all solid world. For example, we all rely on the flow of two fluids, air and blood, for the life essential transportation of oxygen from the atmosphere to our cells. Some people may disagree on calling air a fluid, but from a physics point of view fluids include gases, liquids and plasmas. These have in common the ability to flow and the inability carry static shear loads.

Most flows that we encounter in our macroscopic world are turbulent. Also the airflow down to our lungs and the blood-flow in our aortae may be turbulent. Turbulence arises due to the nonlinear behaviour of flowing fluids, which makes small disturbances grow. The degree of nonlinearity is determined by a parameter called the *Reynolds number* that describes the ratio between the nonlinear inertia forces and the, disturbance damping, viscous forces. Turbulence arises at large Reynolds numbers and the number is named in honour of the British engineer Osborne Reynolds, who in the early 1880s was the first to show the relevance of this ratio for the onset of turbulence (Rott 1990).

Turbulent flow is characterised by irregular and three-dimensional motion of the fluid on a wide range of scales both in space and time. This is demonstrated in figure 1.1 showing a plume of smoke from a volcanic eruption. We can see that the Reynolds number of the plume is large from the wide range of scales present in the photograph. This is because the ratio of the largest and the smallest length scales of a turbulent flow is proportional to $Re^{3/4}$, where Reis a Reynolds number based on the large turbulent scales. The above relation was derived on by the Russian mathematician Andrej Kolmogorov in the early 1940s. The derivation is rather simple and is made on dimensional grounds, but it is based on a very important concept in our present understanding of turbulence, the spectral energy cascade. The basic idea of the energy cascade concept is that the kinetic energy of the turbulent motions is successively transferred from the larger eddies to smaller until viscous dissipation (or internal friction) transforms the kinetic energy into heat. We can then say, a bit simplified, that increasing the energy in the large scale turbulence (increasing the Reynolds number) will allow the kinetic energy to cascade down to even smaller scales before the viscosity is able to damp it out.

1. INTRODUCTION

2



FIGURE 1.1. Mt. St. Helens, May 18, 1980. Photograph by Austin Post, USGS.

The above described property of turbulence, that the range of scales increases with the Reynolds number, is what makes makes accurate predictions turbulent flows so complicated. The computational effort needed to resolve a turbulent flow grows very rapidly with increasing Reynolds number, it is proportional to $Re^{11/4}$ (the required spatial resolution increases in each dimension as $Re^{3/4}$ and the required temporal resolution is proportional to $Re^{1/2}$). As an example Moin & Kim (1997) writes that with a supercomputer capable of 10^{12} floating point operations per second (1 teraflops) it would take several thousand years to make a computation that simulates the flow over a transport aeroplane for one second of flight time. That statement was written nearly ten years ago, before the first teraflop computer, today the fastest computer is capable of approximately 300 teraflops, but even with this terrific computer the simulation would still require nearly a decade of computational time.

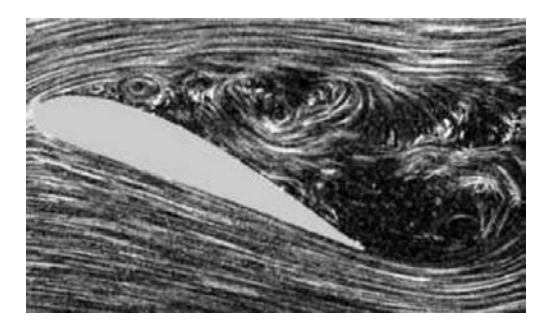


FIGURE 1.2. Flow separation on a wing at high angle of attack.

Spending years of computational time for one second of real time flow over an aeroplane is difficult to motivate. In aeronautics as well as in all other engineering fields that include flow at large Reynolds numbers, other methods have to be used for the evaluation and development of new designs. A natural and traditional way is to use experimental testing to learn about a flow or evaluate a design. Preliminary designs of aeroplanes or cars are often tested using down-scaled models in a wind-tunnel. However, it is not in all cases, economically or physically, feasible to do experimental testing and in those situations the common approach is to use some sort of model for the turbulence in order to circumvent the problem with insurmountable computational times. Much of the engineering turbulence research today is motivated by the need to gain knowledge that can be used to improve modelling predictions.

Shearing (or straining) is a necessary ingredient for disturbance growth and for turbulence to occur and be sustained. A fluid in relative motion to a solid object forms a boundary layer in which the relative velocity between the fluid and the solid is gradually decreased until it is zero at the surface of the solid object. The velocity gradient in a boundary layer causes a shearing of the fluid and boundary layers are thus likely to be turbulent if the Reynolds number is large.

The subject of the present thesis is separating flows. Separation occurs when the flow in the boundary layer next to a solid surface is slowed down and eventually reversed, forming a region of circulating flow between the surface and the outer flow. Figure 1.2 shows a typical example of flow separation, the stall of an aerofoil at high angle of attack. Other situations where separation might occur are the rear end cars and trucks where it leads to increased air resistance and fuel consumption. In ventilation systems the large scale fluctuations of a separation can result in noise and decreased performance. In fact, there are countless number of applications where internal flow separation can be of importance since the phenomenon is quite likely to occur wherever a pipe,

4 1. INTRODUCTION

channel or duct that is used to transport a fluid is subject to a change in geometry or direction.

CHAPTER 2

Basic concepts

2.1. Governing equations

The motions of liquids or gases, which are both fluids, are always consequences of a large number of discrete interactions between the molecules of the fluid. The ways in which the molecules interact determine the bulk properties of the fluid, such as the density, viscosity, heat-transfer coefficient, heat-capacity etc. In many cases it is not necessary to consider the interactions of individual molecules but instead regard the fluid as a continuum. This is what one usually does in fluid mechanics and what will be done in the remaining parts of this thesis.

The flow considered in this thesis and many other flows at moderate speeds can be described by the incompressible Navier-Stokes equations,

$$\rho \left(\frac{\partial \tilde{u}_i}{\partial t} + \tilde{u}_j \frac{\partial \tilde{u}_i}{\partial x_j} \right) = -\frac{\partial \tilde{p}}{\partial x_i} + \frac{\partial}{\partial x_j} \left(\mu \frac{\partial \tilde{u}_i}{\partial x_j} \right) \tag{2.1}$$

$$\frac{\partial \tilde{u}_i}{\partial x_i} = 0. {(2.2)}$$

Cartesian tensor notation has been used when the above equations were formulated and Einstein's summation convention should be applied when the tensorial expression is expanded. The velocity tensor \tilde{u}_i is of first rank and contains the velocities corresponding to the three spatial directions x_i , the scalar \tilde{p} is the pressure and ρ and μ are constants for the density and dynamic viscosity, respectively. The Navier-Stokes equations can be derived by using Newton's second law of motion to relate the change of momentum of an infinitesimal volume of fluid to the forces acting on the same volume. The forces acting in the normal directions on the sides of the control volume can be identified as pressure and give rise to the first term in the right hand side of equation 2.1. Shearing of the fluid give rise to forces that are tangential to the sides of the control volume. If the tangential forces are linearly proportional to the rate of the shearing the fluid is said to be Newtonian. Two of our most common fluids, air and water, have this behaviour. Therefore, much of the fluid mechanics research, including the present work, is concentrated on Newtonian fluids. Viscosity is the property of the fluid that determines how large the tangential force on the control volume sides will be for a given rate of shear, this property is thus a constant in isothermal Newtonian fluids. Equation 2.2 is called the continuity equation and describes the conservation of mass in an incompressible fluid.

When analysing turbulent flows, it is often useful to make a decomposition of the velocity and pressure fields into a mean part and a fluctuating part,

$$\tilde{u}_i = U_i + u_i, \tag{2.3}$$

$$\tilde{p} = P + p, \tag{2.4}$$

this is often called Reynolds decomposition. Here capital letter quantities are ensemble averages and lower-case letters represent fluctuations. Taking the ensemble average of equations 2.1 and 2.2 yields the following equations for the mean flow,

$$\rho\left(\frac{\partial U_i}{\partial t} + U_j \frac{\partial U_i}{\partial x_j}\right) = -\frac{\partial P}{\partial x_i} + \frac{\partial}{\partial x_j} \left(\mu \frac{\partial U_i}{\partial x_j} - \rho \overline{u_i u_j}\right)$$
(2.5)

$$\frac{\partial U_i}{\partial x_i} = 0. {(2.6)}$$

These equations are called the Reynolds equations or Reynolds averaged Navier-Stokes (RANS) equations and are the equations that are solved in turbulence model computations. Note the last term in equation 2.5, which is a derivative of the Reynolds stress tensor $-\rho \overline{u_i u_j}$. The overline is used to indicate that it is an ensemble average. The Reynolds stress appears in the equations for the mean velocity as an unknown extra stress caused by the turbulent fluctuations. The objective of RANS turbulence models is to predict this terms, as accurately as possible, from a limited amount of flow information. Modelling is needed since equations 2.5 and 2.6 only constitute four equations but the number of unknowns are ten (six unknowns in the Reynolds stress tensor due to index symmetry). This is called the closure problem of turbulence modelling.

2.2. Turbulence modelling

Historically, most turbulence models have been based on the concept of a turbulent viscosity or eddy-viscosity. This concept make use of the notion that the momentum transfer in a turbulent flow is dominated by the motion of the large energetic turbulent eddies. In 1877, the same era Osborne Reynolds did his famous pipe-flow experiment in, Joseph Boussinesq suggested that the effects of the turbulent motion in a boundary-layer type of flow could be described by an additional turbulent viscosity. This basic idea is expressed in the generalised Boussinesq hypothesis as

$$a_{ij} = -2\frac{\nu_T}{K}S_{ij},\tag{2.7}$$

which says that the Reynolds stress anisotropy

$$a_{ij} \equiv \frac{\overline{u_i u_j}}{K} - \frac{2}{3} \delta_{ij} \tag{2.8}$$

is linearly proportional to the strain rate tensor of the mean flow

$$S_{ij} \equiv \frac{1}{2} \left(\frac{\partial U_i}{\partial x_j} + \frac{\partial U_j}{\partial x_i} \right). \tag{2.9}$$

K is the turbulent kinetic energy defined as $\overline{u_i u_i}/2$.

The simplest turbulence models describes the turbulent viscosity, ν_T , explicitly in mean flow quantities, the next level of modelling is to introduce one extra transport equation e.g. for the turbulent viscosity as in the Spalart-Allmaras model. These types of models can often perform quite well in well defined flows and are typically used in aeronautics. However, if a model should be able to give reasonable predictions in a wide range of flows, at least two transport equations are needed, by which a turbulence length-scale and a turbulent velocity-scale and hence a turbulent viscosity can be deduced. A large majority of the turbulence models used in engineering applications today can be categorised as two-equation models.

In practically all two-equation models a transport equation for the turbulent kinetic energy, K, is used in order to get a turbulence velocity scale. Then if $K^{1/2}$ is used as a measure of the turbulent velocity scale the turbulent viscosity can be expressed as

$$\nu_T \propto K^m Z^n, \tag{2.10}$$

where Z is the auxiliary 'length scale determining quantity'. A common choice for Z is the turbulence dissipation rate, ε , (giving m=2, n=-1) (Chou 1945) but other quantities such as the inverse of the turbulence time-scale ($\omega=\varepsilon/K, m=1, n=-1$) (Kolmogorov 1942; Wilcox 1988) or the turbulence time-scale ($\tau=K/\varepsilon, m=1, n=1$) are also used.

Models based on the Boussinesq hypothesis usually performs reasonably well in flows where a single component of the Reynolds stress tensor is of significant importance, such as attached boundary-layer flows. However, in more complex flows and flows where effects of rotation are important the eddy-viscosity assumption will fail and more elaborate models have to be used. The natural next step, if an eddy-viscosity model fails, is to use a set of transport equations for the components of the Reynolds stress tensor (6 equations) plus one for the 'length scale determining quantity' (see e.g Launder et al. 1975; Sjögren & Johansson 2000). Such models, called differential Reynolds stress models (DRSM), will in a natural way include history effects for the individual Reynolds stresses and rotational effects on the turbulence. However, the increased computational cost and complicated near-wall modelling have prevented DRSMs from becoming widely used.

An intermediate type of models, that capture more of the turbulence physics than eddy-viscosity models but still only need two transport equations for turbulence quantities, is the family of explicit algebraic Reynolds stress models (EARSM) (see *e.g.* Speziale *et al.* 1991; Wallin & Johansson 2000).

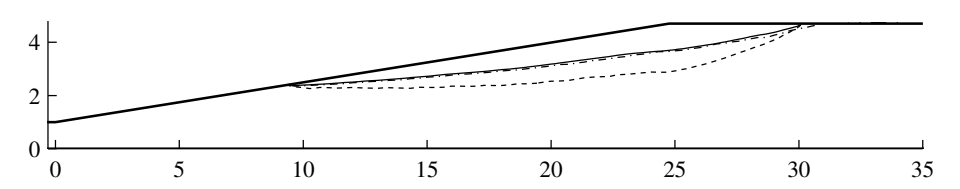


FIGURE 2.1. Comparison between different definitions of the separation bubble; dividing streamline (- - -), zero streamwise mean velocity (—) and backflow 50% of the time $(- \cdot -)$.

An EARSM uses an explicit relation between the Reynolds stress anisotropy and the mean strain and rotation rate tensors. The explicit relation is derived from the transport equations for the Reynolds stress anisotropy after having dropped the advection and diffusion terms under the assumption that the anisotropy varies slowly in space and time.

A fundamentally different approach to turbulence modelling is large eddy simulations (LES) where the large scale turbulent motions are resolved and a model is used to account for the effects of the smaller scales. LES can be expected to capture more of the flow physics as compared to single point closures at the price of an increased computational effort.

Solving the Navier-Stokes equations without any model is often called direct numerical simulation (DNS). This is an accurate but very computationally expensive approach that is limited to flows at relatively small Reynolds numbers.

2.3. Turbulent separation

Separating flows can in general be divided into two main categories depending on the cause of the separation, the two categories are here denoted *geometry induced* and *pressure-gradient induced* separation. In a geometry induced separation a recirculating region forms due to the presence of a sharp edge, for example a corner. The flow is unable to follow the shape of the surface since that would involve extreme acceleration of the flow. A pressure gradient induced separation is a gradual process that occurs in decelerating flows.

2.3.1. Definition of the separated region

Turbulent boundary-layer separation is, in contrary to most laminar separations, a non-stationary phenomenon and the location of the point on the wall where backflow first occurs will fluctuate. The combination of energetic turbulent motions with large spatial scales and a mean flow with low velocities makes the instantaneous flow appear very different from the mean. The most common definition of the separation point is that it is the location where the mean wall shear stress is zero but this measure does not tell us anything about

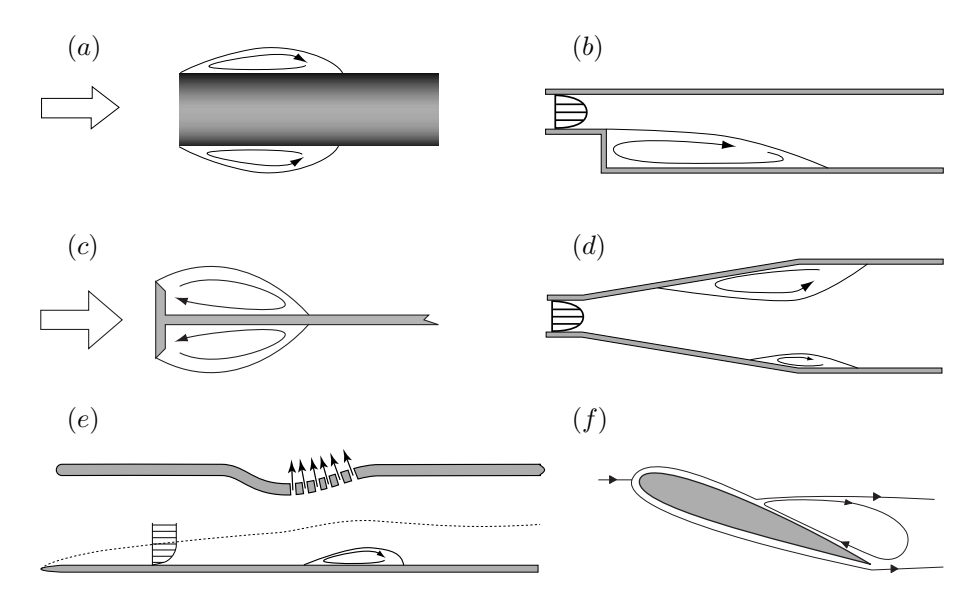


Figure 2.2. Typical geometries for flow separation.

where instantaneous separation may occur. However, the backflow coefficient, χ , defined as the fraction of time that the flow is reversed does tell us something about the separation point movement. Simpson *et al.* (1981*a*) use the term *incipient detachment point* to denote the position where χ =0.01 and defined the detachment point as the point where χ =0.5. Most investigations indicate that χ =0.5 coincide with the point of vanishing wall shear stress (Simpson 1989).

I have found no firm definition of the term separation bubble in the literature. I have encountered three different definitions or interpretations for the limits of a separation bubble: (i) the separation bubble is the mean recirculating region within the dividing streamline (also called separation streamline) reaching between the stagnation points on the wall at the separation and reattachment points, (ii) the separation bubble is the region with mean backflow i.e. below the curve of zero mean velocity and (iii) the separation bubble is the region with backflow more than 50% of the time ($\chi = 0.5$). The differences between these three definitions are illustrated in figure 2.1. In the present thesis the first definition will be used. This seems also as the most established one in the literature.

2.3.2. Typical flow configurations

A few typical flow configurations used in fundamental studies of separating flows are depicted in figure 2.2.

Figure 2.2a shows the geometry induced separation on a blunt edge, the edge can be either the front end of a cylinder or a flat plate. This type of flow has been investigated experimentally by e.g. Cherry et~al.~(1984), Kiya & Sasaki (1983, 1985) and Sigurdson (1995).

The backward-facing step flow depicted in figure 2.2b has been the subject of a multitude of investigations, the inlet flow is usually either a channel flow or a boundary-layer with a free-stream. Experimental investigations of the flow over a backward-facing step are e.g. Etheridge & Kemp (1978), Armaly $et\ al.$ (1983), Jovic & Driver (1994, 1995), Kasagi & Matsunaga (1995) and Yoshioka $et\ al.$ (2001a,b). The flow-case has also been investigated in a direct numerical simulation by Le $et\ al.$ (1997).

Another frequently studied geometry induced separation is that behind a fence or flow-normal plate, shown in figure 2.2c. This type of flow was used in the investigations by Ruderich & Fernholz (1975), Castro & Haque (1987) and Hancock (1999, 2000).

Investigations of pressure gradient induced separation are not quite as common as those where the separation occurs on a sharp edge. Naturally, also this category of separating flows allows for a variety of experimental configurations. Figure 2.2d shows one of many conceivable configurations for internal flow separation, or diffuser separation studies. The present thesis deals with a flow falling under the diffuser category, so the literature related to plane asymmetric diffusers is omitted here and described in more detail in section 3.1. Examples of studies of separating diffuser flow in other geometries are Yin & Yu (1993) and Brunet $et\ al.\ (1997)$.

Flows of the kind illustrated by figure 2.2e, where a boundary-layer under a free-stream is forced to separate and reattach on a plane wall, are found in several investigations e.g. Perry & Fairlie (1975), Dianat & Castro (1991) and Angele (2003); Angele & Muhammad-Klingmann (2005). Comparable axisymmetric geometries are also used in some investigations e.g. Dengel & Fernholz (1990) and Alving & Fernholz (1995, 1996). I include also in this category flows with a free-stream and pressure gradient induced separation and reattachment on smoothly curved walls such as the ones used in the investigations of Stratford (1959) and Song $et\ al.\ (2000)$; Song & Eaton (2002a, 2004b,a). Direct numerical simulations of boundary-layer separation on plane walls have been made by for example Spalart & Coleman (1997), Na & Moin (1998) and Skote & Henningson (2002).

Flows with open, 'aerofoil-like', separations, as the one illustrated in figure 2.2f, have a natural connection to aerospace application and have been covered in several studies. Most notable is perhaps the series of articles by Simpson and co-workers (Simpson et al. 1981a,b; Shiloh et al. 1981).

2.3.3. The boundary-layer flow before separation

Boundary-layer separation on a smooth surface occurs if the boundary-layer is subjected to a strong enough adverse pressure gradient (APG) and if the duration of the APG is long enough. APG boundary-layers grow more rapidly than for instance zero pressure gradient (ZPG) boundary-layers since an APG is associated with a deceleration of the external flow and we get from the continuity equation (equation 2.6) that the wall normal velocity component V will depend on the deceleration of the streamwise velocity U as

$$V(x,y) = -\int_0^y \frac{\partial U(x,y')}{\partial x} dy', \qquad (2.11)$$

in a two-dimensional flow where W=0. The boundary layer will hence grow not only due to momentum diffusion, as in the ZPG case. If the APG is sustained, the velocity in the near-wall region will continue to decelerate and eventually reverse and form a separated region. Turbulent boundary layers can sustain adverse pressure gradients longer than laminar ones due to the increased momentum diffusion caused by the turbulence that more efficiently brings down high-velocity fluid towards the wall.

Another important feature of APG boundary-layers is that the velocity profiles must have an inflection point. This is readily seen if we consider equation 2.5 evaluated at the wall¹,

$$\frac{1}{\rho} \frac{\partial P}{\partial x} = \nu \frac{\partial^2 U_1}{\partial y^2} \bigg|_{y=0}.$$
 (2.12)

Since $\partial P/\partial x$ is positive when we have an adverse pressure gradient $\partial^2 U/\partial y^2|_{y=0}$ must also be positive. But at the outer edge of the boundary-layer $\partial^2 U/\partial y^2$ must be negative, thus the velocity profile must have an inflection point somewhere between the wall and the outer edge. This inflection point will of course coincide with the point of maximum shear in the boundary-layer. With a sustained pressure gradient the inflection point will move further out from the wall according to equation 2.11 and moving with it is also the position of maximum Reynolds shear stress, $-\rho \overline{u}\overline{v}$, since the turbulence production will have its maximum near the inflection point (see e.g. Alving & Fernholz 1996). As the peak in $-\rho \overline{u}\overline{v}$ moves away from the wall the momentum transfer to the near-wall region will diminish and thus facilitate reversal of the near-wall mean flow. The turbulence production $(-\overline{u_iu_j}\partial U_i/\partial x_j)$ in adverse pressure gradient boundary-layers may, in contrast to the turbulence production in zero pressure gradient boundary-layers, have quite large contributions from the normal Reynolds stresses due to the decelerating flow in the streamwise direction (Alving & Fernholz 1996; Simpson et al. 1981a). Alving & Fernholz suggest also that the

 $[\]overline{{}^{1}\text{Note that }} \frac{\partial \overline{uv}}{\partial y} \Big|_{y=0} = \frac{\partial \overline{vv}}{\partial y} \Big|_{y=0} = 0.$

12

reduced shear rates in an APG boundary-layers may decrease the dissipation rate of turbulence due to reduced vortex stretching.

2.3.4. Motions of the separated region

For geometry induced separations several authors have reported a low frequency motion where the reattachment point moves back and forth in a quasi-periodic manner (see e.g. Kiya & Sasaki 1985; Le et al. 1997). In pressure gradient induced separations this type of motion appears to be less organised and no reports of motion at distinct frequencies have been found. However, motions on low frequencies, or wavenumbers, do exist and they are highly energetic but they are spread out evenly in the spectrum (Buice & Eaton 1997). One can speculate that the static separation point in the geometry induced separations gives a more stationary shear layer in which the quasi-periodic motions can appear, and conversely that the constantly changing upstream condition of a pressure induced separation hinders the onset of any periodic motion of the reattachment point. In fact, thinking about the separated region as a coherent region stretching between the separation and reattachment points is a mistake for most flows with pressure gradient induced separation. The PIV velocity fields of the present investigation clearly show that the region of mean backflow is caused by instantaneous backflow in smaller regions often with regions of forward flow in between. The same behaviour is observed in Angele & Muhammad-Klingmann (2005)

2.3.5. Reattachment region

It is well known that the Reynolds stresses decreases rapidly in the downstream direction in the region where reattachment occurs while most other flow quantities undergo changes at a considerably lower rate. Bradshaw & Wong (1972) suggested in an early investigation that the large eddies from the shear-layer were torn apart at reattachment and that one part was convected 'upstream' by the backflow and the other downstream. The size of the vortices would thus be approximately halved. Later investigations have however shown that the sizes of the large scale vortices are similar before and after reattachment.

Song & Eaton (2002b) hypothesise that the positive streamwise velocity gradient, $\partial U/\partial x$, stretch the streamwise vortices so that \overline{vv} and \overline{ww} increase while \overline{uu} is decreased. But they also say that this would successively lead to a redistribution of energy from \overline{vv} to \overline{ww} and back to \overline{uu} due to the presence of the wall or that the energy is dissipated.

In conclusion it may be said that there are still some important open questions remaining to be answered regarding the reattachment flow.

2.3.6. Boundary layer recovery after reattachment

After reattachment a new boundary-layer starts to develop on the wall, the circumstances under which it forms are however rather unusual since large scale turbulence created at the separation is continuously supplied from upstream. Many investigations (e.g. Bradshaw & Wong 1972) report a scenario where a new boundary layer, following the logarithmic law, grows out from the surface under influence of the turbulence from the separation. The turbulence quantities generally recover more slowly than the mean velocities.

2.4. Experimental techniques

The present thesis is mainly based on experimental work. It can be seen from the Navier-Stokes equations (2.1) that the important variables in an incompressible flow are the velocity vector and the pressure. Balancing equation 2.1 in a turbulent flow requires simultaneous measurements of the velocity vectors (knowing all velocities, it is not necessary to measure the pressure in an incompressible flow) in a volume with a spatial and temporal resolution fine enough to resolve the smallest scales of the flow. This is usually not possible in practise, and perhaps not even desired in many cases due to the enormous amount of data such measurements would produce. Instead a common approach in turbulence research is to measure the statistical properties of the flow. Hence the equations subject to balancing are the RANS equations rather than the Navier-Stokes equations.

Measurement techniques applicable to separating flows are limited to methods that are able to determine both the magnitude and direction of the flow. This exclude the use of constant temperature hot-wire anemometry (CTA), an otherwise very common and accurate measurement technique for turbulent flows. In separating flows the traditional measurement methods are instead pulsed hot-wire anemometry (see e.g. Bradbury & Castro 1971) and laser Doppler velocimetry (LDV) (see e.g. Tropea 1995). Both these methods measures the velocity in a single point, or rather the spatial average velocity in a small volume. Such measurement methods have the advantage that a large number of samples can be collected without accumulating unwieldy amounts of data and thus facilitate averaging of a turbulent flow. Particle image velocimetry (PIV), a technique extensively used in the present thesis, is also able to determine both the magnitude and the direction of the flow (if crosscorrelation PIV is used cf. section 2.4.1) and is thus, at least in that aspect, qualified as an appropriate tool for investigations of separating flows. PIV is, in contrast to pulsed hot-wires and LDV, a whole field technique that, in a plane of the flow, instantaneously measures the velocities at several locations. Getting whole field measurements of the flow is of course advantageous if spatial structures are of interest. Drawbacks of PIV are the large amounts of data

14 2. BASIC CONCEPTS

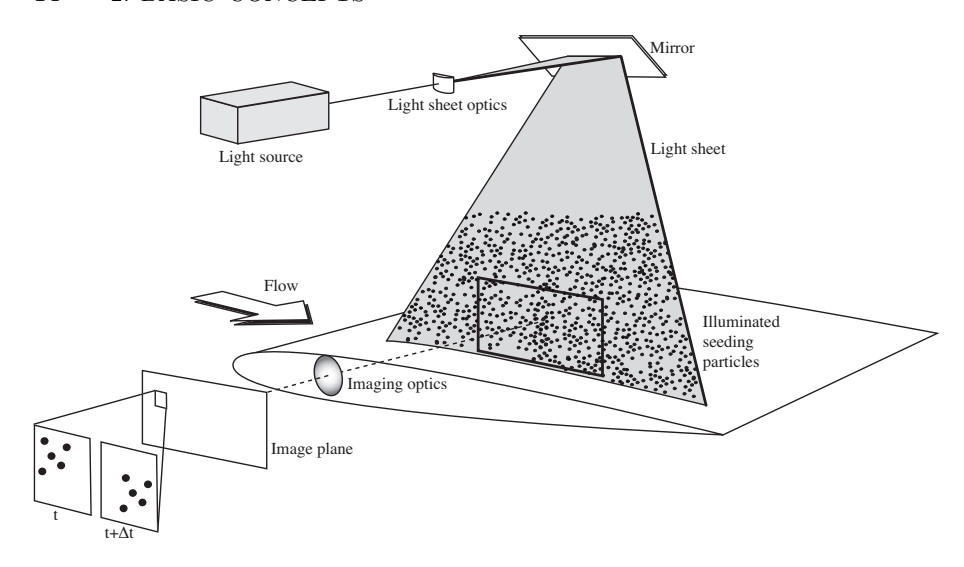


FIGURE 2.3. Sketch of a basic setup for particle image velocimetry.

that have to be processed and stored and the spatial averaging that may bias the measured turbulence levels.

2.4.1. Particle image velocimetry

Measuring the velocity of a moving fluid can be done in many different ways and the present thesis work is based mainly on measurements by particle image velocimetry. A sketch of a basic PIV-setup is shown in figure 2.3. In PIV, particles are used as indicators of the fluid motion, the particles are visualised by illuminating a plane of the flow with a light-sheet. Two consecutive images, separated by the time Δt are taken of the particle pattern. By analysing the displacement of the particle pattern between the images the velocity can be calculated. Introductions to the PIV technique are given in e.g. Westerweel (1993) and Raffel et al. (1997).

A pulsed laser is often used as light-source, the pulses typically have a duration that is smaller than 100 ns and can thus freeze the moving particle pattern. The two images of the particle pattern can either be recorded on two different frames or on the same frame by keeping the camera shutter open and flashing the light-source twice. The latter method is simpler to implement but has a directional ambiguity, which makes it unsuitable for separating flows. The measurement noise is also higher for double exposure PIV. The first method requires that the camera is able to record two individual frames within the time interval Δt , this usually requires special equipment if applied to flows with large velocities e.g. wind-tunnel flows. The advancements in digital image recording techniques during the last decade have made PIV a more versatile and

used measurement technique and digital PIV, *i.e.* PIV using digital cameras, is today the by far most used technique.

The common approach to determine the particle displacements between the two consecutive images is to divide the images into a number of smaller interrogation areas (IAs) cf. figure 2.3. Each IA is used to determine a velocity vector. The average particle displacement within an IA is determined by calculating a spatial correlation, in the case of a double exposed frame it will be an auto-correlation and if two frames are used it is a cross-correlation between the corresponding IAs of the two frames. The two methods are thus often called auto-correlation and cross-correlation PIV respectively. The location of the peak of the correlation function corresponds to the displacement that gives the best match of the particle patterns. The fastest and most common method to compute the correlations is to use discrete Fourier transforms.

Much of the PIV development have been in the methods and algorithms used to determine the particle displacement. Modern algorithms are usually iterative and begin by calculating a large-scale velocity field using large size IAs. The large scale field is then used in order to shift the interrogation areas in the consecutive iteration, this usually leads to a better signal to noise ratio and an increased dynamic range. The iterative process can be continued with smaller IAs until the average number of particles present in a IA becomes the limiting factor. Another method, used in conjunction with an iterative algorithm, is to deform the IAs in correspondence with the flow deformation. The interested reader is referred to e.g. Stanislas et al. (2005) for a review on modern PIV algorithms.

In planar PIV a single camera with its optical axis perpendicular to the light-sheet plane is used. With this method the two velocity components in the light-sheet plane are obtained, therefore this is sometimes called two-component (2C) PIV. In stereoscopic PIV two cameras are used to image the particles in the light sheet and at least one of the cameras has an optical axis not perpendicular to the light sheet plane. This makes it possible to determine the out of plane particle displacement from the displacements measured by the two cameras and a calibration function (see e.g. Scarano et al. 2005; Wieneke 2005). Stereoscopic PIV is hence sometimes also called three-component (3C) PIV.

CHAPTER 3

Results

3.1. Experiments

The papers 1, 2 and 6 of this thesis are directly related to experiments made in a plane asymmetric diffuser flow. The diffuser has an opening angle of 8.5° and the geometry of this flow-case is shown in figure 3.1. Upstream the diffuser is a long plane channel in which a fully developed turbulent channel flow is generated. Smooth radii are used in the transitions between the straight walls and the inclined in order not to introduce disturbances and avoid geometry induced separation at the upstream corner.

The flow in a 10° plane asymmetric diffusers has been studied experimentally earlier by Obi and co-workers, their investigations include LDV measurements of the mean flow and in-plane turbulence components, separation control and Reynolds number dependencies (Obi et al. 1993a,b, 1997, 1999). Another experimental investigation of the 10° diffuser was performed by Buice & Eaton (2000). Several turbulence model investigations have used the plane asymmetric diffuser as a reference case, see e.g. Obi et al. (1993a, 1999), Hellsten & Rautaheimo (1999), Apsley & Leschziner (1999), Gullman-Strand (2004) and Sveningsson (2006). Large eddy simulation (LES) was used to compute the diffuser flow in the investigations of Kaltenbach et al. (1999) and Wu et al. (2006) who studied the general flow characteristics and an internal layer forming on the non-separating side of the diffuser respectively. Herbst et al. (2006) made large eddy simulations of both the 8.5° and 10° diffuser, studying e.g. the Reynolds number dependence of the flow.

The motivation for designing an experiment with a smaller diffuser angle, as compared to the previous experiments, was to get a smaller separation that was expected to: facilitate keeping the flow two-dimensional, make the flow-case more challenging for turbulence models and be more sensitive to control with moderate actuation amplitudes.

Figure 3.2 shows profiles of the average U-velocity, the figure shows also the dividing streamline between the recirculating region and the outer flow. The flow is characterised by a jet-like high velocity region that follows the straight wall and low velocity region along the inclined wall. In between these two regions is a layer of strong shear. From $x/H\approx 6$ and downstream the

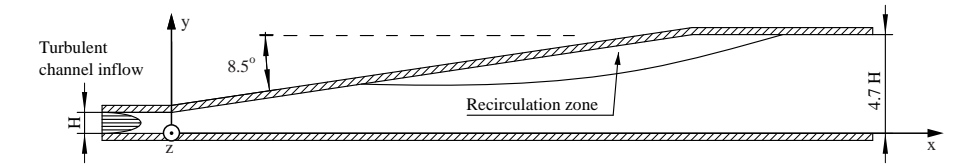


Figure 3.1. The plane asymmetric diffuser.

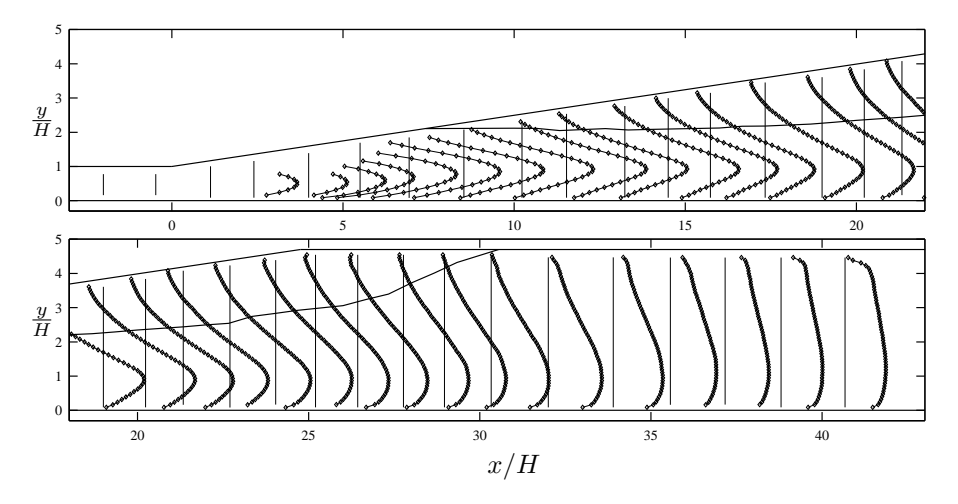


Figure 3.2. Profiles of mean streamwise velocity.

peaks of the U-velocity profiles stay at approximately the same distance from the straight wall, although the peaks are quite vague in the most downstream profiles. A relatively high peak velocity is maintained over the region in x where the separation bubble height is increasing because the effective diffuser angle is nearly zero here due to displacement from the recirculation region. The small decrease in peak velocity which is yet seen in this region is mainly due to a spreading of the peak that most likely can be attributed to turbulent diffusion.

There are easily recognisable inflection points on the low velocity side of the profiles but less pronounced inflection points are also found on the straight wall side of the velocity peak in a region between $x/H\approx 5$ and 10. The inflectional profile on the low velocity side of the diffuser eventually leads to a recirculating region with flow reversal near the inclined wall. The recirculation region, indicated with a solid line in figure 3.2, starts at x/H=7.4 and extends to $x/H\approx 30.5$. A maximum backflow velocity of approximately $0.1U_b$ is found around x/H=21. After reattachment there is a slow development of the profiles towards a symmetric shape although the most downstream of the presented profiles is still asymmetric.

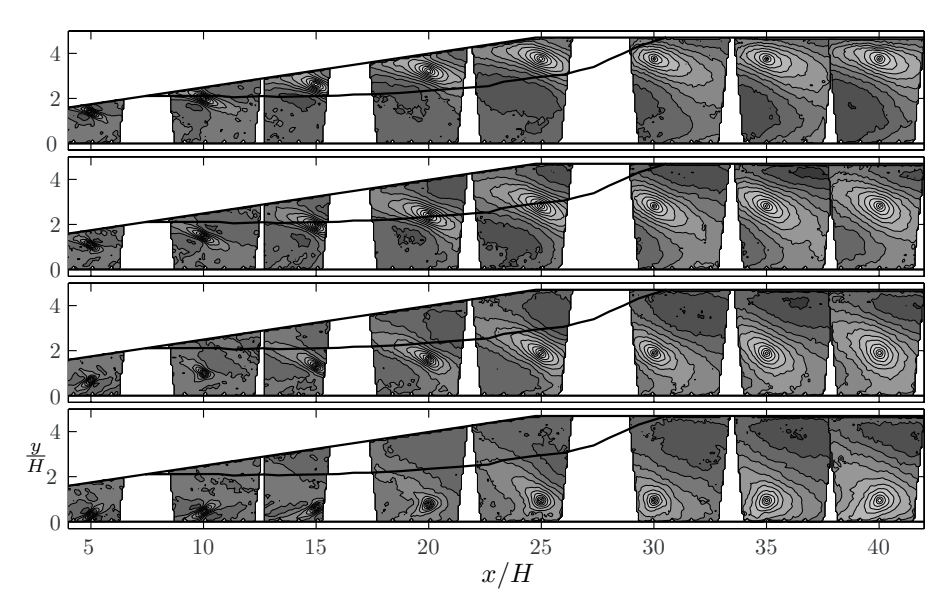


FIGURE 3.3. Auto-correlation functions for the spanwise velocity component at $x_0/H = 5$, 10, 15, 20, 25, 30, 35, 40 and $y_0/h(x) = 0.2$, 0.4, 0.6, 0.8 where h(x) is the local height.

The wide and strong shear-layer below the backflow region in figure 3.2 is the major producer of turbulence energy as it interacts with the incoming turbulence from the channel flow. All the non-zero components in the Reynolds stress tensor, $(\overline{uu}, \overline{vv}, \overline{ww})$ and \overline{uv} have their maxima within this shear-layer.

The peaks of the auto-correlation functions

$$R_{ww}(x,y) = \frac{\overline{w(x_0, y_0)w(x, y)}}{\sqrt{\overline{ww}(x_0, y_0)\overline{ww}(x, y)}},$$
(3.13)

shown in figure 3.3, have a pronounced inclined shape, bearing large resemblance with structures frequently seen in instantaneous realisations of the flow. These inclined structures of spanwise fluctuations have been observed to come in pairs of one positive and one negative structure and negative correlations are indeed found on both sides of the auto-correlation peaks along the minor axes of the peaks. This shape of the correlations can be interpreted as an indication of frequent appearance of large scale vortices with their axes inclined approximately 45° relative to the main flow direction. Horseshoe-like, or hairpin-like vortices are known to appear frequently in turbulent boundary-layers and are described in for example Head & Bandyopadhyay (1981), Robinson (1991), Adrian et al. (2000) and Carlier & Stanislas (2005). The observed structures could be interpreted as the legs of hairpin vortices, this is also supported, in paper 2, by a temporal sequence of instantaneous velocity fields. The sequence

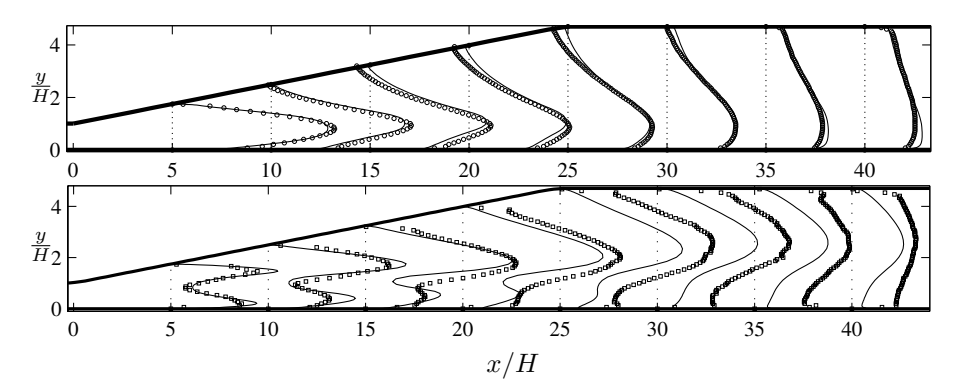


FIGURE 3.4. Comparison between an EARSM computation and experimental data. The top figure compares the streamwise mean velocity and the bottom figure the turbulent kinetic energy.

shows how one of the above described structures (supposedly) moves in the spanwise direction out of the measurement plane followed by the appearance of a typical hairpin vortex head. Studies of structures of the spanwise velocity fluctuations in an xy-plane are surprisingly few so I have not found any investigation discussing these structures and particularly not in conjunction to hairpin or horseshoe vortices. An increased backflow rate was observed as a possible consequence of the ejection from a hairpin vortex, but many aspects of the importance of these structures for the backflow region remains to be revealed.

3.2. Turbulence modelling

Papers 3 and 4 in this thesis involve turbulence model based computations of the flow in the plane asymmetric diffuser. In paper 3 a differential Reynolds stress model (DRSM) is applied to the 8.5° diffuser-flow and in paper 4 the predictions of an explicit algebraic Reynolds stress model (EARSM) are compared to experimental data in both the 8.5° and the 10° diffuser flow.

Making accurate predictions of the plane asymmetric diffuser flow is an extremely difficult task and the turbulence models of today have to evolve further before satisfactory results can be achieved. The diffuser flow is characterised by rapid changes of the mean flow, first at the diffuser inlet a sudden retardation and turning of the flow occurs, then in the flow through the diffuser the mean flow profiles are continuously changing and finally after reattachment the gradients of the mean flow are rapidly diminished. All these rapid changes make history effects of the turbulence important since turbulence produced in one location will immediately be advected to a new location where the circumstances are different. Different levels of modelling are, to different degrees able

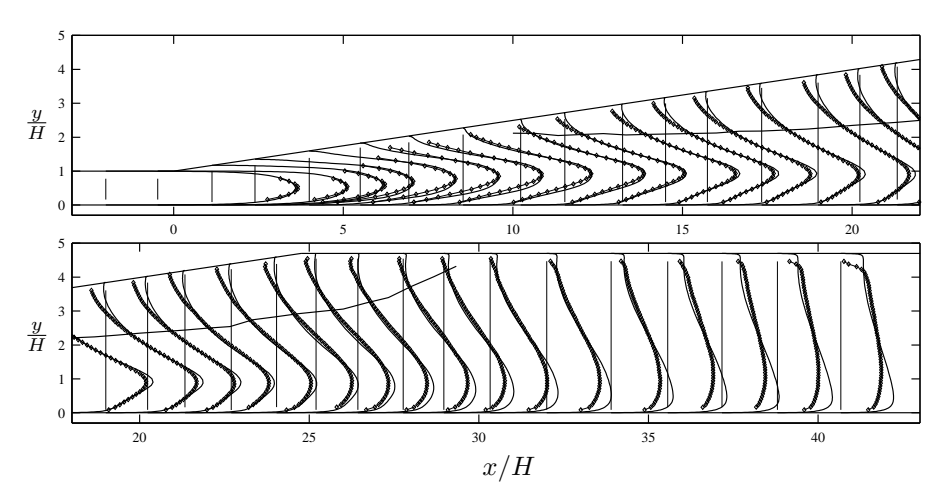


FIGURE 3.5. Mean streamwise velocity profiles from the DRSM computation (solid lines) and the experiment (symbols). The dividing streamline from the experimental data is also included.

to capture history related features. A DRSM can capture the advection and diffusion of Reynolds stress anisotropy while this is not possible in a two-equation model. Therefore it is especially interesting to see how an EARSM can predict this flow, where the advection and diffusion of anisotropy are neglected (in a chosen frame of reference) under an assumption of weak equilibrium implying that the anisotropy variations should be slow in space and time (see e.g. Wallin & Johansson 2000, 2002).

Figure 3.4 compares the EARSM predictions of mean streamwise velocity and turbulent kinetic energy with the experimental data. In comparison with many other models tested in the diffuser (see Hellsten & Rautaheimo 1999) the agreement with experimental data of the present EARSM results can be considered as good. However, the EARSM solution is not totally satisfactory. The most striking difference in the mean flow is perhaps the smaller reverse flow velocity seen in the EARSM solution, this is a problem common to nearly all turbulence models and paper 5 in this thesis give some ideas to the reason behind this. The decreased backflow, results in a reduced size of the separation bubble, which affects the whole flow field. Therefore it is difficult to draw conclusions regarding the reasons behind the underestimated levels of turbulent kinetic energy also shown in figure 3.4 but a hypothesis put forward in paper 4 is that the dissipation rate is overestimated in the EARSM. The overestimated dissipation rate can be interpreted as an underestimation of the turbulence integral length-scale, a quantity that appears to be relatively large and grow fast in the real flow judging from the correlations in paper 2. The predicted separation size for the EARSM was in better agreement with the experimental data (from Buice & Eaton 1997) for the 10° case. This support the idea that the 8.5° diffuser is an even more challenging test for turbulence models due to the weaker pressure gradient.

In paper 3 a differential Reynolds stress model is used, the model uses a recalibrated version of the linear pressure strain rate model presented by Launder et al. (1975). A modified elliptic blending model (see e.g. Manceau 2005) is used for the near wall treatment of the Reynolds stress equations. The inverse turbulence timescale, ω , is used as the auxiliary length-scale determining quantity, the modelling of this equation is essentially the same as that of Wilcox (1994), including the low Reynolds number treatment.

The differential Reynolds stress model gives a good agreement with the experimental data outside the separation from the inlet and down to roughly x/H=25 (see figure 3.5), where the velocity peak in the computation is starting to move towards the straight wall while the experiment shows a velocity peak at an approximately constant distance from the straight wall. After reattachment the gradients of the experimental profiles are reduced faster in the streamwise direction as compared to the computation. This indicates that the DRSM as well as the EARSM has problems with predicting the turbulent length-scales of the flow correctly and thus do not predict the turbulent diffusion correct either. This in not surprising since the two models use the same ω -model to determine the turbulence length-scale. However, it is not believed that simply switching to another length-scale determining quantity will solve this problem. The largest discrepancies between the DRSM solution and the experiment are seen in the separated region where the predicted strength of the backflow is too small.

The presented computations show that more advanced turbulence models are able to describe many of the important features of the diffuser flow but that both more model development and better knowledge of the physics of separating flows are needed to further improve the predictions.

3.3. Separation control model

A new way of modelling the effects of vortex generators in flows where one spatial direction is homogeneous is presented in paper 3. The increased mixing due to the vortex generators is introduced as additional Reynolds stresses through a source term in the Reynolds stress equations. The magnitude of the source term is determined by a model for the vortex generators that is based on wing-theory and the Lamb-Oseen model for viscous vortices. The model takes into account the oncoming flow distribution and use volume forces to account for the induced drag of the vortex generators.

The model was used to test how the position of the vortex generator in the plane asymmetric diffuser affect their efficiency. The integrated flux of

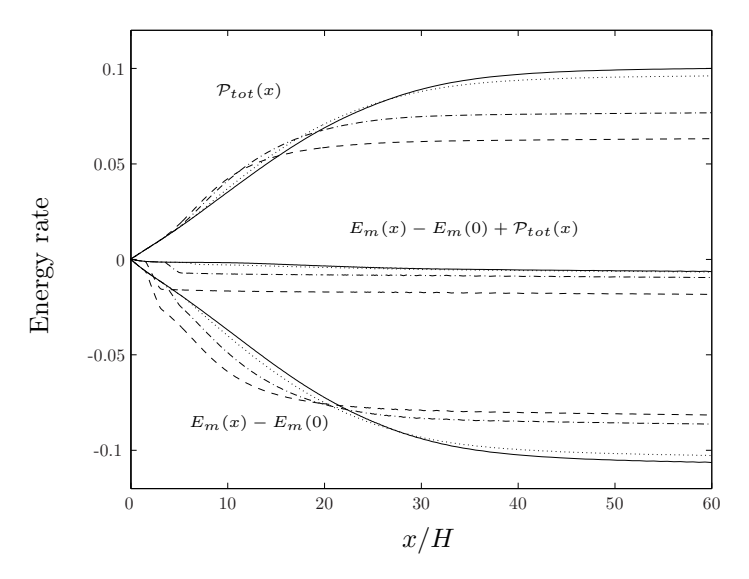


FIGURE 3.6. Redistribution of energy through the diffuser. Line styles corresponds to different x_{VG} -positions of the vortex generators: (—) unperturbed, (—) 1.3H, (—) 3.3H, (…) 5.3H. The lowest set of curves shows the flux of mechanical energy, $E_m(x) - E_m(0)$. The uppermost set of curves shows the total turbulent kinetic energy production, $\mathcal{P}_{tot}(x)$.

mechanical energy over a cross-section,

$$E_m(x) = \int U(x,y) \left(P(x,y) + \frac{1}{2} \rho \left(U(x,y)^2 + V(x,y)^2 \right) + \rho \overline{u}\overline{u}(x,y) \right) dy,$$
(3.14)

shown in the lower set of curves in figure 3.6, was used as a measure of the total efficiency. The decrease of this quantity is a measure of the total pressure loss and it was found that E_m decreases mainly as a consequence of production of turbulence kinetic energy. This is shown in figure 3.6 where also the integrated production rate of turbulent kinetic energy,

$$\mathcal{P}_{tot}(x) = \int_0^x \int \rho \mathcal{P}(x', y) dy dx' \quad \text{where} \quad \mathcal{P} = -\overline{u_i u_j} \frac{\partial U_i}{\partial x_j}, \tag{3.15}$$

is plotted in the uppermost set of curves. The middle set of curves is the sum of E_m and \mathcal{P}_{tot} and can be seen as a representation of the losses due to viscous dissipation and retardation due to the vortex generator drag.

It is apparent from figure 3.6 that in the more efficient configurations the major losses of mechanical energy occur more upstream in the diffuser due to the combined effect of the vortex generator drag and an increase in production rate there. It can also be seen that the increased efficiency is entirely due to

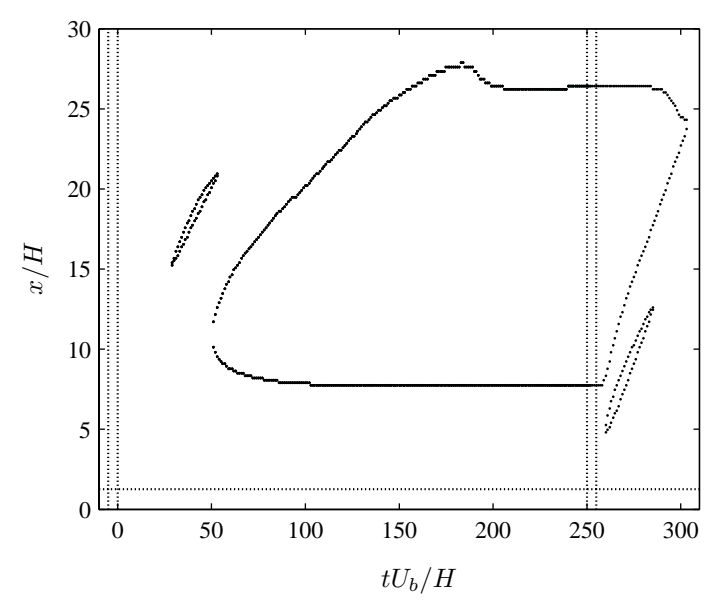


FIGURE 3.7. Separation and reattachment points as functions of time after the forcing is removed and subsequently applied.

a lower integrated production rate of turbulence and that the total pressure losses due to vortex generator drag and viscous dissipation are larger for the more efficient cases.

Profiles of the streamwise velocity reveal that the momentum transfer towards the inclined wall is very efficient in the beginning of the diffuser in the two cases with x_{VG} =1.3 and 3.3. The large levels of momentum near the wall decrease the sensitivity to the adverse pressure gradient and prevent separation. This is achieved by increasing the turbulent momentum diffusion near the wall at an early stage in the diffuser thus avoiding the formation of a separation and a large, strong, turbulence producing shear-layer. The turbulence levels in the worst performing case, x_{VG} =5.3, increase to approximately twice the magnitude of the other cases due to this, which is comparable to the levels in the uncontrolled case. The most efficient of the cases is the one with the flattest velocity profiles and hence with the smallest regions of large mean shear, reflecting the fact that turbulence production, which is proportional to the mean shear, is the major cause of energy losses in this flow.

The temporal evolution of the separation after the vortex generator control is turned off and then on again was investigated using time-accurate quasi-steady RANS-computations. The instantaneous separation and reattachment points are shown in figure 3.7, the dotted vertical line-pairs on the left and right hand sides of the figure indicate the regions where the forcing is ramped down

and up respectively. The vortex generator location, indicated by a horizontal dotted line, and parameters are the same as in the case with x_{VG} =1.3.

We can see that it takes approximately 30 non-dimensional units of time before any separation is formed on the inclined wall, and then it is only a relatively small separation that drifts downstream and eventually disappears. The main separation does not form until 50 time units have passed since the forcing was totally turned off. The main separation spreads out from a position near x/H=11 and reaches a stationary state at $tU_b/H\approx200$ after some transient behaviour where it for a while is larger than the stationary size. The separation point position becomes stationary relatively early as compared to the reattachment point.

When the control subsequently is turned on again the response is surprisingly quick, the separation length starts to diminish 4 units of time after the forcing has reached full strength. A short separated region forms around x/H=5, moves downstream and disappears. The main separation diminishes in a manner, close to, linear with time as the separation point moves downstream. The reattachment point is for nearly 30 units of time unaffected by the control and after approximately 50 time units the separation is totally removed.

An analysis of the instantaneous flow losses during the above described cycle indicates that a net gain could be achieved by turning the control on and off in a cyclic manner.

3.4. Negative production in the reattachment zone

The influences that negative production rates of turbulence kinetic energy may have on the reattachment flow of a separation are discussed in paper 5 of the thesis. A scenario explaining how negative production of turbulent kinetic energy can occur in the reattachment region of separating flows is presented together with data supporting the described scenario.

The production rate of turbulence kinetic energy appears in both the transport equation for the mean-flow kinetic energy and in the transport equation for the turbulent kinetic energy. The production term has opposite sign in the two equations and is normally a dissipative sink term for the mean-flow and consequently normally a source term for the turbulence. Several previous investigations of turbulent separating flows have reported negative production rates, but the magnitude of the negative values have been considered small in comparison with other terms in the turbulence kinetic energy equation. However, in a comparison with the terms in the mean-flow kinetic energy equation, the negative production rates may very well be of significant magnitude. Such a comparison is shown in figure 3.8 and it is easy to see that the negative values plays an important role for the balance of the mean-flow kinetic energy.

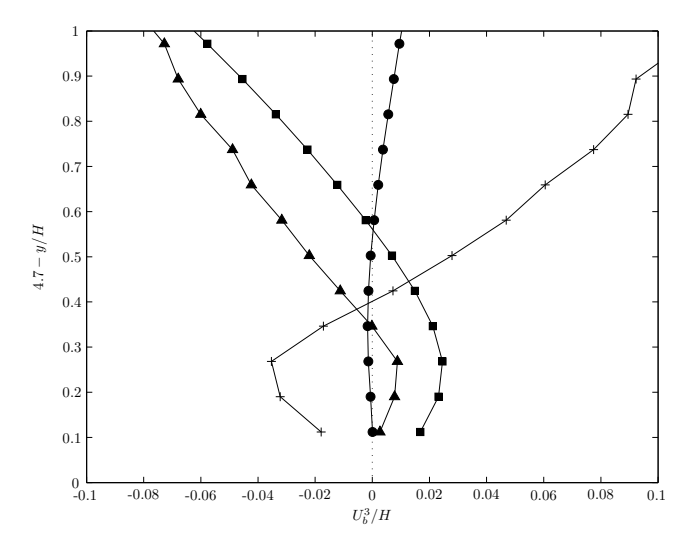


FIGURE 3.8. Measured budget for terms in the transport equation for mean-flow kinetic energy. (\blacktriangle) production rate of turbulent kinetic energy, (\blacksquare) transport related to the mean pressure, (\bullet) advective transport, (+) turbulent diffusion.

Negative production can explain the frequently reported rapid decay of the Reynolds stresses in the vicinity of reattachment. The turbulent energy is partly transferred to the mean flow.

It is also possible that negative production can explain why nearly all turbulence models predict a too small magnitude of the reversed flow velocity in separated flows. Transfer of energy from the turbulence to the mean reversed flow can explain what is missing in the models, in order to capture the correct backflow velocity magnitude.

CHAPTER 4

Concluding remarks and outlook

Different aspects of the flow in a plane asymmetric diffuser with an 8.5° opening angle have been investigated in the present thesis. A majority of the conclusions drawn are believed to be applicable and of importance also in other separating flows.

The experimental investigation of the mean flow and turbulence properties revealed a flow with several interesting characteristics: strong and suddenly imposed shearing, non-equilibrium turbulence, separation, reattachment and turbulence relaxation. All these flow-features are important for turbulence models to predict in an accurate manner in order to get reasonably accurate solutions of the flow as a whole. Evaluation of stereoscopic PIV-data either requires large computational resources or lots of time, therefore there are still many features of the flow that could be investigated, using the already collected images.

The investigation of flow structures revealed some new interesting features of the separating flow. Most interesting is perhaps the inclined structures of the spanwise velocity fluctuations, clearly seen both in the instantaneous realisations of the flow and in the two-point correlations. I have not been able to find any previous report mentioning these kinds of structures, the reasons for this is probably that stereoscopic PIV measurements are still quite rare. The structures can be seen in for example figure 21 in Le et al. (1997), showing an instantaneous field, but the structures are not commented in the text. The role of these structures for the flow is still unclear, but observations made in this thesis indicate that they are likely to be signatures of 'hair-pin like' structures. Further investigations of these structures is one natural continuation of the present work.

The two papers involving turbulence modelling indicate that accurate predictions of the diffuser flow are within reach of today's more advanced turbulence models, but that both models tested had problems with predicting correctly the back flow rate and the long range momentum diffusion occurring after reattachment.

Connected to turbulence modelling is also the finding in paper 5, that negative production rates of turbulent kinetic energy are of importance for the back-flow region. Although DRSMs theoretically can reproduce negative production they are usually not formulated with this phenomenon in focus. Therefore an investigation of model requirements for correct correct predictions of negative production rates is needed. With the EARSM formulation used in Wallin & Johansson (2000) it is not possible to predict negative production.

The vortex generator model is perhaps the result of this thesis that most directly could be useful in engineering fluid mechanics. Some interesting results were also found when applying the model to the diffuser flow. A maybe not so surprising but still important observation was that a vast majority of the flow losses in the diffuser can be directly related to the production of turbulence. The time accurate computations of the formation and removal of a separation give good hope of being able to increase the energy efficiency of the control by successively turning it on and off. This type of quasi-steady results are produced naturally in the present implementation since the system of equations is iterated to steady state in a time-accurate manner. This is however in many cases unnecessarily time consuming, and a continuation of the work on the vortex generator model should include developing a faster route to the steady state solution of the system of RANS and DRSM equations. Then, if the computations are reasonably fast, optimisation of the vortex generator parameters could be performed.

Acknowledgements

First of all, I would like to express my gratitude to my supervisor Professor Arne Johansson for accepting me as his student and for sharing with me parts of his great knowledge in turbulence. I especially appreciate how he has always taken time to discuss my work, seemingly independent of his own workload.

I would also like to thank my co-worker, friend and former office-mate Björn Lindgren for introducing me to the field of fluid mechanics experiments and for being an excellent collaborator.

Special thanks to Stefan Wallin, for his experienced guidance in turbulence modelling and computations as well as for reading and commenting the manuscript of my thesis. Many thanks also to Timmy Sigfrids and Svante Törnblom for their valuable comments on the manuscript.

Gustav Amberg and Minh Do-Quang are acknowledged for answering numerous questions related to the FEMLego package.

I am very grateful to everyone at the department of mechanics for contributing to a stimulating, enjoyable, friendly and relaxed atmosphere. I have particularly enjoyed the coffee breaks, not so much for the coffee as for the vivid discussions and many laughs.

The Swedish Energy Agency are gratefully acknowledged for financing my doctoral studies. The PIV measurement system was acquired with funding from the Knut and Alice Wallenberg foundation which is also gratefully acknowledged.

Lastly and most importantly, I want to thank my wife Jenny and my son Kalle, for their love.

Bibliography

- Adrian, R. J., Meinhart, C. D. & Tomkins, C. D. 2000 Vortex organization in the outer region of the turbulent boundary layer. *J. Fluid Mech.* **422**, 1–54.
- ALVING, A. & FERNHOLZ, H. 1995 Mean velocity scaling in and around a mild, turbulent separation bubble. *Phys. Fluids* 7, 1956–1969.
- ALVING, A. & FERNHOLZ, H. 1996 Turbulence measurements around a mild separation bubble and downstream of reattachment. J. Fluid Mech. 322, 297–328.
- ANGELE, K. 2003 Experimental studiens of turbulent boundary layer separation and control. Ph.D. Thesis, Department of Mechanics, KTH, Stockholm, Sweden, TRITA-MEK 2003:08.
- Angele, K. P. & Muhammad-Klingmann, B. 2005 PIV measurements in a weakly separating and reattaching turbulent boundary layer. *Eur. J. Mech. B/Fluids* **25**, 204–222.
- APSLEY, D. D. & LESCHZINER, M. A. 1999 Advanced turbulence modelling of separated flow in a diffuser. Flow, Turbulence and Combustion 63, 81—112.
- Armaly, B. F., Durst, F., Pereira, J. C. F. & Schönung, B. 1983 Experimental and theoretical investigation of backward-facing step flow. *J. Fluid Mech.* **127**, 473–496.
- BRADBURY, L. J. S. & CASTRO, I. P. 1971 A pulsed-wire technique for velocity measurements in highly turbulent flows. J. Fluid Mech. 49, 657–691.
- BRADSHAW, P. & WONG, F. Y. F. 1972 The reattachment and relaxation of a turbulent shear layer. J. Fluid Mech. 52, 113–135.
- Brunet, L., Calzalbou, J. B., Chassaing, P. & Jervase, L. 1997 Experimental and computational study of pressure effects on turbulent flow in an asymmetric plane diffuser. In 11th Symp. on Turbulent Shear Flows, Grenoble, France, pp. 114–119.
- Buice, C. U. & Eaton, J. K. 1997 Experimental investigation of flow through an asymmetric plane diffuser. *Tech. Rep.*. Department of mechanical engineering, Stanford university.
- Buice, C. U. & Eaton, J. K. 2000 Experimental investigation of flow through an asymmetric plane diffuser. *J. Fluids Eng.* **122**, 433–435.
- Carlier, J. & Stanislas, M. 2005 Experimental study of eddy structures in a

- turbulent boundary layer using particle image velocimetry. J. Fluid Mech. 535, 143–188.
- CASTRO, I. P. & HAQUE, A. 1987 The structure of a shear layer bounding a separation region. J. Fluid Mech. 179, 439–468.
- CHERRY, N. J., HILLIER, R. & LATOUR, M. E. M. P. 1984 Unsteady measurements in a separated and reattaching flow. *J. Fluid Mech.* 144, 13–46.
- Chou, P. Y. 1945 On velocity correlations and the solutions of the equations of turbulent motion. Brown University Quart. App. Math. 3 (1), 38–54.
- Dengel, P. & Fernholz, H. 1990 An experimental investigation of an incompressible turbulent boundary layer in the vicinity of separation. *J. Fluid Mech.* **212**, 615–636.
- DIANAT, M. & CASTRO, I. P. 1991 Turbulence in a separated boundary layer. J. Fluid Mech. 226, 91–123.
- ETHERIDGE, D. W. & KEMP, P. H. 1978 Measurements of turbulent flow downstream of a rearward-facing step. J. Fluid Mech. 86, 545–566.
- Gullman-Strand, J. 2004 Turbulence and scalar flux modelling applied to separated flows. PhD. Thesis, KTH Mechanics, Stockholm, Sweden, TRITA-MEK 2004:16.
- HANCOCK, P. E. 1999 Measurements of mean and fluctuating wall shear stress beneath spanwise-invariant separation bubbles. *Exp. in Fluids* **27**, 53–59.
- HANCOCK, P. E. 2000 Low reynolds number two-dimensional separated and reattaching turbulent shear flow. J. Fluid Mech. 410, 101–122.
- HEAD, M. & BANDYOPADHYAY, P. 1981 New aspects of turbulent boundary-layer structure. J. Fluid Mech. 107, 297–338.
- Hellsten, A. & Rautaheimo, P., ed. 1999 Workshop on refined turbulence modelling. ERCOFTAC/IAHR/COST.
- Herbst, A. H., Schlatter, P. & Henningson, D. S. 2006 Simulations of turbulent flow in a plane asymmetric diffuser. To be published .
- JOVIC, S. & DRIVER, D. 1994 Backward-facing step measurements at low Reynolds number, Re_h =5000. NASA technical memorandum 108807. Ames research center
- JOVIC, S. & DRIVER, D. 1995 Reynolds number effect on the skin friction in separated flows behind a backward-facing step. *Exp. in Fluids* **18** (6), 464–467.
- Kaltenbach, H.-J., Fatica, M., Mittal, R., Lund, T. S. & Moin, P. 1999 Study of flow in a planar asymmetric diffuser using large-eddy simulation. *J. Fluid Mech.* **390**, 151–185.
- Kasagi, N. & Matsunaga, A. 1995 Three-dimensional particle-tracking velocimetry measurements of turbulence statistics and energy budget in a backward-facing step flow. *Int. J. Heat and Fluid flow* 16, 477–485.
- KIYA, M. & SASAKI, K. 1983 Structure of a turbulent separation bubble. J. Fluid Mech. 137, 83–113.
- KIYA, M. & SASAKI, K. 1985 Structure of large-scale vortices and unsteady reverse flow in the reattaching zone of a turbulent separation bubble. J. Fluid Mech. 154, 463–491.
- KOLMOGOROV, A. N. 1942 Equations of turbulent flow of an incompressible viscous liquid. *Journal of Physics USSR* **6** (5), 227–228.

- LAUNDER, B., REECE, G. & RODI, W. 1975 Progress in the development of a Reynolds-stress turbulence closure. J. Fluid Mech. 68, 537–566.
- LE, H., Moin, P. & Kim, J. 1997 Direct numerical simulation of turbulent flow over a backward-facing step. J. Fluid Mech. 330, 349–374.
- Manceau, R. 2005 An improved version of the elliptic blending model application to non-rotating and rotating channel flows. In *Turbulence and shear flow phenomena* 4.
- Moin, P. & Kim, J. 1997 Tackling turbulence with supercomputers. Scientific American Magazine .
- NA, Y. & Moin, P. 1998 Direct numerical simulation of a separated turbulent boundary layer. J. Fluid Mech. 374, 379–405.
- Obi, S., Aoki, K. & Masuda, S. 1993a Experimental and computational study of turbulent separating flow in an asymmetric plane diffuser. In *Ninth Symp. on Turbulent Shear Flows*, p. 305. Kyoto, Japan.
- Obi, S., Ishibashi, N. & Masuda, S. 1997 The mechanism of momentum transfer enhancement in periodically perturbed turbulent separated flow. In 2nd Int. Symp. on Turbulence, Heat and Mass Transfer, Delft, The Netherlands, pp. 835–844.
- Obi, S., Nikaido, H. & Masuda, S. 1999 Reynold number effect on the turbulent separating flow in an asymmetric plane diffuser. In *Proceedings of FEDSM99*, *FEDSM* 99-6976. ASME/JSME Fluids Engineering Division Summer Meeting.
- Obi, S., Ohizumi, K., Aoki, K. & Masuda, S. 1993b Turbulent separation control in a plane asymmetric diffuser by periodic perturbation. In *Engineering turbulence modelling and Experiments* 2, pp. 633–642.
- PERRY, A. E. & FAIRLIE, B. D. 1975 A study of turbulent boundary-layer separation and reattachment. J. Fluid Mech. 69, 657–672.
- RAFFEL, M., WILLERT, C. & KOMPENHANS, J. 1997 Particle Image Velocimetry, A practical guide. Springer Verlag.
- ROBINSON, S. 1991 Coherent motions in the turbulent boundary layer. *Ann. Rev. Fluid Mech.* 23, 601–639.
- ROTT, N. 1990 Note on the history of the Reynolds number. Ann. Rev. Fluid Mech. 22, 1–11.
- Ruderich, R. & Fernholz, H. H. 1975 An experimental investigation of a turbulent shear flow with separation, reverse flow, and reattachment. *J. Fluid Mech.* 163, 283–322.
- Scarano, F., David, L., Bsibsi, M. & Calluaud, D. 2005 S-PIV comparative assessment: image dewarping+misalignment correction and pinhole+geometric back projection. *Exp. in Fluids* **39**, 257–266.
- SHILOH, B. G., SHIVAPRASAD, B. G. & SIMPSON, R. L. 1981 The structure of a separating turbulent boundary layer. Part 3. Transverse velocity measurements. *J. Fluid Mech.* **113**, 75–90.
- Sigurdson, L. 1995 The structure and control of a turbulent reattaching flow. *J. Fluid Mech.* **298**, 139–165.
- SIMPSON, R. L. 1989 Turbulent boundary-layer separation. Ann. Rev. Fluid Mech. 21, 205–234.

- SIMPSON, R. L., CHEW, Y.-T. & SHIVAPRASAD, B. G. 1981a The structure of a separating turbulent boundary layer. Part 1. Mean flow and Reynolds stresses. *J. Fluid Mech.* **113**, 23–51.
- SIMPSON, R. L., CHEW, Y.-T. & SHIVAPRASAD, B. G. 1981b The structure of a separating turbulent boundary layer. Part 2. Higher order turbulence results. J. Fluid Mech. 113, 53–73.
- SJÖGREN, T. & JOHANSSON, A. V. 2000 Development and calibration of algebraic nonlinear models for terms in the Reynolds stress transport equations. *Phys. Fluids* 12 (6), 1554–1572.
- SKOTE, M. & HENNINGSON, D. 2002 Direct numerical simulation of a separated turbulent boundary layer. J. Fluid Mech. 471, 107–136.
- Song, S., Degraaff, D. B. & Eaton, J. K. 2000 Experimental study of a separating, reattaching, and redeveloping flow over a smoothly contoured ramp. *Int. J. Heat and Fluid flow* 21, 512–519.
- Song, S. & Eaton, J. K. 2002a The effects of wall roughness on the separated flow over a smoothly contoured ramp. *Exp. in Fluids* **33**, 38–46.
- Song, S. & Eaton, J. K. 2002b Reynolds number effects on a turbulent boundary layer with separation, reattachment, and recovery. Technical report TSD-146. Mechanical engineering department, Stanford university.
- Song, S. & Eaton, J. K. 2004a Flow structures of a separating, reattaching and recovering boundary layer for a large range of Reynolds number. *Exp. Fluids* **36**, 642–653.
- Song, S. & Eaton, J. K. 2004b Reynolds number effects on a turbulent boundary layer with separation, reattachment, and recovery. Exp. in Fluids 36, 246–258.
- Spalart, P. R. & Coleman, G. N. 1997 Numerical study of a separation bubble with heat transfer. *Eur. J. Mech. B/Fluids* **16** (2), 169–189.
- SPEZIALE, C. G., SARKAR, S. & GATSKI, T. B. 1991 Modelling the pressure-strain correlation of turbulence: an invariant dynamical systems approach. J. Fluid Mech. 227, 245–272.
- STANISLAS, M., OKAMOTO, K., J., K. C. & WESTERWEEL, J. 2005 Main results of the second international PIV challenge. *Exp. in Fluids* **39**, 170–191.
- STRATFORD, B. S. 1959 An experimental flow with zero skin friction troughout its region of pressure rise. *J. Fluid Mech.* 5, 17–35.
- Sveningsson, A. 2006 Turbulence transport modelling in gas turbine related applications. PhD thesis, Chalmers Tekniska Högskola.
- Tropea, C. 1995 Laser Doppler anemometry: recent developments and future challenges. *Meas. Sci. Technol.* **6**, 605–619.
- Wallin, S. & Johansson, A. V. 2000 An explicit algebraic Reynolds stress model for incompressible and compressible turbulent flows. J. Fluid Mech. 403, 89–132.
- Wallin, S. & Johansson, A. V. 2002 Modelling streamline curvature effects in explicit algebraic Reynolds stress turbulence models. *Int. J. Heat and Fluid Flow* 23, 721 730.
- Westerweel, J. 1993 Digital particle image velocimetry theory and application. PhD thesis, Technische Universiteit Delft.

- WIENEKE, B. 2005 Stereo-PIV using self-calibration on particle images. *Exp. in Fluids* 39, 267–280.
- WILCOX, D. C. 1988 Reassessment of the scale-determining equation for advanced turbulence models. AIAA Journal 26 (11), 1299–1310.
- WILCOX, D. C. 1994 Simulation of transition with a two-equation turbulence model. AIAA Journal 32 (2), 247–255.
- Wu, X., Schlüter, J., Moin, P., Pitsch, H., Iaccarino, G. & Ham, F. 2006 Computational study on the internal layer in a diffuser. *J. Fluid Mech.* **550**, 391–412.
- YIN, J.-F. & Yu, S.-Z. 1993 Investigation of turbulent separation-reattachment flow in a curved-wall diffuser. Int. J. Heat and Fluid flow 14 (2), 129–137.
- Yoshioka, S., Obi, S. & Masuda, S. 2001a Organized vortex motion in periodically perturbed turbulent separated flow over a backward-facing step. *Int. J. Heat and Fluid flow* 22, 301–307.
- Yoshioka, S., Obi, S. & Masuda, S. 2001b Turbulence statistics of periodically perturbed separated flow over backward facing step. *Int. J. Heat Fluid Flow* 22, 391–401.

Paper 1

Measurements of mean flow statistics in a plane asymmetric diffuser with 8.5° opening angle

By Olle Törnblom, Björn Lindgren and Arne V. Johansson

KTH Mechanics, SE-100 44 Stockholm, Sweden

The flow in a plane asymmetric diffuser with an opening angle of 8.5° has been studied in detail experimentally with focus on the time averaged flow properties. The inlet condition was fully developed turbulent channel flow at a Reynolds number based on the inlet channel height and bulk velocity of Re = 38000. All non-zero mean velocity and Reynolds stress components have been measured using stereoscopic particle image velocimetry. A separated region is found on the inclined wall with a mean separation point at 7.4 and a mean reattachment point at 30.5 inlet channel heights downstream the diffuser inlet (the inclined wall ends 24.8 channel heights downstream the inlet). Instantaneous flow reversal never occurs upstream of 5 inlet channel heights but may occur far downstream the point of reattachment. A strong shear layer in which high rates of turbulence production are found is located in a region outside the separation. The static wall pressure through the diffuser is presented and used in an analysis of the balance between pressure forces and momentum change. It is demonstrated that production of turbulence stands for the major losses of mean flow kinetic energy.

1. Introduction

Wall bounded fluid flow at large Reynolds numbers may, due to rather small changes in the wall direction or pressure gradient, detach from the wall and form a region of reversed flow next to the wall. This phenomenon is referred to as flow separation. The properties of a flow that separates and a flow in a similar geometry that stay attached can be completely different and separating flow is often associated with decreasing performance of a device due to increased losses of mechanical energy.

Diffusers, *i.e.* ducts with a cross-sectional area that is increasing in the streamwise direction, are necessary in many engineering applications. A typical example is the outlet, or draft-tube, after a hydropower turbine, where it is beneficial to have as low velocity as possible of the water when it leaves the outlet. This is typically achieved with a diffuser. However, if the flow in the draft-tube separates the advantages of expanding are likely to be lost or even

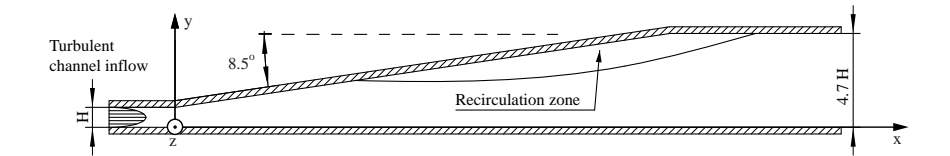


FIGURE 1. The plane asymmetric diffuser of the present investigation. A part of the inlet channel is seen to the left and part of the outlet channel is seen to the right. The view is from the top as referred to figure 2.

turned in to disadvantages due to increased energy losses. A separation will also often introduce low frequency fluctuations in a flow, that in the case of a hydropower plant can lead to increased dynamical loads on the turbine. The draft-tube was used here as one of many possible examples to illustrate the implications of diffuser flow separation, other applications where diffusers are important are: ventilation ducts, rear part of the underside of cars and exhaust ducts of gas-turbines to pick a few examples.

Many studies have been performed on geometry-induced separated flow and adverse pressure gradient flows with separation. The backward facing step and the blunt plate have been investigated by e.g. Cherry et al. (1984), Eaton & Johnston (1981) and Kiya & Sasaki (1983). Ruderich & Fernholz (1975) performed an investigation on a normal bluff plate with a splitter plate using pulsed hot-wire anemometry. Some investigations closer to ours on turbulent boundary layer separated flow are reported by e.g. Perry & Fairlie (1975) Dianat & Castro (1991) and Angele & Muhammad-Klingmann (2005). There is also a review on the topic by Simpson (1989). Here, however we will concentrate on the plane asymmetric diffuser flow with fully developed turbulent channel flow as inlet condition, see figure 1.

The flow in a geometry very similar to ours has previously been studied experimentally by Obi $et\ al.\ (1993a,b,\ 1997,\ 1999)$ and Buice & Eaton (1997, 2000). The opening angle of the diffuser was in all these studies 10° , while it is 8.5° in the present work. Another difference is that the Reynolds number in the previous studies was approximately half of that in the present. The reason for choosing a smaller diffuser opening angle was to reduce the size of the separated region and thereby reduce the unsteadiness of the separation and reattachment points and in combination with a high aspect ratio of the diffuser, achieve a flow less prone to be three-dimensional. It is also likely that predicting a correct separation in a geometry with a smaller opening angle is a more demanding challenge for turbulence models. Support for this presumption was found in

Gullman-Strand *et al.* (2004) where a model giving a reasonably accurate size of the separation bubble in the 10° case predicted too small a bubble when the angle was 8.5° .

The plane asymmetric diffuser flow, originally introduced by Shinnosuke Obi, is a suitable case for fundamental studies of internal flows where the separation occurs on a smooth wall. The inlet conditions are well defined and can in a consistent manner be replicated in computations. The asymmetric shape favours separation on the side with the diverging wall and in this way avoids the problem with an alternating asymmetric separation that one may have in a symmetric geometry. The flow is two-dimensional which facilitates the implementation of the geometry in codes for large-eddy simulation (LES) or direct numerical simulation (DNS) and it also enables averaging in the spanwise direction when computing turbulence statistics. The two-dimensionality will, of course, also simplify testing of turbulence models. The geometry is fairly simple which makes it easy to achieve good computational grids and it has been shown in Brüger et al. (2004) that a numerical conformal mapping for an orthogonal curvilinear grid can be derived for the diffuser. However, the flow taking place inside the diffuser is in contrast to the geometry very complex as it includes a wide range of scales, high turbulence intensities, non-equilibrium turbulence, and high rates of strain.

The first detailed investigation of the plane asymmetric diffuser in the literature known to the present authors, is the investigation by Obi et al. (1993a). In that study the in-plane velocities and Reynolds stresses in a 10° diffuser were measured using a single component laser Doppler velocimeter (LDV) and compared to computations with two different turbulence models. Obi et al. (1993b) continued to study the same flow experimentally by inserting a periodic perturbation to the flow. The perturbation was generated by periodic blowing and suction through a slit in the spanwise direction. They investigated the influence of the perturbation frequency on the size of the separation bubble and found that the largest reduction of the separation size occurred at a non-dimensional frequency, based on the inlet channel height and the inlet channel centreline velocity, around St = 0.03. In Obi et al. (1993b) the location of the separation and reattachment points of the unperturbed flow are determined to be x/H = 10.5 and 26 respectively. The locations were determined by extrapolation from velocity profiles. The curvature radii of the upper and lower corners of the inclined wall were in these studies 4.3H. Obi et al. (1997) further investigated the effect of the perturbation on the production of the turbulent Reynolds shear stress separating the contributions from the perturbation and the mean flow. They found that at the optimum frequency, regarding separation reduction, both the production of Reynolds shear stress and the interaction between the mean flow and the perturbation were enhanced. Obi et al. (1999) investigated the Reynolds number dependence of the 10° diffuser flow, and found that the separation, measured in the centre

region of the diffuser, diminished with decreasing Reynolds number. However, a substantial deficiency in the two-dimensionality of the flow at the lower Reynolds numbers made it difficult to draw any general conclusions regarding the Reynolds number dependency.

Another experimental data-set of the 10° diffuser is presented in Buice & Eaton (1997, 2000). This study had a larger aspect ratio of the inlet channel as compared to the Obi experiment and the corners had a radius of curvature of 9.7H. The investigators primarily used pulsed hot-wires to determine the flow in the separated region and thermal tufts were used to find the separation and reattachment points. They also measured the wall shear-stress using pulsed wall-wire probes. The separation and reattachment points were found at x/H = 6.5 - 7.0 and 29 respectively.

The plane asymmetric diffuser has also been subject to a few computational studies of fundamental character. An extensive numerical study of the 10° case was made by Kaltenbach et al. (1999), who performed a large eddy simulation at a Reynolds number of 1000 based on the inlet channel height and the inlet friction velocity. The LES study by Kaltenbach et al. (1999) used data from the experiments both by Obi and co-workers and by Buice and Eaton for comparison. Kaltenbach et al. scrutinised the data from both experiments and concluded that Obi's experimental data do not satisfy two-dimensional mass conservation in the exit channel of the diffuser and that it is likely that this is a consequence of a significant secondary flow.

The Kaltenbach $et\ al.$ LES data showed good agreement for velocity profiles with the experimental data of both Obi $et\ al.$ and Buice & Eaton. The point of separation agreed well with that found by Buice & Eaton but some discrepancy was found in the location of the reattachment point. A possible reason for this can be the relatively small spanwise width of the computational domain (4H) which may tend to artificially enhance spanwise coherence of large scale structures. Kaltenbach $et\ al.$ (1999) found that the sub-grid scale model plays an essential role to calculate the flow correctly, since sub-grid stresses give a major contribution to the wall-shear stress. The sub-grid scale model must also adapt to the increase in turbulence level in the downstream part of the diffuser.

LES was also the tool used in the study by Herbst et al. (2006) where primarily the Reynolds number dependency of the 8.5° diffuser flow was investigated. Simulations performed at $Re_H = U_b H/\nu = 9000$, 18000 and 40000 revealed a trend towards an increasing size of the separation with increasing Reynolds number. However, the Reynolds number dependence appeared to be diminishing with increasing Reynolds number so that one may expect a constant separation size for Reynolds numbers over a certain limit. Much of the physics behind this, slightly counter-intuitive, phenomenon remains to be clarified. Herbst et al. also shows that the tendency towards separation on

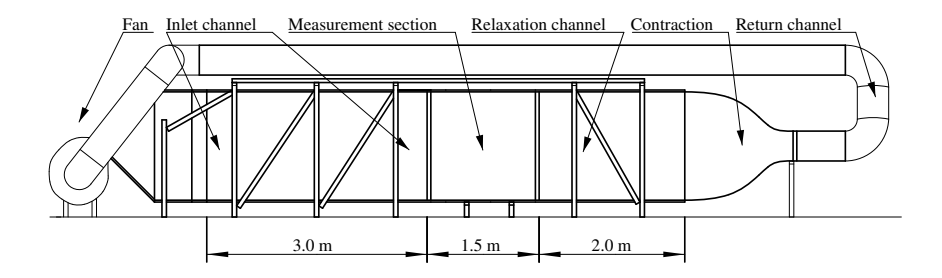


FIGURE 2. The wind-tunnel used in the experiments. The flow is circulating counter clockwise.

the curved upper corner due to flow curvature follows an opposite trend, at the lowest Reynolds number a small separation is seen but it disappears with increasing Reynolds number.

Several turbulence model investigations have used the plane asymmetric diffuser as a reference case. In an Ercoftac workshop (Hellsten & Rautaheimo 1999) the results from computations of the 10° case using a great number of turbulence models are summarised. Gullman-Strand (2004) made an extensive investigation of the performance of explicit algebraic Reynolds stress and scalar flux models in both the 8.5° and the 10° diffuser.

In this study, we will concentrate on the flow in the diffuser and its nearby surroundings, with the main purpose of providing data of average flow properties, such as mean velocities, all non-zero Reynolds stress components and mean pressure. Integrated quantities describing conservation of mass, momentum balance and transformation of mean flow mechanical energy are also presented. The separated region is given special attention in that we look at measures such as the back-flow coefficient and the dividing streamline for the separated region.

2. Experimental setup

The experimental setup and the measurement procedures are described in detail in Törnblom *et al.* (2006).

2.1. Description of the wind-tunnel

The experiments were performed in a closed loop wind-tunnel built specifically for this investigation. The wind-tunnel can be seen in figure 2. It consists of a blowing centrifugal fan delivering 11 kW of power followed by a section transforming the rectangular cross section shape of the blower outlet to another one with much higher aspect ratio. In this section splitter plates and screens ensure an even distribution of the fluid over the cross section area. The transformer is

followed by a straight duct (settling chamber) which contains two screens at its upstream end to further even out mean flow variations. The settling chamber is followed by a two-dimensional contraction. The contraction further evens out mean flow variations and decreases the cross section height to 30 mm.

The contraction is followed by a turbulence generating grid and a 3.2 m long channel with a cross section area (width to height) of $1525 \times 30 \text{ mm}^2$. The length to height ratio of the channel is thus larger than 100 ensuring fully developed channel flow at the outlet (see Comte-Bellot 1965), this is important in order to obtain a well defined inlet condition to the diffuser. At the end walls (limiting the spanwise width of the channel) the boundary layers are removed by means of suction trough a 100 mm long perforated region located at the downstream end of the inlet channel. This is done to prevent the end wall boundary layer from separating in the adverse pressure gradient of the diffuser since such a separation would destroy the two-dimensionality of the mean flow. The high aspect ratio, 50 at the diffuser inlet, is another important premise for achieving a high degree of spanwise uniformity.

The inlet channel is followed by the diffuser, which has an inclined wall on one side and a straight wall on the other. The end walls are straight and equipped with three rows of vortex generators to further minimize the risk of boundary layer separation. The inclined wall has an angle of 8.5° , see figure 1. Both the convex upstream and the concave downstream corners of the inclined wall are rounded with a radius of 300 mm (10H). The inclined wall is made of a framework of solid aluminium beams and 25 mm thick plywood plates. A glass window along the centreline of the inclined wall gives optical access to the measurement section. The straight wall and the end walls are made of plexiglas so as to enable the use of optical measurement techniques such as LDV and PIV. The straight wall is equipped with pressure taps in a row along the centreline in the downstream direction at an interval of 25 mm. There are also pressure taps in a spanwise directed row 100 mm upstream the diffuser inlet at 100 mm interval. These pressure taps are used to check the two-dimensionality of the incoming flow.

The diffuser is followed by an outlet channel which is 141 mm high (4.7H) and 2.5 m long. The purpose of this channel is to avoid upstream influence on the flow from devices located further downstream. This channel is partly made of plexiglas to facilitate measurements and partly of plywood. Here, there are also two hatches giving access to the inside of the tunnel. Along the extent where the outlet channel is made of plexiglas there are also pressure taps along the centreline with the same interval as in the diffuser. Open slots at the end of the outlet channel ensure that the pressure in the measurement section is near that of the atmosphere, minimizing the risk of a changed diffuser geometry due to bulging of the diffuser walls. The slots are also important in that they give a point with constant reference pressure in the wind-tunnel circuit.

The outlet channel is followed by a three-dimensional transformer changing the aspect ratio of the cross section area towards unity. The contraction is followed by a heat exchanger which is necessary in a closed return wind-tunnel to keep the temperature steady. A temperature sensor is located in the outlet channel and a computer logged the temperature which was found to be steady within ± 0.5 °C. This is sufficient since the experiments performed here are not very temperature sensitive, due to the fact that an optical measurement technique is used instead of e.g. hot-wire anemometry.

Following the heat exchanger the cross section is converted from a rectangular to a circular shape. A pipe with 400 mm diameter then leads the flow back to the fan. At the end of the pipe the seeding particles, in this case smoke, see section 3.2) are injected into the flow.

3. Measurements

3.1. Pressure measurements

Pressures were measured using a Furness Control FCO 510 differential pressure transducer with an accuracy of 0.25% of full scale (2000 Pa). The holes through which the pressure is measured are drilled directly in the plexiglas of the plane diffuser wall and have a diameter of 0.4 mm.

The skin-friction of the inlet channel flow was measured at x/H=-3.3 using a Preston tube. The friction velocity was calculated using

$$u_{\tau} = \frac{(a\Delta p^{+2} + b\Delta p^{+3.5})^{1/8}\nu}{d} \tag{1}$$

(see e.g. Österlund 1999, page 150), where a=28.44 and $b=6.61\cdot 10^{-6}$ are empirical coefficients, $\Delta p^+ = \Delta p d^2/(\rho \nu^2)$ is the non-dimesionalised pressure difference measured with the Preston tube, ν is the kinematic viscosity of the air and d is the outer diameter of the Preston tube.

During the PIV-measurements the Preston tube was used to continuously monitor u_{τ} and regulate the fan-speed in order to have a constant velocity. The air density and viscosity used in equation 1 was calculated based on continuous measurements of the atmospheric pressure and the air temperature in the wind-tunnel.

3.2. PIV measurements

Here, a brief description of the PIV-setup and measurements is given, interested readers are referred to Törnblom *et al.* (2006), for more details. Stereoscopic PIV was used to measure the mean velocities and turbulence statistics in all three spatial directions. The setup for the measurements is shown in figure 3. The laser light sheet is horizontal and in the diffuser mid-plane, the two cameras image the measurement plane at an angle of around 30 degrees with respect to its normal direction. The laser head and the cameras are mounted

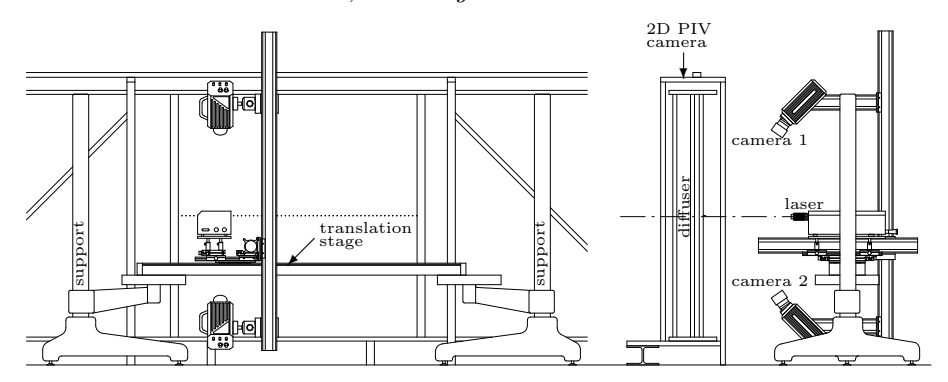


FIGURE 3. A sketch of the PIV setup. The y- and x-directions (cf. figure 1) are perpendicular into the paper plane in the left and right views respectively.

on a translation stage which allows the setup to be moved for measurements at different streamwise stations without changing the camera-lightsheet geometry.

The PIV-system consists of a New Wave Pegasus diode pumped Nd:YLF laser with dual heads, two Photron Ultima APX-RS cameras with 1024×1024 pixels and acquisition hardware and software from LaVision. Nikon f=50 mm lenses are used on the cameras at a large aperture together with a Scheimpflug arrangement which enable oblique focusing on the light sheet. The average light sheet thickness was estimated to 1.5 mm by analyzing the correlation peak widths of cross-correlations between particle images from different cameras, taken at the same instant (Wieneke 2005).

When sampling for statistics, double image sets are recorded at a rate of 750 Hz, every 10th set is then transferred to the computer giving a set of 308 samples. At each measurement position this procedure is repeated ten times, so that a set of totally 3080 samples are collected. The total time required for collecting such a set is approximately one hour. The procedure was repeated for 18 different streamwise positions in the diffuser. The time between frames was optimized for each set of pictures and varied with the downstream position.

An original calibration of the stereoscopic setup was first performed in the wider outlet channel of the diffuser using a calibration plate. Then, at each measurement position a correction of the original calibration was made using the self-calibration method in the DaVis software (see Wieneke 2005). This procedure gave a matching of the images from the two cameras which deviated less than 0.1 pixels.

The recorded images are preprocessed by subtracting a sliding average of five, in the time sequence, consecutive images. The velocity vector fields are calculated using multi-pass cross-correlation where the first pass is performed

with 64×64 pixel interrogation areas followed by two passes with 32×32 pixel areas, the interrogation areas are 50 percent overlapping. The physical size of the 32×32 pixel interrogation areas is 4.7×4.7 mm², or $0.16 \times 0.16H^2$ in non-dimensional units. The cross-correlations are calculated on images that are dewarped according to the calibration mapping function and deformed according to the displacement field determined in previous passes, the method is similar to that of Scarano & Riethmuller (2000).

Close-up measurements were performed in a region near the separation point, using two-component PIV. The camera was then positioned over the measurement section as indicated in figure 3 and interrogation area size was $0.94 \times 0.94 \text{ mm}^2$.

The air was seeded with smoke from a smoke-generator using a mixture of glycerol and water. The smoke was inserted just upstream of the fan and was sufficiently spread out in the measurement section due to the mixing in the fan and in the inlet channel. An estimate of the particle size based on recorded particle images and using relations for the Airy pattern given in Raffel et al. (1997), gave that the particles are approximately 3 μ m in diameter. Assuming Stokes drag, this particle diameter corresponds to a response time of the same order as the Kolmogorov time-scale of the inlet channel flow.

3.3. Measurement quality

A typical value for the measurement error in digital PIV with 32×32 pixel interrogation areas is 0.05 to 0.1 pixel (Westerweel 1997), given that the measurement conditions fulfil a number of criteria. In the forthcoming these conditions and criteria are discussed in conjunction with the present experiment.

It was ensured in all measurements that the particle concentration was sufficient, i.e. $\geq \! 10$ particles in each interrogation area according to Keane & Adrian (1992) .

The average out of plane velocity is zero and the maximum turbulent velocity, $\sqrt{\overline{ww}}$ is approximately 1.3 m/s. If the distribution of w is assumed to be Gaussian, the light sheet thickness is 1.5 mm and the time between frames $100~\mu s$, one will find than 99% of the samples will fulfil the "one quarter rule" given by Keane & Adrian (1990). Hence, errors due to out of plane loss of pairs should be small. Problems with in-plane loss of pairs are avoided in the cross-correlation algorithm used, by shifting the correlated areas according to the local displacement. Furthermore, will the interrogation window deformation of the cross-correlation algorithm reduce the correlation noise due to velocity gradients (Scarano & Riethmuller 2000).

The degree of peak-locking in the measured data has been investigated and found to be very small. Contributing to the small degree of peak-locking is the particle image diameter, which is around 2 pixels, and the Wittaker interpolation used in the cross-correlation algorithm.

The present stereoscopic setup will result in a decreased uncertainty of the measured in-plane components as compared a similar non-stereoscopic setup. The uncertainty of the out of plane component is approximately twice that of the in-plane components.

3.4. Comparison between fine and coarse resolution measurements

Fine resolution measurements, using two-component PIV, were performed in a region around the separation point. Figures 5, 9 and 12 compare the measurements with finer and coarser resolution. The agreement in the streamwise mean velocity is very close and the wall normal mean velocities collapse without any visible bias, although the profiles are somewhat shaky.

The measured second order statistics appears to be biased towards smaller values in the coarse data-set. This is most likely due to the, in PIV inevitable, spatial low-pass filtering which follows from the integration over the interrogation areas. Stereoscopic PIV will, in one direction, suffer more from spatial filtering as compared to two-dimensional PIV (see van Doorne 2004). This is because of the oblique viewing through a light-sheet with a nonzero thickness. In the present stereoscopic setup the measurement volume is largest in the ydirection, in which the effective measurement volume size can be determined, using the interrogation area size (4.7 mm), the light sheet thickness (1.5 mm) and the camera angle, to be $4.7 + 1.5 \tan(30^{\circ}) \approx 5.6$ mm as compared to 4.7 and 1.5 mm in the x and z-directions respectively. The stronger spatial filtering in the y-direction can be seen in the comparison of the measurements of \overline{vv} in figure 9b where the discrepancy is larger than in the measurements of $\overline{u}\overline{u}$ shown in figure 5b. The spatial filtering has a smaller impact on the fine resolution measurements where the length scale of the interrogation areas is 1/5 of that in the coarser measurements and the viewing direction is perpendicular to the light-sheet.

The spatial filtering can be expected to have larger impact on the fluctuation levels measured close to walls and in the upstream part of the diffuser where a larger part of the turbulence energy spectrum resides in scales smaller than the measurement volume.

4. Results

We here focus on the mean velocity components and fluctuation intensities. Results are also presented for the turbulent kinetic energy and its production. Properties of the stream function and back-flow coefficient, which both characterize the mean properties of the separated region, are presented. The static pressure coefficient along the straight wall is also shown as well as some integrated quantities which give insight into the mass, force and energy balance of the flow.

4.1. Velocity components

Here, results for all mean velocity components and all nonzero Reynolds stress components are presented with the exception of the mean spanwise component which is zero within the measurement accuracy. A right-handed coordinate system is defined with x in the "streamwise" direction, y in the "wall-normal" direction and z in the spanwise direction, see figure 1. The corresponding average velocities are denoted by U, V and W respectively. The y-component is of course only normal to the lower, straight wall, but because of the relatively small opening angle, we prefer here to refer to the x and y velocity components as streamwise and wall-normal. In all figures the spatial coordinates are normalized with the inlet channel height, H = 30 mm, and the velocities are normalized with the inlet channel bulk velocity, $U_b = 18.8$ m/s, defined as

$$U_b = \frac{1}{H} \int_0^H U \, \mathrm{d}y. \tag{2}$$

Due to lack of near wall data from the inlet channel U_b is approximated using the centreline velocity, U_{cl} , in the inlet channel and Dean's empirical relation

$$\frac{U_{cl}}{U_b} = 1.28 \left(\frac{U_b H}{2\nu}\right)^{-0.0116}.$$
 (3)

Measurement points near the walls have deliberately been removed in the figures showing the coarser data-set of the complete diffuser. This was done because of the increased measurement uncertainty of these data-points due to possible overlap of the relatively large interrogation areas and the wall.

4.1.1. Streamwise mean and fluctuating velocities

The diffuser flow is characterised by a jet-like high velocity region that follows the straight wall and low velocity region along the inclined wall, see figures 4 and 5a. In between these two regions is a layer of strong shear. From $x/H\approx 6$ and downstream the peaks of the U-velocity profiles stay at approximately the same distance from the straight wall, although the peaks are quite vague in the most downstream profiles. A relatively high peak velocity is maintained over the region in x where the separation bubble height is increasing because the effective diffuser angle is nearly zero here due to displacement from the recirculation region. The small decrease in peak velocity which is yet seen in this region is mainly due to a spreading of the peak that most likely can be attributed to turbulent diffusion.

There are easily recognisable inflection points on the low velocity side of the profiles but less pronounced inflection points are also found on the straight wall side of the velocity peak in a region between $x/H\approx 5$ and 10. The inflectional profile on the low velocity side of the diffuser eventually leads to a recirculating region with flow reversal near the inclined wall. The recirculation region, indicated with a solid line in figure 4, starts at x/H=7.4 and

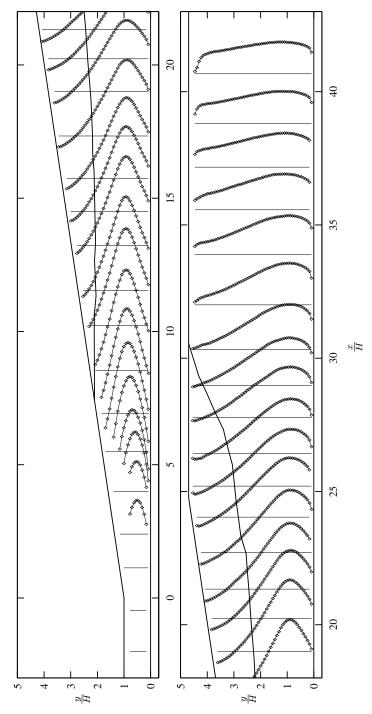


FIGURE 4. Streamwise mean velocity, $(U_{\rm fig} = 5U/U_b + x/H)$. The vertical lines indicate zero level for each streamwise velocity profile and a solid contour indicates the path of the dividing streamline.

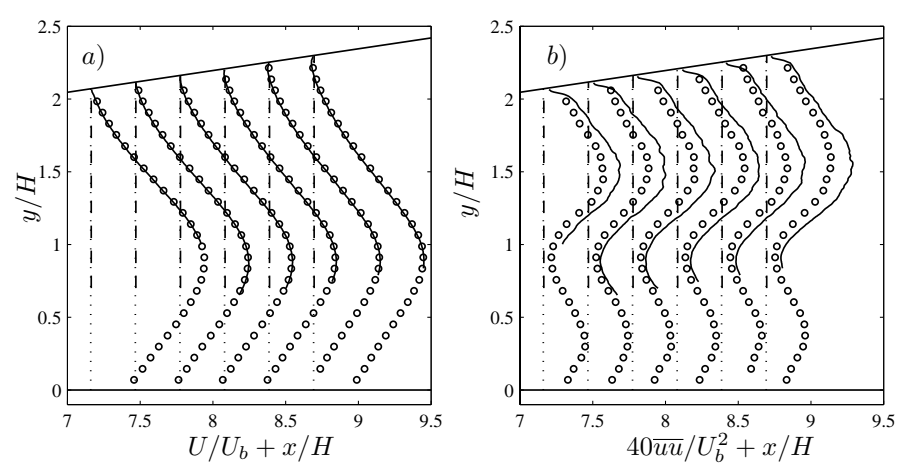


FIGURE 5. Fine resolution PIV measurements around the separation point (solid lines) compared with the courser data-set (symbols).

extends to $x/H\approx30.5$. A maximum backflow velocity of approximately $0.1U_b$ is found around x/H=21. After reattachment there is a slow development of the profiles towards a symmetric shape although the most downstream of the presented profiles is still asymmetric.

The wide and strong shear-layer below the backflow region in figure 4 is the major producer of turbulence energy as it interacts with the incoming turbulence from the channel flow. All the non-zero components in the Reynolds stress tensor, $(\overline{uu}, \overline{vv}, \overline{ww})$ and $\overline{uv})$ have their maxima within this shear-layer.

The fluctuating streamwise velocity is in general very large in this flow. The fully developed turbulent inlet flow generates a \overline{uu} distribution that is symmetric, with peaks close to each wall and a local minimum at the centreline where the streamwise velocity gradient is zero. The development of these two peaks is rather different as the flow propagates downstream through the diffuser. The peak close to the straight wall is eventually almost overtaken by the growing local maximum emerging from the upper part of the inlet channel. This peak grows and reaches its maximum at about x/H=20-25, see figure 6. The location of this peak detaches from the inclined wall and follows the strong shear-layer outside the separated region. Eventually the fluctuating streamwise velocity reaches an almost flat distribution across the outlet channel with small variations along the profile. As the flow in the outlet channel is developing, a turbulent channel flow distribution will eventually be recovered far downstream. It can be noted that this channel flow will have the same Reynolds number as the inlet channel flow.

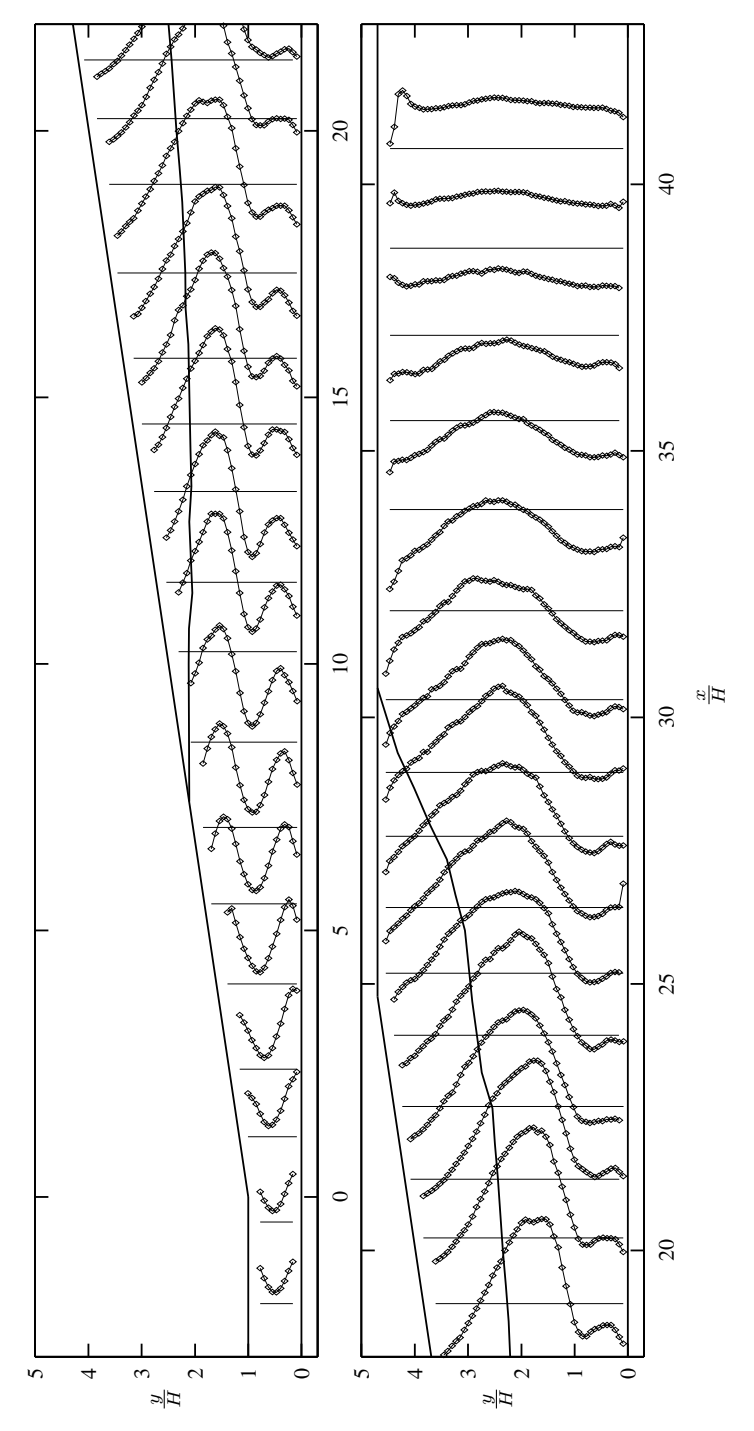


FIGURE 6. Variance of the streamwise fluctuating velocity, $(\overline{u}\overline{u}_{\mathrm{fig}} = 200\overline{u}\overline{u}/U_b^2 + x/H)$.

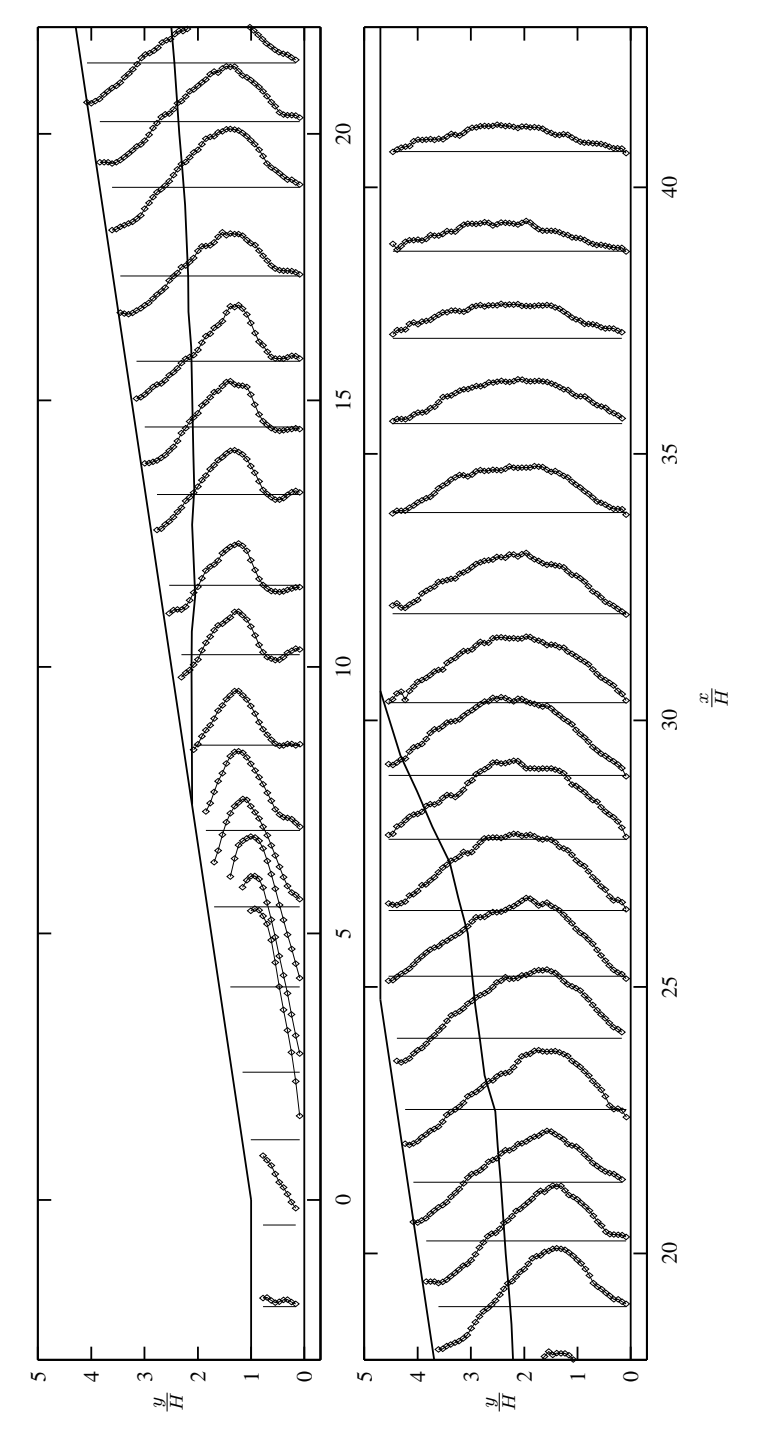


FIGURE 7. Wall-normal mean velocity, $(V_{\rm fig}=100V/U_b+x/H)$.

4.1.2. Wall-normal mean and fluctuating velocities

The wall-normal velocity, V (i.e. normal to the straight wall, and almost normal to the inclined wall) is very small in most parts of the diffuser, typically around 20 times smaller than U. Close to the corner at the diffuser inlet, where the rather abrupt change in the direction of the wall causes the flow to turn, locally high values of the wall-normal velocity are found, see figure 7.

Several conclusion regarding the mean flow can be drawn from the V-profiles, bearing in mind the direct relation between velocity gradients $(\partial V/\partial y = -\partial U/\partial x)$ following from the continuity equation. It can be seen that the positions of maximum positive gradient of V corresponds to the positions of the maximum velocity peaks in U, which means that the deceleration of U is largest at its peaks. The small regions of negative slopes in the V-profiles near the plane wall between x/H=10 and 15 indicate that U is increasing in the x-direction here, most probably due to diffusion of momentum from the region of high velocity above.

Relatively large values of negative V are found near the inclined wall in the recirculation region, this is due to the backflow and the slope of the wall. The centre of the recirculating motion can be estimated by examining where V=0 coincides with U=0, this point is located around x/H=23 and y/H=3.3.

After reattachment V is positive over the whole exit channel with profile maxima near the centre, reflecting the development of the U-profiles towards a symmetric channel flow.

In the beginning of the diffuser, the wall-normal fluctuations \overline{vv} , shown in figure 8, behave much like the streamwise fluctuating velocity with peaks on both sides of the centreline in the inlet channel and with a growth of the peak closest to the inclined wall and a reduction of the other peak. However, the \overline{vv} -peak near the straight wall disappears at an earlier x-position as compared to its counterpart in the streamwise direction, \overline{uu} . This can be seen as an indication that both the turbulence length-scale and its magnitude is increasing rapidly in the region between x/H=10 and 25, and that the wall normal fluctuations hence are damped over a larger distance by the presence of the wall. The far-reaching damping of \overline{vv} appears to persist throughout the exit channel.

4.1.3. Spanwise fluctuations and Reynolds shear stress

The development of the spanwise velocity fluctuations, \overline{ww} , shown in figure 10, resembles very much its streamwise counterpart. The main difference lies in the smaller magnitude of the spanwise component. The wall-normal location of the maximum is also slightly different, with the maximum for the spanwise fluctuating velocity closer to the inclined wall, but still within the shear-layer outside the separated region. The production term in the transport equation for this component is zero in this flow, since W=0, hence \overline{ww} gains all its energy from the other turbulence components via the pressure strain rate term. The

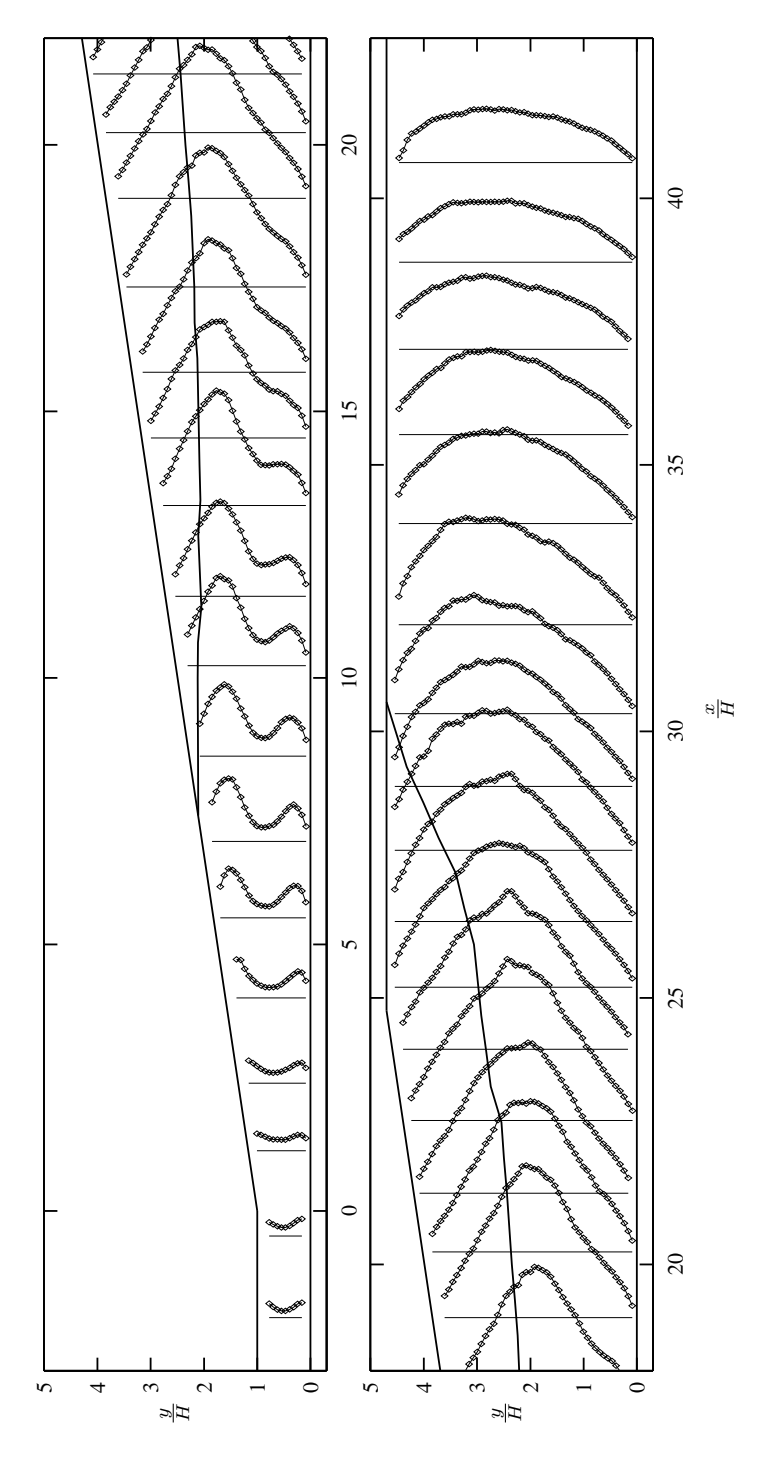


FIGURE 8. Variance of the wall-normal fluctuating velocity, $\left(\overline{vv}_{\rm fig} = 400\overline{vv}/U_b^2 + x/H\right)$.

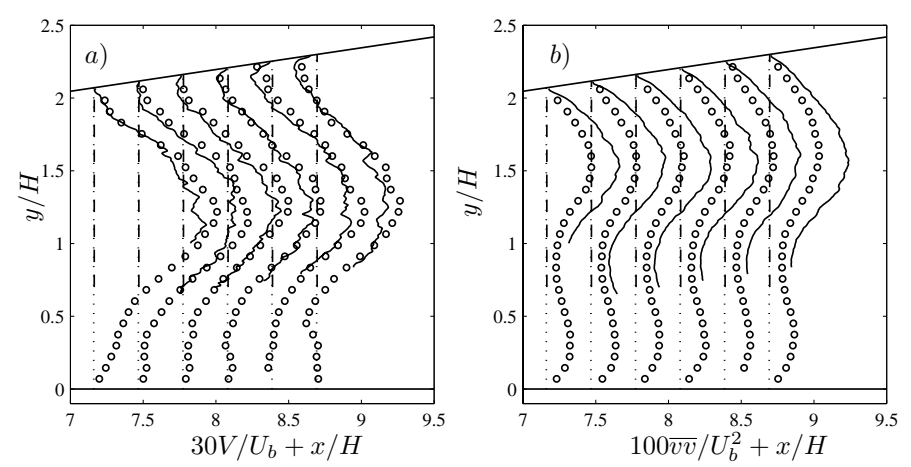


FIGURE 9. Fine resolution PIV measurements around the separation point (solid lines) compared with the courser data-set (symbols).

maximum levels of \overline{ww} are found at x/H = 20 - 25 which is similar to that for the other normal Reynolds stresses.

The Reynolds shear-stress is a very important quantity since it redistributes momentum from high velocity regions to low velocity regions. The Reynolds shear-stress in the streamwise wall-normal plane is antisymmetric in the inlet channel (for simplicity we here show \overline{uv} although the Reynolds shear stress is actually $-\rho \overline{uv}$). With this coordinate system the negative peak is near the straight wall and the positive peak closer to the inclined wall. As the flow develops downstream in the diffuser the positive peak grows while the negative peak is suppressed, see figure 11. The maximum magnitudes of \overline{uv} are found at x/H=20-25 and thereafter \overline{uv} decreases. The location of the positive peak follows the location of maximum shear in the shear-layer outside the separated region. At the end of the measurement region \overline{uv} attains an almost symmetric profile with a maximum located near the outflow channel centreline.

No change of sign is visible for \overline{uv} in the region of back-flow, where the mean velocity gradient changes sign, this could be a consequence of the lack of near wall data-points, but judging from the slope and magnitude of the profiles in this region it seems quite likely that no sign-change occurs. The question if \overline{uv} changes sign or not, is relevant for turbulence modellers since the predicted sign of the Reynolds stresses is directly related to the sign of the mean velocity gradient in many turbulence models.

4.1.4. Magnitude and production rate of turbulent kinetic energy

The turbulent kinetic energy, K, is a primary quantity for comparisons with turbulence model predictions since most models rely on transport equations

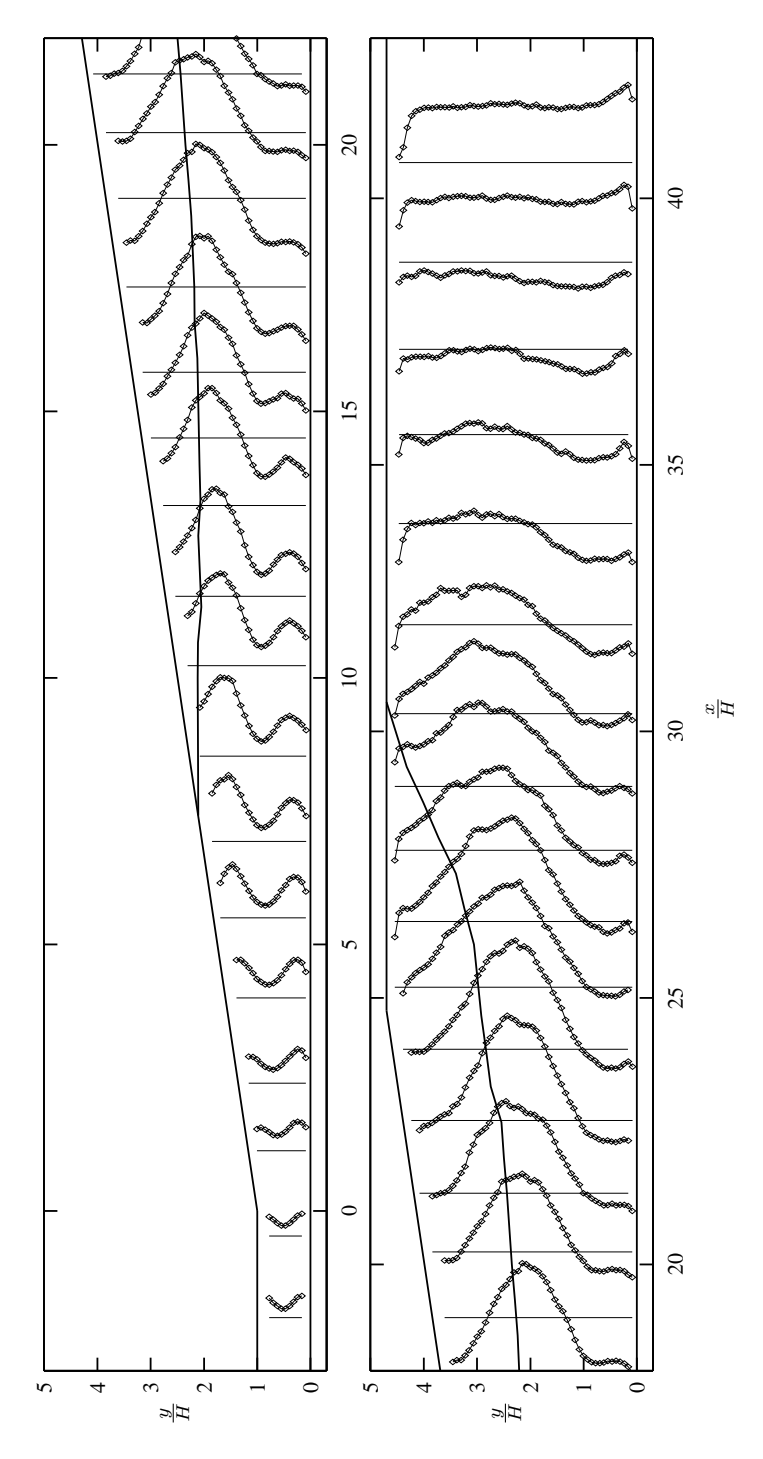


FIGURE 10. Variance of the spanwise fluctuating velocity, $(\overline{w}\overline{w}_{\rm fig} = 400\overline{w}\overline{w}/U_b^2 + x/H)$.

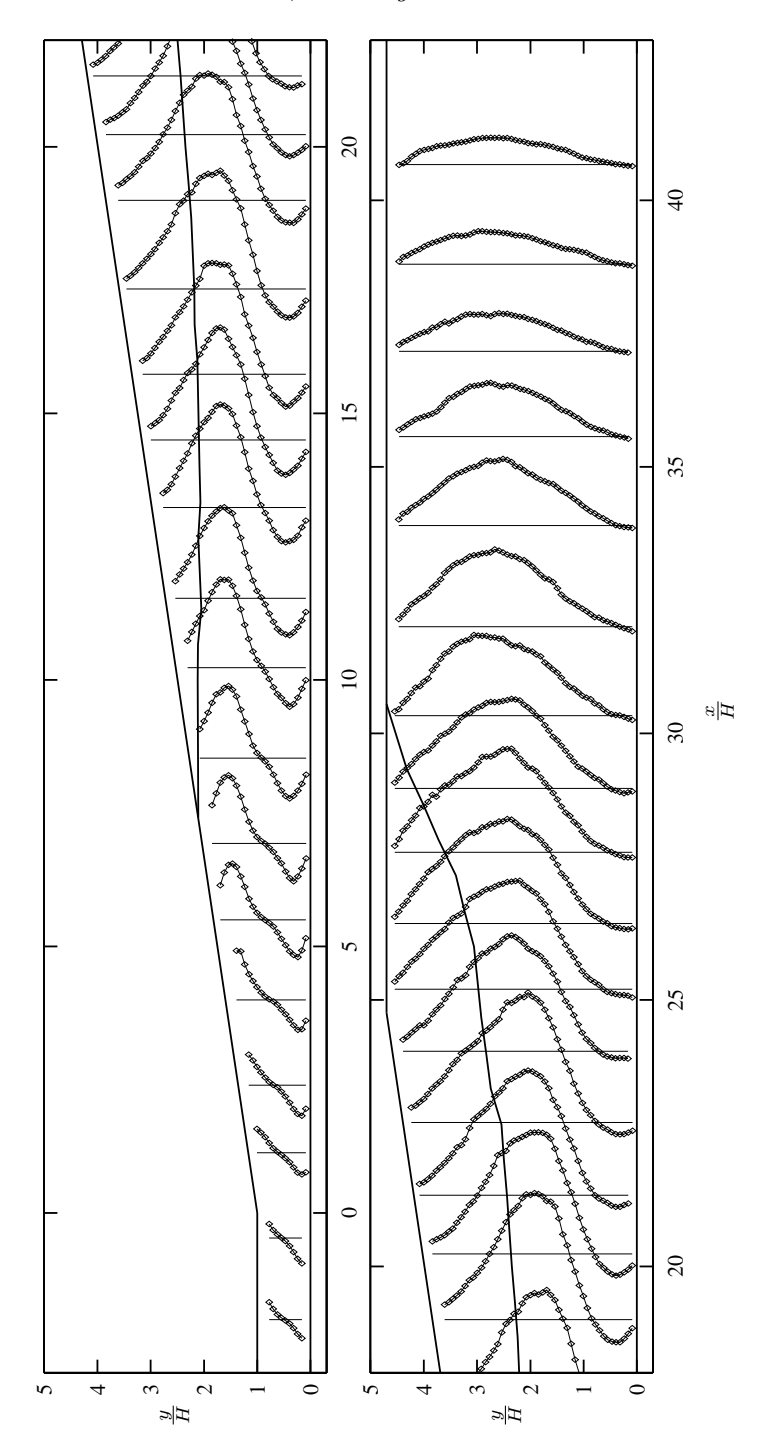


FIGURE 11. Reynolds shear stress in the streamwise wall-normal plane, $(\overline{uv_{\rm fig}} = 400\overline{uv}/U_b^2 + x/H)$.

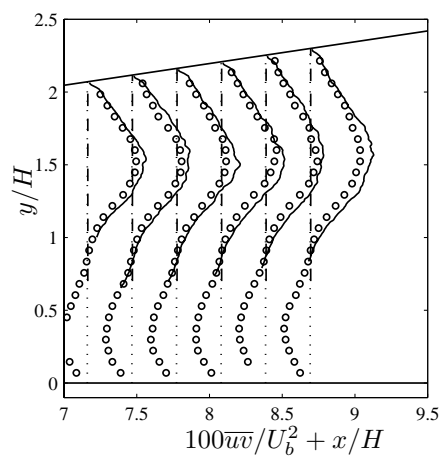


FIGURE 12. Fine resolution PIV measurements around the separation point (solid lines) compared with the courser dataset (symbols).

for this quantity where one or more terms have to be modelled. The turbulent kinetic energy shown in figure 13 is for natural reasons, similar in character to the individual intensities shown in previous figures. It is defined as

$$K = \frac{1}{2} \left(\overline{u}\overline{u} + \overline{v}\overline{v} + \overline{w}\overline{w} \right). \tag{4}$$

The maximum value is, as for the individual fluctuating components, located at about x/H = 20 - 25 in the shear-layer outside the separated region.

The production rate of turbulent kinetic energy,

$$\mathcal{P} = -\overline{u_i u_j} \frac{\partial U_i}{\partial x_j},\tag{5}$$

is shown in figure 14. The profiles of the production rate are in many aspects similar to those of the produced quantity. Directly after the diffuser inlet, two large production peaks form along each wall, the peak closest to the inclined wall grows both in magnitude and width as we go downstream while the peak near the straight wall diminishes. A difference as compared to the profiles of the Reynolds stresses is that the maximum value of the production rate is reached around x/H=10, quite far upstream the positions of maximum Reynolds stresses. From x/H=10 and downstream, the dominant peak widens and decrease in magnitude, after reattachment comparatively little turbulence is produced.

Close to the wall in the downstream part of the separated region small values of negative \mathcal{P} are found. A negative production rate implies that the mean flow is gaining energy from the turbulence. The importance of negative

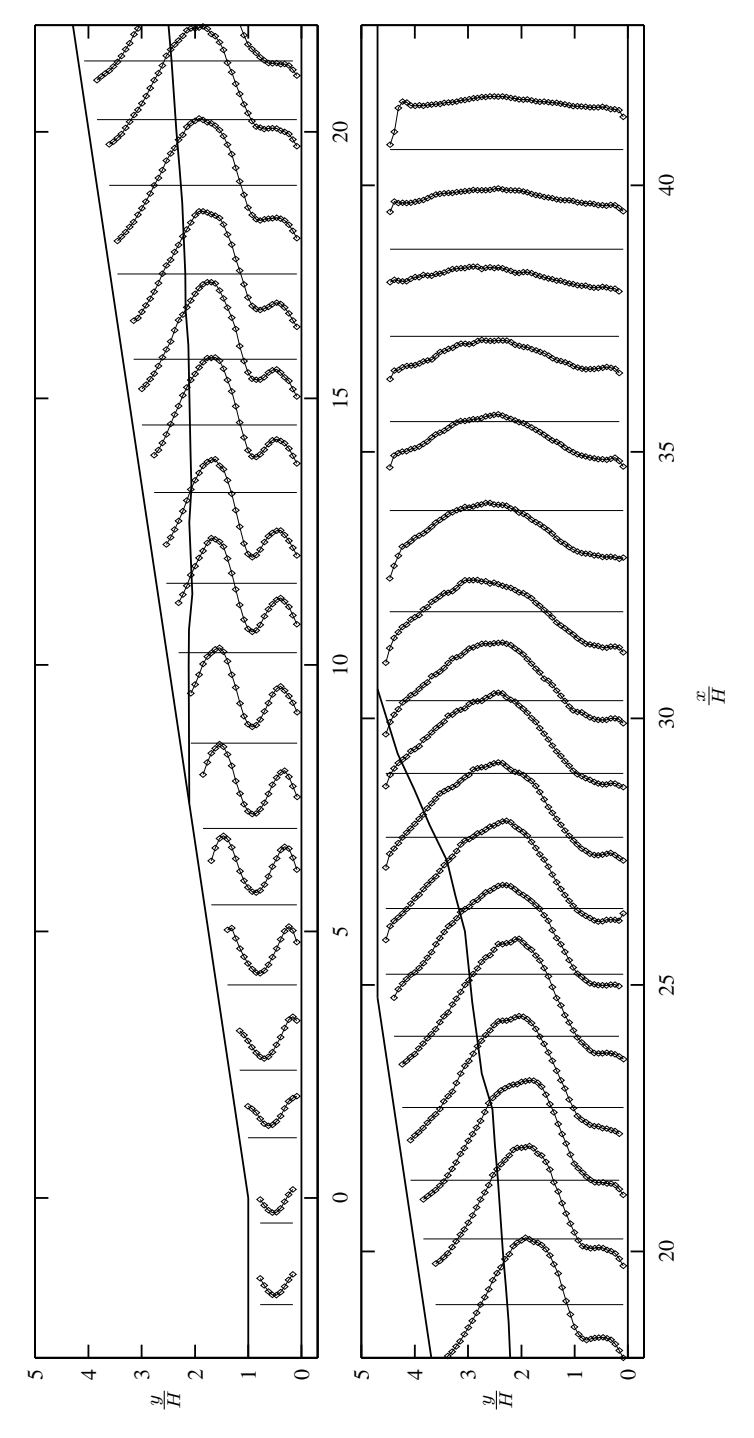


Figure 13. Turbulent kinetic energy, $\left(K_{\mathrm{fig}}=200K/U_{b}^{2}+x/H\right)$.

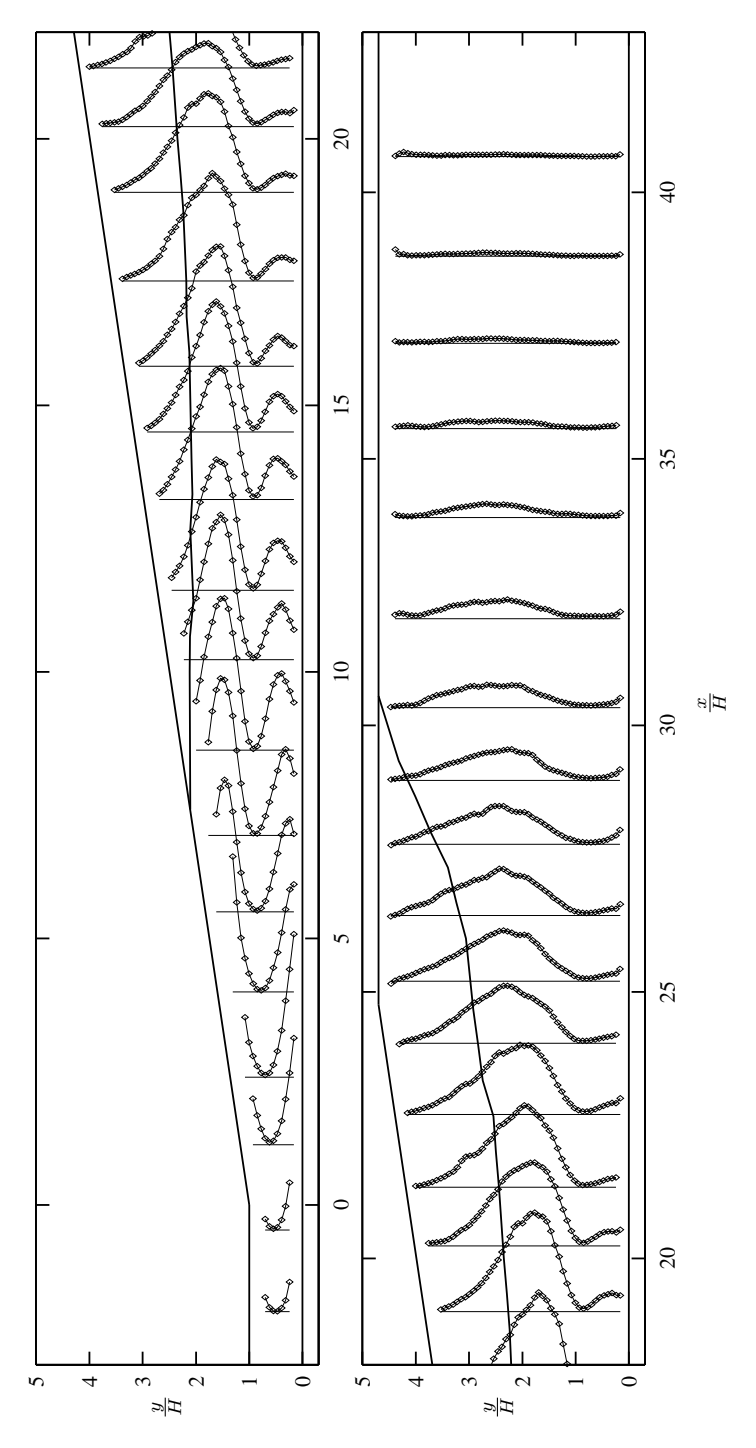


Figure 14. Production rate of turbulent kinetic energy, $(\mathcal{P}_{\text{fig}} = 1000\mathcal{P}H/U_b^3 + x/H)$.

production for the mean reversed flow is discussed and investigated in Törnblom & Johansson (2006).

4.2. Characterization of the separated region

To further study the separated region, extending the information gained by looking at the velocity profiles the stream-function and the back-flow coefficient are useful tools.

4.2.1. Stream-function

The stream-function is here defined as

$$\Psi(x,y) = 1 - \frac{1}{HU_b} \int_0^y U(x,y') dy'.$$
 (6)

In figure 15, constant values of the stream function (streamlines) are plotted in a region around the separation point. The above definition of the stream function gives a value of $\Psi=0$ at the dividing streamline. The dividing streamline that separates the (averaged) recirculation zone from the outer flow is included in many of the previously shown profile plots, e.g. figure 4, and is indicated with a thicker line in figure 15. The two positions where the dividing streamline reaches the "upper" wall are the mean separation and reattachment points, respectively. From figure 15, the mean separation point is found to be located at 7.4 channel heights downstream the diffuser inlet $(x/H\approx7.4)$ and the mean reattachment point located at $x/H\approx30.5$ was determined from the coarser data-set. The contours i figure 15 may seem a little shaky but they are computed directly from the "raw" average velocity field without any prior smoothing and the velocities determining the shape of the dividing streamline are typically 3–4 orders of magnitude smaller than the maximum velocities measured in the same image.

The determined separation point position should be accurate within $\pm 0.1 H$ considering the detailed measurements performed in this region. The position of the reattachment position has not been determined with the same precision, it was taken from the coarse data-set as the mid position between the two measurement positions in the x-direction where U changes sign. Due to integration over the interrogation areas it is more probable that the reattachment position is underestimated than overestimated since the height of the separation bubble will become thinner than the interrogation area size before reattachment.

The angle of the dividing streamline as it detaches from the wall at the separation point is interesting from a turbulence modelling point of view as many models have been seen to give separation bubbles that are very thin a relatively long distance downstream the point of vanishing wall shear stress followed by a rather abrupt growth of the bubble height. The angle between the wall and the measured separation streamline in figure 15 appears to be smaller near the separation point than further downstream but it does not

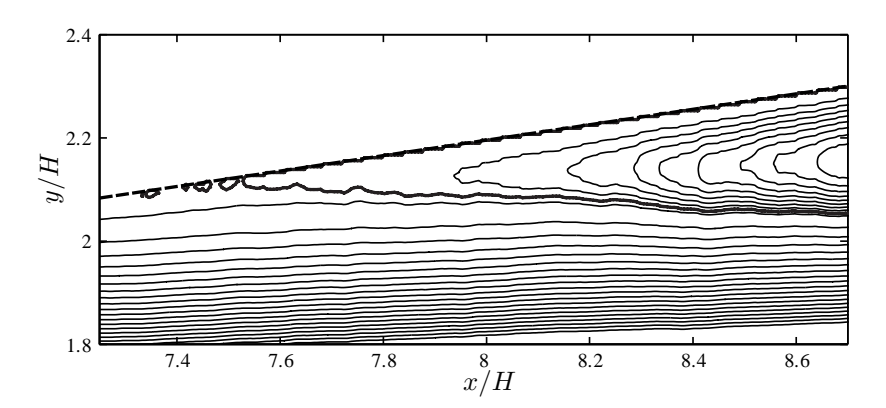


FIGURE 15. Streamlines around the separation point, the dividing streamline, Ψ =0, is shown with a thicker line.

support the turbulence model results, that there should be a long thin region of mean backflow before the bubble starts to grow faster.

4.2.2. Back-flow coefficient

An interesting and useful quantity is the back-flow coefficient which relates the number of samples with negative velocity (along the inclined wall) to the total number of samples. A back-flow coefficient of 1 means that all samples have negative velocity and a back-flow coefficient of zero means that all samples have positive velocity. The back-flow coefficient then reads

$$\chi(x,y) = \frac{1}{N} \sum_{k=1}^{N} \frac{1 - \text{sgn}\left[u_k(x,y)\cos(\alpha) + v_k(x,y)\sin(\alpha)\right]}{2},$$
 (7)

where N is the total number of samples, sgn is the sign function, u_k the streamwise velocity in the kth sample, v_k the wall-normal velocity in the kth sample and $\alpha = 8.5^{\circ}$ the diffuser opening angle.

First, we notice in figure 16 that along the straight wall there seems to be no samples with back-flow. It is important that there is no separation on the straight wall since this may destroy the "stability" of the separation bubble on the inclined wall with a separation altering side from the inclined wall to the straight wall back and forth.

Focusing our attention on the separation bubble on the inclined wall the back-flow coefficient gives us the streamwise locations on the inclined wall for the most upstream instantaneous separation point that in figure 16 is shown to be $x/H \approx 5$. The flow is separated >75% of the time downstream $x/H \approx 11$. The contour of $\chi=0.5$ should, according to available data from other separating

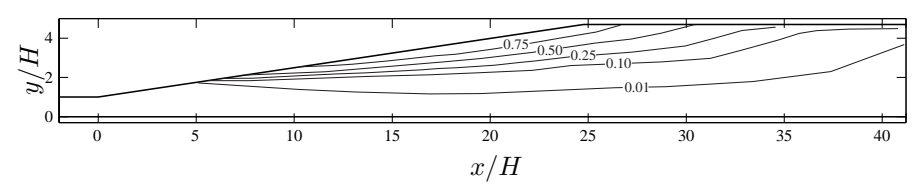


FIGURE 16. Backflow coefficient, χ .

flows, coincide with the mean dividing streamline at the points of separation and reattachment (Simpson 1989). This was checked for and found to be true both in the fine resolution and coarser measurements. Nowhere in the diffuser was backflow found in >90% of the samples. However, this does not necessarily imply that the flow is fully attached everywhere in the diffuser at some instances of time, it merely says that occasionally the instantaneous flow is in the streamwise direction also near the inclined wall but nothing about the spatial extent of the particular events. Following the χ =0.01 contour in figure 16 where 99% of the samples are in the streamwise direction, we find that while being limited to a rather short region upstream the mean reparation point instantaneous flow reversal may occur far downstream the mean reattachment point. This behaviour is probably caused by turbulence structures that have velocity scales larger than the mean velocity downstream the reattachment point that are created over the separated region and then advected downstream.

4.3. Static wall-pressure distribution

The static wall-pressure has been measured along the spanwise centreline in the downstream direction. Measurements on both the inclined and straight walls were performed but with a much better spatial resolution on the straight wall. The measurements on the inclined wall showed that the static pressure is equal on the two sides, for constant x, (within our measurement accuracy) with an exception for the upstream corner where the rapid change in wall direction leads to strong curvature of the streamlines and consequently pressure differences between the two sides.

Shown in figure 17 is the pressure coefficient, C_p , defined as

$$C_p(x) = \frac{p_w(x) - p_w(x=0)}{\frac{1}{2}\rho U_b^2},$$
(8)

where p_w is the static wall-pressure and ρ the density of the air. The adverse pressure gradient is strongest in the beginning of the diffuser and diminishes in the downstream direction until $x/H \approx 13$ where a region with nearly constant pressure gradient is reached. This flat region is caused by the constriction to the flow through the diffuser constituted by the recirculation region. The pressure gradient increases slightly in the reattachment region of the separation bubble.

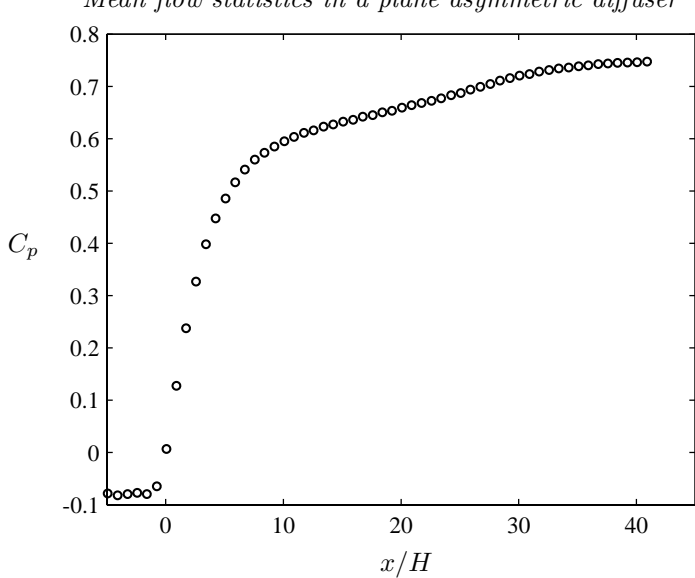


FIGURE 17. Static wall-pressure coefficient, C_p , along the straight diffuser wall.

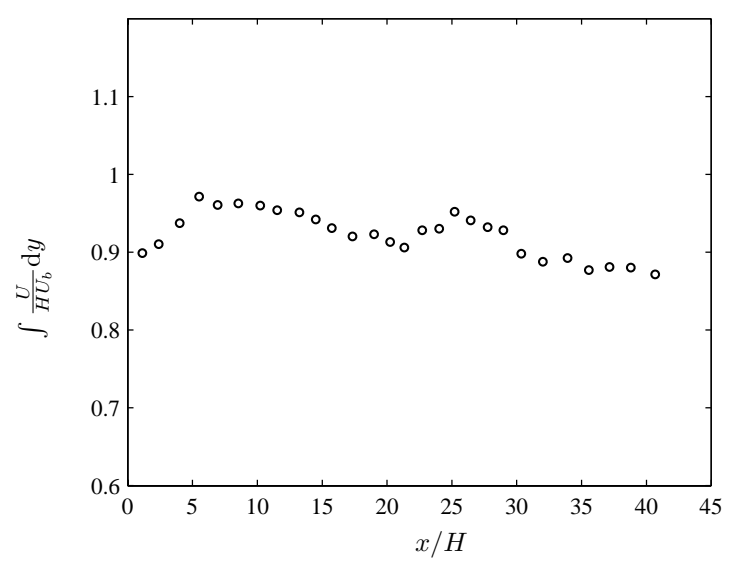


FIGURE 18. Integrated flow rate.

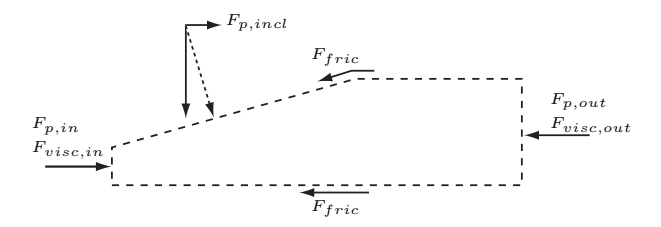


FIGURE 19. Forces acting on a control volume in the diffuser.

4.4. Conservation of mass

Integration of the U-velocity profiles in the y-direction gives a measure of the flow rate through the diffuser at different x-positions. Ideally the flow rate,

$$\int_{\text{bottom}}^{\text{top}} \frac{U}{U_b H} dy, \tag{9}$$

would be constant equal to unity for flawless measurements of a perfectly twodimensional flow. However, figure 18 shows that the measured flow rate is smaller than unity for all profiles. This deficiency can be attributed to the omission of the near-wall measurement points (as explained in section 4.1). Separation on the diffusers end-walls, which is a known problem in this type of flow geometry (see e.g. Buice & Eaton 1997; Kaltenbach et~al. 1999; Obi et~al. 1999), would result in a flow-rate that is increasing in the streamwise direction along the diffuser centreline. Such trends cannot be seen in the present measurements. A weak trend is instead seen towards lower flow-rates for larger values of x. No feasible explanation has been found for this trend, other than that the insufficient near-wall resolution of the integrated profiles gives a general uncertainty of the integrals.

4.5. Momentum balance

Being a two-dimensional flow confined between two walls the consistency between the measured forces on a control volume and the measurements of the resulting momentum flux change can be readily investigated. The x-momentum flux change $\Delta M_x = M_{x,out} - M_{xin}$ between two cross-sections at $x_{in} = 0$ and x_{out} is related to the forces acting on the control volume as

$$\Delta M_x = (F_{p,in} - F_{p,out} + F_{p,incl}) + (F_{visc,in} - F_{visc,out}) - F_{fric}. \tag{10}$$

Figure 19 shows how the different forces act on the control volume. Being a two-dimensional flow all quantities are per unit depth in the spanwise direction. The pressure forces acting on the inlet or outlet cross-sections and in the x-direction on the inclined wall are here defined as

$$F_{p,x} = \int_{bottom}^{top} P(x,y) \mathrm{d}y \quad \text{and} \quad F_{p,incl} = \int_{in}^{out} P(s) \sin(\alpha(s)) \mathrm{d}s$$

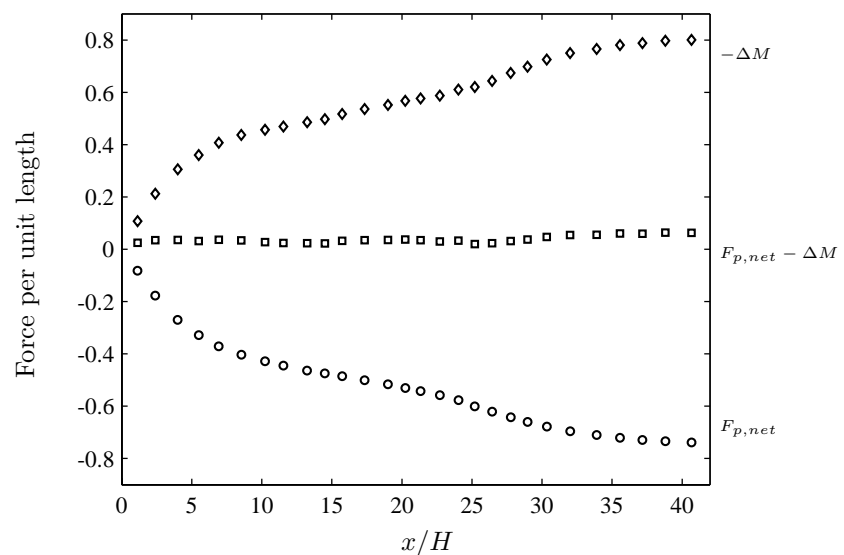


FIGURE 20. Terms in the momentum balance equation, $F_{p,net}=F_{p,in}-F_{p,out}+F_{p,incl}$. The data is normalised by (ρHU_b^2) .

respectively. The second integral is evaluated along the walls and $\alpha(s)$ is the angle between the x-axis and the wall. The skin-friction and viscous forces are here defined as

$$F_{visc,x} = \int_{bottom}^{top} -\mu \frac{\partial U}{\partial x} dy$$
 and $F_{fric} = \int_{in}^{out} \tau_w \cos(\alpha(s)) ds$,

where μ is the dynamic viscosity and τ_w is the wall shear stress. The momentum flux through a vertical cross section is given by

$$M_x = \int_{bottom}^{top} \rho(U^2 + \overline{u}\overline{u}) dy.$$
 (11)

With the present experimental data-set the pressure was taken to be constant over the cross-sections equal to the static pressure at the straight wall, the errors due to this approximation should be small, considering that the measured pressure is equal on both walls for the same x-position (cf. section 4.3). It should be noted that the interior pressure distribution over the cross-sections can be computed by integrating the y-momentum equation, however this will change $F_{p,x}$ by less than 1%. The viscous forces are at the Reynolds number considered negligible and are thus not considered in the present analysis of the momentum balance. Measurements of the wall shear stress has not been made in the present experiment and the frictional forces can therefore not be included in the balance, the implication of this will be discussed further on.

Figure 20 illustrates the balance between the left- and right-hand side of equation 10. It is seen that the pressure forces are the, by far, largest contributors to the change in momentum. The residual visible in the middle curve of figure 20 can probably to a large extent be attributed to the neglected skin-friction term in equation 10 which according to Kaltenbach $et\ al.\ (1999)$ accounts for approximately 5% of the momentum balance in the similar 10° diffuser case.

4.6. Energy balance

Using tensor notation, the Reynolds averaged transport equation for the mean flow kinetic energy $Q = \rho U_i^2/2$ may be written as:

$$\frac{\partial}{\partial x_j}(U_jQ) = -\frac{\partial}{\partial x_j}\left(U_jP + \rho U_i\overline{u_iu_j}\right) + U_i\frac{\partial}{\partial x_j}\left(\mu\frac{\partial U_i}{\partial x_j}\right) + \rho\overline{u_iu_j}\frac{\partial U_i}{\partial x_j}$$
(12)

The last term is a source term, that is usually negative, transforming mean kinetic energy to turbulence, the term is identical to the production term in the transport equation for the turbulent kinetic energy, but with opposite sign. By integrating equation 12 over a control volume extending across the diffuser in the y-direction and from $x=x_{in}$ to x_{out} and using Gauss' theorem we arrive at the expression

$$\mathcal{P}^{tot} = -\left(E_m^{tot}(x_{out}) - E_m^{tot}(x_{in})\right) + \int_{x_{in}}^{x_{out}} \int_{bottom}^{top} \mu\left(U\nabla^2 U + V\nabla^2 V\right) dxdy$$
(13)

where

$$\mathcal{P}^{tot} = \int_{x_{in}}^{x_{out}} \int_{bottom}^{top} \rho \mathcal{P}(x, y) \, dy dx$$
 (14)

is the total rate of production of turbulent kinetic energy and

$$E_m^{tot}(x) = \int_{bottom}^{top} U(x, y) \left(P(x, y) + Q(x, y) + \rho \overline{uu}(x, y) \right) dy \tag{15}$$

can be interpreted as a flux of mechanical energy over a cross-section. Both E_m^{tot} and \mathcal{P}^{tot} are given per unit depth in the spanwise direction. E_m^{tot} will diminish trough the diffuser as the mean kinetic energy is transformed into turbulent kinetic energy and heat. All the turbulent kinetic energy will in essence eventually also be transformed into heat. There are two paths that the mechanical energy drained from the mean flow can take, it can be transformed to turbulent energy or it can be directly transformed into heat by viscous dissipation due to the mean flow gradients. In the following we will investigate the balance of equation 13 using the present experimental data.

The loss of mechanical energy from the mean flow from $x_{in}=0$ and down-stream is depicted in the lower curve of figure 21. The loss at the most down-stream measurement station amounts to approximately 15% of the available mechanical energy of the mean flow at the diffuser entrance. The upper curve

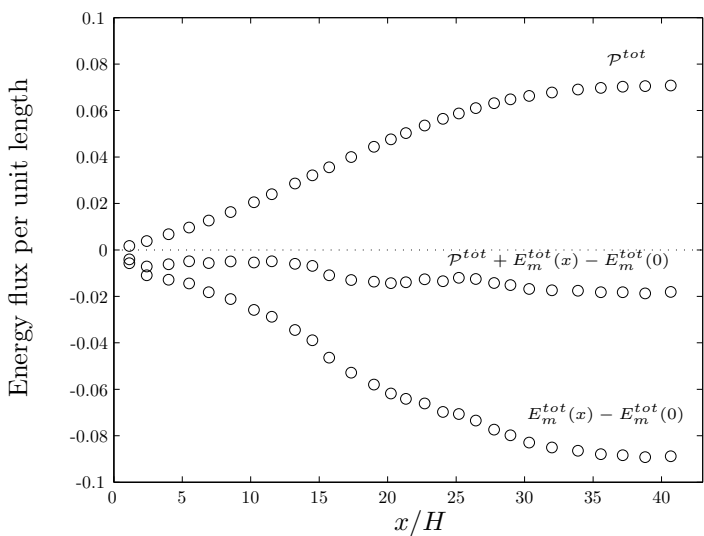


FIGURE 21. The mechanical energy of the mean flow (lower curve), \mathcal{P}^{tot} between $x_{in}=0$ and $x_{out}=x/H$ (upper curve) and their residual (middle curve). The data is normalised by ρHU_b^3 .

in figure 21 shows the total amount of energy transferred from the mean flow to the turbulence from $x_{in}=0$ and downstream, the resemblance of the upper and lower curves shows that the main path taken by the energy drained from the mean flow is through transformation into turbulence. The middle curve in figure 21, showing the residual between the upper and the lower curves, represents the losses of mean flow energy due to direct viscous dissipation by mean flow shear.

5. Summary and conclusions

The flow in an asymmetric plane diffuser has been studied with extra attention paid to ensuring good two-dimensionality of the mean flow and minimising the measurement errors. The focus in this paper is on the time averaged flow characteristics, *i.e.* mean velocities, turbulence intensities, Reynolds stresses and pressure together with an investigation of the separated region using streamlines and the back flow coefficient. The Reynolds number based on the inlet bulk flow velocity, U_b , and the inlet channel height, H, was approximately 38000.

The profiles of the streamwise mean velocity, U, reveals a flow divided into a high velocity region following the plane wall and a low velocity region with flow reversal near the inclined wall. In between these regions is a strong shear layer. The differences between the regions diminish gradually in the exit channel after reattachment. The wall-normal velocity, V, is very small in most parts

of the diffuser, but close to the upstream corner at the diffuser inlet where the change in the direction of the wall is rather abrupt, locally high values of the wall-normal velocity and strong streamline curvature are found. The mean flow separates on the inclined wall at 7.4 inlet channel heights downstream from the diffuser inlet. Instantaneous flow reversal occurs upstream the mean separation point but never above x/H=5 as shown by the back-flow coefficient. Instantaneous flow reversal occurs far downstream the mean reattachment point which was found to be at x/H=30.5. The back-flow coefficient shows that nowhere in the diffuser is the flow reversed more than 90% of the time.

High turbulence levels were found in the strong shear layer forming between the separation bubble and the high velocity region. The normal Reynolds stresses have similar profiles, with broad global maxima between x/H=20-25. The streamwise turbulence component has the largest magnitude, about twice that of the other two normal components. The production rate of turbulent kinetic energy is shown to peak further upstream as compared to the Reynolds stresses. Negative values of the production rate indicate that the mean flow gains energy from the turbulence close to the wall in the downstream end of the reversed flow region. This is an aspect that will be investigated in more detail in a separate study.

The relation between the momentum loss in the diffuser and the pressure forces was investigated and it was found that most of the momentum losses are due to the pressure forces and that only a small part of the momentum loss is caused by skin friction on the walls. An investigation of terms in the mean kinetic energy equation show that production of turbulence is the main consumer of mean flow mechanical energy in the diffuser.

The 8.5° plane asymmetric diffuser flow-case has been shown to exhibit several interesting phenomena that challenge the turbulence models of today, such as plane wall separation and reattachment, strong and sudden shearing, non-equilibrium turbulence and turbulence relaxation.

Acknowledgements

The authors would like to thank Ulf Landén and Marcus Gällstedt for aiding in the manufacturing of the flow device. The Swedish Energy Agency and the Swedish Research Council are gratefully acknowledged for their financial support.

References

Angele, K. P. & Muhammad-Klingmann, B. 2005 PIV measurements in a weakly separating and reattaching turbulent boundary layer. *Eur. J. Mech. B/Fluids* 25, 204–222.

- Brüger, A., Nilsson, J., Kress, W., Stålberg, E., Gustafsson, B., Lötstedt, P., Johansson, A. V. & Henningson, D. S. 2004 A hybrid high order method for incompressible flow in complex geometries. Technical report TRITA-MEK 2004:11. KTH Mechanics.
- Buice, C. U. & Eaton, J. K. 1997 Experimental investigation of flow through an asymmetric plane diffuser. *Tech. Rep.*. Department of mechanical engineering, Stanford university.
- Buice, C. U. & Eaton, J. K. 2000 Experimental investigation of flow through an asymmetric plane diffuser. *J. Fluids Eng.* **122**, 433–435.
- Cherry, N. J., Hillier, R. & Latour, M. E. M. P. 1984 Unsteady measurements in a separated and reattaching flow. *J. Fluid Mech.* **144**, 13–46.
- Comte-Bellot, G. 1965 Écoulement turbulent entre deux paroix parallèles. Publications scientifiques et techniques 419. Ministère de l'air, 2, Avenue de la Porte-d'Issy, Paris.
- DIANAT, M. & CASTRO, I. P. 1991 Turbulence in a separated boundary layer. *J. Fluid Mech.* **226**, 91–123.
- VAN DOORNE, C. W. H. 2004 Stereoscopic PIV on transition in pipe flow. PhD. Thesis, Technische Universiteit Delft, ISBN 90-9018499-6.
- EATON, J. K. & JOHNSTON, J. P. 1981 A review of research on subsonic turbulent flow reattachment. AIAA J. 19, 1093–1100.
- GULLMAN-STRAND, J. 2004 Turbulence and scalar flux modelling applied to separated flows. PhD. Thesis, KTH Mechanics, Stockholm, Sweden, TRITA-MEK 2004:16.
- Gullman-Strand, J., Törnblom, O., Lindgren, B., Amberg, G. & Johansson, A. V. 2004 Numerical and experimental study of separated flow in a plane asymmetric diffuser. *Int. J. Heat Fluid Flow* **25**, 451–460, (**Paper 4**).
- Hellsten, A. & Rautaheimo, P., ed. 1999 Workshop on refined turbulence modelling. ERCOFTAC/IAHR/COST.
- HERBST, A. H., SCHLATTER, P. & HENNINGSON, D. S. 2006 Simulations of turbulent flow in a plane asymmetric diffuser. *To be published*.
- Kaltenbach, H.-J., Fatica, M., Mittal, R., Lund, T. S. & Moin, P. 1999 Study of flow in a planar asymmetric diffuser using large-eddy simulation. *J. Fluid Mech.* **390**, 151–185.
- KEANE, R. & ADRIAN, R. 1992 Theory of cross-correlation in PIV. Applied scientific research 49, 191–215.
- Keane, R. D. & Adrian, R. J. 1990 Optimization of particle image velocimeters. Part I; double pulsed systems. *Meas. Sci. Technol.* 1, 1202–1215.
- KIYA, M. & SASAKI, K. 1983 Structure of a turbulent separation bubble. J. Fluid Mech. 137, 83–113.
- Obi, S., Aoki, K. & Masuda, S. 1993a Experimental and computational study of turbulent separating flow in an asymmetric plane diffuser. In *Ninth Symp. on Turbulent Shear Flows*, p. 305. Kyoto, Japan.
- Obi, S., Ishibashi, N. & Masuda, S. 1997 The mechanism of momentum transfer enhancement in periodically perturbed turbulent separated flow. In 2nd Int. Symp. on Turbulence, Heat and Mass Transfer, pp. 835–844. Delft, The Netherlands.

- Obi, S., Nikaido, H. & Masuda, S. 1999 Reynold number effect on the turbulent separating flow in an asymmetric plane diffuser. In *Proceedings of FEDSM99*, *FEDSM* 99-6976. ASME/JSME Fluids Engineering Division Summer Meeting.
- OBI, S., OHIZUMI, K., AOKI, K. & MASUDA, S. 1993b Turbulent separation control in a plane asymmetric diffuser by periodic perturbation. In *Engineering turbulence modelling and Experiments* 2, pp. 633–642.
- ÖSTERLUND, J. M. 1999 Experimental studies of zero pressure-gradient turbulent boundary layer flow. PhD thesis, Royal Institute of technology, Department of Mechanics, ISRN KTH/MEK/TR-99/16-SE.
- Perry, A. E. & Fairlie, B. D. 1975 A study of turbulent boundary-layer separation and reattachment. J. Fluid Mech. 69, 657–672.
- RAFFEL, M., WILLERT, C. & KOMPENHANS, J. 1997 Particle Image Velocimetry, A practical guide. Springer Verlag.
- Ruderich, R. & Fernholz, H. H. 1975 An experimental investigation of a turbulent shear flow with separation, reverse flow, and reattachment. *J. Fluid Mech.* 163, 283–322.
- SCARANO, F. & RIETHMULLER, M. L. 2000 Advances in iterative multigrid piv image processing. *Exp. Fluids* **29** [Suppl.], S51–S60.
- SIMPSON, R. L. 1989 Turbulent boundary-layer separation. Ann. Rev. Fluid Mech. 21, 205–234.
- TÖRNBLOM, O. & JOHANSSON, A. V. 2006 A note on the influence of negative turbulence production on separating flows. *To be published* (**Paper 5**).
- TÖRNBLOM, O., LINDGREN, B. & JOHANSSON, A. 2006 Experimental procedures for the investigation of the turbulent flow in a plane asymmetric diffuser by means of stereoscopic high-speed PIV. *Tech. Rep.*. KTH Mechanics, (**Paper 6**).
- Westerweel, J. 1997 Fundamentals of digital particle image velocimetry. *Meas. Sci. Technol.* 8, 1379–1392.
- WIENEKE, B. 2005 Stereo-PIV using self-calibration on particle images. *Exp. in Fluids* 39, 267–280.

Paper 2

P2

Structural and temporal characteristics of the flow in a plane asymmetric diffuser with 8.5° opening angle

By Olle Törnblom and Arne V. Johansson

KTH Mechanics, SE-100 44 Stockholm, Sweden

The flow in a plane asymmetric diffuser with an 8.5° opening angle was studied experimentally with focus on the temporal flow properties and flow structures. Time-resolving stereoscopic particle image velocimetry was used in order to capture the evolution of flow events. The inlet condition was chosen as fully developed turbulent channel flow at a Reynolds number based on the inlet channel height and bulk velocity of Re_H =38000. The formation of a local region of reversed flow, near the mean separation point, is illustrated with temporal sequences of vector-fields. The spanwise velocity fluctuations are observed to frequently form structures approximately aligned with the mean shear direction, these structures are possibly signatures of the legs of hairpin vortices. An ejection event likely to be due to a hairpin vortex is illustrated with a sequence of images. Spatial energy spectra of the flow indicate that the turbulence in the separated region has a larger portion of the energy at small scales as compared to the turbulence in regions outside the separation. Spatial auto-correlation functions are presented for all three velocity components at 32 different positions in the flow. The auto-correlations of the spanwise velocity support the observation that inclined structures of this velocity component are frequently appearing in this flow.

1. Introduction

Turbulent separating flows are often known to show large-scale velocity fluctuations. Distinct separation and reattachment points normally can only be seen in the averaged flow fields while instantaneous images of the flow show a gradually increasing, or decreasing, fraction of reversed flow as the separation and reattachment points are approached. Particle image velocimetry (PIV) is a useful tool for visualising and quantifying these processes since it gives access to the instantaneous velocities in a plane, high-speed PIV also adds the possibility to study the temporal evolution of the flow. Several motivations can be given for studying the structural and temporal characteristics of turbulent separating flows, the major ones are: (i) to gather information that can help the

development of better predictive models for non-equilibrium types of flows (ii) to gain insight of flow features that can be exploited for affecting or controlling the flow (iii) to get an understanding of the underlying dynamics governing the commonly measured flow features, such as averages and turbulence intensities.

Literature on the structural character of turbulent flows separating from smooth walls is quite scarce, but a recent investigation is that by Song & Eaton (2004) who studied the flow structures of a separating, reattaching and recovering boundary layer over a smooth ramp, using instantaneous PIV realisations of the flow and auto-correlations of the in plane velocities. They found evidence for the existence of roller vortices, generated by the Kelvin-Helmholtz instability of the separated shear layer. They also concluded that around, and after, reattachment these roller vortices are often distorted by the mean flow gradients (both $\partial U/\partial y$ and $\partial U/\partial x$ contribute) forming structures similar to the hairpin vortices in a flat plate boundary layer. Although undergoing the same processes (separation from a smooth wall, reattachment and recovery) the flow studied by Song & Eaton differs from the present in at least two important aspects, viz. (i) the present flow is confined between two walls without a defined free-stream (ii) the separated region in the present flow is substantially larger in relation to the upstream boundary layer thickness.

In a series of studies Simpson and co-workers (Simpson et al. 1981a,b; Shiloh et al. 1981) investigated an aerofoil type of flow where a turbulent boundary layer separated on a flat plate (due to an adverse pressure gradient) and evolved into a free shear layer. One of their observations was that it appeared as if the back-flow was supplied intermittently and locally by large scale structures passing through the separated flow and not from far downstream as is suggested by the mean streamline pattern.

The structure of flows where the separation is induced by an abrupt change in geometry has been the subject of more studies than the smooth wall separating flows. One good example is Kiya & Sasaki (1985) who investigated the structure of large-scale vortices and the unsteady reverse-flow properties in the reattachment zone of a two-dimensional separation bubble formed at the leading edge of a blunt flat plate. By the use of conditional hot-film sampling based on pressure signals they could conclude that the unsteadiness of the reattachment flow, in their case, was governed by two types of motions: high-frequency motion resulting from the passage of large-scale vortices (that are smaller than the length of the separated region) and a low-frequency unsteadiness that is coupled to the growing and shrinking (often called "shear-layer flapping") of the separation bubble. It was also suggested that the strength of the large scale vortices is coupled to the low-frequency motion.

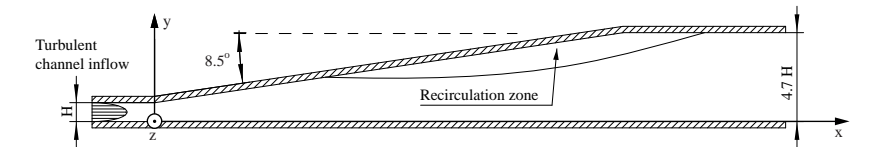


Figure 1. The flow geometry.

1.1. The plane asymmetric diffuser

The plane asymmetric diffuser flow studied here represents a complex flow in an idealised geometry, suitable for both experimental and computational investigations. The present experiment is performed in a plane asymmetric diffuser with 8.5° opening angle, see figure 1. Törnblom et al. (2006b) describe the average characteristics of this flow, such as mean velocities, Reynolds stresses, turbulent kinetic energy, production rate of turbulent kinetic energy and reverse flow fraction. The experimental setup and measurement procedures are described in some detail in Törnblom et al. (2006a).

Obi et al. (1993a,b, 1997, 1999) used laser Doppler velocimetry (LDV) to measure the velocities in a geometry similar to the one used in the present investigation but with an opening angle of 10°. Obi et al. (1993b) investigate separation control by means of periodic perturbations introduced through a spanwise slit on the inclined diffuser wall upstream the mean separation point. Using the pressure recovery at the diffuser outlet as an indicator of the control efficiency, they found an optimum non-dimensional frequency $0.02 \le St_c \le 0.03$ (where $St_c = fH/U_c$, f is the frequency, H the inlet channel height and U_c the inlet channel centre-line velocity). They concluded that frequencies in this range resulted in an organised oscillatory flow that enhanced the transport of momentum in the wall-normal direction. Obi et al. (1997) further investigated the effects of periodical blowing and suction on the separating flow and concludes that the production of Reynolds shear stress is enhanced at the optimum perturbation frequency and that this 'indirect' effect is more crucial for separation prevention than the direct effect of increased mixing near the perturbation slit.

Another experimental study of the 10° plane asymmetric diffuser is presented in Buice & Eaton (1997, 2000). In this experiment the main measurement tools were pulsed hot-wires and constant-temperature hot-wires. Results of the experiment by Buice & Eaton that can be related to this work are the spanwise auto-correlations of u and the energy spectra. The auto-correlations showed that the length-scale of the spanwise structures grow with increasing x-position in the diffuser, but that the structures are small compared to those found in a plane mixing layer of equivalent character. The correlation coefficient $R_{uu}(\Delta z)$ was shown to drop below zero for $\Delta z/H\approx0.9$, 1.5 and 2.2 at x/H=17.8, 21.2 and 24.6 respectively. The frequency spectra presented by

Buice & Eaton were measured in the exit channel after the diffuser and show that a substantial part of the turbulence energy resides in the low frequency part of the spectra but that no single frequency is dominant.

A difference between the present work and that done previously in plane asymmetric diffuser geometries is that we here use high-speed PIV for the velocity measurements and hence have access to time-series of instantaneous velocity fields as compared to the previous investigations that used point measurement techniques.

2. Results

The inlet channel height H and the inlet channel bulk velocity U_b are commonly used for normalisation of the presented data. All data presented were measured at a Reynolds number $Re_H = HU_b/\nu = 38000$. The time shown in time-sequences of images is only relative to the first image and hence, if nothing else is specifically stated, local in each sequence.

2.1. Formation of backflow near the separation point

The position of the separation point was in Törnblom et al. (2006b) determined to x/H=7.4 and figure 2 shows a time-sequence of instantaneous velocity vector fields in a region near this point. Included in figure 2 are also contours showing the magnitude of the backflow along the inclined wall. From the images we can see that the flow in this region is highly unsteady and that there is a region with relatively low velocity near the wall and a high velocity region further out. The sequence shows the formation of a region of backflow but it is difficult to distinguish any particular cause for the formation of the backflow region. Judging by the size of the forming backflow region, its cause is likely to be some velocity fluctuation with a quite large length-scale, but in figure 2 motion on such scales is somewhat hidden behind velocity variations with smaller length scales and the average flow variations. In an attempt to reveal the large scale velocity variations the vector field was bandpass filtered by subtracting the mean flow and filtering the fluctuations with a two-dimensional Gaussian low-pass filter. In figure 3 the result after such an operation is shown, in this particular case the Gaussian filter has a standard deviation of 5 vectors (it should be noted that every vector in the y-direction is shown in figures 2 and 3, but only every third in the x-direction). In figure 3 one can easily see the connection between the regions of backflow and the velocity vectors, however the formation of the backflow region does not appear to be connected to the passage of a strong vortex. The structure of the large scale fluctuations appears to be more wave-like than vortex-like. Galilean decomposition instead of Reynolds decomposition of the filtered velocity field does not reveal any large scale vortices either.

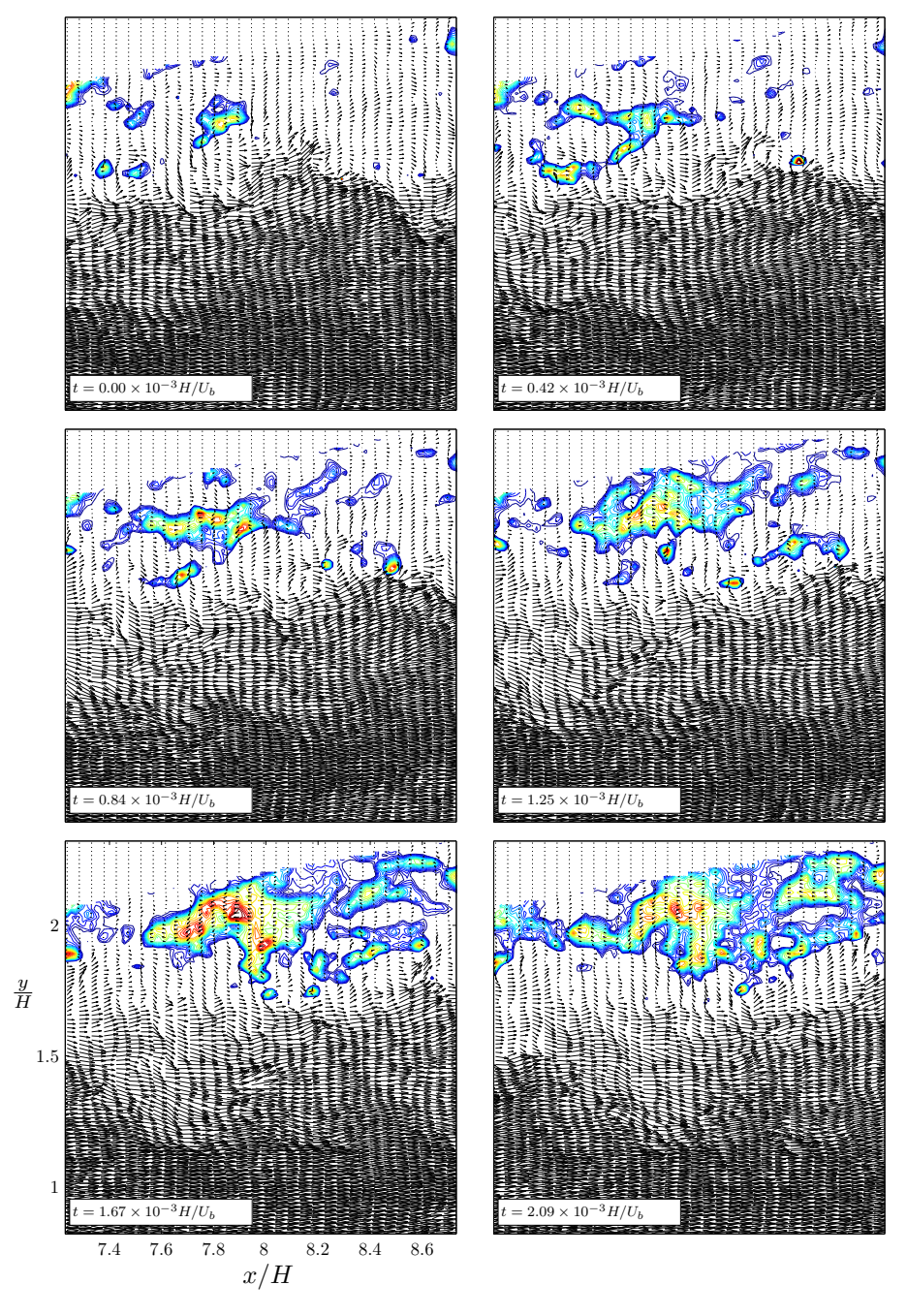


FIGURE 2. Instantaneous vector fields with contours showing the magnitude of the backflow velocity along the inclined wall. Red corresponds to a larger and blue to a smaller backflow rate.

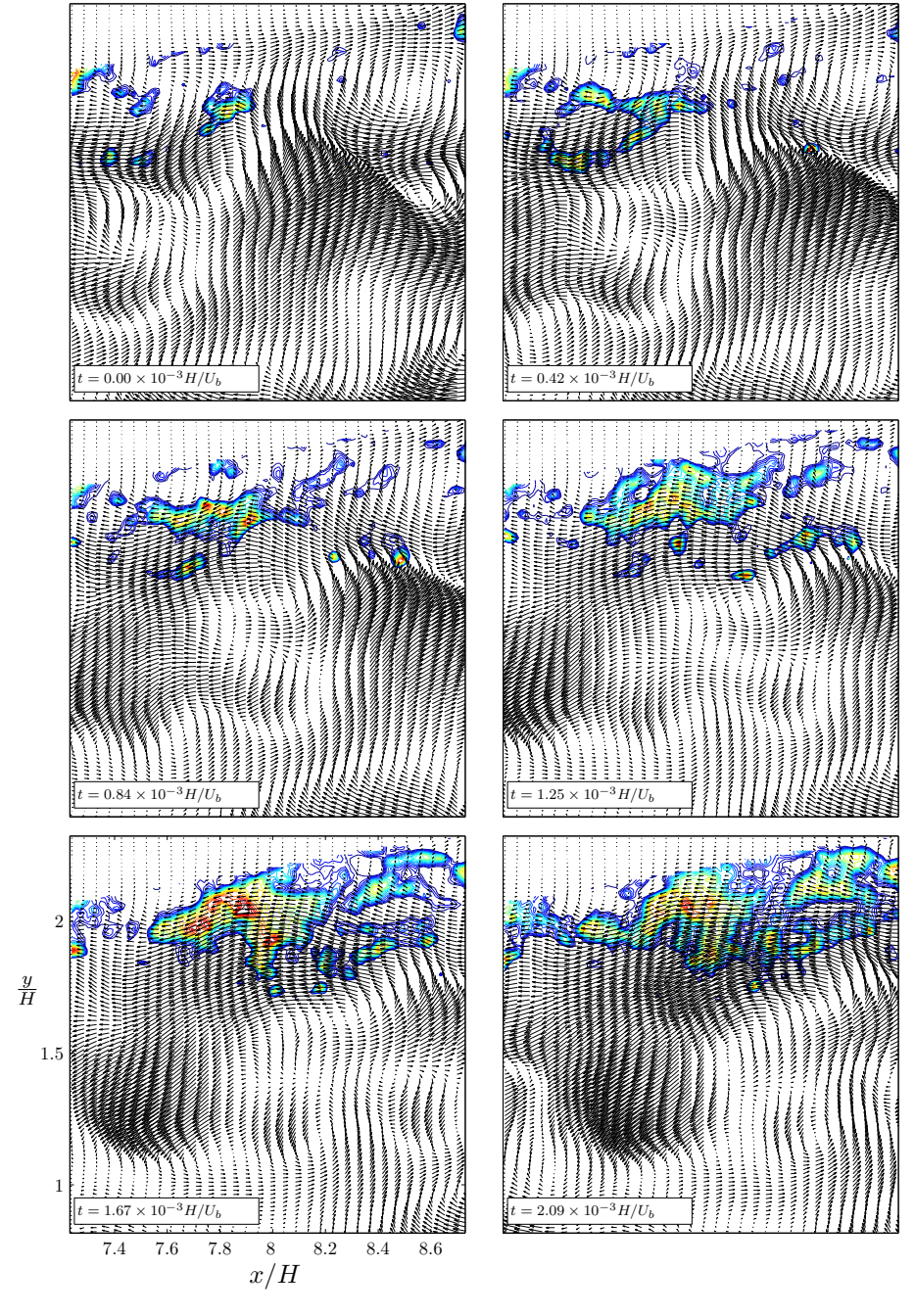


FIGURE 3. Band pass filtered instantaneous vector fields with contours showing the magnitude of the backflow velocity along the inclined wall. Red corresponds to a larger and blue to a smaller backflow rate.

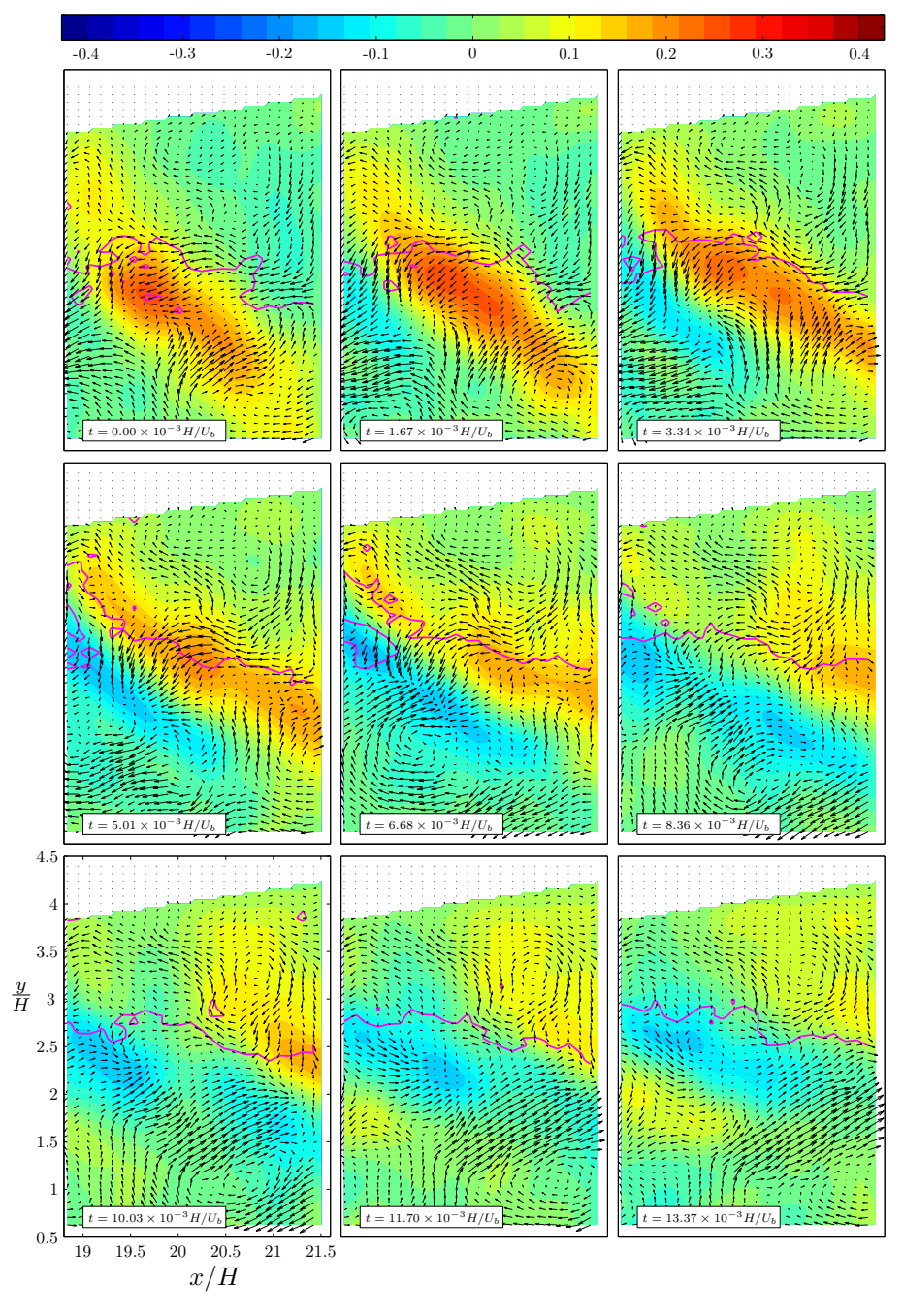


FIGURE 4. Band pass filtered instantaneous vector fields with colour-scale showing the magnitude of the spanwise velocity w/U_b . Magenta contours enclose regions with backflow along the inclined wall.

2.2. Structures of the spanwise velocity fluctuations

Many of the recorded velocity fields show inclined structures of spanwise velocity fluctuations, the structures come in pairs of one positive and one negative structure and appear to be approximately aligned with one of the principal axes of the mean strain rate tensor. Figure 4 shows a sequence of images where such a pair of structures is convected downstream, stretched and smeared out. In the first image an inclined structure of strong positive (red colour) spanwise velocity can be seen, gradually a following structure of negative w appears in the images. The strength of the positive structure is successively diminishing while the strength of the negative increases. The structures appear also to be rotated, or stretched by the flow, towards being horizontal. The structures are eventually smeared out and in the last image the leading positive structure is barely visible. However, another positive structure has appeared now, following the negative structure. In the first five images one can perceive a reducing effect on the region of backflow, indicated with a magenta line, from the structures. It is unclear though if this is a general effect.

It is possible that the structures seen, form one of the legs of a hairpinor horseshoe-like vortex and the new structures following the first could be an indication of a hairpin packet proposed by Adrian *et al.* (2000b) to appear in the outer region of turbulent boundary layers.

2.3. An ejection event and a possible hairpin vortex

Galilean decomposition of a vector field here simply means to display the field in a moving frame of reference by subtracting the reference frame velocity $[U_G, V_G]$ from the flow velocities. When the velocity of the reference frame matches the velocity of a vortex, the vortex will appear as a roughly circular pattern of velocity vectors (Adrian et al. 2000a). The signature of a hairpin vortex in a PIV measurement is by Adrian et al. described as a region of strong second quadrant vectors (pointing upstream and outward from the wall) located upstream and on the wall-side of the vortex, the angle of this region should be approximately 45° relative to the wall.

Figure 5 shows a temporal sequence of four Galilean decomposed vector-fields, the reference frame velocity is displayed in top of each field. In the first image only a quite weak vortex can be distinguished but the background colour-scale showing the spanwise velocity, positive being out of the paper-plane, indicates that there is an inclined structure of the same character as those described in section 2.2 in the upper left corner of the first image. The vortex seen in the second image is also relatively weak but more aligned with the w-structure. The w-structure is not visible in the third image, but here we see instead the signature of a hairpin vortex, a quite strong vortex together with an ejection. The signature of the hairpin vortex can still be seen in the

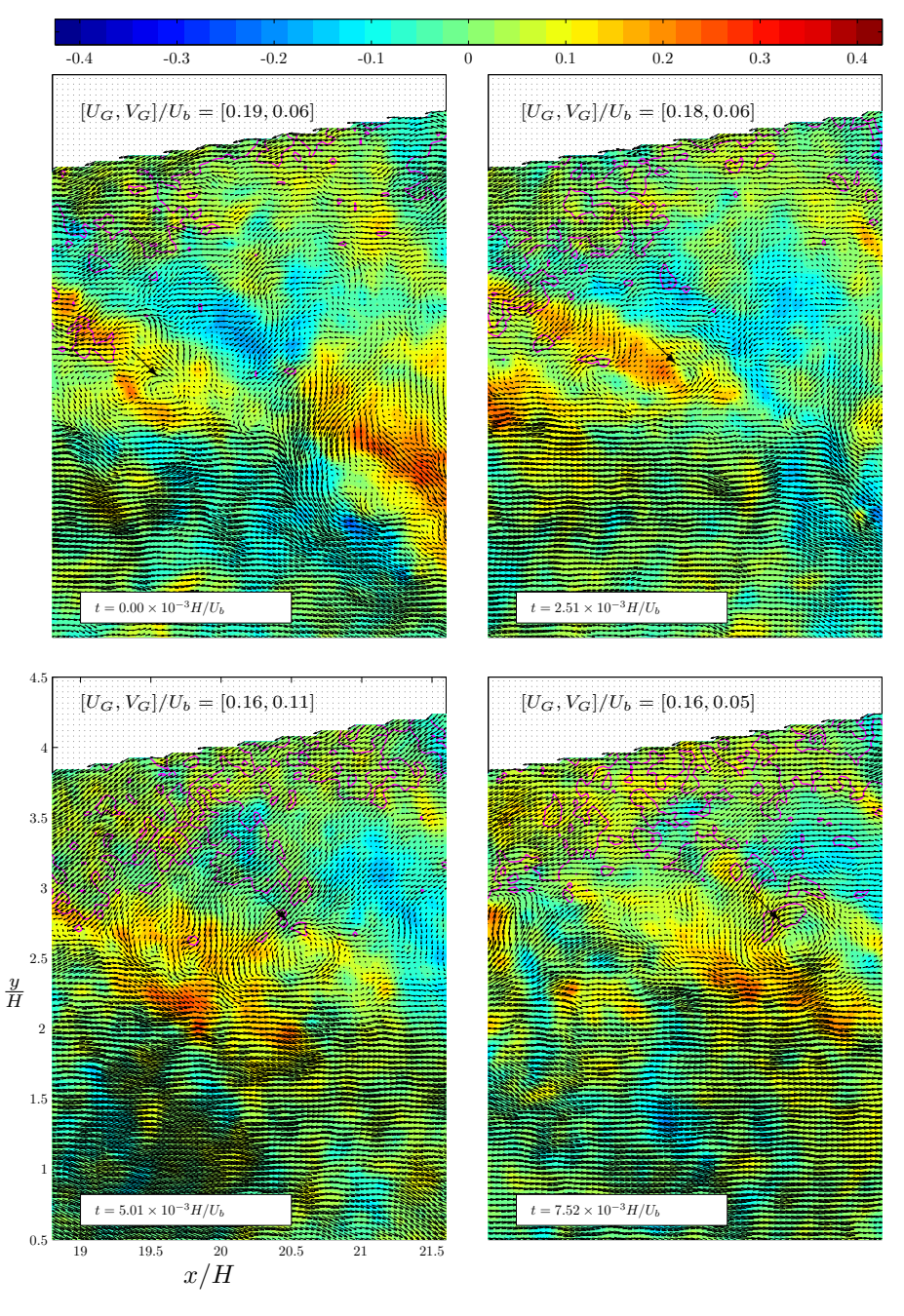


FIGURE 5. Instantaneous vector fields. Background colours show the spanwise velocity w/U_b (see colour-bar). Magenta contours enclose regions with backflow along the inclined wall. Arrows point out the vortex described in the text.

forth image. Notable is also the increased back-flow that seems to be a result of the ejection.

A reasonable explanation of the observed events is that the vortices seen in the first two images are not part of the hairpin vortex and that we instead see a hairpin vortex that in the beginning has its spanwise centre below the measurement-plane but successively moves in the positive z-direction so that its spanwise centre is near the measurement-plane in the last two images. A region of positive velocity in the z-direction, not associated with the structures, that could explain the spanwise translation of the hairpin structure can indeed be observed in the images.

2.4. Spatial spectra

Spectral analysis of turbulence gives information of how the turbulent fluctuations are distributed over different spatial (or temporal) scales. Computing spatial spectra in a direction where the mean flow is inhomogeneous, as is done here, is somewhat questionable. However, the variation of mean flow velocities and turbulence intensities are relatively small along the lines where the spectra have been evaluated, hence the average spectral distribution should not be expected to vary considerably along these lines either.

The presented spectra were calculated as,

$$E_{ii} = \frac{\hat{u'_i}(kH)\hat{u'_i}^*(kH)}{U_{\iota}^2},\tag{1}$$

where $u_i'(kH)$ is the Fourier-transform of the fluctuating velocities measured along a line in space, k is a wave-number and an asterisk denotes the complex conjugate. From a given PIV-setup one is only able to extract spectral information on wavenumbers larger than $k_{min} = 2\pi/L$, with L being the size of the image, and smaller than a wavenumber k_{max} which depends on the physical size of the interrogation areas and the signal to noise level of the measurements. If the noise level is small k_{max} will be equal to the cutoff wavenumber $k_c = 2.8/\Delta L$, where ΔL is the physical length-scale of the interrogation areas. The cutoff wavenumber is here defined as the wavenumber where the signal strength is halved due to the low pass filtering following from the averaging over the interrogation areas. It is shown by Foucaut et al. (2004) that one can calculate an optimal interrogation area size, that for a certain PIV-setup gives the best wavenumber resolution without biasing the results with noise.

Figures 6 and 7 display spectra for u' and v' computed from two-component measurements near the separation point. The noise level of these measurements is quite low and the optimal interrogation area length was concluded to be smaller than 16 pixels, which is the area size used for the presented data. In this region the E_{11} -spectra are similar in shape for all the investigated y-positions across the diffuser, the spectra differ only in magnitude, a difference

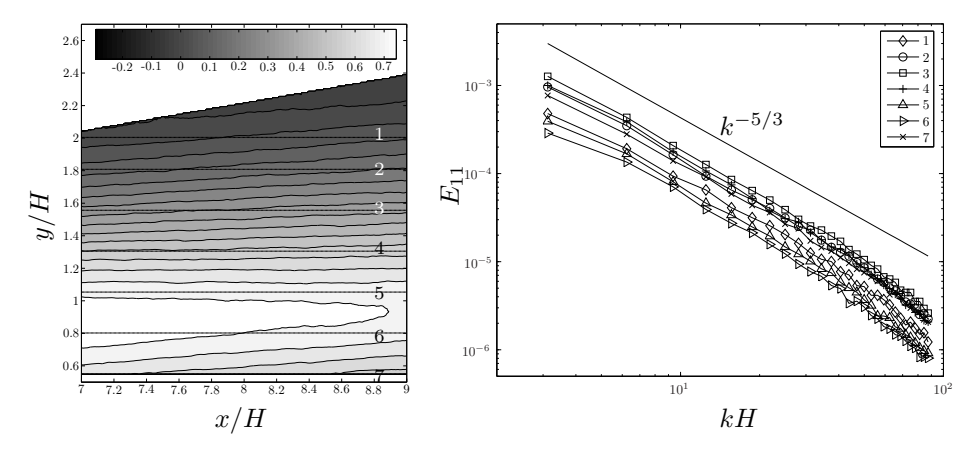


FIGURE 6. The right figure shows spectra of velocities in the x-direction, computed from data taken along the lines indicated in the left figure. The contours in the left figure shows the velocity in the x-direction.

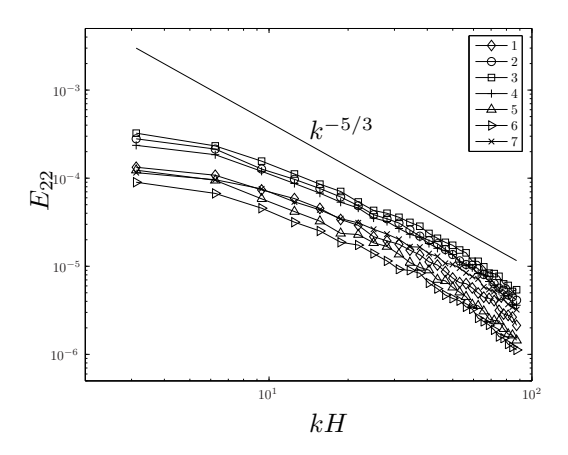


FIGURE 7. Spectra of velocities in the y-direction along lines indicated in figure 6.

that can be related to the magnitude of $\overline{u}\overline{u}$ at the different positions. The slopes of the E_{11} spectra are near -5/3 for an intermediate range of wavenumbers, indicating that there exists an inertial sub-range between the large- and small-scale turbulence.

The E_{22} spectra are also rather similar, independent of the y-position, but have less energy at small wave-numbers as compared to the E_{11} spectra. This is of course only a reflection of the fact that the $\overline{u}\overline{u}$ turbulence component has more energy than the $\overline{v}\overline{v}$ component. At larger wavenumbers though, the

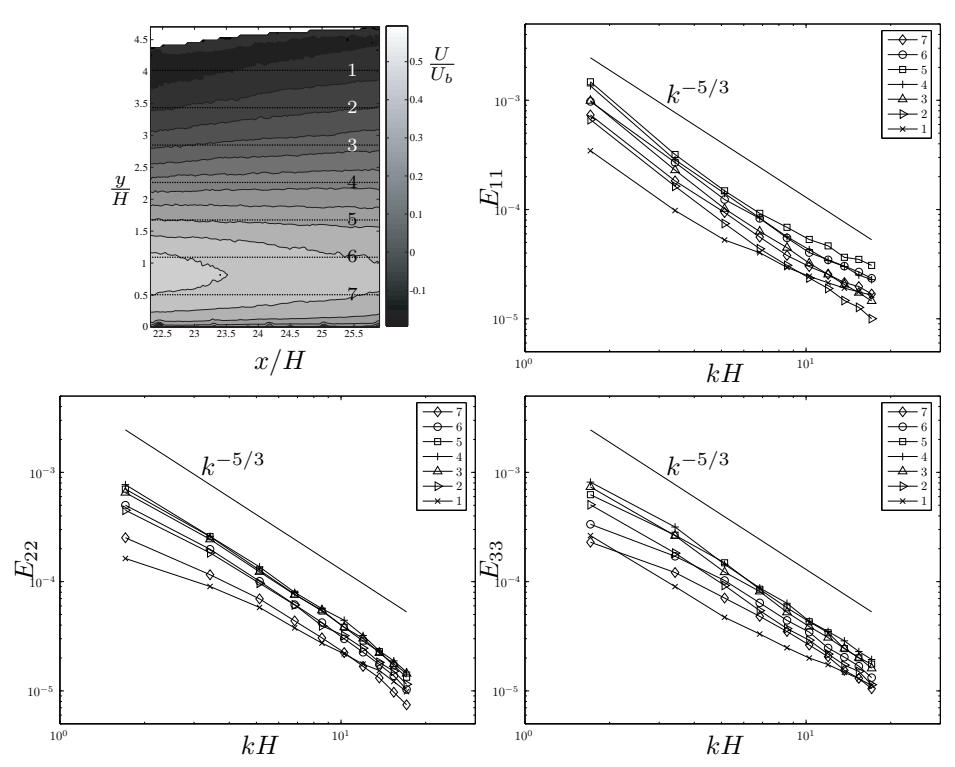


FIGURE 8. Spatial spectra of u', v' and w', computed from data at the lines shown in the upper left image.

energy levels of \overline{vv} are of the same order, or even larger, than those of \overline{uu} (the $k^{-5/3}$ lines are drawn in the same position in the two figures and can be used as a reference). Hence, the turbulence in this region is approximately isotropic at small scales.

For the presented spectra taken from the 3 component measurements the optimal interrogation area length was determined to be around 24 pixels, varying slightly between spectra taken from different y-positions. The stereoscopic setup give effective interrogation areas that are larger in the y-direction than in the x-direction, due to the oblique viewing. This means that it is the E_{11} -spectra that will first suffer from noise degradation when the interrogation area size is diminished and hence determine the optimal interrogation area size. Unfortunately, it was not possible in the software used for the PIV-evaluation to choose freely the interrogation area size, thus the presented spectra from the 3 component measurements were computed with 32 pixels long interrogation areas. Since $k_c = k_{max}$ for 24 pixels long interrogation areas $k_{max} > k_c = 2.8/\Delta L$ for 36 pixels long areas, this ensures that the presented spectra should have a

low bias due to noise since they are limited to wavenumbers between k_{min} and k_c .

The spectra shown in figure 8 are taken along the numbered lines shown in the upper left picture, globally this region is located just upstream the downstream corner of the diffuser. In this region the turbulent velocities reach their maximum values, the turbulence production however reach its maximum peaks further upstream (Törnblom et al. 2006b). Most of the E_{11} -spectra shown in figure 8 have a slightly concave shape. This shape can be interpreted as a result of the turbulence not being in local equilibrium with the meanflow and that the relatively large levels of small scale turbulence are due to turbulence produced elsewhere that have been transported to this spatial region and broken down to smaller scales along the way. This effect is seen in the spectra of all three components at the position closest to the inclined wall where probably a major part of the turbulence is produced elsewhere since the production rate of turbulence is small in this region.

2.5. Spatial correlations

Spatial auto-correlations give an indication of the dominating scale of the velocity fluctuations, the presented correlations are calculated as

$$R_{u_i u_i}(x, y) = \frac{\overline{u_i'(x, y)u_i'(x_0, y_0)}}{\sqrt{\overline{u_i'u_i'(x, y)}}\sqrt{\overline{u_i'u_i'(x_0, y_0)}}},$$
(2)

where u_i' is the fluctuating velocity in the x_i -direction and (x_0, y_0) are the coordinates of the fixed point around which the correlation is computed.

Figure 9 shows the spatial auto-correlation for the velocities in the streamwise direction, R_{uu} , computed at 8 different streamwise stations at heights y/h(x)=0.2, 0.4, 0.6 and 0.8, with h(x) being the local duct height. The figure reveals that the turbulence length-scale grows with increasing x in the diffusing part and that the length-scale in the exit channel is nearly constant. In the diffusing part, between $x/H \approx 15$ and 25, there are apparent negative correlations between u' in the centre region and u' close to the straight wall, these are likely to be due to the motion of the 'jet-like' high velocity region emanating from the inlet channel. There is a strikingly distinct boundary in the correlations with a y-position in the vicinity of the maximum mean U-velocity and the gradients of the correlation-coefficients become very steep as this boundary is approached. The u'-fluctuations in the separated region appears to be rather unaffected by events occurring near the straight wall. It can also be noted that the correlation peaks' main axes are inclined in the first part of the diffuser but become close to horizontal further downstream. For zero pressure gradient turbulent boundary layers Krogstad & Antonia (1994) reports an angle of about 10° for the R_{uu} correlation.

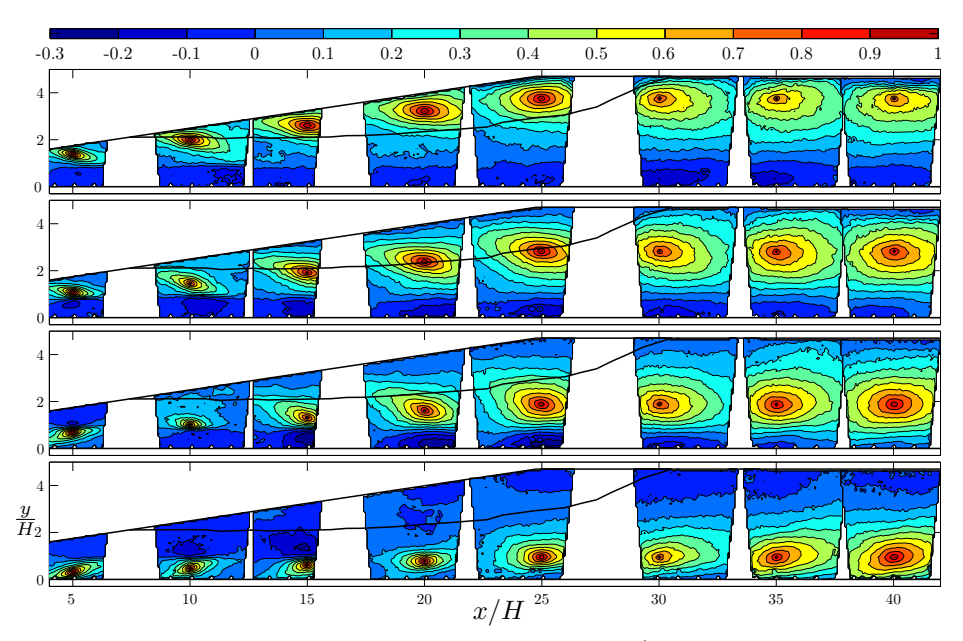


FIGURE 9. Correlation coefficients R_{uu} at x/H = 5, 10, 15, 20, 25, 30, 35, 40 and y/h(x) = 0.2, 0.4, 0.6, 0.8. Contour levels between -0.3 and 1 are shown with an increment of 0.1. The thick black contour shows the mean streamline enclosing the recirculation region.

The auto-correlations of v', shown in figure 10, also display an increased length-scale in the diffusing part and a nearly constant length-scale in the exit channel. In general the lengths over which v' is correlated are smaller than for u', the R_{vv} -peaks are also more circular although they are slightly elongated in the y-direction. The negative correlations are less pronounced for this velocity component but they exist and are, as for R_{uu} , likely to be due to the motions of the high velocity region. A rough estimate of the 'wave-length' of this motion based on R_{vv} in the lowest image in figure 10 gives that it is on the order of 5H. Some weak indications of roller vortices (with a spanwise axis) in, or near, the separated region can be seen as a negative correlation in the x-direction.

The peaks of R_{ww} , shown in figure 11, have a pronounced $\sim 45^{\circ}$ inclined shape, resembling the shape of the structures described in section 2.2. Negative correlations are found on both sides of the peaks along the minor axes of the peaks. This shape of the correlations can be interpreted either as a sign of a wave-like wiggling motion in the spanwise direction or that large scale vortices with their axes aligned with the major axes of the R_{ww} correlation peaks are common in this flow.

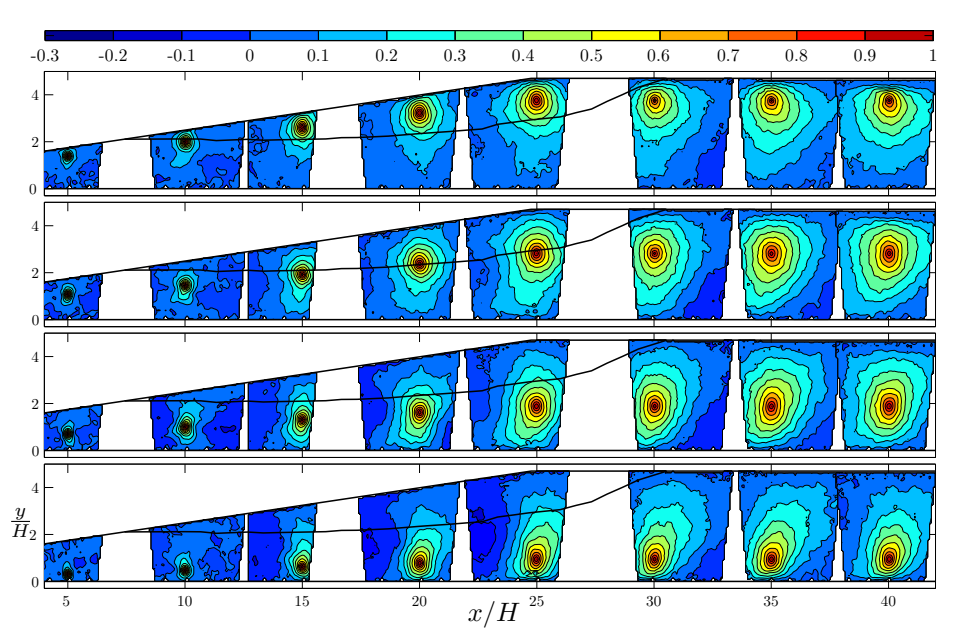


FIGURE 10. Correlation coefficients R_{vv} . Positions and contour levels are the same as in figure 9.

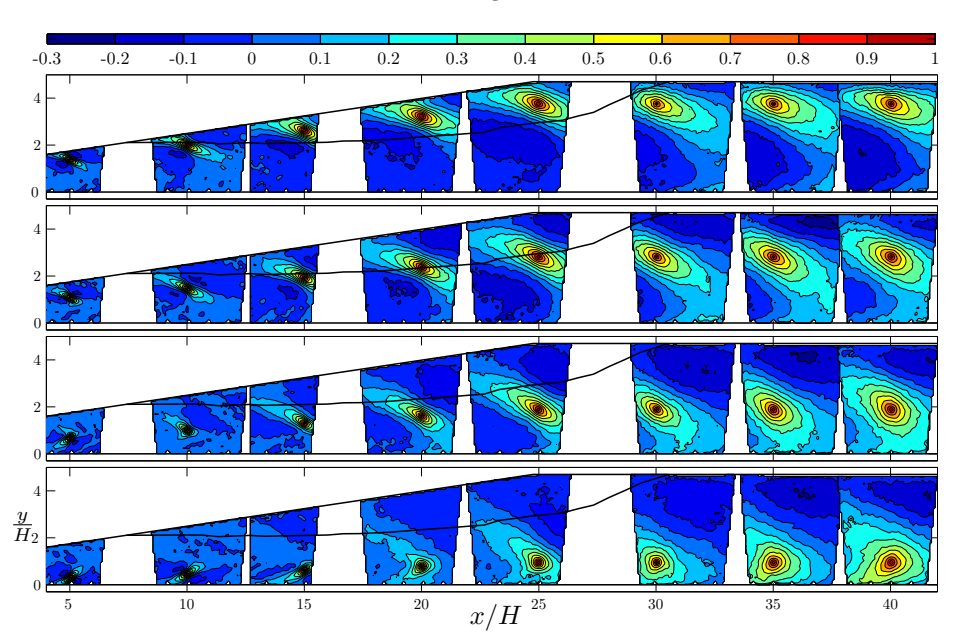


FIGURE 11. Correlation coefficients R_{ww} . Positions and contour levels are the same as in figure 9.

Studies of structures of the spanwise velocity fluctuations in an xy-plane are surprisingly few so I have not found any investigation discussing these structures and particularly not in conjunction to hairpin or horseshoe vortices.

3. Summary and conclusions

Some of the temporal and structural features of the flow in a plane asymmetric diffuser with 8.5° opening angle have been investigated experimentally using time-resolving stereoscopic PIV.

Energy spectra, instantaneous velocity fields and spatial auto-correlations indicate that the turbulence is partly broken down to smaller scales in the separated region near reattachment.

The existence of large scale hairpin- or horseshoe-like structures in this flow is supported by (i) the shape of the auto-correlation functions of the spanwise velocity (ii) the frequently observed pairs of, one positive and one negative, elongated and inclined structures of spanwise velocity (ii) the sequence of vector-fields showing the disappearance of a pair of the previously described structures, due to large scale spanwise fluctuations, and the subsequent appearance of an ejection event.

The formation of large-scale regions of back-flow near the separation point appear to be a result of large scale fluctuations of undulating character that cannot be related to any distinct vortices. However, further downstream it is observed that ejection events related to hairpin structures could give rise to local regions of flow reversal.

Future studies could involve estimating the importance of the observed hairpin structures for the backflow using more elaborate evaluation techniques, such as e.g. conditional averaging.

Acknowledgements

The authors would like to thank Björn Lindgren for contributing to the present experiment in its early stages. Ulf Landén and Marcus Gällstedt are acknowledged for aiding in the manufacturing of the flow device. The Swedish Energy Agency is gratefully acknowledged for the financial support.

References

- Adrian, R. J., Christensen, K. T. & Liu, Z.-C. 2000 a Analysis and interpretation of instantaneous turbulent velocity fields. *Exp. Fluids* **29**, 275–290.
- Adrian, R. J., Meinhart, C. D. & Tomkins, C. D. 2000b Vortex organization in the outer region of the turbulent boundary layer. J. Fluid Mech. 422, 1–54.
- Buice, C. U. & Eaton, J. K. 1997 Experimental investigation of flow through an asymmetric plane diffuser. *Tech. Rep.*. Department of mechanical engineering, Stanford university.

- Buice, C. U. & Eaton, J. K. 2000 Experimental investigation of flow through an asymmetric plane diffuser. *J. Fluids Eng.* **122**, 433–435.
- FOUCAUT, J., CARLIER, J. & STANISLAS, M. 2004 PIV optimization for the study of turbulent flow using spectral analysis. *Meas. Sci. Technol.* **15**, 1046–1058.
- KIYA, M. & SASAKI, K. 1985 Structure of large-scale vortices and unsteady reverse flow in the reattaching zone of a turbulent separation bubble. J. Fluid Mech. 154, 463–491.
- KROGSTAD, P.-Å. & ANTONIA, R. A. 1994 Structure of turbulent boundary layers on smooth and rough walls. J. Fluid Mech. 277, 1–21.
- Obi, S., Aoki, K. & Masuda, S. 1993a Experimental and computational study of turbulent separating flow in an asymmetric plane diffuser. In *Ninth Symp. on Turbulent Shear Flows*, p. 305. Kyoto, Japan.
- Obi, S., Ishibashi, N. & Masuda, S. 1997 The mechanism of momentum transfer enhancement in periodically perturbed turbulent separated flow. In 2nd Int. Symp. on Turbulence, Heat and Mass Transfer, pp. 835–844. Delft, The Netherlands.
- Obi, S., Nikaido, H. & Masuda, S. 1999 Reynold number effect on the turbulent separating flow in an asymmetric plane diffuser. In *Proceedings of FEDSM99*, *FEDSM* 99-6976. ASME/JSME Fluids Engineering Division Summer Meeting.
- Obi, S., Ohizumi, K., Aoki, K. & Masuda, S. 1993b Turbulent separation control in a plane asymmetric diffuser by periodic perturbation. In *Engineering turbulence modelling and Experiments* 2, pp. 633–642.
- SHILOH, B. G., SHIVAPRASAD, B. G. & SIMPSON, R. L. 1981 The structure of a separating turbulent boundary layer. Part 3. Transverse velocity measurements. *J. Fluid Mech.* **113**, 75–90.
- SIMPSON, R. L., CHEW, Y.-T. & SHIVAPRASAD, B. G. 1981a The structure of a separating turbulent boundary layer. Part 1. Mean flow and Reynolds stresses. J. Fluid Mech. 113, 23–51.
- SIMPSON, R. L., CHEW, Y.-T. & SHIVAPRASAD, B. G. 1981b The structure of a separating turbulent boundary layer. Part 2. Higher order turbulence results. J. Fluid Mech. 113, 53-73.
- Song, S. & Eaton, J. K. 2004 Flow structures of a separating, reattaching and recovering boundary layer for a large range of Reynolds number. *Exp. Fluids* **36**, 642–653.
- TÖRNBLOM, O., LINDGREN, B. & JOHANSSON, A. 2006a Experimental procedures for the investigation of the turbulent flow in a plane asymmetric diffuser by means of stereoscopic high-speed PIV. *Tech. Rep.*. KTH Mechanics, (**Paper 6**).
- TÖRNBLOM, O., LINDGREN, B. & JOHANSSON, A. V. 2006b Measurements of mean flow statistics in a plane asymmetric diffuser with 8.5° opening angle. To be submitted (Paper 1).

Paper 3

P3

A Reynolds stress closure description of separation control with vortex generators in a plane asymmetric diffuser

By Olle Törnblom and Arne V. Johansson

KTH Mechanics, SE-100 44 Stockholm, Sweden

A way to model the effects of streamwise vortices in a turbulent flow with one homogeneous direction is presented. The Reynolds averaged Navier-Stokes (RANS) equations are solved with a differential Reynolds stress turbulence model with elliptic blending near-wall treatment. Assuming that the vortices can be approximated with the Lamb-Oseen model, wall-normal Reynolds stress distributions are calculated, corresponding to the spanwise variances of the estimated velocity distribution downstream the vortex generators. The Reynolds stress distributions that are due to the vortex generators are added to the Reynolds stresses from the turbulence model so as to mimic the increased mixing due to the vortex generators. Volume forces are applied in the mean momentum equations to account for the drag of the vortex generators. The model is tested and compared with experimental data from a plane asymmetric diffuser flow which is separating without vortex generators. The results indicate that the model is able to mimic the major features of vortex generator flow control and that the flow case in question is susceptible to separation control. The model results show that the pressure recovery of the diffuser could be increased by almost 10 percent by applying vortex generators and that, if keeping the shape of the vortex generators fixed, their optimal position is close to the diffuser inlet. It is demonstrated that the increased pressure recovery when applying vortex generators is to a very high degree a result of a decreased turbulence production. A test is performed, using time-dependent but quasi-steady RANS, regarding the temporal evolution of the separation after a sudden removal and a subsequent reapplication of the vortex generator control. The test showed that the time it takes to remove a separation after the control is turned on is substantially shorter than the time it takes to form an equivalently large separation after the control is turned off.

1. Introduction

Vortex generators are common in many flow applications for the purpose of control of flow separation and computational fluid dynamics (CFD) based on turbulence models is widely used in fluid-dynamic design. The basic principle behind separation control with vortex generators is that the vortices increase the transport of momentum through the boundary layer, from high velocity regions down towards the solid boundaries. It is generally favourable to make a design where separation is avoided without any means of control, but in some cases this cannot be achieved. In such cases it is an advantage if the effects of using vortex generators can be investigated early in the design work. A vortex generator model could also be useful when seeking ways to improve already existing designs.

The most straightforward way to investigate the effects of vortex generators in a flow simulation is to include the geometry of the vortex generators in the computational geometry and resolve the flow around the vortex generator. However, this approach will lead to a rather large increase in computational effort in comparison to the same case without vortex generators, due to the increased number of grid points needed to resolve the flow around the generators. In addition the computation has to be done in three spatial dimensions even if the flow is statistically two-dimensional. A simpler approach is to replace the vortex generator geometries with volume forces that create vortices similar to those behind vortex generators. This is computationally more efficient but mesh refinement and three dimensional computations are still required. Both of the approaches described above are studied in e.g. Waithe (2004), Jirásek (2005) and Dudek (2005). The model presented herein requires neither mesh refinement nor three-dimensional computations.

The model describing the vortex flow field as a function of the vortex generator wing parameters is to some extent inspired by Wendt (2001), who did a parametric study of the dependence of vortex circulation and peak vorticity on vortex generator geometry. The present computational model uses averaging in a homogeneous transverse direction and is here tested in the case of a plane asymmetric diffuser.

2. Vortex generator model

The modelled vortex generators are assumed to consist of small aerofoils protruding perpendicularly out from the wall, so that the wing tip vortices generate the desired mixing. The good agreement between experimentally observed and model predicted vortices in Wendt (2001) indicates that the chosen model should be accurate enough for the present purpose. The wings are mounted in pairs with opposite angles of attack producing counter rotating vortex pairs, see figure 1. The distance between the wings in a pair is δ and the distance between the pairs is D.

2.1. Determining the circulation

The circulation distribution $\Gamma(y')$, along the wings is calculated using lifting line theory (see e.g. Glauert 1947). Knowing the oncoming flow distribution,

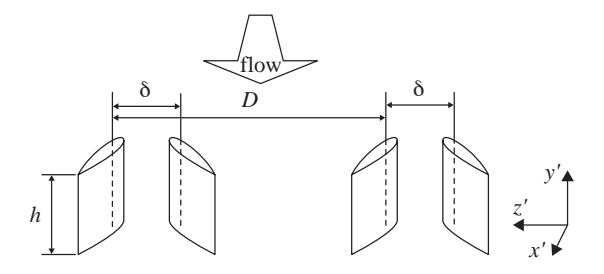


Figure 1. Geometry of the vortex generator array.

U(y'), the cord of the aerofoil, c, and K, the slope of the lift coefficient curve at zero angle of incidence, the circulation is given by,

$$\Gamma(y') = \frac{K}{2}U(y')c\left(\alpha - \frac{w(y')}{U(y')}\right),\tag{1}$$

where the wing-normal induced velocity is

$$w(y') = \frac{1}{4\pi} \int_{-h}^{h} \frac{d\Gamma}{dy'_1} \frac{1}{y' - y'_1} dy'_1.$$
 (2)

The integral in equation 2 is taken over the whole span of the vortex generator wing and its mirror image. K is approximated with the value for a Joukowski aerofoil (2π) . The resulting equation is solved by expressing Γ as a Fourier series,

$$\Gamma(\theta) = 4hU_{max} \sum_{n=1}^{\infty} A_n \sin(n\theta), \tag{3}$$

replacing the co-ordinate y' with θ so that $y'=-h\cos\theta$. Inserting 3 into 2 the wing-normal velocity distribution now becomes

$$w(\theta) = \frac{U_{max}}{\pi} \int_0^{\pi} \frac{\sum n A_n \cos(n\theta_1)}{\cos(\theta_1) - \cos(\theta)} d\theta_1 = U_{max} \sum_{n=1}^{\infty} n A_n \frac{\sin(n\theta)}{\sin(\theta)}.$$
 (4)

For details on the solution of the integral in equation 4 the reader is referred to e.g. Glauert (1947). Now, by using 1, 3 and 4 we get,

$$\sum_{n=1}^{\infty} A_n \sin(n\theta) \left(n\mu + \sin(\theta) \right) = \mu \frac{U(y')}{U_{max}} \alpha \sin(\theta), \tag{5}$$

where $\mu = Kc/8h$. The coefficients A_n in 5 can now be approximated by truncating the series and solving the resulting linear system of equations. Knowing the coefficients A_n , Γ can be determined using 3.

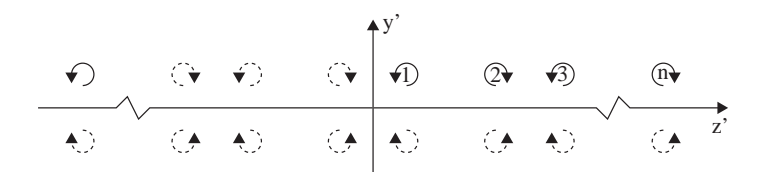


FIGURE 2. The vortex system behind the wings. The mirror image vortices are drawn as dashed turning arrows.

2.2. Vortex flow field

The vortex sheets behind the wings are assumed to roll up into self similar Lamb-Oseen vortices (see *e.g.* Lamb (1932)) with the azimuthal velocity distribution,

$$u_{\phi}(r) = \frac{\Gamma_{max}}{2\pi r} \left[1 - \exp\left(\frac{-r^2}{r_0^2}\right) \right],\tag{6}$$

where Γ_{max} is the maximum value of $\Gamma(y')$, determined as described in section 2.1, and r_0 is approximately corresponding to the radius of the viscous core of the vortex. The maximum vorticity at the centres of the vortices is related to the circulation and r_0 as $\omega_{x'}(r=0) = \Gamma_{max}/r_0^2$. The positions, in the z'-direction, of vortices with velocity distributions $\pm u_{\phi}$ are determined by,

$$z'_{n} = \delta \frac{-1^{n+1}}{2} + D \frac{-1^{n} + 2n - 1}{4}, \qquad n = 1, 2, ..., \infty.$$
 (7)

The vortex centres are located at the height h above the wall, equal to the height of the vortex generator wings. Superposing the velocity fields from the n vortices positioned at y'=h and $z'=\pm z'_n$ and their mirror images at y'=-h, $z'=\pm z'_n$ (cf. figure 2) results in the a velocity distribution given by,

$$[v'(y',z'),w'(y',x')] = \sum_{n=1}^{\infty} (-1)^{n+1} \sum_{m=1}^{4} (-1)^{m+1} u_{\phi}(r_m) [\cos(\phi_m), -\sin(\phi_m)],$$
(8)

where

$$\begin{split} r_1 &= \sqrt{(y'-h)^2 + (z'-z_n')^2}, & \phi_1 &= \arctan\left((y'-h)/(z'-z_n')\right), \\ r_2 &= \sqrt{(y'+h)^2 + (z'-z_n')^2}, & \phi_2 &= \arctan\left((y'+h)/(z'-z_n')\right), \\ r_3 &= \sqrt{(y'+h)^2 + (z'+z_n')^2}, & \phi_3 &= \arctan\left((y'+h)/(z'+z_n')\right), \\ r_4 &= \sqrt{(y'-h)^2 + (z'+z_n')^2} & \text{and} & \phi_4 &= \arctan\left((y'-h)/(z'+z_n')\right). \end{split}$$

An example of the resulting velocity field is shown in figure 3a.

2.3. Reynolds stress forcing levels

The proposed model is meant to work in two-dimensional geometries, hence the vortex flow field described in section 2.2 cannot be added to the flow as

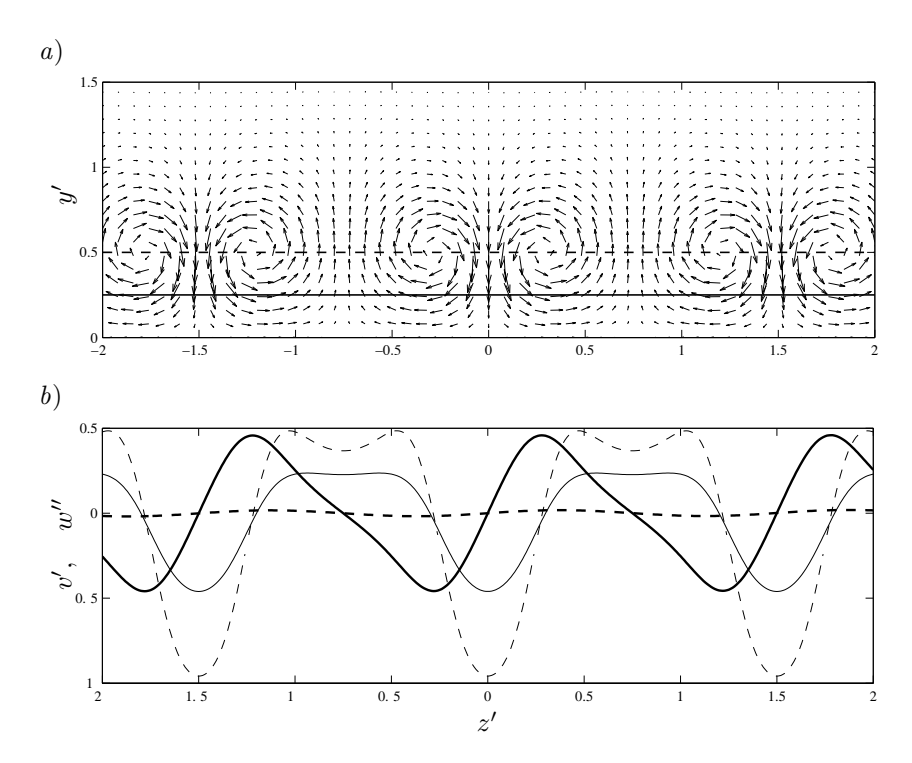


FIGURE 3. Velocities in the y'z'-plane. Image a) shows the vortices behind a row of vortex generators with $h{=}0.5$, $D{=}1.5$ and $\delta{=}0.5$. Image b) shows the v' (thin lines) and w' (bold lines) velocities along the lines at $y'{=}0.25$ (—) and 0.5 (---) shown in image a).

it is, since it extends in the z-direction which is normal to the plane in which the two-dimensional RANS computation is made. The idea of the model is instead to calculate the spatial variances in the z'-direction of v'(y',z') and w'(y',z') and add those to the turbulence model's distributions of \overline{vv} and \overline{ww} respectively. The additional contributions to the Reynolds stresses will hence be

$$\Delta \overline{u_i' u_j'}(y') = \frac{1}{D} \int_0^D u_i'(y', z') u_j'(y', z') dz'$$
(9)

which are non-zero for $\Delta \overline{v'v'}$ and $\Delta \overline{w'w'}$ only. Due to the periodicity of the vortex generator array, the variance need only be calculated from z'=0 to D. It should also be noted that the averages of v' and w' are zero if evaluated over one period for a constant value of y', cf. figure 3b. An example of typical $\Delta \overline{v'v'}$ and $\Delta \overline{w'w'}$ distributions is shown in figure 4. In order not to violate

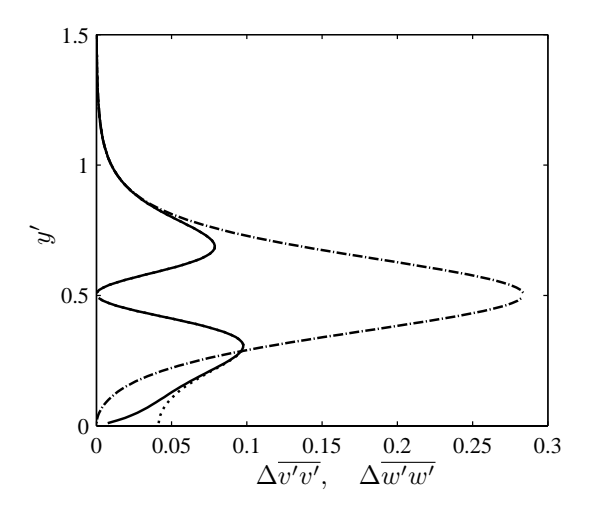


FIGURE 4. The distributions of $\Delta \overline{v'v'}$ (dash dotted line) and $\Delta \overline{w'w'}$ (solid line). The dotted line shows the behaviour of $\Delta \overline{w'w'}$ without the damping function applied.

the no slip boundary condition imposed at the wall for the Reynolds stresses, a damping function $(1-\exp(-20y'/h))$ is applied to $\Delta \overline{w'w'}$. The distributions of $\Delta \overline{w'w'}$ with and without the damping function are shown in figure 4.

2.4. Volume forces in the mean flow equations

The drag of the vortex generators will cause a velocity deficit in the mean flow. This is included in the model by the application of volume forces in the mean flow equations. Using the circulation distribution along the vortex generator wings, given by equation 3, the force per unit volume in the x'-direction, to apply at height y' can be calculated as

$$F(y') = \lambda(x', y') \frac{2}{DL} \rho w(y') \Gamma(y'), \tag{10}$$

where

$$L = \int \lambda(x', 0) \mathrm{d}x' \tag{11}$$

is the effective length in the x'-direction of the window function λ which applies the forcing smoothly and limits the forcing to act only in the region where the vortex generators are located. The forcing from equation 10 is added to the Reynolds averaged Navier-Stokes equations so that the resulting equation becomes:

$$\rho \frac{DU_i}{Dt} = -\frac{\partial P}{\partial x_i} + \frac{\partial}{\partial x_j} \left(\mu \frac{\partial U_i}{\partial x_j} - \rho \overline{u_i u_j} \right) - F_i \tag{12}$$

with F_i being F(y')'s component in the x_i -direction.

When forcing the Reynolds stress equations the idea is to add a forcing, $\Delta \overline{v'v'}(y')$ and $\Delta \overline{w'w'}(y')$, to the corresponding Reynolds stresses, so that the additional stresses according to equation 9 should be obtained by integrating in the streamwise direction. This is achieved, in an approximative way, by adding a term,

$$F_{\underline{u_i'u_j'}} = \lambda(x', y') \Delta \overline{u_i'u_j'}(x', y') \frac{U(x', y')}{L}$$
(13)

to the Reynolds stress equations. In the above equation $\Delta \overline{u_i'u_j'}$ correspond to the forcing levels as calculated in section 2.3 and U is the mean flow velocity in the x'-direction.

As previously mentioned, the forcing is applied in a smooth manner in order to avoid numerical difficulties. This is achieved by using the smoothly varying function

$$S(x) = \begin{cases} 0 & x \le 0\\ 1/[1 + \exp(\frac{1}{x-1} + \frac{1}{x}] & 0 < x < 1\\ 1 & x \ge 1 \end{cases}$$
 (14)

and using it so that

$$\lambda(x', y') = \left[S\left(\frac{x'}{\Delta_{rise}}\right) - S\left(\frac{x' - x'_{end}}{\Delta_{rise}} + 1\right) \right] S\left(\frac{y'_{end} - y'}{\Delta_{rise}}\right). \tag{15}$$

This yields a smooth rectangular window between x'=0, y'=0 and $x'=x'_{end}$, $y'=y'_{end}$. The parameter Δ_{rise} determines the width of the region where λ is increasing (or decreasing).

3. Turbulence model

In order to follow how the velocity fluctuations, or extra Reynolds stresses, $\Delta \overline{v'v'}$ and $\Delta \overline{w'w'}$, induced by the vortex generators are transported we need a turbulence model that is able to predict the advective and diffusive transport of the individual Reynolds stresses. With a two equation model, such as a $K-\varepsilon$ model, the effect of the wall-normal mixing due to $\Delta \overline{v'v'}$ would be diminished since the transported quantity, the turbulent kinetic energy K, is scalar. The same argument holds also, to some extent, for explicit algebraic Reynolds stress models (EARSM) where the advection and diffusion terms (for the Reynolds stress anisotropy) are neglected in a certain frame of reference. However, a differential Reynolds stress model (DRSM) should have the desired properties.

A DRSM is based on the transport equations for the Reynolds stress tensor, $R_{ij} = \overline{u_i u_j}$ (the Reynolds stress tensor is actually $-\rho \overline{u_i u_j}$), and will hence consist of up to six transport equations for R_{ij} plus one for an auxiliary quantity needed to determine the turbulence length-scale. In the following we will use a notation

where U_i is the velocity in the x_i direction and P is the pressure. Upper and lower case letters represent mean and fluctuating quantities respectively. A line over a quantity denotes the ensemble average. Subscripts after a comma represent derivatives in the corresponding direction.

3.1. Reynolds stress transport equations

The Reynolds stress transport equations in a non-dimensional form can be written as

$$\frac{DR_{ij}}{Dt} = \mathcal{P}_{ij} - \varepsilon_{ij} + \Pi_{ij} - \frac{\partial}{\partial x_k} \left(J_{ijk} - \frac{1}{Re_H} R_{ij,k} \right) + F_{\overline{u_i u_j}}$$
 (16)

where

$$\begin{split} \mathcal{P}_{ij} &\equiv -R_{im}U_{j,m} - R_{jm}U_{i,m} \\ \varepsilon_{ij} &\equiv \frac{2}{Re_H} \overline{u_{i,m}u_{j,m}} \\ \Pi_{ij} &\equiv 2\overline{p}s_{ij} \\ J_{ijk} &\equiv \overline{u_iu_ju_m} + \overline{u_jp}\delta_{im} + \overline{u_ip}\delta_{jm} \\ Re_H &= \frac{U_0H}{u_j}. \end{split}$$

 U_0 and H are typical velocity and length scales of the mean flow and ν is the kinematic viscosity. The last term is the (normalised) expression from equation 13. All terms in the right hand side of equation 16 need to be modelled, with the exception of the production, \mathcal{P}_{ij} , and the molecular diffusion term which are explicit in the Reynolds stresses and the mean flow velocities.

The dissipation rate tensor, ε_{ij} , can be divided into an isotropic part and a trace-less deviatoric part, $\varepsilon_{ij} = \varepsilon(e_{ij} + 2\delta_{ij}/3)$. The isotropic part is modelled using the auxiliary length-scale determining quantity (in this case ω) and the deviatoric part, also called the dissipation rate anisotropy, is modelled together with the pressure strain-rate tensor, Π_{ij} .

The pressure strain-rate tensor Π_{ij} involves pressure fluctuations and is hence associated with the non-local interaction of the turbulent fluctuations. Being trace-less, Π_{ij} can only have a redistributive effect on the Reynolds stresses. The most general quasi-linear (*i.e.* tensorially linear) model for the pressure strain-rate tensor lumped together with the dissipation rate anisotropy can be written as

$$\frac{\Pi_{ij}}{\varepsilon} - e_{ij} = -\frac{1}{2} \left(C_1^0 + C_1^1 \frac{\mathcal{P}}{\varepsilon} \right) a_{ij} + C_2 \tau S_{ij}
+ \frac{1}{2} C_3 \tau \left(a_{ik} S_{kj} + S_{ik} a_{kj} - \frac{2}{3} a_{kl} S_{lk} \delta_{ij} \right)
- \frac{1}{2} C_4 \tau \left(a_{ik} \Omega_{kj} - \Omega_{ik} a_{kj} \right).$$
(17)

Model	C_1^0	C_1^1	C_2	C_3	C_4
Present	3.6	0.0	0.8	2.07	1.05
Launder et al. (1975)	3.0	0.0	0.8	1.75	1.31
Wallin & Johansson (2002)	4.6	1.24	0.47	2.0	0.56
Wallin & Johansson (2000)	3.6	0.0	0.8	2.0	1.11
Speziale et al. (1991) (linearised)	3.4	1.8	0.36	1.25	0.40

TABLE 1. Values of the constants in equation 17 for the present model and some commonly used models.

In the model expression in equation 17, $\mathcal{P}=\mathcal{P}_{ii}/2$ is the production rate of the turbulent kinetic energy, $a_{ij}=R_{ij}/K-2\delta_{ij}/3$ is the Reynolds stress anisotropy tensor, $S_{ij}=(U_{i,j}+U_{j,i})/2$ and $\Omega_{ij}=(U_{i,j}-U_{j,i})/2$ are the mean strain-rate and rotation-rate tensors respectively and $\tau=K/\varepsilon$ is the turbulence timescale.

By altering the values of the five constants in equation 17 one can realise many of the quasi-linear models described in the literature. Table 1 shows the values of some commonly used models. Note that the values presented for the SSG-model by Speziale et al. (1991) are those found after a linearisation around a homogeneous shear flow in equilibrium. If the values chosen for the present model are expressed in the same fashion as in the pioneering paper by Launder et al. (1975) they would correspond to having c_1 =1.8 and c_2 =0.6. All models in table 1 were tested in the asymmetric diffuser flow case and it was found that the size of the predicted separation is very sensitive to changes in pressure strain-rate coefficients. The coefficients used in the present paper were chosen mainly because they give a reasonably large separation in comparison to the other sets of coefficients in table 1.

The term J_{ijk} has a spatially redistributive function and is often approximated with a gradient diffusion type of model. Both the model by Daly & Harlow (1970), which has an anisotropic diffusivity, and the 'standard' eddy viscosity model was tested in the present investigation. However, since no significant differences could be observed in the solutions with the two different models, the presented results were computed using the simpler model

$$J_{ijk} = \frac{\nu_T}{\sigma_K} \frac{\partial \overline{u_i u_j}}{\partial x_k},\tag{18}$$

where σ_K is a Schmidt number and the eddy-viscosity was defined as $\nu_T = K/\omega$.

3.2. Transport equation for the auxiliary length-scale determining quantity The model uses the inverse time scale, ω , as the length scale determining quantity. The dissipation rate is then determined as

$$\varepsilon = \beta^* K \omega, \tag{19}$$

where β^* is a model parameter. The transport equation used for ω is in principle the same as the one in Wilcox (1993). But by splitting ω into two parts, of which one is algebraic, we avoid problems related to the singular behaviour at solid boundaries, where ω will increase asymptotically as d^{-2} with decreasing wall normal distance d. The splitting method, where ω is decomposed so that $\omega = \tilde{\omega} + \omega_w$, is described in Gullman-Strand (2004). If the near wall asymptotic behaviour is treated algebraically by setting

$$\omega_w = \frac{6}{Re_H \beta d^2} \tag{20}$$

the resulting transport equation for $\tilde{\omega}$ becomes

$$\frac{D\tilde{\omega}}{Dt} = -U_k \frac{\partial \omega_w}{\partial x_k} + \alpha \omega a_{kl} S_{lk} - \beta (\tilde{\omega}^2 + 2\tilde{\omega}\omega_w)
+ \frac{\partial}{\partial x_j} \left[\frac{1}{Re_H} \frac{\partial \tilde{\omega}}{\partial x_j} + \frac{\nu_T}{\sigma_\omega} \frac{\partial \omega}{\partial x_k} \right].$$
(21)

The splitting procedure allows $\tilde{\omega}$ to be set to zero at solid boundaries. The Schmidt numbers σ_K and σ_{ω} appearing in equations 18 and 21 were both set to 2.0, *i.e.* the values given in Wilcox (1993).

3.3. Near wall treatment

In separating flows, the use of so called 'wall functions' or 'log-layer' boundary conditions is not applicable since the friction velocity scaling fails near, and in, regions of separation. Hence, in a separating flow the turbulence model equations need to be integrated to the wall. But special treatment is required in order to predict the highly anisotropic state of turbulence in the vicinity of walls, since most turbulence models are derived and calibrated to give good predictions in nearly isotropic flows at high Reynolds number.

There exists a multitude of near wall modifications for differential Reynolds stress models in the literature. Many of these models are based on extensions of the damping model by van Driest (1951) applied to the terms of the pressure strain rate and dissipation rate tensors. A selection of such models are reviewed in So *et al.* (1991). Another way of handling the near wall flow, that is called elliptic relaxation, was introduced Durbin (1991). Elliptic relaxation was first applied to the K- ε model, resulting in the now popular v^2 -f-model, and later in Durbin (1993) the concept was extended to differential Reynolds stress models.

The basic idea of elliptic relaxation is the knowledge that non-local effects, such as the damping of the wall normal velocity in the vicinity of a wall, are described by elliptic-type differential equations. In the original model by Durbin (1993) the pressure strain-rate and dissipation rate anisotropy terms are solved for using a set of non-homogeneous Helmholtz equations, one for each Reynolds stress component. In the right hand side of the Helmholtz equations are the corresponding high Reynolds number or 'far from wall' values of the

terms and a turbulence length-scale measure is used in order to set the scale over which the solution changes. The boundary conditions of the Helmholtz equations are set so that the Reynolds stresses get the desired asymptotic behaviour. Different boundary conditions are used depending on whether the Reynolds stress is normal or tangential to the wall.

However, the elliptic relaxation method has some drawbacks. The boundary conditions of the elliptic equations are formulated as a fraction of two quantities that both go asymptotically as d^2 as the wall normal distance $d \to 0$. The sensitivity of the boundary condition means that the elliptic equations have to be strongly coupled with their corresponding Reynolds stress equation in order to avoid convergence problems. Many computational codes for the Reynolds averaged Navier-Stokes equations use segregated solvers and will hence have problems implementing the elliptic relaxation method. Another drawback of elliptic relaxation is the added computational cost of the elliptic equations.

In an attempt to diminish the problems associated with the elliptic relaxation method Manceau & Hanjalić (2002) derived a near wall model that they called the elliptic blending model. Later on, in Manceau (2005), a revised version of the elliptic blending model was presented where some computational difficulties had been removed. The present investigation has been made using a slightly modified version of this model. The elliptic blending model uses only one elliptic equation

$$f - L^2 \nabla^2 f = 1, \tag{22}$$

with homogeneous boundary conditions that allows the use of segregated solvers. The quantity f will hence be zero at solid walls and unity far away from walls. The size of the intermediate region, where f changes from 0 to 1, will be proportional to the turbulence length scale

$$L = C_L \max \left[\frac{k^{3/2}}{\varepsilon}, C_\eta \left(\frac{1}{Re_H^3 \varepsilon} \right)^{1/4} \right], \tag{23}$$

where C_L =0.08 and C_{η} =70 are model constants which have been slightly adjusted, as compared to those in Manceau (2005), to fit the present formulation. The quantity f is used in the Reynolds stress equations as a blending function for the pressure strain rate and dissipation rate tensors so that

$$\Pi_{ij}^* = f^3 \Pi_{ij} + (1 - f^3) \Pi_{ij}^w \tag{24}$$

$$\varepsilon_{ij}^* = f^3 \frac{2}{3} \varepsilon \delta_{ij} + (1 - f^3) \frac{\overline{u_i u_j}}{K} \varepsilon.$$
 (25)

It should be noted that the exponent of f is set to 2 in the model by Manceau (2005). The only motivation given in Manceau (2005) for setting f's exponent to 2 is that the blending function should approach zero at a faster rate than the wall normal distance d. This is fulfilled since $f \sim d$ as $d \to 0$. However in the original elliptic blending model in Manceau & Hanjalić (2002) it is stated that one should ensure that the blending function is $\sim d^3$. Tests with the present

formulation in plane channel flow indicated that slightly better results were achieved if the exponent was set to 3.

For the dissipation rate, the blending implies that an isotropic model is used far from the walls and that the model suggested in Rotta (1951) is used near the wall. The near wall model for ε_{ij} amounts to saying that the dissipation rate anisotropy, e_{ij} , is equal to the Reynolds stress anisotropy, a_{ij} .

The near wall model of the pressure-strain rate tensor Π_{ij}^w is configured in such a way that it, for Reynolds stresses with wall normal components, should balance the dominant terms in the near wall region (i.e. the viscous diffusion and the dissipation rate) if the corresponding Reynolds stresses have the correct limiting behaviour. For tangential Reynolds stress components it is the balance between the viscous dissipation and the dissipation rate alone that ensure the correct behaviour and Π_{ij} will be negligible as compared to the dominant terms. Hence, in the tangential components Π_{ij}^w is set in such a way that the traceless character of the pressure strain rate term is preserved. The above criteria are fulfilled if, in a near wall turbulent flow where x_2 -direction is wall normal

$$\begin{split} \Pi_{11}^w &= \frac{1}{2}\Pi_{22}^w, \quad \Pi_{22}^w = -5\frac{\varepsilon}{K}\overline{u_2u_2}, \quad \Pi_{33}^w = \frac{1}{2}\Pi_{22}^w, \\ \Pi_{12}^w &= -2\frac{\varepsilon}{K}\overline{u_1u_2}, \quad \Pi_{13}^w = 0 \quad \text{and} \quad \Pi_{23}^w = -2\frac{\varepsilon}{K}\overline{u_2u_3}. \end{split}$$

The expressions for Π_{12}^w and Π_{23}^w are in the present model set in such a way that they should have the correct limiting behaviour ($\sim d^3$). Manceau & Hanjalić (2002) and Manceau (2005) use a different form which gives a limiting behaviour $\sim d^4$ and claim that this improved their results. A frame independent form of the above relations for Π_{ij}^w can be written as

$$\Pi_{ij}^{w} = -5\frac{\varepsilon}{K} \left[\frac{2}{5} \left(\overline{u_i u_k} \hat{n}_k \hat{n}_j + \hat{n}_i \hat{n}_k \overline{u_k u_j} \right) - \frac{1}{2} \overline{u_k u_l} \hat{n}_k \hat{n}_l \left(\delta_{ij} - \frac{7}{5} \hat{n}_i \hat{n}_j \right) \right], \quad (26)$$

where \hat{n}_i is the wall normal vector. For a more detailed view on how the expressions for Π_{ij}^w are derived the reader is referred to *e.g.* Durbin (1993), Pettersson Reif & Andersson (2002) or Manceau & Hanjalić (2002).

Near wall treatment is also used for the ω -formulation. Here the low Reynolds number version from Wilcox (1994) was adopted. In this model the parameters α and β^* in equation 21 are defined as functions of the turbulence Reynolds number $Re_T = Re_H K/\omega$ so that

$$\beta^* = \frac{9}{100} \frac{5/18 + (Re_T/R_\beta)^4}{1 + (Re_T/R_\beta)^4},\tag{27}$$

and

$$\alpha = \frac{5}{9} \frac{\alpha_0 + Re_T/R_\omega}{1 + Re_T/R_\omega} \frac{1}{\alpha^*} \quad \text{where} \quad \alpha^* = \frac{\beta/3 + Re_T/R_K}{1 + Re_T/R_K},$$

$$R_\beta = 10, \quad R_\omega = 2.7, \quad R_K = 6, \quad \alpha_0 = 1/10 \quad \text{and} \quad \beta = 3/40.$$

The primary reason for adding the damping functions in the present model is to get the correct limiting behaviour for the dissipation rate, which should be $\varepsilon=2K/(Re_Hd^2)$ as $d\to 0$. Noting that ω is governed by equation 20 near the wall, it can be seen that $\beta^*/\beta=1/3$ in order to have the correct limiting behaviour on ε . This is ensured by equation 27 if the 'standard' value $\beta=3/40$ is used. The value of R_β in the present model was changed to 10 as compared to 8 which is used in the model by Wilcox (1994).

4. Numerical procedure

The variational form of the transport equations for U_i , R_{ij} and $\tilde{\omega}$ are discretised using finite elements and a Galerkin method based on piecewise linear polynomials. The computational code for both the vortex generator model and the turbulence model was completely given in terms of a high level definition, written in the mathematics software Maple. The Fortran computer code was then automatically generated using the femLego toolbox together with Maple. Details on the femLego toolbox can be found in Amberg et al. (1999). FemLego is a tool developed mainly for solving time dependent systems, hence marching in time using finite differences is used to reach the steady state solution. Marching accurately in time gives a higher computational cost, but adds the advantage of being able to study the temporal evolution of the flow field after the control forcing has been applied. Evaluation of feedback control schemes is also possible.

The velocity and pressure solutions of the Reynolds averaged Navier-Stokes (RANS) equations are separated and solved using the fractional step algorithm from Guermond & Quartapelle (1997). A stabilisation term is used in the Poisson equation for the pressure in order to avoid violation of the Babuška–Brezzi condition.

The mesh used for the computations of the plane asymmetric diffuser flow case consists of 28300 nodes and 55836 triangular elements. The mesh has 100 nodes in the cross-stream direction and the first node in the wall normal direction in the inlet channel is located at $y^+\approx 0.5$.

5. Results

The vortex generator model has been tested in a two-dimensional asymmetric diffuser flow. The diffuser geometry which is shown in figure 5 has an expansion ratio of 4.7. It consists of an inlet channel, with the height H, where the flow is fully developed followed by an asymmetric expansion and a straight exit channel. The inclined wall has an angle of 8.5° and the two corners, one convex at the upstream end and one concave at the downstream end of the inclined wall, are rounded with a radius of 10H.

The plane asymmetric diffuser flow has been used quite extensively as a test case for turbulence models, see e.g. Obi et al. (1993), Hellsten & Rautaheimo

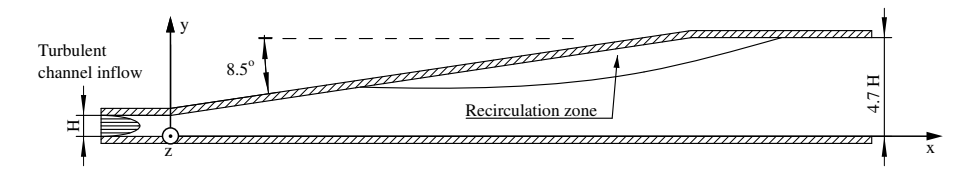


FIGURE 5. The geometry and coordinate system of the plane asymmetric diffuser.

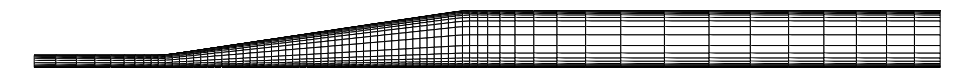


FIGURE 6. The computational domain. For clarity, only every fourth node point is included in the image.

(1999), Apsley & Leschziner (1999) and Gullman-Strand et al. (2004). Most earlier studies have been made in a geometry identical to the one in figure 5, with the exception that the angle was 10°. However, the flow in the 8.5° diffuser is believed to be more decisive for turbulence models since the flow is closer to being attached. The Reynolds number based on the full inlet channel height and inlet bulk velocity, $Re_H = HU_b/\nu$, was 40000 in all computations. This Reynolds number resulted in a friction velocity Reynolds number, $Re_\tau = u_\tau H/(2\nu)$, of 985. This corresponds approximately to the conditions in the experimental study by Törnblom et al. (2006).

The computational domain is shown in figure 6. The inlet channel is $\sim 10H$ long and the exit channel is $\sim 45H$ long in order to avoid boundary condition influences on the separating flow. Slightly more than 60 percent of the computational nodes are located in the diverging part of the diffuser. The inlet conditions were produced by doing a separate channel flow computation, with the same node distribution in the y-direction as on the inlet for the diffuser geometry, where it was ensured that the channel flow was fully developed.

5.1. The unperturbed flow

The inlet mean velocity profile and the Reynolds stresses at the inlet are shown in figures 7 and 8 respectively. The mean velocity agreement with the DNS by Del Álamo et al. (2004) is reasonable. It can be mentioned that better agreement for the channel flow could be achieved by choosing another calibration of the pressure strain-rate model, but that it would be at the price of a worse prediction of the separating diffuser flow. It can be seen that the model prediction of the near-wall asymptotic behaviour of the Reynolds stresses is decent by DRSM standards. Especially, the damping of \overline{vv} is satisfactory.

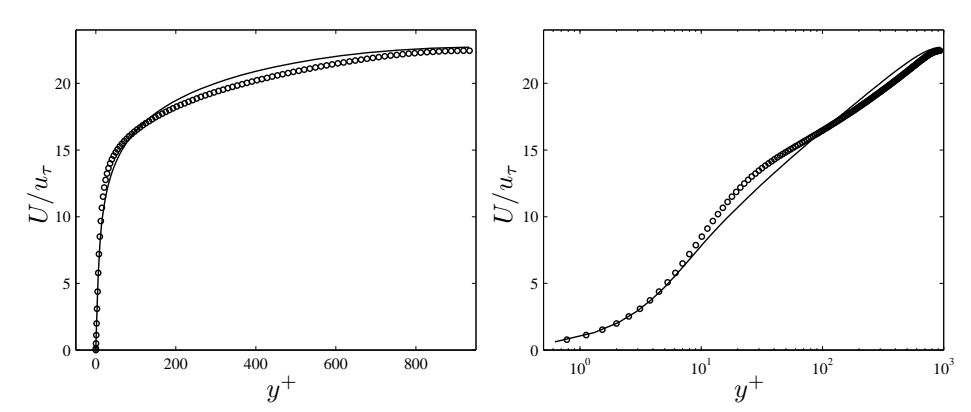


FIGURE 7. Channel flow inlet mean velocity profile in viscous scaling. Lines show turbulence model results and symbols DNS at $Re_{\tau} \approx 950$ by Del Álamo *et al.* (2004).

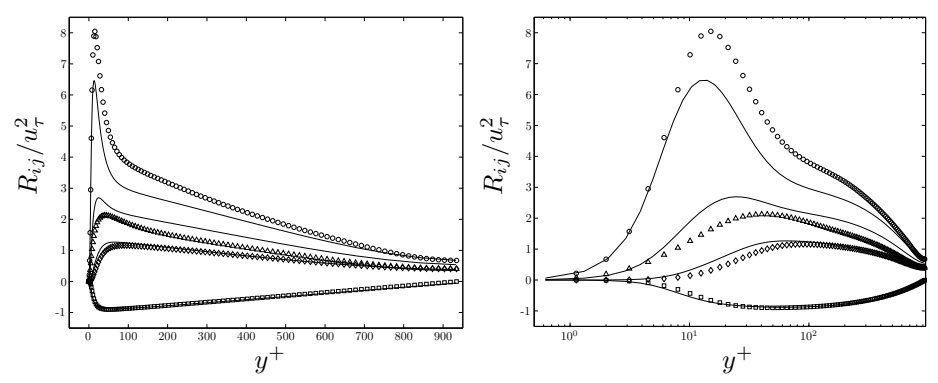


FIGURE 8. Channel flow inlet Reynolds stress profiles in viscous scaling. Lines show turbulence model results and symbols DNS by Del Álamo *et al.* (2004); $\circ \overline{u}\overline{u}$, $\triangle \overline{w}\overline{w}$, $\diamond \overline{v}\overline{v}$ and $\Box \overline{u}\overline{v}$.

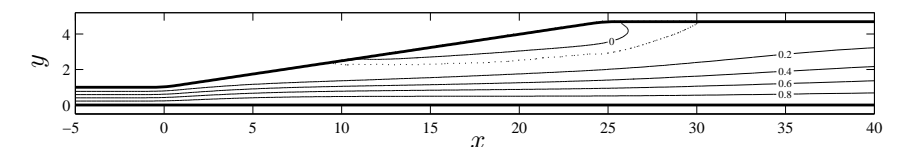


FIGURE 9. Streamlines of the unperturbed diffuser flow, contour labels indicate the value of the stream-function. The dotted line shows the separation bubble from the experiments in Törnblom $et\ al.\ (2006)$.

Figure 9 shows the streamfunction of the unperturbed flow. The streamfunction contour with value zero corresponds to the dividing streamline between the recirculating region and the outer flow. The size of the computed separation is considerably smaller than the one found in the experiments by Törnblom *et al.* (2006), indicated as a dotted line in figure 9. The separation and reattachment points of the computation are located at x/H=7.8 and 26.4 respectively.

A velocity profile comparison with the experimental data of Törnblom et al. is shown in figure 10. The agreement is good outside the separation from the inlet and down to roughly x/H=25, where the velocity peak in the computation is starting to move towards the straight wall while the experiment shows a velocity peak at an approximately constant distance from the straight wall. After reattachment the gradients of the experimental profiles are reduced faster in the streamwise direction as compared to the computation. This indicates that the turbulence model has problems with predicting the strong diffusion caused by the large scale turbulence which is produced in the diffuser and advected downstream. When focusing on the separated region it is apparent that the model predictions are very far from the experimental data. Most striking is the strength of the backflow which is only a fraction of that in the experiment. However, a review of previous DRSM computations in the similar 10° diffuser reported in Obi et al. (1993), Hellsten & Rautaheimo (1999) and Apsley & Leschziner (1999) showed that DRSMs in general seems to give rather accurate predictions of the flow outside the separation but that the backflow rate is always severely underestimated.

The predicted pressure distribution, shown in figure 11, agrees reasonably well with the experimental data. The concave plateau region in the pressure curve, resulting from the entrainment caused by the recirculating region, is less pronounced in the computation as compared to the experiment due to the smaller size of the separation.

The realisability of the predicted anisotropy states was checked for all interior points and all states were found to fall within the anisotropy invariant map introduced by Lumley (1978).

5.1.1. Anomalies in the reattachment flow

It can be noted, in figure 9, that the computed dividing streamline has an odd shape near reattachment, this is something that has been observed also in other investigations where differential Reynolds stress models are used. The bent shape of the dividing streamline is caused by a thin region of forward flow close to the wall with a region of backflow outside of it. Without the thin region of forward flow near the wall the streamline would have a more physically realistic shape.

Lasher & Taulbee (1992) found that the use of an anisotropy dependent Rotta parameter (C_1^0) helped to diminish, but not totally remove, the anomaly. In their backstep flow the Rotta parameter's value changed from 1.5 to roughly 2.5. Hanjalić & Jakirlić (1998) confirmed the findings of Lasher & Taulbee, that modifying the pressure strain rate parameters could diminish the problem, but used a local correction term in the ε -equation (a modified Yap correction), which increases the dissipation rate in the reattachment region, to remove the anomaly.

The reattachment region has a non-equilibrium character. The mean flow gradients are small in the wall normal direction, as compared to the flow upstream and downstream reattachment, and little turbulence is generated here. In fact, negative production of turbulence kinetic energy is often observed in this region. Much of the turbulence found in this region is hence produced somewhere else in the flow and is transported to the reattachment region by diffusion and advection. Eddy-viscosity based models, in which the turbulence anisotropy is determined locally, do not seem to give this type of reattachment flow but will on the other hand never come near a correct description of the physics in this region. For example, in the present model, $\overline{u}\overline{v}$ is always positive in the separation bubble in contrast to an eddy viscosity model which would predict negative values of \overline{uv} close to the wall in the separated region, due to the direct relation between this quantity and the mean flow gradient. However, the experiment by Törnblom et al. and the direct numerical simulations by Skote & Henningson (2002) and Le et al. (1997) all indicate that the positive sign of \overline{uv} is likely to be correct and that the key to a proper modelling of the reattachment region seems to be more complex than just assuring a sign change of \overline{uv} close to the wall, as is hinted in Hanjalić & Jakirlić (1998).

5.2. Dependencies on the streamwise position of the vortex generators

One of the first issues to investigate in an application where vortex generators are to be used is the optimisation of the position of the vortex generators. Three different positions along the inclined wall, denoted x_{VG} , were tested in the present investigation. The geometry of the vortex generator arrangement was kept fixed with $h{=}0.6H$, $c{=}H$, $\delta{=}H$, $D{=}2H$, $\alpha{=}15^{\circ}$ and $r_0{=}0.1H$. The forcing was applied using the smooth window, described by equation 15, extending 2H tangentially along the inclined wall and 1.5H in the normal direction of the inclined wall, including a Δ_{rise} of 0.5H.

Before the interpretation of the results begin, a short discussion of the effects that a variation of x_{VG} might have on the diffuser flow could be useful. The perhaps most apparent observation to make is that a more upstream position of the vortex generator means that the oncoming flow have more momentum and therefore generate stronger vortices, but it also means that the mean velocity deficit caused by the vortex generators will be larger. Furthermore, if

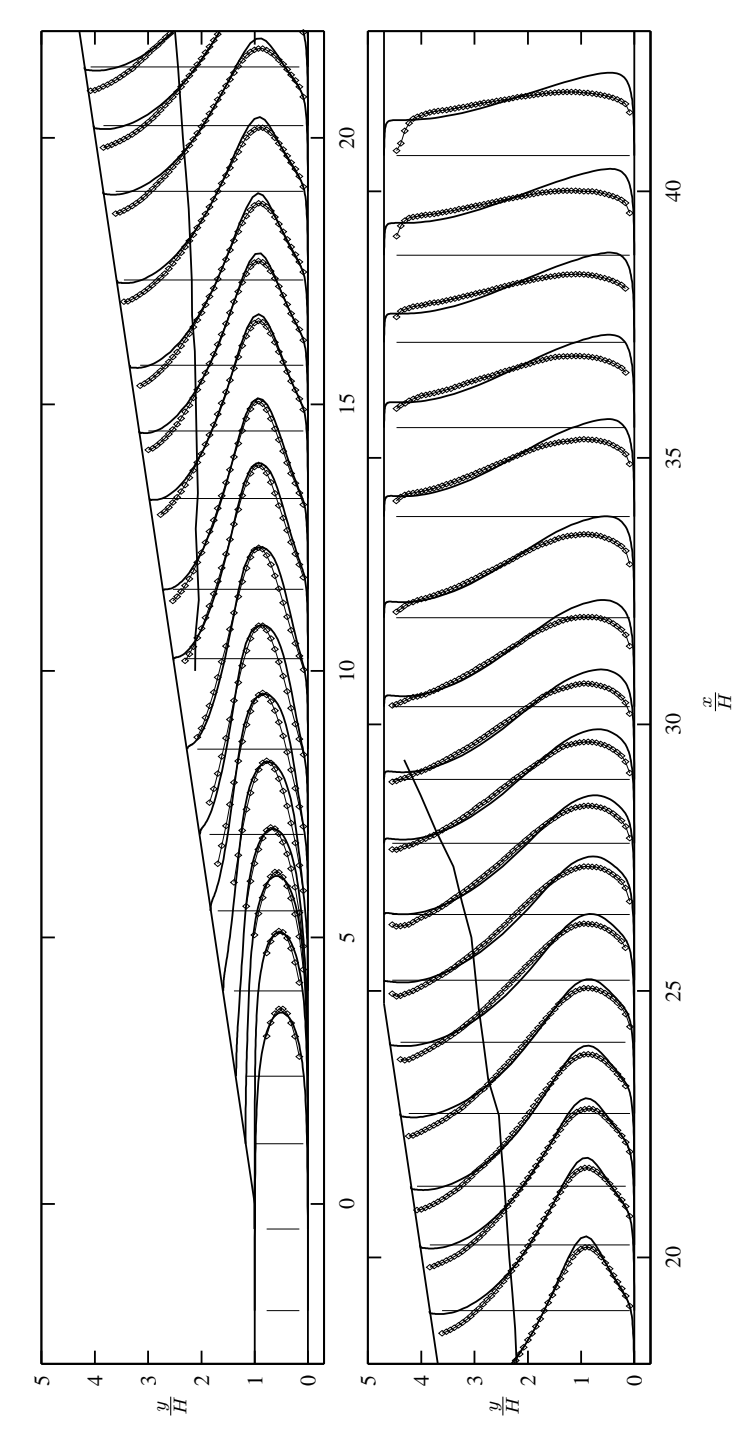


FIGURE 10. Streamwise mean velocity, $(U_{\rm fig} = 5U/U_b + x/H)$, Solid line profiles are from the current DRSM and symbols are experimental data from Törnblom et al. (2006). The vertical lines indicate zero level for each streamwise velocity profile. The dividing streamline from the experimental data is shown as a solid contour.

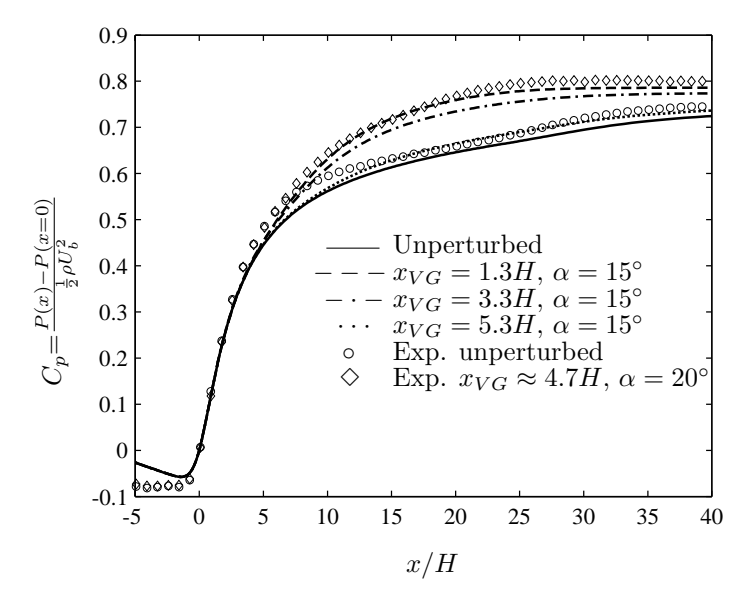


FIGURE 11. Pressure coefficient along the straight diffuser wall, lines show different configurations of the model and symbols are from the experiments by Törnblom *et al.*.

the vortex generators are put at a more upstream position, the generated turbulence will have to travel a longer distance and may decay, before it reaches the region where separation might occur. Another quantity that changes when altering x_{VG} , given that h is kept constant, is the y-position of the vortex centres, due to the inclination of the wall.

Figure 11 shows the pressure coefficients, $C_p = (P(x) - P(0))/(\frac{1}{2}\rho U_b^2)$, for computations with different positions of the vortex generators. The pressure rise through the diffuser for an ideal flow without losses can readily be derived from Bernoulli's equation and one-dimensional continuity to be $C_p^{max} = 1 - ER^{-2} = 0.95$, where ER = 4.7 is the expansion ratio of the diffuser. The difference between C_p^{max} and the actual C_p at the outlet will therefore be an indicator of the energy losses. The contributors to mean flow energy losses are production of turbulence, viscous dissipation due to mean shear and the mean flow retardation due to the vortex generator drag.

From figure 11 it can be seen that, of the configurations tested, the best diffuser efficiency is found for the most upstream position of the vortex generator. There is a monotonic decrease in efficiency for increasing x_{VG} . The separation is completely removed in the two cases with $x_{VG}=1.3H$ and 3.3H and a very small separation is seen in the case with $x_{VG}=5.26H$, with a backflow rate one order of magnitude smaller than in the unperturbed case.

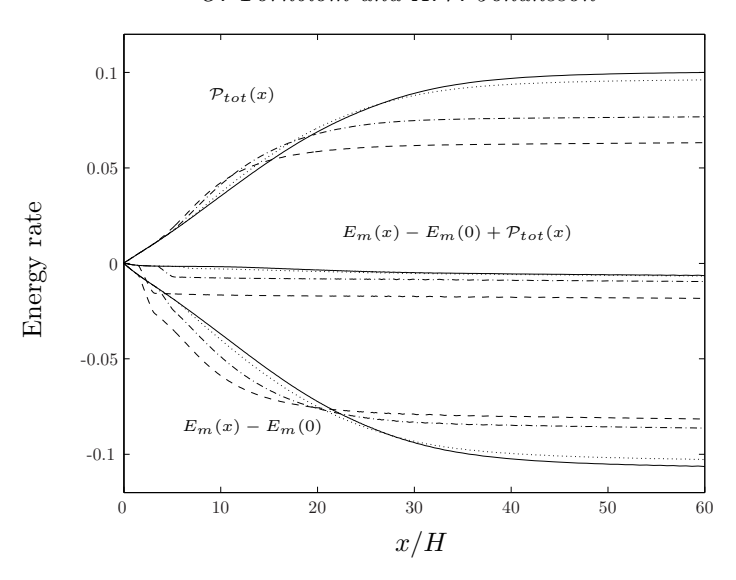


FIGURE 12. Redistribution of energy through the diffuser. Line styles are the same as in figure 11. The lowest set of curves shows the total pressure $E_m(x) - E_m(0)$. The uppermost set of curves shows the total amount of turbulent kinetic energy $\mathcal{P}_{tot}(x)$. The middle set of curves shows the corresponding sums of the upper and lower sets.

The integrated flux of mechanical energy over a cross-section (per unit depth)

$$E_m(x) = \int U(x,y) \left(P(x,y) + \frac{1}{2} \rho \left(U(x,y)^2 + V(x,y)^2 \right) + \rho \overline{u}\overline{u}(x,y) \right) dy,$$
(28)

is shown in the lower set of curves in figure 12. The decrease of this quantity is a measure of the total pressure loss. E_m decreases mainly as a consequence of production of turbulence kinetic energy. This can be seen in figure 12 where also the integrated production rate of turbulent kinetic energy,

$$\mathcal{P}_{tot}(x) = \int_0^x \int \rho \mathcal{P}(x', y) dy dx'$$
 (29)

is shown in the uppermost set of curves. The middle set of curves is the sum of E_m and \mathcal{P}_{tot} and can be seen as a representation of the losses due to viscous dissipation and retardation due to the vortex generator drag. The turbulence forcing introduced in the vortex generator model is not included in \mathcal{P}_{tot} but the result from the forcing, *i.e.* increased turbulence levels, is to some extent included through $\overline{u}\overline{u}$ in E_m .

It is apparent from figure 12 that in the more efficient configurations the major losses of mechanical energy occur more upstream in the diffuser due to the combined effect of the vortex generator drag and an increase in production rate there. It can also be seen that the increased efficiency is entirely due to a lower integrated production rate of turbulence and that the total pressure losses due to vortex generator drag and viscous dissipation are larger for the more efficient cases.

In figure 13 it can be seen from profiles of the streamwise velocity that the momentum transfer towards the inclined wall is very efficient in the region between $x/H\approx7$ and 10 in the two cases with $x_{VG}=1.3$ and 3.3. The large levels of momentum near the wall decrease the sensitivity to the adverse pressure gradient and prevent separation. The efficient momentum transport can be explained by the large magnitude and wall normal position of the peaks in the turbulent kinetic energy profiles in the same region. These are shown in figure 14. Further downstream in the diffuser the turbulence levels of the case with $x_{VG}=5.3$ increase to approximately twice the magnitude of the other cases, but the peak is located in the centre region of the diffuser so the momentum transfer towards the walls is less efficient. The price of this production is a decreased diffuser efficiency.

The momentum transfer towards the straight wall is in the case with $x_{VG}=3.3$ slightly smaller as compared to the $x_{VG}=1.3$ case, the mean velocity develops to an inflectional profile on the straight wall side of the diffuser and the velocity peak is shifted towards the inclined wall. The most efficient of the cases is the one with the flattest velocity profiles and hence with the smallest regions of large mean shear, reflecting the fact that turbulence production, which is proportional to the mean shear, is the major cause of energy losses in this flow.

5.3. Vortex generator removal and subsequent reapplication

The temporal evolution of the separation after the vortex generator control is turned off and then on again was investigated using time-accurate computations with the above described modelling approach. This should be seen as time-dependent but in a sense quasi-steady RANS-computations. The instantaneous separation and reattachment points are shown in figure 15, the dotted vertical lines indicate the regions where the forcing is either ramped down or up using a ramp function with a width of $5H/U_b$. The vortex generator location, indicated by a horizontal dotted line, and parameters are the same as in the the case with $x_{VG}=1.3$, described in the previous section.

The motivation for studying the temporal evolution in this way is that the knowledge gained could be useful for designing efficient control strategies. It could for example be advantageous, from a total efficiency point of view, if the control forcing could be turned off some fraction of the time. This idea is

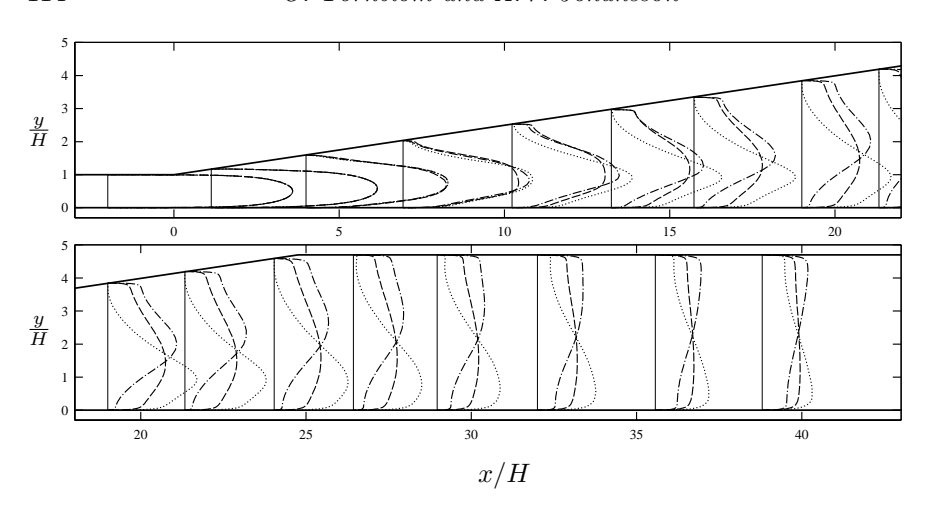


FIGURE 13. Streamwise mean velocity, $U_{\rm fig} = 5U/U_b + x/H$. The linestyles are the same as in figure 11. The vertical lines indicate zero level for each streamwise velocity profile.

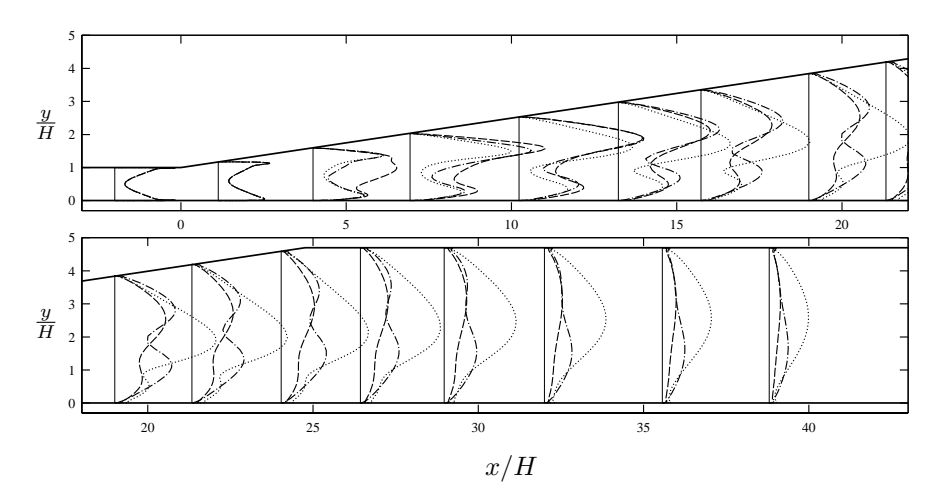


FIGURE 14. Turbulent kinetic energy, $U_{\rm fig}=160K/U_b^2+x/H$. The linestyles are the same as in figure 11. The vertical lines indicate zero level for each streamwise velocity profile.

perhaps more apparent when considering control actuators that imply addition of energy, such as inclined jets, but it could also be beneficial in a case with, for example, retractable vortex generators since the average drag would be reduced.

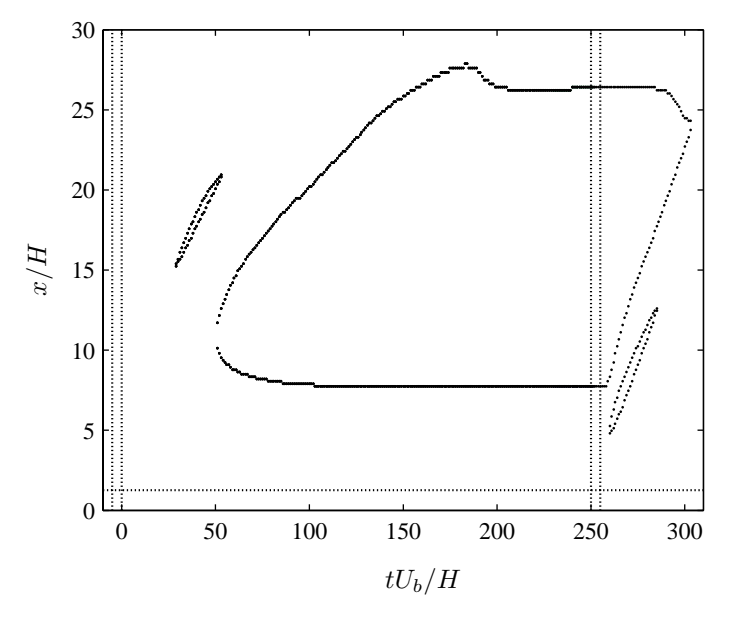


FIGURE 15. Separation and reattachment points as functions of time after the forcing is removed and reapplied. The dotted vertical lines indicate the regions where the control forcing is ramped up or down and the dotted horizontal line shows the position of the vortex generator.

Looking again at figure 15 we see that, after approximately 29 non-dimensional units of time a small separation is formed on the inclined wall, this zone then drifts downstream and eventually disappears. The main separation starts to form approximately 50 time units after the forcing is totally turned off and spreads out from a position near x/H=11. The separation length reaches a stationary state at $tU_b/H\approx 206$ after some transient behaviour where it for a while is larger than the stationary length. The separation point position becomes stationary relatively early as compared to the reattachment point.

When the control subsequently is turned on again the response is surprisingly quick, the separation length starts to diminish $4H/U_b$ after the forcing has reached full strength. After $4H/U_b$ a short separated region forms around x/H=5, this region then moves downstream and disappears. The main separation diminishes in a, close to, linear manner with time as the separation point moves downstream. The reattachment point is unaffected by the control until $29H/U_b$ has passed after the control reached full strength and the separation is totally removed after $49H/U_b$. The almost linear withdrawal of the separation point is a bit surprising as the expected convective velocity ought to diminish with increasing x due to the diffuser expansion.

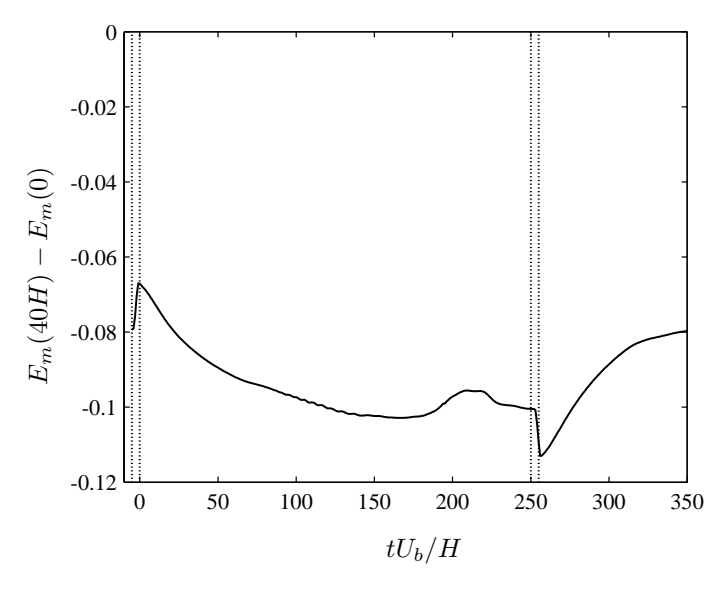


FIGURE 16. Loss of total pressure flux. The vertical dotted lines have the same meaning as in figure 15.

Figure 16 shows the difference in the fluxes of mechanical energy, cf. equation 28, between x=40H and x=0. First, when the control is turned off, the losses decrease because the vortex generator drag is removed, then, as the separation begins to form the losses increase. When the control is turned on again, there is steep increase in the losses, this time because of the added drag, followed by a gradual decrease of the losses. However, this decrease is faster than the corresponding increase of losses following the turning off of the control.

The result is encouraging from a control point of view since it suggests that the separation response to removal of the control is slower than that to turning it on. This supports the idea that it could be possible to have the control turned off a fraction of time to save energy. However, a more detailed study is necessary in order to say if any net gain can be achieved in this way.

6. Concluding remarks

The vortex generator model appears to be able to imitate the effects of vortex generators in a realistic manner. It is shown that the model can be used as a tool when studying the qualitative effect of different vortex generator configurations. The strength of the vortices are related to the geometry of the vortex generators by wing theory which directly gives the forcing in the momentum and turbulence equations. However, the size of the viscous core is undetermined and rather important, which implies that a thorough calibration including comparisons with experiments and simulations would be needed if

quantitative conclusions are to be drawn from the model. Other types of separation control methods, *e.g.* inclined jets, could also be investigated using the same basic idea of adding forcing to the Reynolds stress equations.

The differential Reynolds stress turbulence model used is able to make a satisfactory prediction of the overall flow characteristics but fails in the prediction of the separation zone in general, particularly the back-flow rate is underestimated and the reattachment region shows an anomalous flow. It was found that very small changes in the model coefficients of the pressure strain rate tensor have a dramatic effect on the size of the predicted separation bubble. The near wall modelling using an elliptic blending model allows for a reasonable prediction of the incoming channel flow. The impact of the near wall model on the predictions of the flow in the diffuser is unclear since this is not investigated in this study. Another thing that is not investigated, but that would be interesting to know, is the necessity to solve the elliptic equation in the near wall model. This equation poses a non-negligible computational effort in the present implementation and if e.q. a van Driest type of damping function could replace the elliptic equation in the blending model, this would be preferable. Manceau (2005) points out that the solution to the elliptic equation 22 is indeed equivalent to a van Driest damping if the length scale L is a constant.

The investigation of the dependence of the diffuser efficiency on the vortex generator position indicate that vortex generators should be placed near the diffuser inlet and that an early change of the mean flow profiles is essential for controlling the pressure loss. It was found that the by far largest contributor to energy losses in the considered flow case is the production of turbulent kinetic energy and that a small increase of the turbulence kinetic energy, *i.e.* an increase of the mixing, in an early stage of the diffuser could change the mean flow so as to prevent the large increase further downstream that occurs the uncontrolled case.

The test, using the present RANS-based approach, of the response of the flow to a sudden change in control forcing indicate that the model could serve as a tool for development of open or closed loop separation control schemes. The fact that the response to turning on the control appears to be faster than that to turning it off is of-course positive for the possibility of controlling of the flow in an energy efficient way.

The model presented here offers the possibility of exploring vortex generator control with many different types of parameter variations at a low computational cost.

Acknowledgements

Professor Gustav Amberg is acknowledged for his guidance in issues related to the femLego software package. Doctor Stefan Wallin is gratefully acknowledged for his guidance and good ideas on turbulence modelling and numerical aspects of this work as well as for his valued comments on the manuscript. The financial support from the Swedish energy agency is gratefully acknowledged.

References

- Amberg, G., Törnhardt, R. & Winkler, C. 1999 Finite element simulations using symbolic computing. *Mathematics and Computers in Simulation* **44**, 275–274.
- Apsley, D. D. & Leschziner, M. A. 1999 Advanced turbulence modelling of separated flow in a diffuser. Flow, Turbulence and Combustion 63, 81–112.
- Daly, B. J. & Harlow, F. H. 1970 Transport equations in turbulence. *Int. Phys. Fluids* 13, 2634–2649.
- Del Álamo, J. C., Jiménez, J., Zandonade, P. & Moser, R. D. 2004 Scaling of energy spectra of turbulent channels. *J. Fluid Mech.* **500**, 135–144.
- VAN DRIEST, E. R. 1951 Turbulent boundary layer in compressible fluids. *J. Aeronaut. Sci.* **18** (3), 145–160.
- Dudek, J. C. 2005 An empirical model for vane type vortex generators in a Navier-Stokes code. *Tech. Rep.* NASA/TM-2005-213429. NASA Glenn research center.
- Durbin, P. A. 1991 Near-wall turbulence closure modeling without "damping functions". *Theoret. Comput. Fluid Dynamics* **3** (1), 1–13.
- Durbin, P. A. 1993 A Reynolds stress model for near-wall turbulence. *J. Fluid Mech.* **249**, 465–498.
- GLAUERT, H. 1947 The elements of aerofoil and airscrew theory, 2nd edn. Cambridge university press.
- Guermond, J. L. & Quartapelle, L. 1997 Calculation of incompressible vicous flow by an unconditionally stable projection FEM. *Journal of Computational Physics* **132** (CP965587), 12–33.
- GULLMAN-STRAND, J. 2004 Turbulence and scalar flux modelling applied to separated flows. PhD. Thesis, KTH Mechanics, Stockholm, Sweden, TRITA-MEK 2004:16.
- Gullman-Strand, J., Törnblom, O., Lindgren, B., Amberg, G. & Johansson, A. V. 2004 Numerical and experimental study of separated flow in a plane asymmetric diffuser. *Int. J. Heat Fluid Flow* **25**, 451–460, (**Paper 4**).
- Hanjalić, K. & Jakirlić, S. 1998 Contribution towards the second-moment closure modelling of separating turbulent flows. *Computers and Fluids* **27** (2), 137–156.
- Hellsten, A. & Rautaheimo, P., ed. 1999 8th ERCOFTAC/IAHR/COST workshop on refined turbulence modelling, Report 127. Helsinki University of Technology, Department of Mechanical Engineering, Laboratory of Applied Thermodynamics.
- JIRÁSEK, A. 2005 Vortex-generator model and its application to flow control. J. Aircraft 42 (6), 1486–1491.
- Lamb, H. 1932 Hydrodynamics. New York Dover Publications.
- LASHER, W. C. & TAULBEE, D. B. 1992 On the computation of turbulent backstep flow. *Int. J. Heat Fluid Flow* 13 (1), 30–40.
- Launder, B., Reece, G. & Rodi, W. 1975 Progress in the development of a Reynolds-stress turbulence closure. *J. Fluid Mech.* **68**, 537–566.

- LE, H., Moin, P. & Kim, J. 1997 Direct numerical simulation of turbulent flow over a backward-facing step. J. Fluid Mech. 330, 349–374.
- Lumley, J. L. 1978 Computational modeling of turbulent flows. *Adv. Appl. Mech.* 18, 123–176.
- Manceau, R. 2005 An improved version of the elliptic blending model application to non-rotating and rotating channel flows. In *Turbulence and shear flow phenomena* 4.
- MANCEAU, R. & HANJALIĆ, K. 2002 Elliptic blending model: a new near-wall Reynolds stress turbulence closure. *Phys. Fluids* **14** (2), 744–754.
- Obi, S., Aoki, K. & Masuda, S. 1993 Experimental and computational study of turbulent separating flow in an asymmetric plane diffuser. In *Ninth Symp. on Turbulent Shear Flows*, p. 305. Kyoto, Japan.
- Pettersson Reif, B. A. & Andersson, H. I. 2002 Prediction of turbulencegenerated secondary mean flow in a square duct. Flow, turbulence and combustion 68, 41–61.
- ROTTA, J. C. 1951 Statistische theorie nichthomogener turbulenz. Z. Phys 129, 547–572.
- SKOTE, M. & HENNINGSON, D. 2002 Direct numerical simulation of a separated turbulent boundary layer. J. Fluid Mech. 471, 107–136.
- So, R. M. C., LAI, Y. G. & ZHANG, H. S. 1991 Second-order near wall turbulence closures: a review. AIAA Journal 29 (11), 1819–1835.
- Speziale, C. G., Sarkar, S. & Gatski, T. B. 1991 Modelling the pressure-strain correlation of turbulence: an invariant dynamical systems approach. *J. Fluid Mech.* 227, 245–272.
- Törnblom, O., Lindgren, B. & Johansson, A. V. 2006 Measurements of mean flow statistics in a plane asymmetric diffuser with 8.5° opening angle. *To be submitted* (Paper 1).
- Waithe, K. A. 2004 Source term model for vortex generator vanes in a Navier-Stokes computer code. In *The 42nd AIAA Aerospace Sciences Meeting and Exhibit*.
- Wallin, S. & Johansson, A. V. 2000 An explicit algebraic Reynolds stress model for incompressible and compressible turbulent flows. J. Fluid Mech. 403, 89–132.
- WALLIN, S. & JOHANSSON, A. V. 2002 Modelling streamline curvature effects in explicit algebraic Reynolds stress turbulence models. *Int. J. Heat and Fluid Flow* 23, 721 – 730.
- Wendt, B. J. 2001 Initial circulation and peak vorticity behavior of vortices shed from airfoil vortex generators. *Tech. Rep.* NASA/CR-2001-211144. NASA Glenn.
- WILCOX, D. C. 1993 Turbulence modeling for CFD. DCW Industries Inc.
- WILCOX, D. C. 1994 Simulation of transition with a two-equation turbulence model. AIAA Journal 32 (2), 247–255.

Paper 4

 $\overline{P4}$

Numerical and experimental study of separated flow in a plane asymmetric diffuser

By Johan Gullman-Strand, Olle Törnblom, Björn Lindgren, Gustav Amberg and Arne V. Johansson

KTH Mechanics, SE-100 44 Stockholm, Sweden

Published in International Journal of Heat and Fluid Flow, vol. 25

Computations of the turbulent flow through plane asymmetric diffusers for opening angles from 8° to 10° have been carried out with the Explicit Algebraic Reynolds Stress Model (EARSM) of Wallin & Johansson (2000). It is based on a two-equation platform in the form of a low- $Re\ K-\omega$ formulation, see e.g. Wilcox (1993). The flow has also been studied experimentally for the 8.5° opening angle using PIV and LDV. The models under-predict the size and magnitude of the re-circulation zone. This is, at least partially, attributed to an over-estimation of the wall normal turbulence component in a region close to the diffuser inlet and to the use of damping functions in the near-wall region. By analysing the balance between the production and dissipation of the turbulence kinetic energy we find that the predicted dissipation is too large. Hence, we can identify a need for improvement of the modelling the transport equation for the turbulence length-scale related quantity.

Keywords Plane asymmetric diffuser, separated flow, explicit algebraic Reynolds stress model, EARSM, automated code generation

1. Introduction

Separation is common in many fluid flow applications. Separation can cause a substantial reduction of efficiency of a device, such as a diffuser. Hence, being able to predict separation accurately and in a time-efficient way is very desirable. The tested explicit algebraic Reynolds stress models (EARSM) increases the computational effort only slightly as compared to ordinary two-equation models, that rely on the eddy-viscosity hypothesis, while significantly more flow physics are captured. Therefore, EARSMs are strong candidates for becoming the next generation of industrial turbulence models. However, it is of great importance to also be aware of the limitations of this type of closure, an issue that will be addressed in this paper.

Flows in plane asymmetric diffusers (see figure 1) have previously been studied experimentally by Obi et al. (1993a), Obi et al. (1993b), Buice & Eaton

(1997) and Buice & Eaton (2000). However, in all these studies the angle of the inclined wall was 10° while we have chosen a slightly smaller angle of 8.5° . The reason for choosing a smaller opening angle in this project was to reduce the size of the separated region, and thereby, in combination with a high aspect ratio of the experimental diffuser, achieve a high degree of two-dimensionality of the mean flow. Furthermore, by investigating a plane asymmetric diffuser flow with an opening angle of 8.5° , which is almost on the verge of being fully attached (fully attached flow is predicted to occur for angles around 7°), the sensitivity to model details regarding separation prediction is increased.

Our intention, when using a two-dimensional test-case such as the plane asymmetric diffuser, is to have a case which: is challenging, demands a moderate computational effort, is simple to quantitatively compare with reference data and simplifies (as compared to a 3D-case) the task of drawing conclusions regarding the model behaviour. Although one cannot generally expect a model that predicts a 2D separation correctly to do the same in a 3D-case, we chose a 2D-configuration since it still poses a great challenge to all existing turbulence models.

Simulations and model prediction studies on the geometry with 10° opening angle have been performed in a number of previous investigations. An extensive numerical study of the plane asymmetric diffuser flow was made by Kaltenbach et al. (1999), who performed a Large Eddy Simulation (LES) at a Reynolds number, based on half inlet channel height and inlet channel friction velocity, of 1000. Their data showed good agreement with the experimental data by Buice & Eaton (2000) for mean velocity profiles. The location of the separation point also agreed well but some discrepancy was found in the location of the reattachment point. A possible reason for this can be the relatively small spanwise width (4H) of the computational domain which (when using periodic boundary conditions) tend to artificially enhance spanwise coherence of large scale structures. Kaltenbach et al. (1999) found that the subgrid-scale model plays an essential role in calculating the flow correctly, since sub-grid stresses contributed substantially (up to 8%) to the total shear stresses, at the resolutions used.

Other numerical studies using the Reynolds averaged Navier-Stokes (RANS) set of equations, involving more or less advanced closures based on eddy-viscosity models, (differential) Reynolds stress models and explicit algebraic Reynolds stress models, have been performed by a number of research groups. For instance, Apsley & Leschziner (2000) tested both linear and non-linear eddy-viscosity models as well as differential stress-transport models. They found that strain dependent coefficients and anisotropy resolving closures are needed. However, no models tested were capable of resolving all flow features in the diffuser. Apsley & Leschziner (2000) also point out the possibility to encounter problems related to "flapping" motion of the unsteady separation. In an ERCOFTAC workshop (Hellsten & Rautaheimo (1999)), different numerical

approaches with varying turbulence models were tested and compared to the Buice & Eaton (2000) data-set. Models used comprised $K-\varepsilon$, $K-\omega$, RSM and LES. The agreement was, for the more simple models, in general fairly poor indicating that more complex models are needed to capture the flow physics. The plane asymmetric diffuser has also been used as a test case for commercial codes. The investigation performed by Iaccarino (2000) aimed at finding the limits of the versatile commercial codes in this complex flow. The codes tested were CFX, Fluent and Star-CD. Two turbulence models were tested, $(K-\varepsilon$ and $\overline{v^2}-f)$ in these three codes. The results were compared to the Obi et al. (1993a) and Buice & Eaton (2000) data-sets. The $K-\varepsilon$ model was unable to capture the recirculation zone but the $\overline{v^2}-f$ model (Durbin (1995)) did so with an accuracy in separation length of 6%. The agreement for the friction coefficient was also fairly good.

In this study, two EARSMs are tested. The concept of an EARSM is to use an explicit relation between the individual Reynolds stress and the strain and rotation rates of the mean flow. The EARSM used in this study is described in Wallin & Johansson (2000) and the streamline curvature modelling is described in Wallin & Johansson (2002). The model will herein be referred to as WJ-EARSM.

In all figures in this article the coordinate system origin is located on the plane wall at the same streamwise position as the upstream corner of the inclined wall. The coordinate system is oriented according to figure 1. Mean velocities in the x, y and z directions are referred to as U, V and W respectively and velocity fluctuations are denoted by the corresponding lower-case letters. The Reynolds number based on the inlet channel height (H) and inlet channel bulk velocity (U_b) is 40 000 both in the experiment and in the computations.

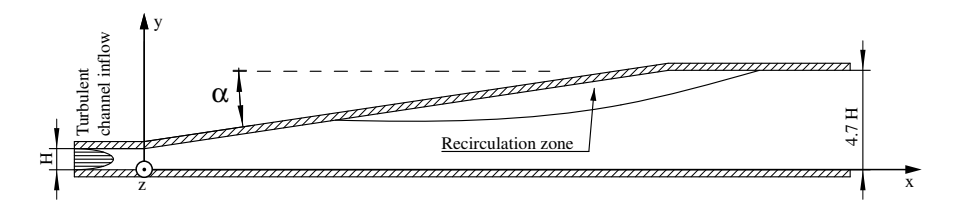


FIGURE 1. The cross-section of the diffuser. A part of the inlet channel is seen to the left and part of the outlet channel is seen to the right.

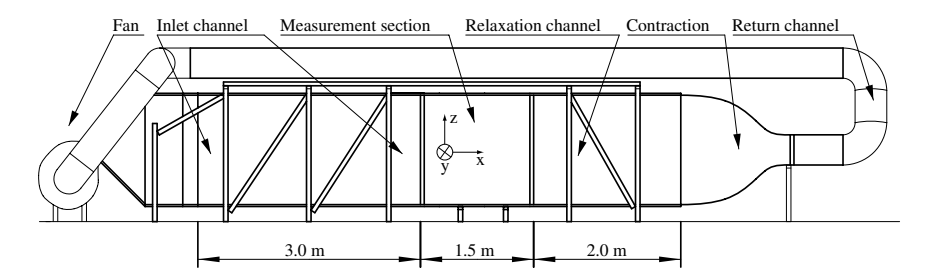


FIGURE 2. The wind-tunnel used in the experiments. The flow is circulating counter clockwise.

2. The experiment

2.1. Description of the wind-tunnel

The experiments were performed in a closed loop wind-tunnel built specifically for this investigation. The wind-tunnel can be seen in figure 2. It consists of a blowing centrifugal fan delivering 11 kW of power followed by a section transforming the rectangular cross section shape of the blower outlet to another one with much higher aspect ratio. The transformer is followed by a straight duct (settling chamber) which contains two screens at its upstream end to even out mean flow variations. The settling chamber is followed by a two-dimensional contraction which is followed by a turbulence generating grid and a 3.2 m long inlet channel with a cross section area (width to height) of $1525 \times 30 \text{ mm}^2$. The length to height ratio of the channel is thus larger than 100 ensuring fully developed channel flow at the downstream end (see e.g. Comte-Bellot (1965)). This is important in order to obtain a well defined inlet condition to the diffuser which can be easily produced in numerical calculations. At the downstream end of the inlet channel, the end walls (limiting the spanwise width of the channel) are perforated with 2 mm holes. This section is 100 mm long and the end wall boundary layers are removed through these holes by means of suction to prevent end wall boundary layer separation in the diffuser. Such a separation would destroy the two-dimensionality of the mean flow.

The inlet channel is followed by the diffuser. The diffuser has an inclined wall on one side and a straight wall on the other. The inclined wall has an angle of 8.5° , see figure 1. At the upstream corner of the inclined wall there is a radius of approximately 100 mm to prevent separation at this corner. The straight wall and the end walls are made of Plexiglas to allow the use of optical measurement techniques such as LDV and PIV. The straight wall is equipped with pressure taps along the centreline in the downstream direction at an interval of 25 mm. There are also pressure taps in the spanwise direction 100 mm upstream the diffuser inlet on each side at 100 mm interval. These pressure taps are used to

check the two-dimensionality of the incoming flow. The high aspect ratio, 50 at the diffuser inlet, is crucial to achieve a high degree of spanwise uniformity. The diffuser is followed by an outlet channel which is 141 mm high (4.7 inlet channel heights) and 2.5 m long. The purpose of this channel is to avoid upstream influence on the flow from devises located further downstream. This channel is partly made of Plexiglas to facilitate measurements. The outlet channel is followed by a transformation section, changing the aspect ratio of the cross section area towards unity. The contraction is followed by a heat exchanger which is necessary in a closed return wind-tunnel to keep the temperature steady. A temperature sensor is located in the outlet channel and a computer logged the temperature which was found to be steady within ± 0.5 °C. A pipe with 400 mm diameter then leads the flow back to the fan. At the end of the pipe the seeding particles are injected into the flow. Just in front of the fan there is a slit ensuring constant pressure at the fan inlet.

2.2. Measurement techniques

The spanwise (z-direction) velocity component was measured using a one component LDV system. The measurement volume diameter using a lens with a focal length of 310 mm and a beam separation of 73 mm was 77 μ m. The measurement volume length was 0.66 mm. The LDV was used in backscatter mode and was calibrated against a rotating wheel. The LDV measurements were made along the spanwise centreline of the diffuser at intervals of 50 mm. A total of 29 profiles were measured. In the wall normal direction, the interval varied with proximity to a wall and the downstream position, from 0.1 mm to 5 mm. Between 25 000 and 100 000 samples were taken at each measurement point and the time for collecting data was set to a minimum of 120 s per point.

In the streamwise and wall normal directions the velocity components were measured using PIV. A light-sheet, with a typical thickness of 1 mm, was produced using a 400 mJ double-pulse Nd-Yag laser and a digital double frame camera was used to image the illuminated particles. The CCD of the camera had 1018×1008 pixels and a grey-scale resolution of 8 bits. A f=60 mm lens was used with a large (f2.8) aperture in order to get images over an area of about the size of the outlet channel height (141 mm) in both directions. 32×32 pixels (physical size $4.5 \times 4.5 \text{ mm}^2$) interrogation areas with a 50% overlap were used. Sub-pixel interpolation assuming a Gaussian distribution was used in the cross-correlation analysis. The time between frames was optimized for each set of pictures and varied with the downstream position. To cover the entire measurement section PIV images were obtained at 11 downstream positions, 2048 image pairs were taken at each position. The image pairs (samples) were collected at a rate of 7.5 Hz and will thus be uncorrelated. Then, if one assumes the velocity distribution to be Gaussian, the statistical uncertainty for the second order moments with 2048 samples will, with 99% confidence, be less than 3%. It is known that a mean velocity gradient through the PIV interrogation areas can give rise to biased data. Therefore, it was always made sure, during the measurements, that the criterion for unbiased data suggested by Keane & Adrian (1992), $\Delta U \Delta t/d \leq 0.03$ was fulfilled, where ΔU is half the velocity difference over the interrogation area, Δt is the time between images and d is the physical interrogation area size. The LDV and PIV data were projected on a common grid with a mesh size of 10 mm by 2 mm in the streamwise and wall-normal directions respectively.

The flow-rate is a good measure of the two-dimensionality of a flow and for this flow a suitable definition of the flow rate is

$$\frac{1}{HU_b} \int U(y) \mathrm{d}y. \tag{1}$$

Where U is the velocity in the x-direction, H is the inlet channel height and U_b is the bulk velocity of the inlet channel flow. Figure 3 shows the flow rate measured with PIV in the centre region of the measurement section. For comparison the flow rates of Obi $et\ al.\ (1993a)$ and Buice & Eaton (1997) (the data have been taken from Kaltenbach $et\ al.\ (1999)$) have been included in the figure.

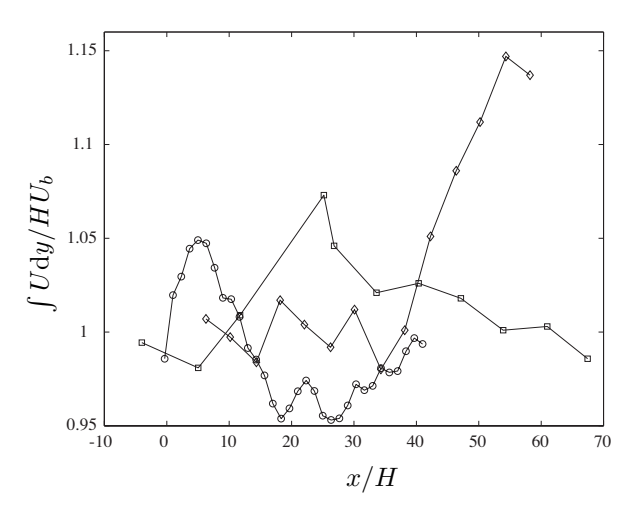


FIGURE 3. Flow rate measured with PIV (\circ) compared to measurements by Obi *et al.* (1993*a*) (\diamond) and Buice & Eaton (1997) (\square).

3. Mathematical model

3.1. Base equations for the turbulence model

The Wilcox (1993) low-Re version of the transport equations for the turbulence kinetic energy, K, and inverse turbulence time-scale, ω , in the EARSM

formulation are

$$\frac{\mathrm{D}K}{\mathrm{D}t} = \mathcal{P} - \beta^* \omega K + \frac{\partial}{\partial x_j} \left[(\nu + \sigma^* \nu_T) \frac{\partial}{\partial x_j} K \right]$$
 (2)

$$\frac{\mathrm{D}\omega}{\mathrm{D}t} = \mathcal{P}_{\omega} - \beta\omega^{2} + \frac{\partial}{\partial x_{i}} \left[(\nu + \sigma\nu_{T}) \frac{\partial}{\partial x_{j}} \omega \right]$$
 (3)

$$\mathcal{P} = -\overline{u_i'u_j'}S_{ij} = -Ka_{ij}S_{ij}, \qquad \mathcal{P}_{\omega} = \alpha \frac{\omega}{K}\mathcal{P}$$
 (4)

with the low-Re functions

$$\alpha^* = \frac{\alpha_0^* + Re_T/R_k}{1 + Re_T/R_k} \tag{5}$$

$$\alpha = \frac{5}{9} \frac{\alpha_0 + Re_T/R_{\omega}}{1 + Re_T/R_{\omega}} \frac{1}{\alpha^*} \tag{6}$$

$$\beta^* = \frac{9}{100} \frac{5/18 + (Re_T/R_\beta)^4}{1 + (Re_T/R_\beta)^4} \tag{7}$$

$$\beta = 3/40
\sigma^* = \sigma = 1/2 \qquad \alpha_0^* = \beta/3 \qquad \alpha_0 = 1/10
R_k = 6 \qquad R_\omega = 2.7 \qquad R_\beta = 8
Re_T = K/(\omega \nu)$$
(8)

The near wall correction coefficients α , α^* and β^* are independent of wall normal distance, in contrast to the wall damping function f_1 of the EARSM, but instead contain the turbulence Reynolds number, or equivalently the ratio $K/\omega\nu$. The molecular viscosity is denoted ν . The near wall limiting behaviour of K and ω are proportional to y^2 and y^{-2} respectively, hence $Re_T \to 0$ as $y \to 0$.

3.2. Modification of the turbulence time scale transport equation

Previously, one disadvantage of using the inverse of the turbulence time scale ω as complementary quantity to the kinetic energy, has been the difficulty to capture the singular behaviour close to solid walls. The rapid variation is described by

$$\omega \to \frac{6\nu}{\beta y^2} \quad \text{for} \quad y \le 2.5 \ \nu/u_{\tau}$$
 (9)

For the destruction and diffusion terms in equation (3), the singular behaviour becomes especially troublesome since the terms behave as y^{-4} as $y \to 0$ in near-wall shear flow. A decomposition is introduced as $\omega = \tilde{\omega} + \omega_{\rm wall}$ with $\omega_{\rm wall}$ given by equation (9) in the whole domain and $\tilde{\omega}|_{y=0} = 0$. The problem of computing the rapid growth of ω has now been transferred to handling the prescribed function $\omega_{\rm wall}$. The near wall diffusion and destruction terms associated with $\omega_{\rm wall}$ cancel and equation (3) simplifies to

$$\frac{D\tilde{\omega}}{Dt} = \mathcal{P}_{\omega} - \beta \left(\tilde{\omega}^2 + 2\tilde{\omega}\omega_{\text{wall}} \right) + \frac{\partial}{\partial x_j} \left[\left(\nu + \sigma \nu_T \right) \frac{\partial}{\partial x_j} \tilde{\omega} \right] +
+ \frac{\partial}{\partial x_j} \left[\sigma \nu_T \frac{\partial}{\partial x_j} \omega_{\text{wall}} \right]$$
(10)

In the EARSM context two terms on the right hand side are still singular at the wall ($\sim y^{-1}$). The main balance in the immediate vicinity of the wall becomes $0=-\alpha\omega_{\rm wall}a_{ij}S_{ij}-2\beta\tilde{\omega}\omega_{\rm wall}$ from which we find that

$$\tilde{\omega}^+ \to -\frac{\alpha}{2\beta} a_{12} \text{ as } y^+ \to 0$$
 (11)

in a plane turbulent channel flow (note that $a_{12} \sim y^+$ as $y^+ \rightarrow 0$) and hence the singular near wall behaviour has been eliminated when solving for $\tilde{\omega}$.

3.3. Explicit algebraic Reynolds stress model

We may consider differential Reynolds stress models (DRSM), (explicit) algebraic Reynolds stress models and eddy-viscosity based two-equation models as three different levels of the description of the evolution of the Reynolds stress anisotropy

$$a_{ij} = \frac{\overline{u_i' u_j'}}{K} - \frac{2}{3} \delta_{ij} \tag{12}$$

In all three cases the turbulence kinetic energy and a length-scale determining quantity $(\varepsilon, \omega, \dots)$, are determined from transport equations. For the DRSM case we may regard the six transport equations for $\overline{u_i'u_i'}$

$$\frac{D\overline{u_i'u_j'}}{Dt} = \mathcal{P}_{ij} - \varepsilon_{ij} + \Pi_{ij} + \mathcal{D}_{ij}$$
(13)

as equivalent to a transport equation for K and a set of five transport equations for a_{ij} . Hence, the relative distribution of energy among the components is here governed by an equation where diffusive and advective effects are taken into account. In equation (13) the terms on the right-hand side describe production, dissipation, pressure-strain-related intercomponent transfer and diffusion, respectively.

At the EARSM level of anisotropy modeling, the advection and diffusion of a_{ij} are neglected in a chosen coordinate system. This is usually referred to as the weak equilibrium assumption (Rodi (1976)). Since the ε_{ij} and Π_{ij} tensors, in this context, are modelled as algebraic expressions in K, ε, a_{ij} and the mean velocity gradient tensor, the weak equilibrium assumption results in a local description of a_{ij} that can be expressed as

$$a_{ij} = a_{ij} \left(S_{ij}, \Omega_{ij} \right) \tag{14}$$

where

$$S_{ij} = \frac{\tau}{2} (U_{i,j} + U_{j,i})$$
 and $\Omega_{ij} = \frac{\tau}{2} (U_{i,j} - U_{j,i})$ (15)

are the mean strain and rotation tensors, normalized with the turbulence time scale

$$\tau = \max\left(\frac{1}{\beta^* \omega}, C_\tau \sqrt{\frac{\nu}{\beta^* K \omega}}\right) \tag{16}$$

In equation (16), ν denotes the molecular viscosity, β^* from equation (7) is used and C_{τ} =6.0.

The EARSM rests on the same platform of two transport equations as eddy-viscosity based two-equation models. In such cases the anisotropy tensor is described by

$$a_{ij} = \text{const.} \times S_{ij}$$
 (17)

where the constant (in high-Re formulations) usually is referred to as $2C_{\mu}$.

Using the weak equilibrium assumption together with an isotropic assumption for the dissipation rate tensor and linear model for the pressure strain rate tensor one can derive an explicit algebraic equation for the anisotropy. The expression for the 2D case treated here reduces to evaluating the explicit relation

$$\mathbf{a} = f_{1}\beta_{1}\mathbf{S} + (1 - f_{1}^{2})\frac{3B_{2} - 4}{2\max(II_{S}, II_{S}^{eq})} \left(\mathbf{S}^{2} - \frac{1}{3}II_{S}\mathbf{I}\right) + \left(f_{1}^{2}\beta_{4} - \left(1 - f_{1}^{2}\right)\frac{B_{2}}{\max(II_{S}, II_{S}^{eq})}\right) (\mathbf{S}\mathbf{\Omega} - \mathbf{\Omega}\mathbf{S})$$
(18)

with damping function

$$f_1 = 1 - \exp\left(-C_{y1}\sqrt{Re_y} - C_{y2}Re_y^2\right), \qquad Re_y = \sqrt{Ky/\nu}$$
 (19)

Coefficients $\beta_{1,4}$ and constants C_{y1}, C_{y2}, B_2 and II_S^{eq} from Wallin & Johansson (2000) are used. Boldface symbols represent matrix notation of the corresponding tensors, $\mathbf{I} = \delta_{ij}$ is the identity matrix and $II_S = S_{ik}S_{ki}$ is the second invariant of the mean strain-rate tensor. In equation (19), y is the wall normal distance.

Effects of system rotation and streamline curvature can also be captured in the EARSM through extensions analysed by e.g. Girimaji (1997), Hellsten et al. (2002) and Wallin & Johansson (2002). This correction is based on a formal derivation of the weak equilibrium assumption in a streamline oriented curvilinear co-ordinate system. In the present paper this type of correction is not applied. It was tested and found to give small effects on the predictions for the present case.

3.4. Wall normal distance function

In turbulence modelling, the need to introduce the wall normal distance in i.e. damping functions often arises. This is also needed in the above defined ω_{wall} as well as the EARSM damping function f_1 . In order to obtain the wall normal distance at any point in the domain, independent of the complexity of the boundary shape, a distance function is computed, using ideas from level set methods, Sethian (1996). By solving the evolution equation

$$\frac{\partial \phi}{\partial t} - (1 - |\nabla \phi|) = \mu_{\phi} \nabla^2 \phi \tag{20}$$

for the scalar ϕ in the whole domain with the solid wall boundary condition $\phi_{\rm wall}=0$, ϕ will take the value of the shortest wall normal distance for each node in the domain. A diffusion term with μ_{ϕ} acting as an artificial viscosity, set proportional to the radius of the local element, is also introduced to damp noise and avoid swallow tail effects (Gullman-Strand (2002)). This enables the introduction of wall normal distance dependent equations, without the need to formulate mesh or domain specific functions. Equation (20) is solved before the flow calculations are initiated and the impact in computational time can thereby be considered to be minimal. The artificial viscosity μ_{ϕ} was successively reduced for the converged solution were the value in each node in the domain is equal to the wall normal distance. Hence $y=\phi$ in equations (19) and (9). Paper in preparation by Gullman-Strand $et\ al.\ (2004)$ that will explain and prove the concept further.

4. Numerical model

Introduction of automated code generation methodology in turbulence model development as well as practical engineering calculations drastically cuts down cycle time for the derivation of the numerical model and coding to a matter of minutes. It also presents the possibility to easily modify a generic set of governing equations for many types of flows.

Using the femLego toolbox (Amberg et al. (1999)) together with an applied mathematics software (in this case Maple), the partial differential equations, the boundary conditions and initial conditions as well as the method of solving each equation is specified in a software worksheet and the FEM code is generated with the femLego toolbox from that sheet. The software presents the equations in a readable and adjustable format and all documentation is contained within the script. It also gives the possibility to derive the equations in the language of applied mathematics.

The fractional step method of Guermond & Quartapelle (1997), originally intended for the unsteady Navier-Stokes equations, was used for the RANS. The order of the finite elements can be chosen from within the worksheet, in this case piecewise linear elements (P1). Once the code is generated and compiled, the mesh is created by a generic unstructured mesh generator.

The unstructured mesh used in the present computations consisted in all three cases of 318×75 nodes in the streamwise and wall normal directions respectively, distributed in a structured fashion. The expanding part of the diffuser consisted of 100×75 nodes. Computations were also performed on a mesh at 8.5° with double node density (635×149) to confirm grid independence. A comparison of mean streamwise velocity between the coarse and fine mesh at 8.5° showed a difference in maximum reversed velocity of 3%. At x/H=20 is the relative error between the coarse and fine solution of the mean streamwise velocity and turbulence kinetic energy K is in the order of 0.4%. Figures 4 and 5 show the two solutions and the negligible impact of grid refinement.

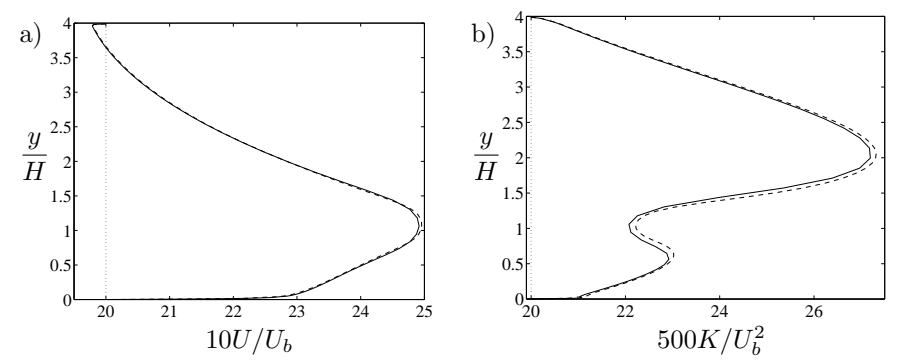


FIGURE 4. a) Mean streamwise velocity (10 U/U_b) and b) turbulence kinetic energy (500 K/U_b^2) at x/H=20 and 8.5°. Solid lines denote the coarse mesh and dashed line the fine mesh.

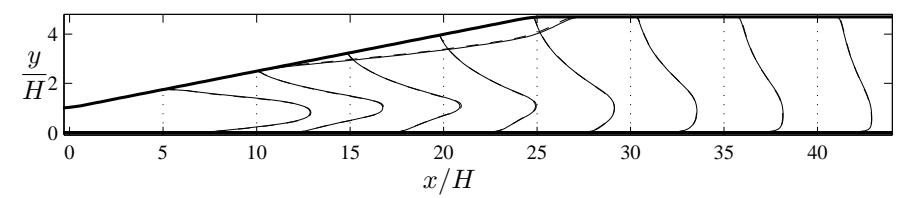


FIGURE 5. Mean streamwise velocity $(10U/U_b)$ and dividing streamline. Legend as in figure 4.

The inlet conditions were obtained from channel flow calculations using the same computational code. The mesh was refined close to the wall with the first node placed at $0.35y_0^+$ in the inlet channel, increasing to $1.63y_0^+$ in the outlet channel, with y_0^+ denoting the wall unit distance in the inlet channel. This was sufficient to resolve the near wall behaviour of the turbulence transport quantities in combination with the decomposition of the inverse turbulence time scale ω .

5. Results

5.1. General description of the flow

When the fully developed turbulent channel flow enters the diffuser inlet it is subjected to a strong adverse pressure gradient. The turbulence here undergoes rapid changes. Thus, it is questionable if the assumption of negligible advection and diffusion of the Reynolds stress anisotropies, made in the EARSM, holds in this region. Other challenging phenomena arising in the region around the inlet are the streamline curvature effects when the flow turns around the convex upstream corner of the diffuser. For instance, the pressure coefficient curves in figure 8b reveal that a 'suction peak' is located on the convex wall giving first a favourable pressure gradient and then an adverse pressure gradient which is approximately twice as strong as the pressure gradient along the straight wall. Kaltenbach et al. (1999) found in their LES that a very small region of reversed flow was located at $x/H \approx 1.2$, this is not observed in the WJ-EARSM computation for this opening angle. However, the presence of this small region of reversed flow reported by Kaltenbach et al. (1999) has not yet been confirmed by any experiment.

Downstream of the diffuser inlet the mean flow stays attached to both the straight and the inclined wall until a large separation bubble forms on the inclined wall (see figure 6). Our PIV-data (for the 8.5° case) give a mean separation point at $x/H \approx 9$ and in the 10° case Buice & Eaton (1997) found it to be at $x/H \approx 6.5 - 7$. The back-flow coefficient χ (sometimes called reverse flow fraction), which has been measured in the present experiment, shows that instantaneous flow reversal occurs on the inclined wall from $x/H \approx 5$. The mean flow reattachment point was found in the exit channel at $x/H \approx 31$ in the present experiment and at $x/H \approx 29$ in the Buice & Eaton (1997) case.

5.2. Mean flow

We begin this comparison between model predictions and experimental results by studying the size and shape of the separation bubble. In figure 6, the dividing streamline, that separates the recirculating region from the outer mean flow, is depicted for the 8.0°, 8.5° and 10° cases. No experimental data are available for the 8.0° case (figure 6a), but the simulation indicates that the separation size diminishes rapidly for angles smaller than 8.5°. In order to investigate this further, simulations were performed for the case with 7.5° angle, and at that angle no region of backflow was obtained. In the 8.5° (figure 6b) case the mean separation point is almost the same in the computation as in the experiment, although this is difficult to see in the figure since the computed bubble is very thin near the separation point. The computed reattachment point is located at $x/H \approx 27$ which is approximately four inlet channel heights upstream of the point measured in the experiments. Maybe more important than the prediction of the length of the bubble is the ability to predict its height, since this directly

determines the character of the outer mean flow. The height of the computed separation bubble for the 8.5° case in figure 6b is approximately 60% of that in the experiment. For the 10° case comparisons are made with experimental data from Buice & Eaton (1997) and the agreement in height is good. The EARSM-predicted flow separates at x/H=4.5 (also here the computed bubble is very thin in its most upstream part), which is $\sim 2H$ upstream of the separation point measured by Buice & Eaton (1997). The reattachment points agree well and they are located at x/H=28 and 29 for the computation and the experiment, respectively.

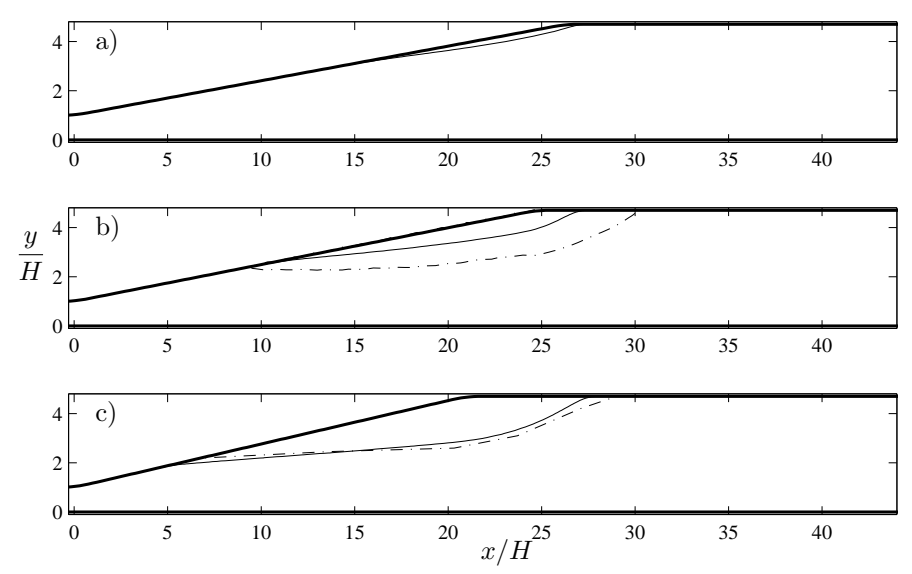


FIGURE 6. Dividing streamline that separates the mean recirculation zone from the outer mean flow for the cases a) 8.0°, b) 8.5° and c)10°. Solid lines show the standard WJ-EARSM and the experimental data is shown as dash-dotted lines.

Figure 7 shows profiles of the mean velocity in the x-direction for the 8.5° and 10° cases. The qualitative shape of the computed profiles agrees rather well with the experimental data, especially in the 10° diffuser, but the strength of the backflow is under-predicted in both cases. The under-predicted size of the separation bubble in the computation of the 8.5° case has a large impact also on the outer flow field due to the smaller geometrical constriction that the bubble poses. The curvature correction of Wallin & Johansson (2002) have little significance in this geometry, at most in the order of 1% for all quantities when present.

Figure 8a shows the skin friction coefficient, $C_f = 2\tau_w/(\rho U_b^2)$, along both the inclined and the straight diffuser wall for the 10° case. (Unfortunately, no

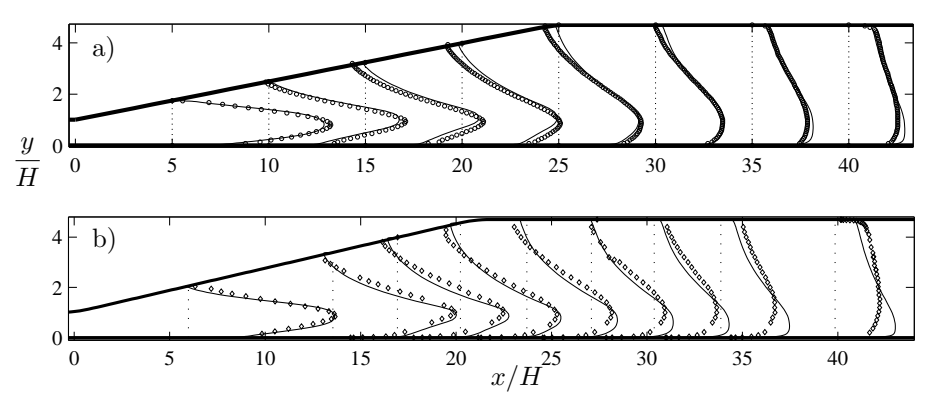


FIGURE 7. U-velocity (parallel to the straight wall) for a) the 8.5° case and b) the 10° case, $10U/U_b$. Experiments (\circ) (data from Buice & Eaton (1997) in b)) and WJ-EARSM predictions (—). Dotted line shows zero-level at each position.

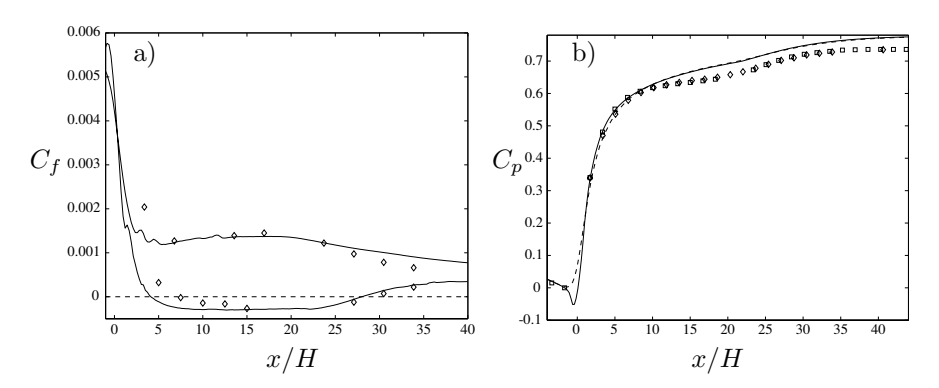


FIGURE 8. a) Skin friction and b) pressure coefficients along the inclined and straight walls for the 10° diffuser. a) WJ-EARSM (—), experimental data from Buice & Eaton (1997) (\diamond). b) Computations inclined wall (—) and straight wall (- - -), experiments inclined wall (\square) and straight wall (\diamond).

skin friction data is currently available from the present experiment on the 8.5° diffuser.) The small region of separation found by Kaltenbach *et al.* (1999) on the convex surface at the diffuser inlet is not present in the EARSM solution. The difference in location of the separation point is easily seen here. The skin friction on the straight wall early in the diffuser is also decreasing faster in the computation than in the Buice & Eaton (1997) experiment. The computed velocity profiles in figure 7b are fuller than the experimental ones near the straight wall in the exit channel. This can also be seen in the C_f -curve as an over-predicted skin friction. As the exit channel flow develops into a channel

flow profile the skin friction coefficients will approach a value of approximately $3.5 \cdot 10^{-4}$ at both walls.

5.3. Turbulence quantities

Since all three velocity components were measured in the current experiment it is possible to compare quantities such as the turbulence kinetic energy, $K = u'_i u'_i/2$, or its production rate $\mathcal{P} = -\overline{u'_i u'_k} \partial U_i/\partial x_k$. The profiles of the kinetic energy shown in figure 9a show a rather good agreement in the most upstream part of the diffuser, but as we go downstream we see that the computed levels of K are smaller than the level measured in the experiment. The computed production rate in figure 9b exceeds the measured in a major part of the diffuser, but is approximately at the measured level in the exit channel. Hence, since the simulated production rate is larger than the experimental while the turbulence kinetic energy stays equal to or is smaller in the simulation, the dissipation rate of turbulence kinetic energy must be over-predicted in the simulation.

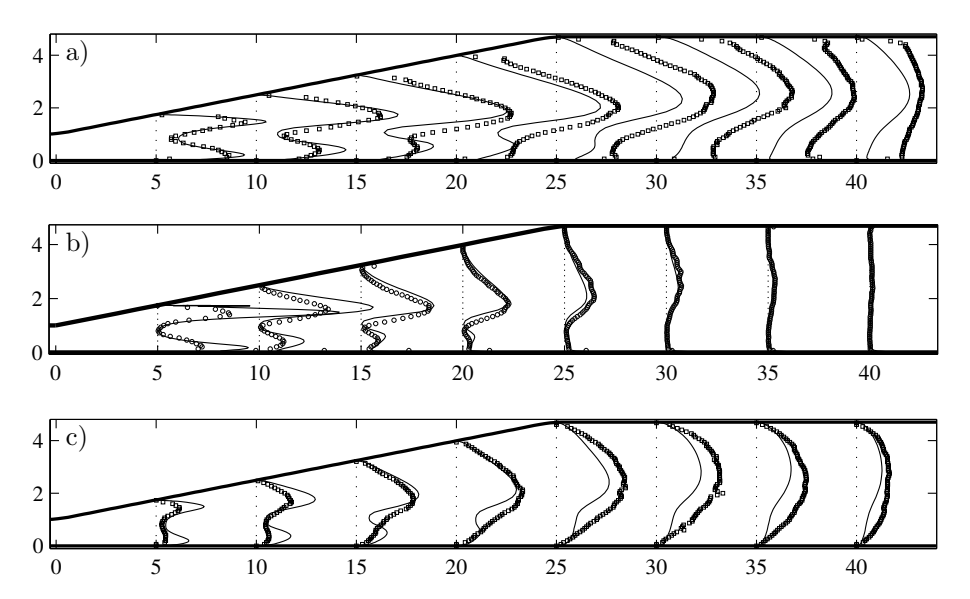


FIGURE 9. Experimental data (\square) and WJ-EARSM (—) predictions for turbulence quantities for the 8.5° case: a) turbulence kinetic energy ($500K/U_b^2$), b) production rate of turbulence kinetic energy ($1500\mathcal{P}H/U_b^3$) and c) variance of the wall-normal (y-direction) velocity component ($500\overline{v'}^2/U_b^2$). Dotted line shows zero-level at each position.

In the upstream part of the diffuser the agreement between measurements and the computation is in general good. But the wall-normal component shown in figure 9c is larger in the computation and is an exception to this. The same behaviour, although not as pronounced, can be observed in the simulation of the 10° case, see figure 10.

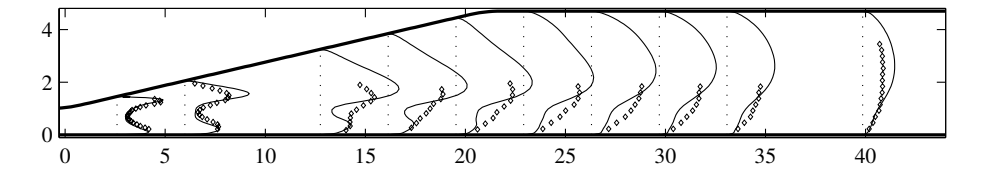


FIGURE 10. Variance of the wall-normal velocity $(500\overline{v'^2}/U_b^2)$ for the 10° case, experimental data by Buice & Eaton (1997) (\circ) and WJ-EARSM (—). Dotted line shows zero-level at each position.

6. Discussion and concluding remarks

The use of near-wall damping functions in the low-Re formulation of the EARSM is not problem-free. The strength of the computed backflow is probably reduced by the damping function. The fact that the dissipation rate of turbulence kinetic energy was overestimated in the computation indicates weaknesses in the modelling in the transport equation for the dissipation rate, or in this case the equation for ω . Especially the modelling of the production term and the turbulent diffusion term in this transport equation could be improved. A natural next step would be to test the diffusion model

$$\frac{\partial}{\partial x_i} \left(c_\omega \frac{K}{\omega} \overline{u_i u_j} \frac{\partial \omega}{x_j} \right), \tag{21}$$

as suggested by Daly & Harlow (1970). Also recent progress by Hellsten (2004) with a re-calibration of a zonal $K-\omega$ for external flow calculations contain possibilities for internal flows.

The over-prediction of the wall normal turbulence component is probably contributing to an exaggerated transport of mean flow momentum towards the inclined wall and hence to the delayed separation observed in the computation.

The 8.5° case has proven to be even more of a challenge to predict accurately using turbulence models than the 10° case. This can be attributed to the weaker adverse pressure gradient and that the flow is on the verge of being attached.

The methodology of generating a FEM-based CFD code through extensive use of automated code generation was demonstrated to be a feasible and attractive approach for analysing the case of asymmetric diffuser flow for a set of different opening angles.

Acknowledgements

The authors like to thank the Swedish Energy Agency, the Swedish Strategic Research Council and the IVS Research School for financial support.

References

- Amberg, G., Törnhardt, R. & Winkler, C. 1999 Finite element simulations using symbolic computing. *Mathematics and Computers in Simulation* **44**, 275–274.
- APSLEY, D. D. & LESCHZINER, M. A. 2000 Advanced turbulence modelling of separated flow in a diffuser. Flow, Turbulence and Combustion 63 (1–4), 81–112.
- Buice, C. U. & Eaton, J. K. 1997 Experimental investigation of flow through an asymmetric plane diffuser. *Tech. Rep.*. Department of mechanical engineering, Stanford university.
- Buice, C. U. & Eaton, J. K. 2000 Experimental investigation of flow through an asymmetric plane diffuser. *J. Fluids Eng.* **122**, 433 435.
- Comte-Bellot, G. 1965 Écoulement turbulent entre deux paroix parallèles. Publications scientifiques et techniques 419. Ministère de l'air, 2, Avenue de la Porte-d'Issy, Paris.
- DALY, B. J. & HARLOW, F. H. 1970 Transport equations in turbulence. Int. Phys. Fluids 13, 2634–2649.
- DURBIN, P. A. 1995 Separated Flow Computations with the $k \varepsilon v^2$ model. AIAA Journal 33, 659–664.
- GIRIMAJI, S. S. 1997 A galilean invariant explicit algebraic Reynolds stress model for turbulent flows. Phys. Fluids 9, 1067–1077.
- Guermond, J. L. & Quartapelle, L. 1997 Calculation of incompressible vicous flow by an unconditionally stable projection FEM. *Journal of Computational Physics* **132** (CP965587), 12–33.
- Gullman-Strand, J. 2002 Turbulence modeling using automated code generation applied to asymmetric diffuser flow. *Tech. Rep.* TRITA-MEK-02/06. Dept. of Mechanics, KTH, Sweden.
- Gullman-Strand, J., Amberg, G. & Johansson, A. V. 2004 A general approach to the evaluation of wall distance applied to turbulent flow computations. Submitted for publication.
- Hellsten, A. 2004 New advanced $k-\omega$ turbulence model for high-lift aerodynamics. In 42nd AIAA Aerospace Sciences Meeting and Exhibit, pp. 1–18. Reno, NV, IISA
- Hellsten, A. & Rautaheimo, P., ed. 1999 8th ERCOFTAC/IAHR/COST Workshop on Refined Turbulence Modelling. Helsinki University of Technology, Finland.

- HELLSTEN, A., WALLIN, S. & LAINE, S. 2002 Scrutinizing curvature corrections for algebraic Reynolds stress models. In 32nd AIAA Fluid Dynamics Conference, pp. 1–15. St. Louis, MO, USA.
- IACCARINO, G. 2000 Prediction of the turbulent flow in a diffuser with commercial CFD codes. *Tech. Rep.*. Center for Turbulence Research.
- KALTENBACH, H. J., FATICA, M., MITTAL, R., LUND, T. S. & MOIN, P. 1999 Study of flow in a planar asymmetric diffuser using large-eddy simulation. J. Fluid Mech. 390, 151–185.
- KEANE, R. & ADRIAN, R. 1992 Theory of cross-correlation in PIV. Applied scientific research 49, 191–215.
- Obi, S., Aoki, K. & Masuda, S. 1993a Experimental and computational study of separating flow in an asymmetric planar diffuser. In 9th Symposium on Turbulent Shear Flows, , vol. 305, pp. 1–4. Kyoto, Japan.
- Obi, S., Ohizumi, K., Aoki, K. & Masuda, S. 1993b Turbulent separation control in a plane asymmetric diffuser by periodic perturbation, pp. 633-642. Elsevier Science Publishers B.V.
- Rodi, W. 1976 A new algebraic relation for calculating the Reynolds stresses. Z. argew. Math. Mech. 56, 219–221.
- Sethian, J. A. 1996 Level Set Methods and Fast Marching Methods. Cambridge University Press.
- Wallin, S. & Johansson, A. V. 2000 An explicit algebraic Reynolds stress model for incompressible and compressible turbulent flows. J. Fluid Mech. 403, 89–132.
- Wallin, S. & Johansson, A. V. 2002 Modelling streamline curvature effects in explicit algebraic Reynolds stress turbulence models. *Int. J. Heat and Fluid Flow* 23, 721 730.
- WILCOX, D. C. 1993 Turbulence modeling for CFD. DCW Industries Inc.

Paper 5

P5

A note on the influence of negative turbulence production on separating flows

By Olle Törnblom & A. V. Johansson

KTH Mechanics, SE-100 44 Stockholm, Sweden

The influence of negative production of turbulent kinetic energy in separating flows is investigated by analysis of data from an experiment in a plane asymmetric diffuser and from a direct numerical simulation (DNS) of a separating flat plate boundary layer. It is explained under what circumstances negative production may occur and a few examples are given. A scenario is presented, explaining how negative production may occur in the reattachment region. In most cases negative production is of negligible importance for the flow development but in the stagnant region near reattachment in a separation, where the magnitude of the turbulent velocities can be several times larger than the mean velocities, it may be crucial for the flow. The presence of negative production in the reattachment region can also explain the rapid decay of the Reynolds stresses after reattachment that has been reported in several investigations of separating flows. It is also suggested that negative production could be part of the reason for the underestimation of the reverse flow velocity frequently seen in turbulence model computations.

1. Introduction

Negative production rates of turbulence kinetic energy is a peculiar phenomenon in that it implies positive production of mean flow kinetic energy. In other words, kinetic energy taken from the unordered turbulent velocity fluctuations is transferred to the ordered mean flow. This is in direct contrast to the general view of turbulent energy transfer where mean flow energy is transferred to the large scale eddies, which in turn supply energy to smaller eddies and so forth until the large shear rates of the smallest turbulence-scales dissipate the energy. This is also what happens in most regions of a turbulent flow, but under certain circumstances negative production can occur.

Observations of negative turbulence productions have been made in several different flows. In rotating plane channel flow at high rotation rates negative production has been observed on the stable side in the vicinity of the maximum velocity peak (Grundestam 2006). Negative production has also been observed

in turbulent wall-jet flow in the interface between the inner and outer shear layers (Tangemann & Gretler 2000).

The phenomenon can also be observed in the results of several investigations of flow separation (Alving & Fernholz 1996; Spalart & Coleman 1998; Le et al. 1997; Skote & Henningson 2002), but its consequences are seldom discussed. The figures from the experimental investigation by Dianat & Castro (1991) suggests that negative production was measured also here, however this is a bit unclear due the the way the data is presented. In all these investigations the negative values are found in the downstream end of the separation bubble and mostly in the region close to the wall. The production is usually presented in a budget where the magnitude of different terms in the turbulence kinetic energy equation are compared. Seen in this context it is tempting to draw the conclusion that the negative values are small and thus negligible. However, if the production is instead compared with the terms in a budget for the mean flow kinetic energy it might be significant, because in the stagnant region around reattachment the mean velocities are typically smaller than the turbulent velocities.

1.1. The causes of negative turbulence production

As was indicated earlier, the production rate of turbulence kinetic energy, \mathcal{P} , is a term appearing both in the transport equation for the turbulent kinetic energy

$$\frac{DK}{Dt} = -\overline{u_i u_j} \frac{\partial U_i}{\partial x_j} - \nu \overline{\left(\frac{\partial u_i}{\partial x_j} \frac{\partial u_i}{\partial x_j}\right)} - \frac{\partial}{\partial x_j} \left(\frac{1}{\rho} \overline{u_j p} + \frac{1}{2} \overline{u_i u_i u_j} - \nu \frac{\partial K}{\partial x_j}\right) \quad (1)$$

and, with opposite sign, in the transport equation for the mean flow kinetic energy

$$\frac{DQ}{Dt} = \overline{u_i u_j} \frac{\partial U_i}{\partial x_j} - \nu \left(\frac{\partial U_i}{\partial x_j} \frac{\partial U_i}{\partial x_j} \right) - \frac{\partial}{\partial x_j} \left(\frac{1}{\rho} U_j P + U_i \overline{u_i u_j} - \nu \frac{\partial Q}{\partial x_j} \right). \tag{2}$$

The production rate is the first term on the right hand side of the above equations, hence the production rate of turbulent kinetic energy is defined as

$$\mathcal{P} \equiv -\overline{u_i u_j} \frac{\partial U_i}{\partial x_j} \tag{3}$$

and it represents the contribution to the deformation work performed by the turbulent stresses. In most cases this contribution is dissipative (Tennekes & Lumley 1972).

Negative turbulence production occur only under certain conditions when turbulence is transported from a region with a certain strain distribution to another region with a different strain distribution. A good example is the case of a rapidly rotating plane channel (see *e.g.* Grundestam 2006) one side of the channel is stabilised by the rotation and becomes laminar and increased levels of turbulence, compared to the non rotating case, are seen on the other side

of the channel. The turbulent shear stress \overline{uv} has the same sign across the whole channel (for certain rotation rates), it is near zero on the laminar side but through transport from the turbulent side, a low level of \overline{uv} is maintained at the laminar side. The flow being homogeneous in the streamwise (x) and spanwise (z) directions the production can simply be expressed as $-\overline{uv}dU/dy$. Thus on the laminar side where dU/dy have opposite sign, as compared to the turbulent side, the turbulence production will be negative.

In the case of a turbulent wall jet negative production can be seen when $\overline{uv} = 0$ is located closer to the wall than the position of the peak in the mean velocity, due to the rapid growth rate of the wall jet mean profiles. In this case it is probably a combination of diffusive and advective transport of turbulence (from upstream positions where the jet height is smaller) that causes the negative production.

The above examples show two situations when the negative production is due to the shear stress part of the turbulence production, which is usually the larger part in shear flows. But it is also possible to have negative production due to the normal stress part. Expanding the expression in equation 3 for a two-dimensional flow that is homogeneous in the z-direction, and using the continuity equation, we arrive at

$$\mathcal{P} = -(\overline{u}\overline{u} - \overline{v}\overline{v})\frac{\partial U}{\partial x} - \overline{u}\overline{v}\left(\frac{\partial U}{\partial y} + \frac{\partial V}{\partial x}\right) \tag{4}$$

where the first term is the normal stress contribution to the production and the second term is the shear stress contribution. Consider now a flow with initially homogeneous isotropic turbulence that is first expanded and subsequently contracted. In the expanding flow the streamwise fluctuations $(\overline{u}\overline{u})$ will be enhanced, due to vortex contraction while the cross stream component on the other hand will be attenuated. So the turbulence will be anisotropic when the flow enters the contraction. In the contraction $\partial U/\partial x > 0$, hence if $\overline{u}\overline{u} > \overline{v}\overline{v}$ we will see negative production due to the normal stresses for the initial part of the straining. It is assumed here that mean flow gradients in the y-direction are small. The above scenario can be investigated from a fundamental perspective by means of rapid distortion theory.

Brethouwer (2005) uses direct numerical simulations and rapid distortion theory to investigate the development of homogeneous turbulence subjected to a rapid imposition of shear and rotation. At certain rotation numbers Brethouwer finds that the production rate attains negative values during the evolution process.

1.2. Categorisation of negative production

We have seen in the previous sections that for negative production to occur the mean flow must be inhomogeneous. In a flow that is temporally homogeneous in a statistical sense but spatially inhomogeneous, spatial transport of Reynolds stresses is required in order to have negative production. Therefore we can differentiate between advection supported and diffusion supported negative production due to spatial inhomogeneities. The expanding-contracting flow being an example of the first and the rotating channel flow an example of the latter. Another possibility is negative production due to temporal inhomogeneities in flows that are spatially homogeneous in a statistical sense. An example of this category is the flow studied by Brethouwer (2005).

Combinations of the different categories are of course possible also. In for example the separating flows that will be discussed later on, the negative production is supported both by advective and diffusive transport.

1.3. Connection to separating flows

A question that has been under some discussion is the cause of the frequently observed rapid decay of the Reynolds stresses in the vicinity of reattachment. A short review of investigations of the flow in the reattachment zone of separations is given in Song & Eaton (2002). The reasons for the decay have often been sought for in the behaviour of the large eddies forming in the shear layer above the separation. The reasons for this can be traced back to Bradshaw & Wong (1972) who in order to explain an observed decrease in the turbulent shear stress hypothesised that the the large eddies are split at reattachment and that one half is convected 'upstream' by the reversed flow and the other continues downstream. After this however, measurements have shown that the size of the large eddies is practically unchanged after reattachment. The problem lies in that the mean flow, and other large scale flow features change quite slowly around reattachment while the Reynolds stresses decay rapidly.

Song & Eaton (2002) describe in a hypothetical scenario that the streamwise velocity gradient $\partial U/\partial x$ is significant near reattachment and that streamwise vortices are stretched increasing \overline{vv} and \overline{ww} while decreasing \overline{uu} as well as the length-scale of the near-wall vortices. They also add, that the presence of the wall will redistribute some of the energy in \overline{vv} back to \overline{uu} and \overline{ww} or result in an increased dissipation rate, depending on the size of the vortices.

Another observation is that turbulence model predictions of separated flows, almost without exceptions, underestimate the velocity of the reversed flow. The authors have found no plausible explanation for this behaviour in the literature. However, if negative production plays a role this would not be captured by the majority of turbulence model that rely on the Boussinesq hypothesis, or eddy-viscosity, to describe the relation between turbulent stresses and the mean flow. This is easy to realise by considering how the approximation for the production rate is expressed in an eddy-viscosity model:

$$\mathcal{P} \approx 2C_{\mu} \frac{K^2}{\varepsilon} S_{ij} S_{ij}. \tag{5}$$

Here C_{μ} is a constant with positive sign, K is the turbulence kinetic energy which is strictly positive, ε is the dissipation rate which is also strictly positive and $S_{ij} = (\partial U_i/\partial x_j + \partial U_j/\partial x_i)/2$ is the mean strain rate tensor. Since S_{ij} is squared and all other multiplicands in equation 5 are positive, negative production will never be predicted.

1.4. Arguments for the existence of negative production near reattachment

In a separating flow the scenario is to some extent similar to the above described idealised example where the flow was expanded and subsequently contracted. A separating flow is always associated with flow deceleration $(\partial U/\partial x < 0)$ and the streamwise turbulence component is usually substantially larger in comparison to the other. The main part of the flow will decelerate and eventually attain an approximately constant velocity after reattachment. However close to the wall in a region before and after the reattachment point $\partial U/\partial x > 0$. In this region \overline{vv} is usually damped by the presence of the wall and consequently \overline{uv} must be small. In addition it is often seen that \overline{uv} does not change sign below the y-position of maximum backflow. All this make it likely that negative production will occur in this region. That in turn will lead to increased mean flow kinetic energy, which implies increased backflow velocity if it occurs inside the separation.

The above scenario is actually quite similar to the ideas expressed by Song & Eaton. They however seem to draw the conclusion that, when stretching the flow, the energy in $\overline{u}\overline{u}$ is transferred to the other turbulence components, while we say that it is transferred to the mean flow.

2. Results

We here present data supporting the ideas that negative turbulence production can occur in the reattachment region and that it can be of importance for the flow development. The data is taken from the plane asymmetric diffuser flow experiment by Törnblom et al. (2006) and from the direct numerical simulation of a separating flat plate boundary layer by Skote & Henningson (2002).

Negative production is observed both in the experimental data and in the DNS. In the experiment, the negative production is found where one would anticipate finding it according to the scenario described in section 1.4, i.e. in a thin region near the wall. In the DNS comparatively larger values of negative production are found in a larger region.

In order to determine the relevance of the negative production budgets for the terms in equation 2 were calculated at a selected x-position in the flow. Figure 1 shows the budget from experimental data taken at x/H=28 which is slightly upstream the reattachment point (the reader is referred to Törnblom et al. for details). The viscous terms were computed and found negligible in comparison to the other terms and are therefore not shown. It can be seen that

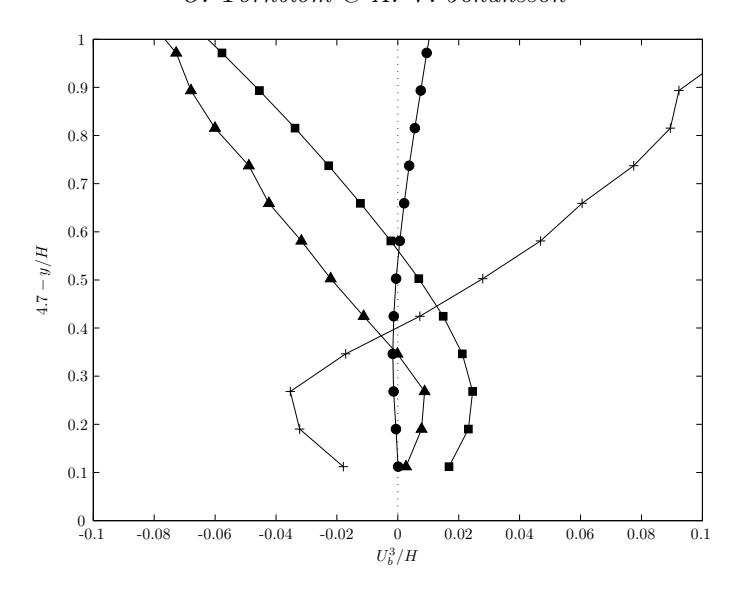


FIGURE 1. Budget of the terms in equation 2. Experimental data from the diffuser flow of Törnblom *et al.* (2006) at x/H=28. (\blacktriangle) $\overline{u_iu_j}\frac{\partial U_i}{\partial x_j}$; (\blacksquare) $-\frac{\partial}{\partial x_j}\left(\frac{1}{\rho}U_jP\right)$; (\bullet) $-U_i\frac{\partial Q}{\partial x_i}$; (+) $-\frac{\partial}{\partial x_j}\left(U_i\overline{u_iu_j}\right)$

the pressure transport and turbulent diffusion terms are dominating but that the negative production clearly is of non-negligible magnitude. In this budget negative production is signified by a positive contribution and is found below 0.3 on the vertical axis. The Reynolds normal and shear stress contributions to the production are shown in figure 2. The normal stress contribution is smaller and negative for all points shown while the shear stress contribution is negative only for the points close to the wall.

In the budget for the DNS data, shown in figure 3, from a position towards the end of the separation bubble, it is instead the production that is the dominating term and it is balanced by either turbulent diffusion or pressure transport depending on the y-position. The plotted data is normalised by the initial boundary layer thickness δ^* and the initial free-stream velocity U_{∞} .

3. Conclusions

A scenario explaining how negative production of turbulent kinetic energy can occur in the reattachment region of separating flows is presented together with data supporting the described scenario.

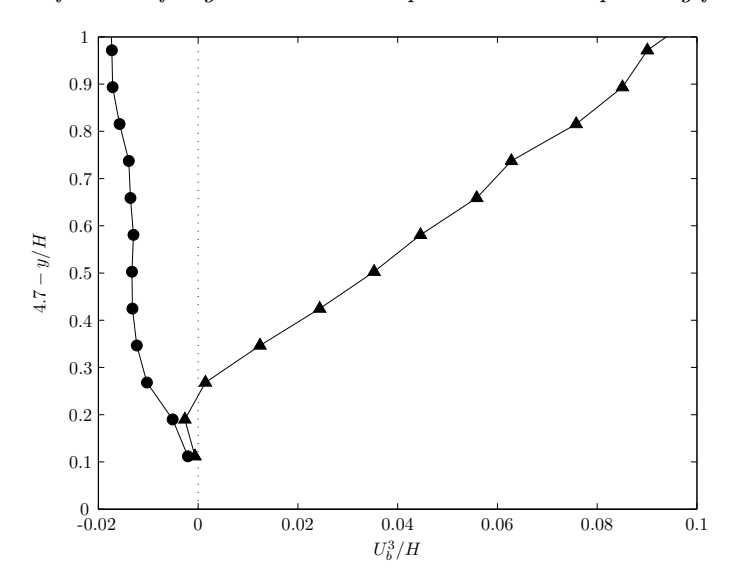


FIGURE 2. Contributions to \mathcal{P} from (\blacktriangle) $-\overline{uv}\left(\frac{\partial U}{\partial y} + \frac{\partial V}{\partial x}\right)$ (•) $-(\overline{uu} - \overline{vv})\frac{\partial U}{\partial x}$. Experimental data from the diffuser flow of Törnblom *et al.* (2006) at x/H=28.

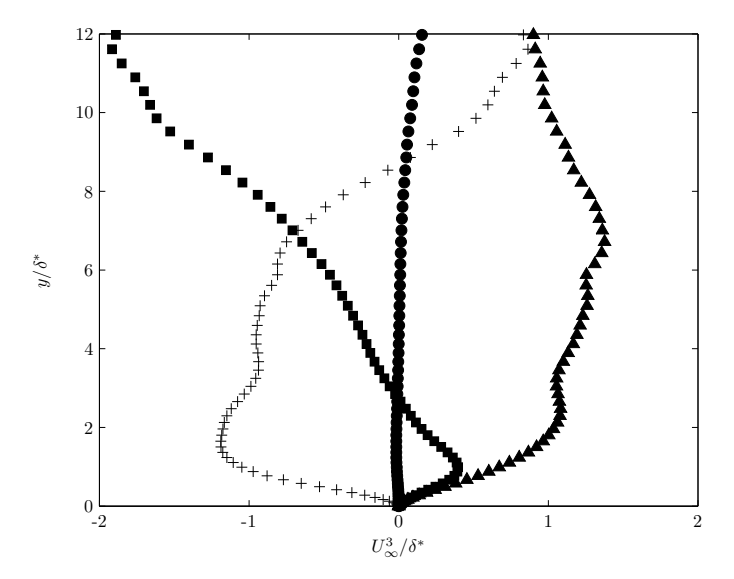


FIGURE 3. Budget of the terms in equation 2. Data from the DNS of a flat plate separation by Skote & Henningson (2002) at x/δ^* =388. Symbols as in figure 1.

Negative production can explain the frequently reported rapid decay of the Reynolds stresses in the vicinity of reattachment. The turbulent energy is partly transferred to the mean flow.

It is also possible that negative production can explain why nearly all turbulence models predict a too small magnitude of the reversed flow velocity in separated flows. Transfer of energy from the turbulence to the mean reversed flow can explain what is missing in the models, in order to capture the correct backflow velocity magnitude.

We already know from the presented data that energy transfer from the turbulence to the mean flow can be of significant character. But further work with measurements or simulations is needed to fully understand its implications.

Acknowledgments

Dr Martin Skote is gratefully acknowledged for giving us permission to use his DNS-data. We are also most grateful to Dr Philipp Schlatter who computed the DNS statistics. The financial support from the Swedish energy agency is acknowledged.

References

- ALVING, A. & FERNHOLZ, H. 1996 Turbulence measurements around a mild separation bubble and downstream of reattachment. J. Fluid Mech. 322, 297–328.
- Bradshaw, P. & Wong, F. Y. F. 1972 The reattachment and relaxation of a turbulent shear layer. *J. Fluid Mech.* **52**, 113–135.
- Brethouwer, G. 2005 The effect of rotation on rapidly sheared homogeneous turbulence and passive scalar transport. linear theory and direct numerical simulation. J. Fluid Mech. **542**, 305–342.
- DIANAT, M. & CASTRO, I. P. 1991 Turbulence in a separated boundary layer. J. Fluid Mech. 226, 91–123.
- Grundestam, O. 2006 Modelling and simulation of turbulence subject to system rotation. PhD thesis, KTH Mechanics, Stockholm, Sweden.
- LE, H., Moin, P. & Kim, J. 1997 Direct numerical simulation of turbulent flow over a backward-facing step. J. Fluid Mech. 330, 349–374.
- Skote, M. & Henningson, D. 2002 Direct numerical simulation of a separated turbulent boundary layer. J. Fluid Mech. 471, 107–136.
- Song, S. & Eaton, J. K. 2002 Reynolds number effects on a turbulent boundary layer with separation, reattachment, and recovery. Technical report TSD-146. Mechanical engineering department, Stanford university.
- Spalart, P. & Coleman, G. 1998 Numerical simulation of a separation bubble with heat transfer. *Eur. J. Mech. B./Fluids* **16**, 169–189.
- Tangemann, R. & Gretler, W. 2000 Numerical simulation of a two-dimensional

The influence of negative turbulence production on separating flows 151

turbulent wall jet in an external stream. Forschung im Ingenieurwesen $\mathbf{66}$, 31-39.

Tennekes, H. & Lumley, J. L. 1972 A First Course in Turbulence. The MIT Press. Törnblom, O., Lindgren, B. & Johansson, A. V. 2006 Measurements of mean flow statistics in a plane asymmetric diffuser with 8.5° opening angle. To be submitted (Paper 1).

Paper 6

Experimental procedures for the investigation of the turbulent flow in a plane asymmetric diffuser by means of stereoscopic high-speed PIV

By Olle Törnblom, Björn Lindgren and Arne V. Johansson

KTH Mechanics, SE-100 44 Stockholm, Sweden

Technical report

The design process of an experimental setup for studying a plane asymmetric diffuser flow is described. Prior to the diffuser the flow passes through a 3 m long and 30 mm high channel to generate a turbulent channel flow as inlet condition to the diffuser. The wind-tunnel is of closed circuit type in order to allow for flow seeding in an indoor environment. The wind-tunnel is driven by an 11 kW radial fan, capable of generating inlet channel flow Reynolds numbers of up to HU_{cl}/ν =60000, H being the channel height and U_{cl} the channel centreline velocity. The setup and calibration of a stereoscopic high-speed PIV-system is described in detail and the measurement circumstances important for the quality of the PIV-data are scrutinised.

1. Introduction

Study of diffuser flows, *i.e.* duct flows subjected to an adverse pressure gradient, is motivated by the large number of applications in which these flows appear and the energy savings that may result from an increased knowledge about proper diffuser designs and separation control. The experimental facility whose design is described herein was built to study a generic flow with separation, both in order to get a database for turbulence model comparisons as well as to study the fundamental physics of the flow.

If one desires to study turbulent separating flow, separation control and provide reference data for computations, in the same geometry, it has to be chosen with care. The most generic way to study separation is to do a flat plate experiment where an adverse pressure gradient is produced by altering the free-stream velocity with a variable geometry of the opposing wind-tunnel wall (see e.g. Perry & Fairlie (1975) and Angele & Muhammad-Klingmann (2005)). Dianat & Castro (1991) used a porous cylinder with a small flap at the trailing edge mounted above a flat plate to generate the pressure gradient.

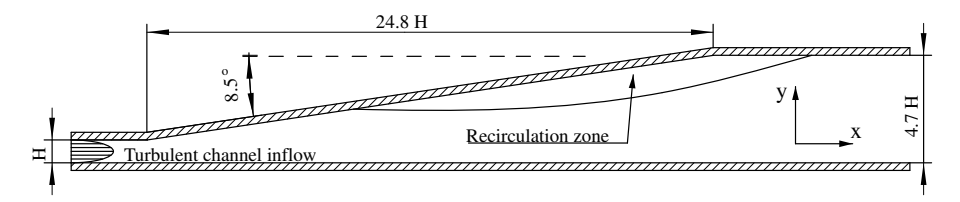


Figure 1. The plane asymmetric diffuser.

Another category of separated flows is that associated with sharp edges or bluff body geometries. Examples are flow over flat plates or cylinders with blunt leading edges (e.g. Cherry et al. (1984) and Ruderich & Fernholz (1975)) or flow over a backward facing step (e.g. Etheridge & Kemp (1978) and Yoshioka et al. (2001)). Symmetric diffuser flows have been investigated by e.g. Sovran & Klomp (1967) and Chithambaran et al. (1984). All of these flow cases have been used to study different aspects of separation, but some are more suited for the study of generic mechanisms and comparison between experiments and numerical simulations. In blunt edge flows and flows over backward facing steps the challenge of predicting the separation point vanishes, as the separation inevitably will occur at the corner. In symmetric diffusers the separation can fluctuate between the two diffuser walls in a random manner and at long time-scales making ensemble averaging a very tedious task. In a CFD calculation, this unstable flow situation may also cause convergence problems.

The plane asymmetric diffuser with turbulent channel inflow, shown in figure 1, has the properties we were looking for. The fully developed turbulent channel flow used as inflow condition is a well known flow, simplifying the task of setting appropriate boundary conditions, both in turbulence model computations and in direct numerical simulations. The asymmetric geometry favours separation on the inclined wall and eliminates the problems associated with symmetric diffusers. If the upstream corner of the inclined wall is sufficiently smooth with a finite radius of curvature, the separation point will be located at the inclined wall, giving a challenging flow to predict in simulations and a location of the separation point sensitive to control. Furthermore, the relatively simple geometry with two dimensional flow and mostly straight walls facilitate CFD grid generation and the determination of positions inside the measurement section.

2. Design

2.1. Pre-design considerations

At the time when the first design steps were taken, there existed two (to the authors known) previous experiments in a very similar geometry *i.e.* those by Obi

et al. (1993) and Buice & Eaton (1997). In particular the latter one, which contains a detailed description of the experimental setup, was studied in order to learn about the difficulties related to the design of a plane asymmetric diffuser experiment. The major difficulty of this flow case is the inherent tendency, of a separating flow, to be three-dimensional. Since we required the flow to be two-dimensional (in an average sense), the three-dimensional behaviour must be controlled. The undesired three-dimensional effects enter the flow via the end walls (the walls which limit the spanwise extent of the diffuser), hence an ideal, but unrealistic, solution would be to have an infinitely wide diffuser. However, a relatively large spanwise width compared to the height of the diffuser (i.e. a large aspect ratio) is a necessary requirement to have a two-dimensional flow field.

A preliminary idea was that the newly built low speed wind-tunnel at the department (cf. Lindgren & Johansson (2002)) could be used for the experiment. But that alternative was abandoned due to the large pressure losses that the inlet channel would cause and because of the limited aspect ratio it would allow.

Another decision which needs to be taken before the actual design-work start is how large the diffuser should be. The size of the facility partly determines what Reynolds number the flow will have and also what fan power is needed to drive the wind-tunnel at the desired flow speeds. In a small facility the flow will be more influenced by small imperfections in the design *e.g.* small edges in joints between different wall sections. A too small test-section also limits the accessibility, due to the physical size of our hands, arms etc. and it also requires better precision in the positioning of the measurement probe than in a larger test-section, for the same relative error.

With these arguments in mind we decided to make our diffuser larger than the ones used in the experiments by Obi et al. (1993) and Buice & Eaton (1997). We also wanted a larger aspect ratio than the previous experiments. Obi's and Buice's inlet channel heights were 20 mm and 15 mm and their spanwise widths were 700 mm and 450 mm respectively. We chose to build a 30 mm high channel and an inlet aspect ratio of 50, giving a channel width of 1500 mm (due to the standard width of plywood sheets the final channel was built with a width of 1525 mm). In turbulent channel flow an aspect ratio of five is the lowest possible in order to have (a reasonably) two-dimensional flow in an about two channel heights wide region in the centre of the channel (Johansson & Alfredsson (1986)). If the aspect ratio is lower than this, secondary flow effects caused by end walls and corners may influence the flow. In our facility this requirement is well fulfilled also in the exit channel where the aspect ratio is 10.8. However, in flows with adverse pressure gradients these rules of thumb can only be considered valid if separation is avoided on the end walls.

In order to produce a fully developed turbulent channel flow it was decided that the length of the inlet channel should be at least 100 channel heights. According to the experiments by Comte-Bellot (1965) the higher order statistical moments are fully developed at 60 channel heights from the inlet. Similar observations were made by Johansson & Alfredsson (1982).

Accordingly, the final choice of channel geometry was a 30 mm high, 3000 mm long and 1500 mm wide channel. It was concluded that, in order to minimize the floor area occupied by the wind-tunnel, the channel should be built so that the spanwise direction was oriented vertically, which is also favourable in the sense of minimizing wall deflections caused by gravity.

One of the obvious difficulties when studying separating flows experimentally is the occurrence of velocities with changing sign, due to the region of backflow. This difficulty makes it impossible to measure with hot-wire anemometry, an otherwise well established and accurate technique. If one wants to determine both the value of the velocity and its direction one has a few alternatives; pulsed hot-wires, laser Doppler velocimetry (LDV) or particle image velocimetry (PIV). The natural choice for us was to use the two latter techniques with emphasis on PIV. LDV and PIV are both optical methods, and thereby require optical access to the flow. Hence, the measurement section of the wind-tunnel has to be made in a transparent material. If one wants to make a large transparent wall, as in a wind-tunnel test section, at a reasonable cost one has practically two choices, window glass or polymer glass. Window glass typically has a more even and precise thickness than polymer glass. An even thickness is of high importance when measuring with LDV, since a distortion of the laser-beams (or rather of one of the beams) can make them misaligned in the measurement volume, resulting in bad, or no, Doppler signals. Furthermore, window glass has a higher modulus of elasticity as compared to polymer glass which allows thinner sheets to be used for a certain desired stiffness. Thinner sheets will also contribute to lowering the optical distortion. If one desires to use polymer glass a popular choice is Plexiglas[®] which is made from polymethyl methacrylate (PMMA). This material is usually cheaper than window glass and not as brittle, furthermore it is easier to machine than window glass. Another material property that could influence the choice is the refractive index, but for PMMA and window glass this can be disregarded since it is approximately 1.5 for both materials. The need to be able to drill pressure taps, the cheaper prize and the possibility to join Plexiglas[®] sheets together with screws made us choose this material for large parts of the measurement section.

2.2. Fan and motor

Having decided the spanwise width and height of the inlet channel and the desired Re_{τ} in the inlet channel the required flow rate can be calculated using

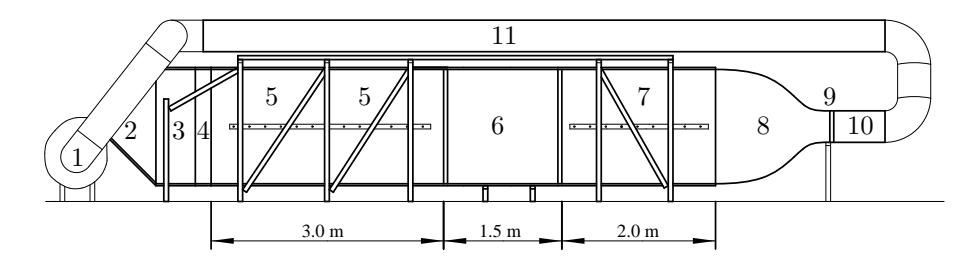


FIGURE 2. A sketch of the complete wind-tunnel. Refer to table 1 for a description of the numbered parts.

Part	Description
1	Fan, 11 kW centrifugal
2	Transformer from $322 \times 229 \text{ mm}^2$ to $1525 \times 100 \text{ mm}^2$
3	Settling chamber, $1525 \times 100 \times 500 \text{ mm}^3$
4	Contraction, from $1525\times100 \text{ mm}^2$ to $1525\times30 \text{ mm}^2$
5	Inlet channel, $1525 \times 30 \times 3000 \text{ mm}^3$
6	Diffuser/measurement section, from $1525\times30~\mathrm{mm^2}$ to $1525\times141~\mathrm{mm^2}$
7	Exit channel, $1525 \times 141 \times 2000 \text{ mm}^3$
8	Contraction, from $1525 \times 141 \text{ mm}^2$ to $400 \times 300 \text{ mm}^2$
9	Heat exchanger
10	Transformer, from 400×300 mm ² to 400 mm diameter
11	Return pipe, 400 mm diameter with five 90° bends

Table 1. Description of the numbered parts in figure 2.

the logarithmic friction law and Dean's relation,

$$\frac{U_{cl}}{u_{\tau}} = \frac{1}{\varkappa} \ln \left(\frac{u_{\tau} H}{2\nu} \right) + C \tag{1}$$

$$\frac{U_{cl}}{U_b} = 1.28 \left(\frac{U_b H}{2\nu}\right)^{-0.0116} \tag{2}$$

with the additive constant C = 6.0 and $\varkappa = 0.4$. Where U_{cl} is the channel centreline velocity, u_{τ} the friction velocity at the wall, U_b the channel bulk velocity and H is the channel height. A desired $Re_{\tau} = u_{\tau}H/\nu = 4000$ gives, according to these relations and the chosen channel area, a volume flux of approximately 1.8 m³/s. In order to choose a fan one has to know also at what pressure the required flow should be delivered. This has to be estimated. A very rough estimate yielded that the wind-tunnel would cause pressure losses corresponding to approximately three times the dynamic pressure of the inlet channel bulk velocity. Later this estimate was proven to be reasonably accurate for the first design, which did not have a return circuit and heat exchanger. When choosing

a fan it is advisable to examine not only the maximum performance, but also the performance over a region of the fan characteristics curve. It is desirable to have a characteristics curve in the volume flow region where the fan will be used, that gives as small a flux variation as possible for a given variation in the pressure, for instance due to a nonstationary separation bubble.

Based on these estimates a centrifugal fan capable of delivering 2.1 m³/s at 3000 Pa was ordered from Ventur tekniska AB. To control the speed of the 11 kW induction motor, the fan was complemented with a frequency converter and a filter, from ABB Motors AB.

2.3. Transformer and settling chamber upstream the channel

The fan has an outlet section of $322 \times 229 \text{ mm}^2$ that has to be transformed into the large aspect ratio cross-section ($1525 \times 30 \text{ mm}^2$) of the inlet channel. This transformation had to take place over a limited length, putting high demand on the design in order to minimize losses and ensure an even flow over the whole cross-section.

A common way to achieve a spanwise homogeneous flow is to have a settling or stagnation chamber, with large cross-section area where the velocity is very low, followed by a contraction into the channel. Here, we chose to have a rather small settling chamber with a cross-section area of $1525 \times 100~\mathrm{mm}^2$. By doing so, the transformer between the fan and the settling chamber will have a shape which diverges in the spanwise direction and contracts in the other direction, see figure 3. The total expansion ratio, *i.e.* the ratio between the cross-section area of the settling chamber and the fan outlet area, is thus only about two. Two splitter plates are mounted immediately after the fan outlet to avoid large scale flow separation here and to direct the flow outwards in the spanwise direction.

Three screens, shown in figure 3, were placed in the transformer and settling chamber in order to even out mean flow variations. The screens used have a wire diameter d of 0.71 mm and a (wire centre to wire centre) mesh width M of 3.2 mm. These values give a porosity $\beta = (1 - d/M)^2 = 0.6$. Using screens will not only even out mean flow variations but also reduce angle deviations relative to the screen according to the relation

$$\phi = \alpha \theta, \tag{3}$$

where θ is the angle of the incoming flow and ϕ the angle of the out-going flow. The constant α is related to the local pressure-loss coefficient K_0 through the empirical relation (see Laws & Livesey (1978))

$$\alpha = \frac{1.1}{\sqrt{1 + K_0}}.\tag{4}$$

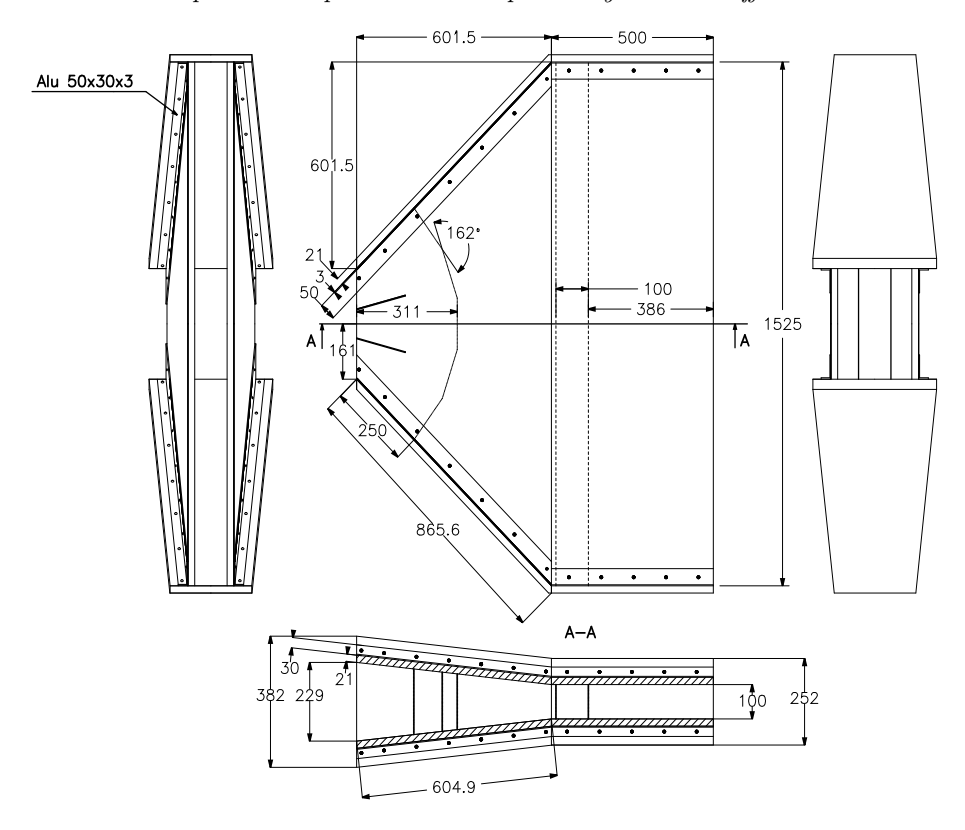


FIGURE 3. Four view drawing of the transformer and settling chamber upstream the channel.

The local pressure-loss coefficient is highly Reynolds number dependent for subcritical Reynolds numbers but can for higher Reynolds numbers be approximated with

$$K_0 = 0.5 \frac{1 - \beta^2}{\beta^2},\tag{5}$$

if $0.6 < \beta < 0.7$. With a volume flow of $2.1 \text{ m}^3/\text{s}$ the wire-diameter Reynolds number will be well above the critical value of $Re_d = 100$. Using equations 4 and 5 it can be seen that the local pressure-loss coefficient will be $K_0 = 0.9$ and that an error in the incoming flow angle relative to the screen will be reduced by a factor 0.8 after the screen. Streamwise mean velocity variations are reduced when the flow passes through a screen according to the expression

$$\frac{\Delta u_2}{\Delta u_1} = \frac{1 + \alpha - \alpha K_0}{1 + \alpha + K_0},\tag{6}$$

derived by Taylor & Batchelor (1949), where Δu_1 and Δu_2 are the variations of the streamwise mean velocity upstream and downstream the screen respectively. For the screens of concern herein this ratio will be 0.4.

In the diffusing part, a bent screen was used in order to both even out mean velocity variations and to direct the flow according to equation 3. Further downstream, in the first part of the settling chamber, two screens are placed to further reduce possible mean flow variations. The screens were mounted onto frames made from 15×15 mm stainless steel tubes and were manufactured by AB Derma in Gråbo, Sweden.

Both the transformer and the settling chamber were manufactured in plywood sheets joined together with L-shaped aluminium profiles and screws and sealed with tightening material. All the wind-tunnel parts are mounted in a framework (as can be seen in figure 2) of $60\times40\times3$ mm³ and $60\times40\times4$ mm³ steel tubes and steel L-profiles respectively. The steel framework is bolted to the concrete floor in the laboratory.

2.4. Contraction and inlet channel

The settling chamber is followed by a two-dimensional contraction, changing the channel height from 100 mm to 30 mm. The shape of the contraction, shown in figure 4, is described by two sinus hyperbolic functions according to the description in Lindgren & Johansson (2002). This shape is an optimal shape regarding the pressure gradient along the walls and it was derived originally for the MTL wind-tunnel by Henrik Alfredsson and Alexander Sahlin at the department, using inviscid/boundary layer calculations. The contraction was manufactured in polystyrene foam that was cut to the appropriate shape using a hot-wire saw. The polystyrene foam was covered with a glassfiber-epoxy laminate in order to have a smooth and hard surface.

The inlet channel consists of two 3000×1525×21 mm³ plywood sheets with plywood end walls joined together with L-shaped aluminium profiles. Four L-shaped aluminium profiles oriented in the spanwise direction are screwed to the large plywood sheets in order to prevent the walls from bulging due to the larger pressure inside the channel. Furthermore, the large plywood sheets are supported along their centrelines with adjustable screws in order to ensure a constant (30 mm) channel height at all locations. The channel height was measured with a movable 30 mm plastic cube (mounted on a long stick to be able to reach all points in the channel) and adjusted with the screws. The horizontal bar with the adjustment screws can be seen in figure 2.

2.5. Measurement section

The measurement section (part number 6 in figure 2) is connected to the inlet channel and the exit channel with high precision joints milled in aluminium with steel guide taps. The joints are held together with three DE-STA-CO®

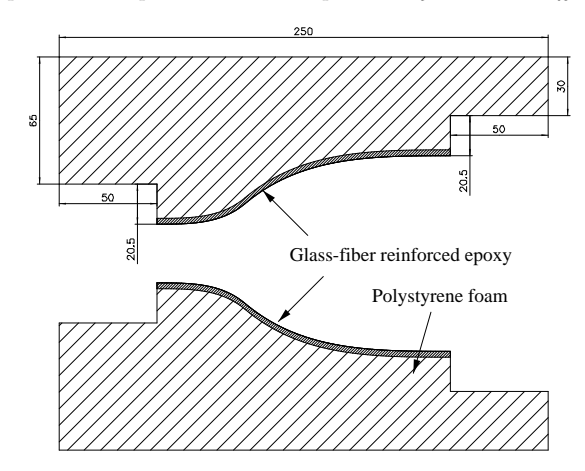


FIGURE 4. The design for the contraction before the inlet channel

clasps at each side. This design allows the measurement section to be removed in order to facilitate modification of the diffuser or measurement installations.

As mentioned in section 2.1, optical access to the measurement section is necessary and Plexiglas® was believed to be the most appropriate transparent material. The plane wall of the measurement section was made from a single $1500\times1525\times25~{\rm mm}^3$ Plexiglas® sheet and the end walls are two $350\times1500\times25~{\rm mm}^3$ sheets. It was discovered that the delivered Plexiglas® varied in thickness as much as $\pm 1~{\rm mm}$, and later on a 4 mm thick float-glass window was inserted to replace the Plexiglas® in the upper end wall. The $1250\times155~{\rm mm}^2$ piece of float-glass was taken from the mid portion of a large glass plate where the thickness homogeneity are best according to a representative for Pilkington floatglas AB in Halmstad, Sweden. The plane wall and the end walls are joined with screws that go through the end walls and are screwed into threaded holes in the plane wall.

The wall opposite to the straight, *i.e.* the wall that is partly inclined, is built up by several different parts and materials. The photograph in figure 5 shows the structure of this wall. The inlet channel part of this wall is made from 25 mm plexiglas, this section which is approximately 200 mm long is screwed to the flange of the upstream corner. The upstream and downstream corners, depicted in figure 6, are made of solid aluminium that was CNC machined to get well defined radii of curvature, the flanges with threaded holes ensure good alignment between the corner parts and the connected wall sections. Three horizontal aluminium beams extend between the two vertical corner beams (see figure 5), a 4 mm thick glass window is held between the upper and the middle beam. The window gives optical access to the measurement section from two directions and reduces wall reflections, allowing for measurements closer to the

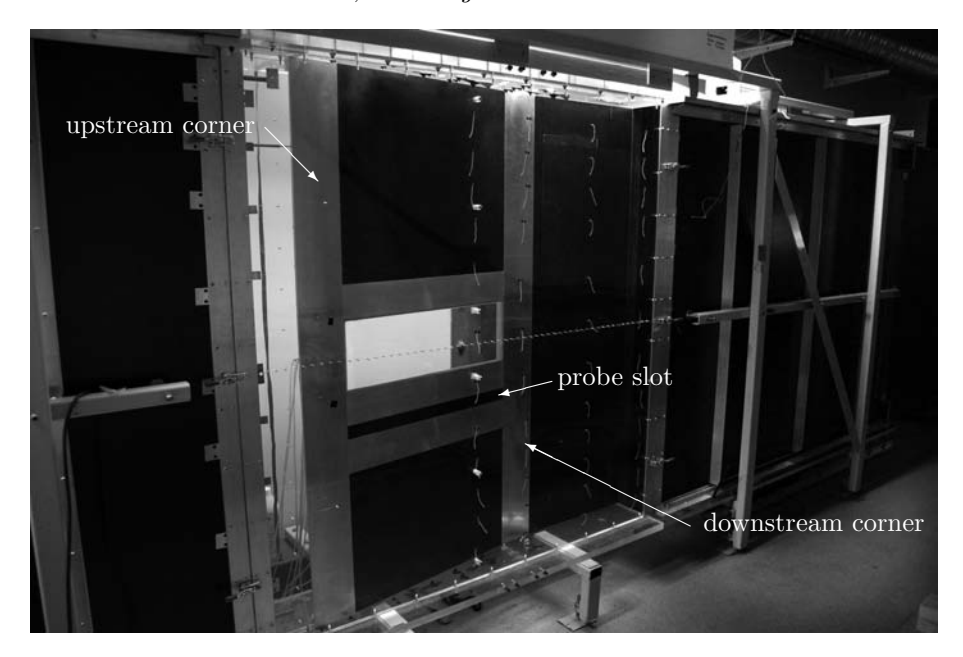


FIGURE 5. Photograph of the measurement section, the flow direction is from left to right.

wall. The space between the middle and the lower horizontal beams is intended to be used as a probe slot for measurements of e.g. wall shear stresses. The large dark coloured wall-parts visible in figure 5 are plywood. Two hatches allowing for access to the measurement section are located downstream the downstream corner.

When the turbulent channel flow develops in the 3 m long inlet channel boundary layers will form on the channel end walls. These boundary layers will decrease the level of momentum in a region near the end walls, making the end wall flow sensitive to adverse pressure gradients. By reducing the thickness of the end wall boundary layers through suction before the diffuser where the adverse pressure gradient starts, end wall separation can be avoided. The suction is applied through a 100 mm long perforated section of the end wall ending 50 mm before the diffuser starts. The suction is produced by a separate fan connected to the perforated parts through hoses. The air that is sucked out is brought back to the wind-tunnel circuit by leading the exit of the fan to a connection on the return channel. After the perforated section a new boundary layer will start to grow and to prevent this boundary layer from separating small vortex generators are put on the end walls in the diffuser.

A row of 57 pressure taps were drilled along the centreline of the plane wall, the distance between the pressure taps is 25 mm and the holes which are

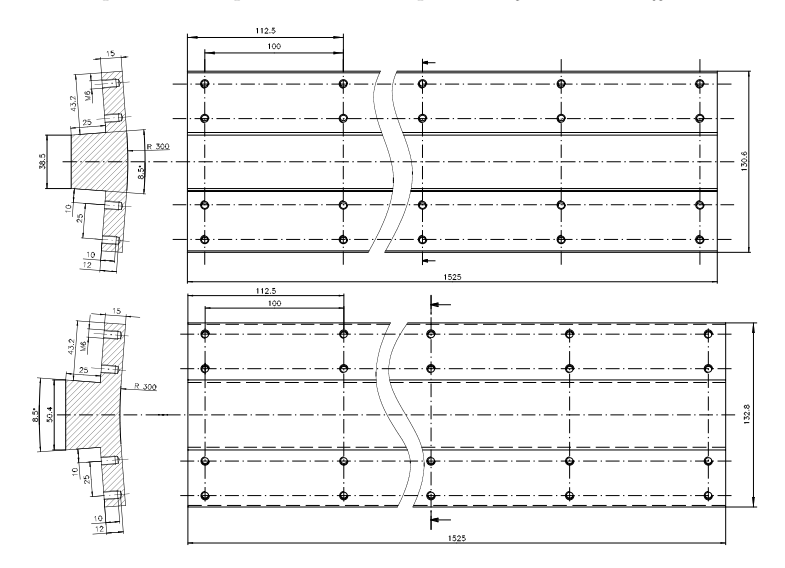


FIGURE 6. Drafts of the up- and downstream corner beams.

drilled directly in the Plexiglas[®] has a diameter of 0.4 mm. Similarly a coarser row of pressure holes were drilled on the opposite side of the diffuser, along the inclined wall. Pressure taps were also drilled in spanwise rows on both walls 100 mm before the upper corner of the diffuser in order to measure the spanwise homogeneity of the incoming flow.

2.6. Exit channel and transformer before the heat exchanger

The exit channel is built in plywood in a similar way as the inlet channel and has the purpose of reducing the effects of the downstream wind-tunnel parts on the flow in the measurement section. The size of the exit channel is $2000 \times 1525 \times 141$ mm³ and stiffening aluminium L-profiles and adjustment screws along the centreline are used, in the same fashion as for the inlet channel, to ensure that these dimensions are kept. An open slot at the downstream end of the exit channel ensure a point in the wind-tunnel circuit with a constant reference pressure (the pressure in the laboratory) and thus avoid pulsating pressures from appearing. The slot also ensures that the pressure inside the measurement section is close to that outside of it, minimising the possibility to have an altered flow geometry due to bulging of the large Plexiglas[®]-window that constitutes the straight wall.

The exit channel is followed by a transformer, changing the cross section to $400\times300~\text{mm}^2$ in order fit the dimensions of the following heat exchanger. The shape of the contraction was determined using the same formula as for the contraction upstream the inlet channel (see section 2.4). Since the transformer

is contracting in one direction and expanding in the other the total contraction ratio is only 1.8, smaller than what one can conceive from figure 2. The sides of the transformer were sawed into the proper shape from a 25 mm thick plywood sheet and the (bent) upper and lower walls were made by steel tinplates nailed to the plywood.

2.7. Heat exchanger and return channel

When running the wind-tunnel, the fan is constantly adding kinetic energy to the 'closed' system. Energy which through viscous dissipation eventually will become heat. This heat has to be removed at the same rate as it is added if a constant flow temperature is desired in the experiment. In order to do so a heat exchanger, consisting of a car radiator (VW Golf II), was built into the wind-tunnel circuit. In the heat exchanger the cooling medium is tap water. No automatic temperature control system has been implemented as the temperature variations proved to be small enough for optical measurement techniques without automatic control.

After the heat exchanger the cross section shape is gradually changed from rectangular to circular with 400 mm diameter. This is done in a 650 mm long transformer section manufactured in glass fibre reinforced epoxy moulded on a plug which was formed from a block of styrofoam using a hot-wire saw.

The return channel is made of standard 400 mm diameter ventilation pipes and standard 90° bends. The total length of the return channel is approximately 12 m and five 90° bends were used. The return channel is supported by consoles bolted to the ceiling. The last bend of the return channel has two connectors for hoses one for introducing seeding particles and one for returning the air from the boundary layer suction (see section 2.5).

3. Flow quality

The wind-tunnel was first built without the return channel and preliminary tests were performed, with the aim to evaluate the inflow conditions and the two-dimensionality of the flow. Yarn tufts were used to visualise the flow direction and to convince us that no large separation was occurring on the diffuser end walls.

3.1. Spanwise homogeneity of the inlet flow

Pitot tube measurements of inlet flow were performed at six different spanwise positions 100 mm upstream of the first corner of the diffuser in order to evaluate the spanwise homogeneity of the inflow. In order to reduce the perturbation of the flow, the pitot tube was positioned at the end of a long carbon fibre reinforced sting (see figure 7). The pitot tube was traversed from the wall towards the channel centre with a DC servo controlled motor operated from a computer. In order to measure from the opposite wall the sting had to be

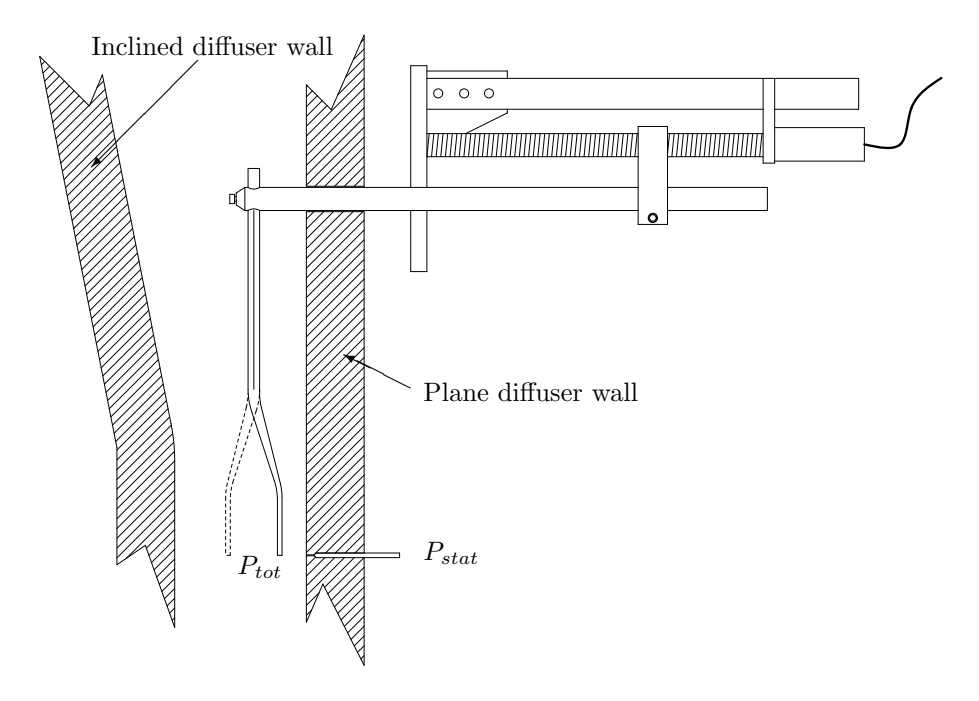


FIGURE 7. Sketch of the setup used for the pitot-tube measurements.

rotated 180° around its axis. The static pressure was measured in a hole on the plane wall and the pressure difference was measured with a Furness Control FCO 510 differential pressure transducer with an accuracy of 0.25% of full scale (2000 Pa). The measured centreline velocities were found to be constant within $\pm 0.9\%$ over the whole spanwise width.

3.2. Two-dimensionality

The previous section concerned the spanwise homogeneity of the inflow but the largest difficulty of this experiment is to get a two-dimensional flow in the adverse pressure gradient region in the diffuser. The methods used to prevent end wall separation are described in 2.5. In order to see if the end wall flow really is attached tufts taped to the end walls were used. With the boundary layer suction turned on, the only backflow that could be observed on the end walls was in the regions where the 'desired' separation is located *i.e.* near the downstream half of the inclined wall and on a limited area downstream of that. Notable is that if the boundary layer suction was turned off, a very large separated region, which was visualized with smoke, formed. This separation could extend 1/3 of the spanwise width from the end walls towards the centre line and would probably give rise to a significant flow rate increase in the downstream parts of the diffuser if measurements were taken along the diffuser centreline.

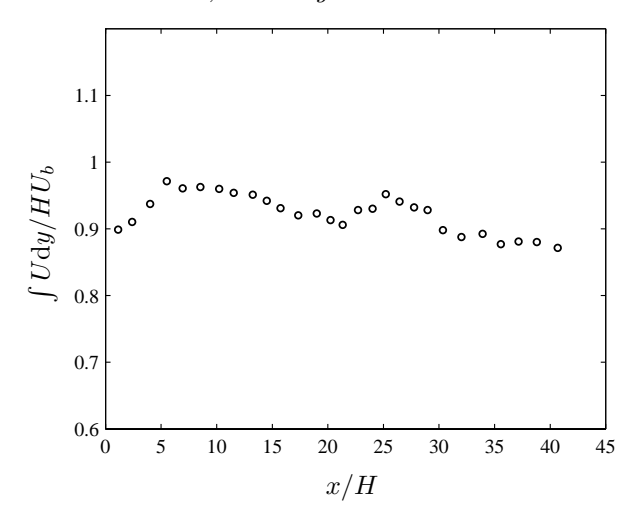


FIGURE 8. Flow rate measured with PIV.

Furthermore, the three-dimensional separation appeared to be stationary on either wall but could be forced to switch side by partially blocking of the flow coming out from the exit channel.

The flow-rate is a good measure of the two-dimensionality of a flow and for this flow a suitable definition of the flow rate is

$$\frac{1}{HU_b} \int U(y) \mathrm{d}y. \tag{7}$$

Where U is the velocity in the x-direction, H is the inlet channel height and U_b is the bulk velocity of the inlet channel flow (i.e. $U_b = \int U_{inlet} dy/H$). Figure 8 shows the flow rate measured with PIV (see Törnblom et al. (2006)) in the centre region of the measurement section. The integrals of the PIV profiles are consequently smaller than the bulk flow predicted from the inlet centreline velocity and Dean's relation. The reason for this could be the lack of near wall points in the PIV-data leading to an underestimation of the integrals. More important however, is it that the data shows no trend towards increasing flow rate with increasing x-position. Such a trend would be an indication of an undesired three-dimensional separation.

3.3. Fan speed control

It was noticed when the first measurements with LDV were taken that the mean values of the measured velocity converged very slowly indicating some very long timescale variation, or drift, of the velocity. In order to handle this problem a LabView program was built, allowing the fan to be controlled from the computer. The LabView program measures the air temperature in the

wind-tunnel with a PT-100 temperature sensor, the friction velocity at the inlet with a Preston tube connected to a Furness Control FCO 510 differential pressure transducer and the ambient pressure with an absolute pressure transducer connected to the FCO 510. From the measured data the density and viscosity of the air is calculated. These values are used to calculate the friction velocity at the inlet and a proportional controller adjusts the fan speed to keep the friction velocity at a constant level.

4. Stereoscopic PIV measurements

4.1. Stereoscopic setup

The setup for the stereoscopic measurements reported in Törnblom et al. (2006) is shown in figure 9. The two cameras and the laser were mounted on a translation stage in order to be able to cover the whole measurement section without changing their relative positions. The translation stage was an Isel LF6, the working length was 2000 millimetre and the position repeatability is stated by the manufacturer to be 0.02 millimetres. A rig of X-95 profiles and FLS-95 rails from Linos were used to mount the cameras and the laser on the translation stage.

Two Photron Ultima APX-RS cameras were used in the setup. The resolution of the cameras' 10 bit grayscale CMOS sensors are 1024×1024 pixels and the maximum frame rate at this resolution is 3 kHz. If the image resolution is reduced it is possible to increase the frame rate up to 250 kHz. The size of the image sensors are $17.9 \times 17.9 \text{ mm}^2$. The internal memory of each camera can store up to 6144 full size images which have to be transferred through a firewire interface to a PC before a new recording can be made.

The laser light sheet was formed using optics mounted directly at the laser head. The sheet optics from LaVision have three lenses, first is a fixed spherical lens with negative focal length, second is a spherical lens with positive focal length whose position is adjustable and last is a fixed cylindrical lens with negative focal length. The position of the middle lens can be altered by turning a focus ring, allowing the position of the beam waist to be adjusted between approximately 0.3 and 2.0 meters. Due to the relatively short distance between the laser and the measurement region following from the experimental setup (see figure 9) a rapidly diverging light sheet is needed in order to illuminate the whole imaged area. Thus, a cylindrical lens with a focal length of -3 millimetres was used.

The thickness of the laser light-sheet was determined by measuring the width of the correlation peaks in the cross correlation between particle images taken at the same time instant by the two cameras (Wieneke 2005). Figure 10 shows how particles, in the light sheet, that will appear at the same position in images of camera 1 will appear at different positions in the images of camera 2 (and vice versa). Therefore the correlation peaks will be smeared out in one

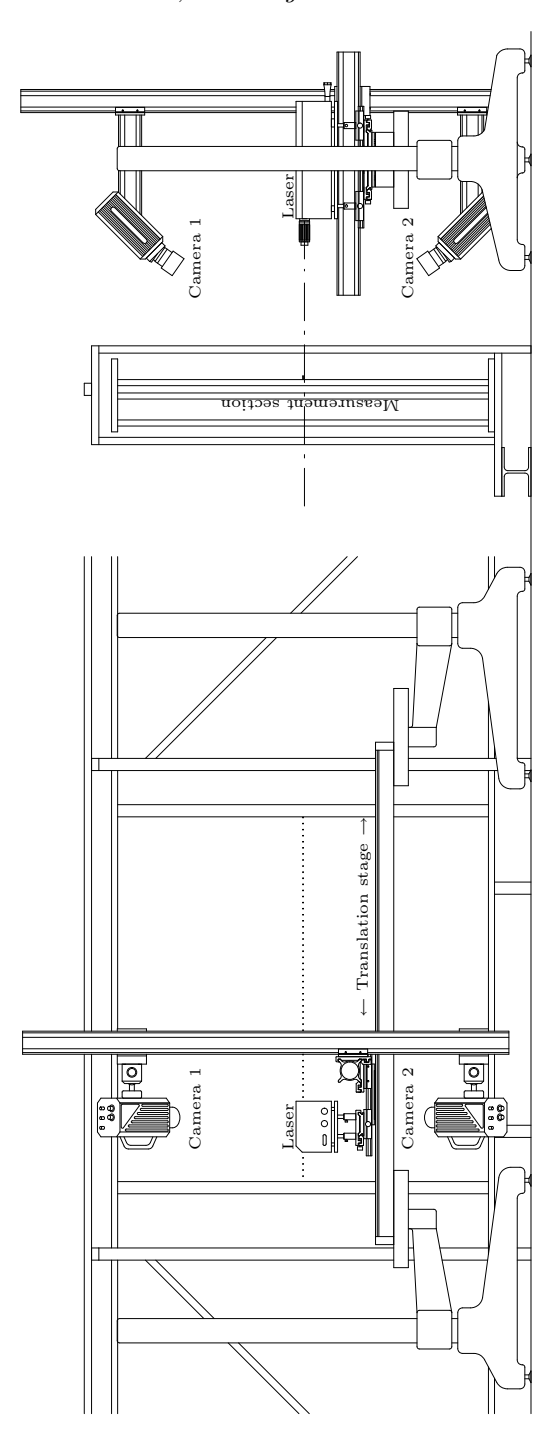


FIGURE 9. Setup for the stereoscopic PIV measurements.

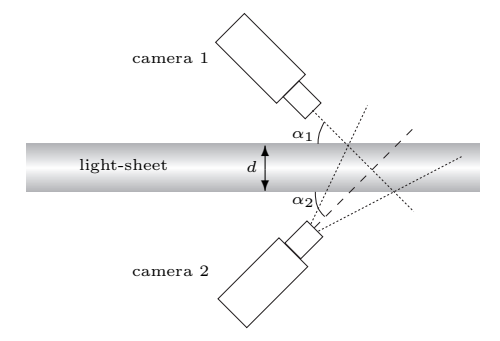


FIGURE 10. Sketch showing the reason for the smearing of correlation peaks and how the peak-width can be related to the light-sheet thickness.

direction. By simple geometrical arguments, the width W_{peak} of the correlation peaks can be related to the light-sheet thickness d according to

$$W_{peak} \approx d \left(\frac{1}{\tan(\alpha_1)} + \frac{1}{\tan(\alpha_2)} \right).$$
 (8)

The definition of the angles α_1 and α_2 can be seen in figure 10. Using this relation, the average light sheet thickness in the experiment, was estimated to 1.5 mm.

The laser used was a New Wave Pegasus Nd:YLF with dual laser heads. Each laser head can emit up to 10000 pulses per second. The energy in each pulse is dependent on the operating frequency and the maximum is 10 mJ at a rate of 1 kHz. The laser head weighs 12 kg and was small enough to be placed on the translation stage.

4.2. Flow seeding

The air was seeded with smoke from a smoke-generator ZR12-AL from Jem using a mixture of glycerol and water. By varying the amount of water the density of the smoke can be optimized to give good results. The smoke was inserted just upstream of the fan and was sufficiently spread out in the measurement section due to the mixing in the fan and in the inlet channel. An estimate of the particle size based on recorded particle images and using relations for the Airy pattern given in Raffel et al. (1997), gave that the particles are approximately 3 μ m in diameter, which is in good agreement with previous investigations of the same type of smoke.

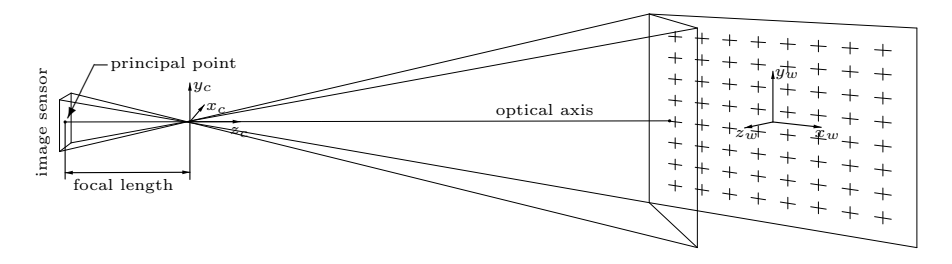


Figure 11. Camera pinhole model.

4.3. Stereoscopic calibration

In order to correctly compute a three component velocity field from the camera images it is necessary to know how the points on each camera's image sensor are related to a common 'world' coordinate system in the measurement region.

There are a few different methods to approximate the mapping functions which are used in stereoscopic PIV e.g. polynomial fitting and the camera pinhole model. For the current investigation the camera pinhole model was chosen, the reason for choosing this model was mainly because it allows for post calibration misalignment corrections, i.e. misalignment between the calibration plate and the actual position of the light sheet, by performing a 'self-calibration' on the recorded images. Another advantage of the pinhole model, as compared to polynomial fitting, is that it allows a small degree of extrapolation of the mapping function, this is important in the present flow case which is bounded by two walls making it hard to have calibration plate markers all the way out to the boundaries. Furthermore, the risk of fitting noise to the mapping function, due to imperfect detection of the calibration plate markers, is larger for the polynomial fit, since this model has about four times as many free parameters as the pinhole model. Polynomial fitting can however be advantageous in situations with large image distortions, where the pinhole model is known to suffer from convergence problems (Wieneke 2005). It should perhaps be emphasised that the chosen method is a calibration-based three-dimensional volume mapping method, not to confuse with purely geometrical ray-tracing methods which require very accurate knowledge about the experimental geometry. The software DaVis 7.0 and 7.1 by LaVision GmbH was used for the calibration.

The camera pinhole model and the self-calibration method is described in detail in Wieneke (2005). The pinhole model is based on simple geometrical relations, see figure 11, and corrections for image distortions. The world coordinate system $\mathbf{x}_w = (x_w, y_w, z_w)$, which is common for both cameras, is related to the each camera's coordinate system $\mathbf{x}_c = (x_c, y_c, z_c)$ according to

$$\mathbf{x}_c = \mathbf{R}\mathbf{x}_w + \mathbf{t},\tag{9}$$

where **R** is a rotation matrix and **t** a translation vector. The relation between the camera coordinate system and the uncorrected image plane system $\mathbf{x}_i^{uc} = (x_i^{uc}, y_i^{uc})$, with its origin at the principal point, is then given by

$$\mathbf{x}_i^{uc} = \frac{f}{z_c} [x_c, y_c],\tag{10}$$

where f is the focal length. Last a correction for first and second order radial lens distortions is made so that image plane coordinates are

$$\mathbf{x}_i = \mathbf{x}_i^{uc} \left(1 + k_1 |\mathbf{x}_i^{uc}| + k_2 |\mathbf{x}_i^{uc}|^2 \right), \tag{11}$$

where k_1 and k_2 are model parameters.

There are hence eleven parameters that should be fitted for each one of the cameras, i.e. the outer parameters which are three Euler angles to form ${\bf R}$ and the three lengths in ${\bf t}$ and the inner parameters; two values for the principal point, the focal length and the two parameters in the correction for radial distortions. The parameters are fitted in an interactive and iterative fashion using algorithms built into the commercial software DaVis. While fitting the parameters the user can set probable initial values and keep some parameters fixed while fitting others.

Images of a calibration plate were taken for three different z_w -positions centred around the anticipated light-sheet position. The calibration plate, see figures 12 and 13, consisted of an overhead film with printed markers fitted between two plexi-glass plates. The position of the calibration plate was changed in steps of one millimeter using a DC servo-motor translation stage.

In the present diffuser experiment it was not possible to calibrate the setup with a calibration plate at each measurement position due to limited access to the measurement section. Instead, at the beginning of a measurement the setup was calibrated in the wider exit channel of the diffuser, where it was possible to fit in a calibration plate. Then the whole setup was traversed to the position where the measurements should be taken. At this position a new calibration was performed using the self-calibration method described in Wieneke (2005).

The the self-calibration is based on cross-correlations between particle-images taken by the two cameras at the same time instant. The method allows for correction of misalignment between the calibration plate position and the actual position of the light sheet. It is also possible to correct for small relative displacements between the cameras. If the alignment between the world coordinate system and the light-sheet is perfect the cross correlation should result in zero centered correlation peaks, but if there is a displacement, such as in figure 14, it will result in a field of disparity vectors. Assuming a planar light-sheet it is then possible to calculate, using the disparity vectors, how the world coordinates should be rotated and translated in order to align the light-sheet plane. In the present experiment the disparity vector field was taken as the average of the correlation between 22 different image pairs.

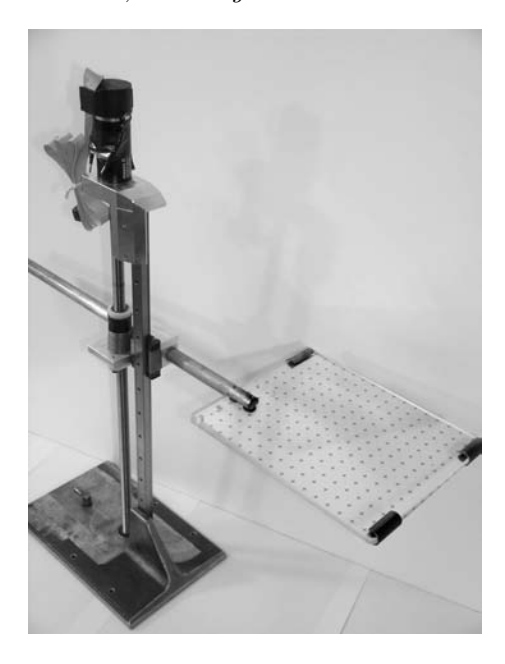


FIGURE 12. The translation stage and calibration plate setup used for the stereoscopic calibration.

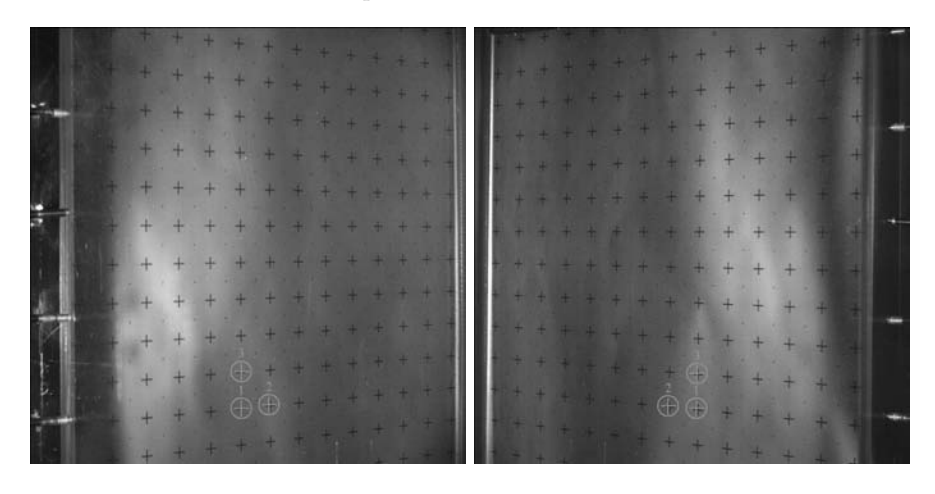


FIGURE 13. Images used for the calibration. The left image was recorded by the upper camera and the right by the lower, c.f. figure 9. The markers seen in the images are used as starting points for the marker search algorithms and for defining the world coordinates.

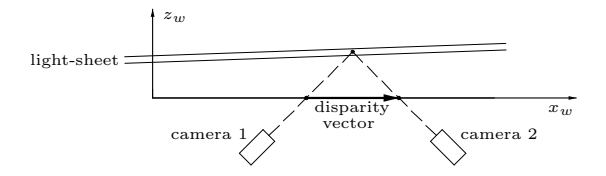


FIGURE 14. Disparity between the two cameras' images of a particle in the case of a laser-sheet and world coordinate system mismatch.

4.4. Vector computation and image pre-processing

Image a) in figure 15 shows a negative raw image taken directly from the camera. It can be seen that the light intensity is varying over the image due to reflections in the inclined wall, e.g. seen as darker band in the center of the channel, and the walls are so bright that the image sensor has been saturated. Tests showed that the best way to remove wall reflections and smooth out intensity variations was to subtract a temporal sliding average from the images. In the present experiment the temporal sliding average was derived from five, in the time series, consecutive images centered around the processed image. The result from the average subtraction is shown in image b) of figure 15. It can be seen that the wall reflections have been substantially diminished and that the particles are appearing more clearly.

The stereoscopic velocity vector fields are calculated using multi-pass cross-correlation where the first pass is performed with 64×64 pixel interrogation areas followed by two passes with 32×32 pixel areas, the interrogation areas are 50 percent overlapping. Before the cross-correlation is computed the images are dewarped according to the calibration mapping function and deformed according to the displacement field determined in previous passes, the method is similar to that of Scarano & Riethmuller (2000). Each one of the two image pairs gives two in-plane velocity components, these four components are combined to form a three component velocity field. The fact that four components are used to compute three is utilized to detect spurious vectors by demanding that the in-plane components of the computed three component field should not deviate more than 0.5 pixels from any of the two two-component fields. Spurious vectors are detected, removed and possibly replaced, using a four stage iterative median filter.

Step 1: Compute the median velocity in each direction for the eight surrounding vectors. Compute the standard deviation, in each direction, of the surrounding vectors, using the medians and disregarding the two velocities that deviate the most. Check, whether the components of the centre vector fulfils the requirement that they should not deviate from

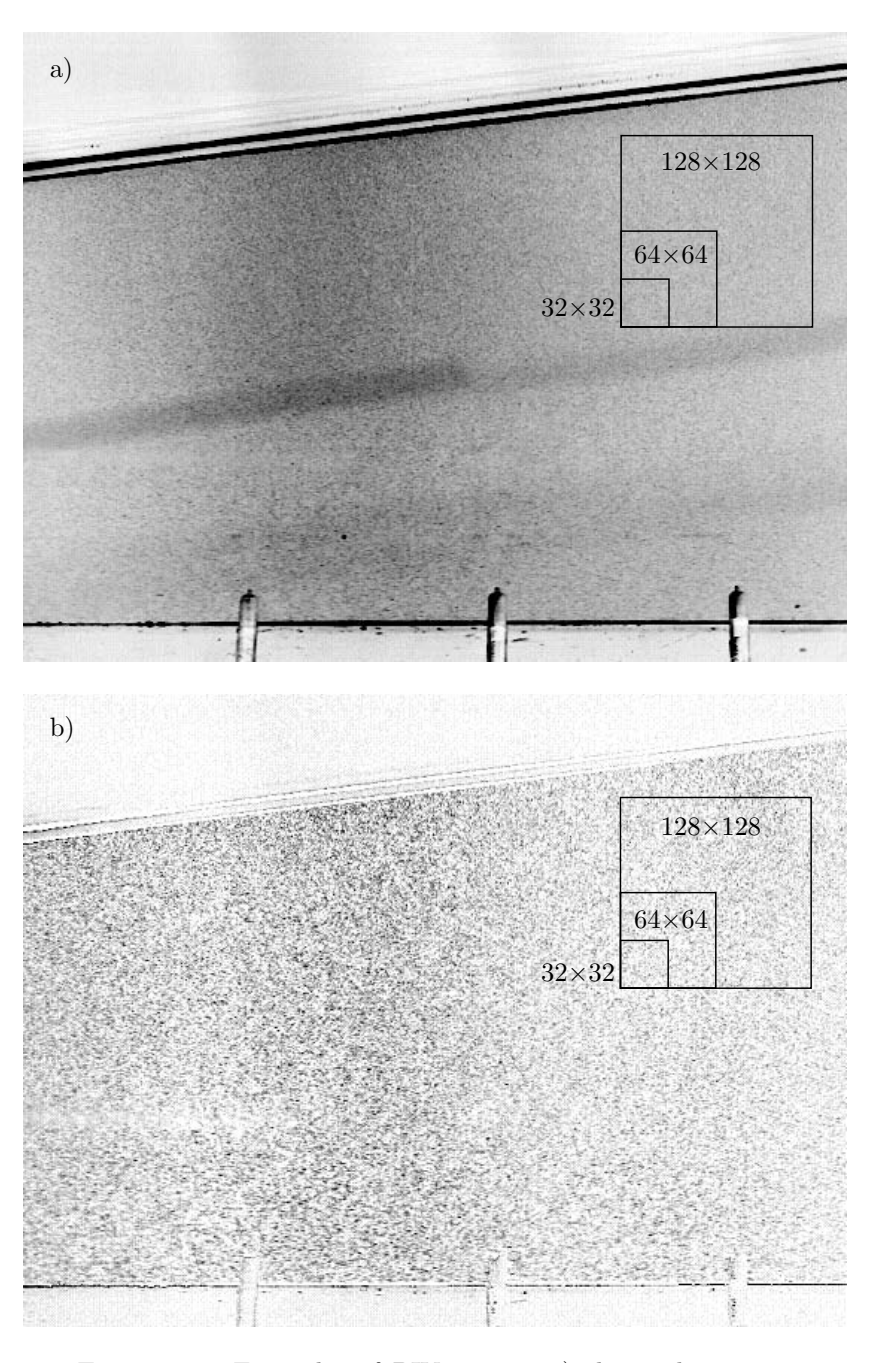


FIGURE 15. Examples of PIV-images, a) shows the unprocessed raw image and b) the image after subtraction of a temporal sliding average. The images are shown as negatives.

the median by more than a factor 2 times the standard deviation of the surrounding vectors and discard the vector if any component does not.

Step 2: Discard vectors with less than 4 neighbours.

Step 3: Fill in vectors that satisfies the requirement of not deviating more than a factor 2.5 times the standard deviation of the neighbouring vectors. The standard deviation is computed in the same way as in step 1. If the velocity given by the highest correlation peak does not satisfy the criterion the second, third and forth correlation peaks are successively tested.

Step 4: Discard any groups containing less than 5 vectors.

This method is applied to both the intermediate fields in the multi-pass processing and to the final vector-fields.

4.5. Sources of errors in PIV

The error level of a statistical quantity acquired with the PIV-technique will depend on contributions from a number of sources. Westerweel (1997) gives a theoretical basis for two-dimensional digital PIV, but most relations applies also to stereoscopic PIV. A typical value for the measurement error in digital PIV with 32×32 pixel interrogation areas is 0.05 to 0.1 pixel (Westerweel 1997), given that the measurement conditions fulfil a number of criteria. In the forthcoming sections these conditions and criteria are discussed in conjunction with the present experiment.

First of all, it is necessary that the particles are able to follow the flow and hence work as indicators of the velocity. Assuming Stokes drag, the relaxation time for a particle exposed to a sudden flow velocity change can be approximated as (Raffel *et al.* 1997),

$$\tau_s = \frac{d_p^2 \rho_p}{18\mu},\tag{12}$$

where d_p and ρ_p are the particle diameter and density and μ is the dynamic viscosity of the fluid. Assuming the particle size to be 3 μ m one finds the particle response time to be of the same order of magnitude as the Kolmogorov timescale in the inlet channel. This rough estimate give support for the underlying assumption that the air motion can be detected in the particle displacements.

PIV random error sources can e.g. be noise which can come from background disturbances, refections, poor image contrast or resolution. By careful design of the experiment these types of errors can be kept small. The background disturbances in the present experiment were kept small by having, wherever it was feasible, a dull black background in the images. Wall reflections were in some cases unavoidable in the present experiment and areas where the measurements could be affected by this was masked before the vector calculations begun. Image contrast was optimized within the restrictions posed by the available laser power by running the laser at a repetition rate close to where the pulse energy is maximal.

4.5.1. Loss of particle pairs

Particles that move into, or out of, the light-sheet, often referred to as loss of pairs, are adding noise to the correlation but may also give a bias if the average velocity perpendicular to the light sheet is nonzero or if there is a nonzero turbulence correlation (i.e. Reynolds stress) between the velocity component perpendicular to the light sheet and a velocity component in the plane of the light sheet. Errors related to loss of pairs can be controlled by adjusting the light sheet thickness and the time between the images. Keane & Adrian (1990) showed that the influence of this type of error was small as long as the relation

$$\frac{|W|\Delta t}{\Delta z} < 0.25,\tag{13}$$

between the cross-plane velocity W, the time between frames Δt and the light-sheet width Δz , is fulfilled.

The perhaps most important condition to meet in order to have a good signal to noise relation is that the particle density should be high enough, Keane & Adrian (1992) recommends that at least seven particle pairs should appear in both interrogation areas, which requires at least ten particle images in each interrogation area if the loss of pairs due to motion out of the light-sheet is kept within the limits given by equation 13.

In the present experiment the cross-plane average velocity is zero and no turbulence correlations exists between the in-plane and cross-plane velocities. The maximum turbulent velocity w_{rms} that was measured was ~ 1.3 m/s, at that measurement position $\Delta t = 100~\mu s$ which together with $\Delta z = 1.5$ mm means that more than 99% of the samples should be within the limits given by equation 13 if the probability distribution is Gaussian. Furthermore, it was made sure in all measurements that the number of particles per interrogation area was sufficient.

Another way in which pairs are lost is when particles are moving into or out from the interrogation area due to in plane motions. A remedy for this problem is to shift the interrogation areas an integer number of pixels, according to an estimate of the local velocity, so that the expected displacement measured by the cross-correlation is between 0 and 0.5 pixels. By shifting the interrogation areas another problem is also resolved, the bias towards lower velocities due to the diminishing interrogation area overlap with increasing displacement. The latter problem can also be completely resolved by dividing the computed correlation with the convolution of the interrogation windows (Westerweel 1997). However, if window shifting is used, this type of weighting of the correlations is in general not necessary since the absolute error due to this bias is very small for displacements between 0 and 0.5 pixels. The method

used in the present investigation uses interpolation to perform window shifting by fractions of pixels and no weighting was applied to the correlation.

4.5.2. Velocity gradients

A velocity gradient over an interrogation area will give rise a broader and lower correlation peak and hence a decreased signal to noise ratio. The broadening of the peak will also make it more susceptible to the type of bias, which is due to the diminishing interrogation area overlap with increasing displacement. The bias problem can, as described above, be resolved by window shifting or weighting but the widening of the peak may decrease the accuracy in the prediction of its center and noise will have a larger influence on the peak shape. Keane & Adrian (1990) and Westerweel (1997) recommends that the rule of thumb

$$\frac{|\Delta U|\Delta t}{S} < 0.03 - 0.05,\tag{14}$$

should be followed in order to maintain a decent signal to noise ratio and hence a low measurement uncertainty. ΔU and S in the above equation are the velocity variation over the interrogation area and the physical size of the interrogation area respectively. It should also be noted that smaller interrogation areas are less sensitive to velocity gradients than larger (Raffel et al. 1997). The DaVis 7.1 software used in the present investigation uses a window deformation method similar to that presented in Scarano & Riethmuller (2000) to increase the signal to noise ratio. The method utilizes the velocity fields from the multi-pass evaluation not only to translate the interrogation areas but also, by image interpolation, to rotate and deform them, this is shown by Scarano & Riethmuller to both reduce noise at small velocity gradients and also allow measurements in a greater range of velocity gradients as compared to traditional methods.

4.5.3. Peak-locking

A specific problem in PIV when using digital images is the so called peak-locking. Peak-locking is the tendency towards integer particle displacement predictions. The most important factor influencing peak-locking is the particle image diameter. Raffel et al. (1997) shows that the optimum diameter for cross-correlation PIV is 2–3 pixels, if the diameter is too small the bias due to peak-locking is dominating the measurement error and if it is too large random errors will have an increased influence on the displacement predictions. The choice of sub-pixel interpolation method used in determining the correlation peak position will also influence the peak-locking errors, e.g. Westerweel (1997) shows that a Gaussian peak fit is superior to a peak centroid in this aspect. The window deformation method introduced by Scarano & Riethmuller (2000), which uses a non-integer interrogation area shift, was shown to efficiently remove peak-locking in an experiment where the particle image diameter was 1.6

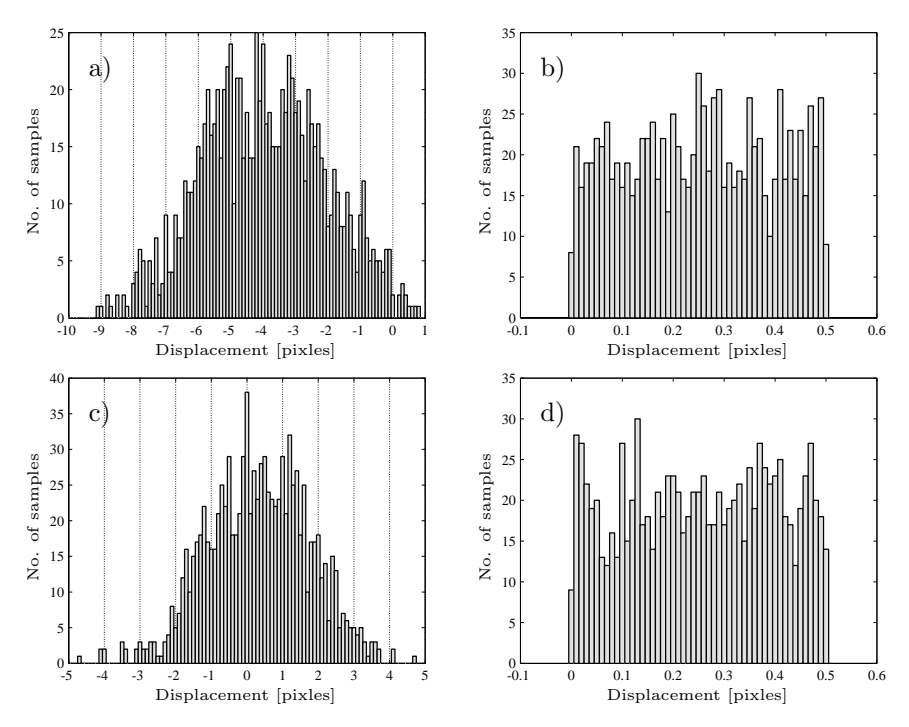


FIGURE 16. Histograms of pixel displacements samples from one point, a) streamwise component (U), b) mod(U,0.5), c) wall-normal component (V), d) mod(V,0.5).

pixels. The particle image size in the present investigation is estimated to be approximately two pixels. Figure 16 shows histograms of the velocities measured at $x \approx 25$ and $y \approx 2.5$, the histograms were taken from cross-correlations of images from a single camera so that smearing of any peak-lock errors due to the three component recombination is avoided. The modulus after division of the displacements with 0.5 is also shown in figure 16, this quantity gives a good indication of the amount of peak-locking that is in the data, with a large ratio of peak-locked samples the modulus is shifted towards zero and with no peak-locking the modulus should be evenly spread out over the interval. The conclusion drawn from figure 16 is that it is reasonable to assume that the peak-locking errors of the measurements are small.

4.5.4. Stereoscopic errors

In the present stereoscopic setup the measured displacements in the x, y and z directions are approximately given by

$$\Delta x \approx \frac{\Delta x_1 + \Delta x_2}{2}$$

$$\Delta y \approx \frac{\Delta y_1 + \Delta y_2}{2\cos 30^{\circ}}$$

$$\Delta z \approx \frac{\Delta y_2 - \Delta y_1}{2\sin 30^{\circ}},$$
(15)

respectively. Indices in the above relations refer to the two cameras and 30° is the angle between the cameras' optical axes and the measurement plane normal. Assuming that the uncertainty of the measured displacements in each image is the same in both directions and that it has the standard deviation ϵ_{rms} results in the following root mean square uncertainties in the displacements:

$$\Delta x_{rms} \approx \frac{\epsilon_{rms}}{\sqrt{2}} \approx 0.7 \epsilon_{rms}$$

$$\Delta y_{rms} \approx \frac{\epsilon_{rms}}{\sqrt{2}\cos 30^{\circ}} \approx 0.8 \epsilon_{rms}$$

$$\Delta z_{rms} \approx \frac{\epsilon_{rms}}{\sqrt{2}\sin 30^{\circ}} \approx 1.4 \epsilon_{rms}.$$
(16)

This means that the precision of the measured in-plane velocities will be slightly better as compared to non-stereoscopic PIV measurements and that the out of plane component will have an uncertainty which is roughly twice that of the other components.

Imperfection in the stereoscopic setup and calibration, such as misalignment between the calibration plate and the light sheet, may introduce considerable errors. Such misalignments will result in a mismatch between the particle images of the two cameras when these are mapped to the measurement plane, the size of this mismatch, δx , is sometimes called registration error. Van Doorne (2004) points out that

$$\left| \frac{\partial U}{\partial x} \right| \Delta t \delta x \ll 0.1 \quad \text{pixel}$$
 (17)

in order for the for the measurement error not to be dominated by the registration errors.

The self-calibration method used in the present investigation ensure that $\delta x < 0.1$ pixel and the maximum Δt in the measurements was 100 μ s, thus $|\partial U/\partial x|$ must be $\ll 10^4$ for equation 17 to be satisfied. This requirement corresponds to the requirement that the distance between two consecutive points in a velocity profile of figure 17 should be $\ll 6.4H$, so equation 17 can be considered fulfilled for all points in figure 17. The points in the first four or

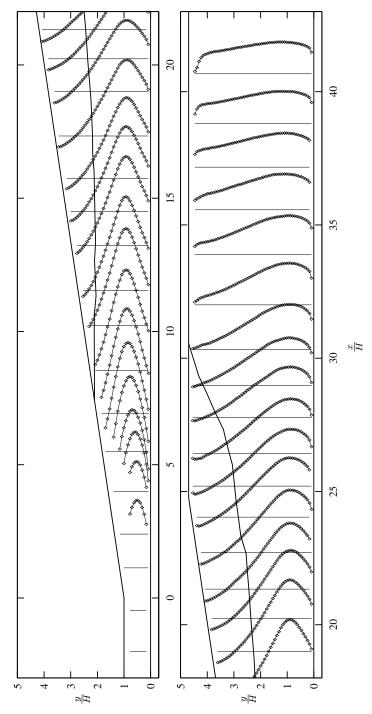


FIGURE 17. Streamwise mean velocity, $(U_{\rm fig} = 5U/U_b + x/H)$. The vertical lines indicate zero level for each streamwise velocity profile and a solid contour indicates the path of the dividing streamline.

five profiles in the diffuser were measured with a Δt of 50–70 μ s so here the requirement is instead that the distance should be $\ll 9-12.8H$.

4.5.5. Spatial filtering

A velocity vector, measured with two-dimensional PIV, will be the average velocity in a measurement volume constituted by the thickness of the light-sheet and the dimensions of the interrogation area. This averaging will, if the size of the measurement volume is larger than the smallest scales of the turbulent flow, result in a spatial low-pass filtering of the velocity field. Measured mean velocities are not affected by the spatial filtering, but the measured second order statistics will be biased towards lower values since the energy residing in the high wave-number part of the turbulence spectrum will be filtered away.

In stereoscopic PIV the measurement volume will be larger than the interrogation areas in one of the in-plane directions due to the oblique viewing. In the present setup, the measurement volumes are elongated in the y-direction. A comparison of the second order turbulence statistics measured in the present stereoscopic setup with finer resolved two-component measurements revealed that the stereoscopic data was biased towards lower turbulence levels due to spatial filtering.

Acknowledgements

The authors would like to thank Ulf Landén and Marcus Gällstedt for aiding in the manufacturing of the wind-tunnel and measurement equipment. The Swedish Research Council and The Swedish Energy Agency are gratefully acknowledged for their financial support.

References

- Angele, K. P. & Muhammad-Klingmann, B. 2005 PIV measurements in a weakly separating and reattaching turbulent boundary layer. *Eur. J. Mech. B/Fluids* **25**, 204–222.
- Buice, C. U. & Eaton, J. K. 1997 Experimental investigation of flow through an asymmetric plane diffuser. *Tech. Rep.*. Department of mechanical engineering, Stanford university.
- CHERRY, N. J., HILLIER, R. & LATOUR, M. E. M. P. 1984 Unsteady measurements in a separated and reattaching flow. J. Fluid Mech. 144, 13–46.
- CHITHAMBARAN, V. K., ASWATHA, P. A. & CHANDRASEKHARA SWAMY, N. V. 1984 Mean velocity characteristics of plane diffuser flows with inlet velocity distortion. J. Indian Inst, Sci. 65(A), 79–93.
- Comte-Bellot, G. 1965 Écoulement turbulent entre deux paroix parallèles. Publications scientifiques et techniques 419. Ministère de l'air, 2, Avenue de la Porte-d'Issy, Paris.

- DIANAT, M. & CASTRO, I. P. 1991 Turbulence in a separated boundary layer. J. Fluid Mech. 226, 91–123.
- VAN DOORNE, C. W. H. 2004 Stereoscopic PIV on transition in pipe flow. PhD. Thesis, Technische Universiteit Delft, ISBN 90-9018499-6.
- ETHERIDGE, D. W. & KEMP, P. H. 1978 Measurements of turbulent flow downstream of a rearward-facing step. J. Fluid Mech. 86, 545–566.
- Johansson, A. V. & Alfredsson, P. H. 1982 On the structure of turbulent channel flow. J. Fluid Mech. 122, 295–314.
- JOHANSSON, A. V. & ALFREDSSON, P. H. 1986 Structure of tubulent channel flows. In *Encyclopedia of Fluid Mechanics*, chap. 25, pp. 825–869. Gulf publishing company.
- Keane, R. & Adrian, R. 1992 Theory of cross-correlation in PIV. Applied scientific research 49, 191–215.
- Keane, R. D. & Adrian, R. J. 1990 Optimization of particle image velocimeters. Part I; double pulsed systems. *Meas. Sci. Technol.* 1, 1202–1215.
- Laws, E. & Livesey, J. 1978 Flow through screens. Ann. Rev. Fluid Mech. 10, 247–266.
- LINDGREN, B. & JOHANSSON, A. V. 2002 Design and evaluation of a low-speed wind-tunnel with expanding corners. Technical report ISRNKTH/MEK/TR-02/14-SE. Dept. of mechanics, KTH.
- Obi, S., Aoki, K. & Masuda, S. 1993 Experimental and computational study of turbulent separating flow in an asymmetric plane diffuser. In *Ninth Symp. on Turbulent Shear Flows*, p. 305. Kyoto, Japan.
- Perry, A. E. & Fairlie, B. D. 1975 A study of turbulent boundary-layer separation and reattachment. *J. Fluid Mech.* **69**, 657–672.
- RAFFEL, M., WILLERT, C. & KOMPENHANS, J. 1997 Particle Image Velocimetry, A practical guide. Springer Verlag.
- Ruderich, R. & Fernholz, H. H. 1975 An experimental investigation of a turbulent shear flow with separation, reverse flow, and reattachment. *J. Fluid Mech.* **163**, 283–322.
- Scarano, F. & Riethmuller, M. L. 2000 Advances in iterative multigrid piv image processing. *Exp. Fluids* **29** [Suppl.], S51–S60.
- SOVRAN, G. & KLOMP, E. D. 1967 Experimentally determined optimum geometries for rectelinear diffusers with rectangular, conical, or annular cross-section. In *Fluid mechanics of internal flow* (ed. G. Sovran), pp. 270–319. Elsevier publishing company.
- Taylor, G. & Batchelor, G. K. 1949 The effect of wire gauze on small disturbances in a uniform stream. *Quart. J. Mech. and App. Math.* 2, part 1,1.
- TÖRNBLOM, O., LINDGREN, B. & JOHANSSON, A. V. 2006 Measurements of mean flow statistics in a plane asymmetric diffuser with 8.5° opening angle. *To be submitted* (Paper 1).
- Westerweel, J. 1997 Fundamentals of digital particle image velocimetry. *Meas. Sci. Technol.* 8, 1379–1392.
- WIENEKE, B. 2005 Stereo-PIV using self-calibration on particle images. *Exp. in Fluids* 39, 267–280.

Yoshioka, S., Obi, S. & Masuda, S. 2001 Turbulence statistics of periodically perturbed separated flow over backward facing step. *Int. J. Heat Fluid Flow* **22**, 391–401.

TRITA-MEK
Technical Report 2006:15
ISSN 0348-467X
ISRN KTH/MEK/TR-06/15-SE
ISBN 91-7178-416-0